

Czech Technical University in Prague

Faculty of Electrical Engineering
Department of Control Engineering



**A phonon-based approach
to describe and harness
nanoscale friction**

Habilitation Thesis

Antonio Cammarata

Prague, 2022

Habilitation Thesis in partial fulfillment
of the requirements to get the title of
“Associate Professor”

Department of Control Engineering
Faculty of Electrical Engineering
Czech Technical University in Prague
Prague, Czech Republic, 2022

To my wife Francesca,
my brother Vincenzo
and my family

Contents

Preface	7
Introduction	9
1 Atom-scale models	13
1.1 Molecular Dynamics	14
1.2 Ab initio	16
1.3 So far, a common approach to model friction	17
2 Phonon theory of friction	21
2.1 Phonons	21
2.2 Sliding and dissipative modes	25
2.3 Phonon-phonon scattering rules	28
2.4 The “Normal-Modes Transition Approximation”	30
2.5 The cophonocity metric	33
2.6 Case study: MX ₂ Transition Metal Dichalcogenides	35
3 Design of new tribological materials	37
4 Effect of load	41
5 The role of charge	47
6 Electrostatic field as an external knob	53
7 Inert intercalant as friction modifier	57
8 Nanofriction in thin films	65
Acknowledgements	73
Copy of selected published papers	85

Preface

When I began my work at the Czech Technical University in Prague, I barely knew what tribology means. I was asked to model nanoscale friction in transition metal dichalcogenides by means of quantum mechanics. The first issue was to understand how to separate the total force acting on moving atomic layers into “cohesive” forces, which keep the atoms together, and “frictional” forces, which oppose the motion and transform the net ordered layer drift into disordered atomic oscillations about their equilibrium positions. Speaking with my colleague Paolo, who uses Molecular Dynamics techniques, I learnt that this could be done with a classical description: the total force is a sum of the interactions between the atoms within each layer plus a term which represents the interaction between the two layers. Still, the latter is also responsible of the integrity of the system... and quantum mechanically this is a nightmare! How could I partition in a unique way the interactions if the system response is the result of the electronic distribution as a whole? I therefore arrived at the conclusion that I had to change point of view and build a general description of the frictional force: instead of focusing on the energetic aspect of the problem, I had to pay more attention on how to properly describe the atom dynamics. There is a universally acknowledged way to partition the interatomic potential into single contributions, yet considering the Hamiltonian as a whole without any a priori partition: the phonon modes. By exploiting the phonon theory, I did not need to identify which terms of the Hamiltonian represent the friction forces any more; instead, I was able to recast the friction definition in terms of phonon decompositions. Each phonon carries the information about the atomic displacements (eigenvector) and the forces generating such displacements (eigenfrequency). Being the phonon eigenvectors a basis, I could then describe the sliding by a linear combination of phonons! And that’s how all this started...

In this thesis, I will use “we” mostly to refer to myself and the readers together: I like to imagine that we are going to build the phonon-based description of friction together, step by step.

Introduction

If we slide one body over another, a force opposing the motion appears; we call such force *friction*. Together with wear, adhesion and lubrication, friction is one of the topics of tribology, i.e., the science studying interacting surfaces in relative motion.^{1,2} Friction is the cause of a significant amount of wear, fault of devices and energy loss in operative conditions, affecting a vast variety of technological applications, spanning transportation, industry, power generation and nanoscale devices:³ active control of friction it is then mandatory for a sustainable development.⁴ Since the first attempts to study the nature of friction,⁵⁻⁷ it was clear that: *i*) the frictional force is directly proportional to the total force acting normal to the sliding surfaces (i.e. *applied load*), *ii*) the frictional force is independent of the apparent area of contact at a constant load, and *iii*) the frictional force depends on the nature of the materials in contact. The latter observation is clearly the crucial one and leads to the following fundamental questions: What is the origin of friction? How can we control it? In order to answer such questions, we need a deep knowledge of the atomic details of the materials and a full comprehension of the fundamental physical processes occurring at the nanoscale. To this aim, in the present thesis, I focus on the elaboration of a nanoscale description of friction based on quantum mechanics; this work is then inserted in the recently emerging field of *nanotribology*, i.e. the study of friction, wear and lubrication at the nanoscale.

It is known that the macroscopic friction is the result of the interplay of several processes occurring at different scales;⁸ the quantum description poses itself in the explanation of the elementary phenomena at the basis of such processes, and finds immediate application in the technological fields involving nanostructured devices. In fact, manipulation and assembly of free-standing atomic layers into final devices, and their use in micro-/nano-electromechanical systems (MEMS/NEMS, e.g. sensors and actuators) require a deep knowledge and control of the friction originating in working regime.⁹ Mobile atomic layers during the device fabrication and its operation are subject to non-conservative forces active during the relative motion of the involved surfaces; those forces limit the output efficiency by producing heat, fatigue and wear up until compromising the correct construction or functioning of the device. Nanofriction and wear occur also in magnetic storage^{10,11} and biotribological devices such as human joint prosthetics, dental materials and skin, among others, where the ecological aspects must be taken into account.¹²⁻¹⁶ Moreover, massive usage of tactile interfaces boosted numerous studies in understanding sensing through contact and friction,¹⁷ and in reproducing interactive haptic feedback.¹⁸⁻²⁰ It is then manifest that the comprehension of the mechanisms governing friction at the nanoscale is a forefront challenge to design new tribological materials, save energy and increase lifetime, sustainability and performance of both miniaturised and macroscopic scale devices.

Usually, experimental models of nanoscale friction are based on trial and error, and are specific of the studied materials; at the moment, there is no theory which

tells us what is the friction coefficient given the atomic description of two surfaces in contact. The control of friction and the design of new tribological materials with target friction response can then be hardly obtained by using purely experimental models. Also, it is auspicious that the friction can be controlled on-the-fly by the user, e.g. by means of electric fields^{21,22} or suitable light irradiation (*photofriction*).²³ In these latter cases, quantum mechanical effects have to be included in the models. An atomic scale definition of friction is therefore mandatory to provide a deep and, possibly, complete understanding and control of the underlying phenomena. Moreover, accurate computational models are crucial to obtain guidelines on how to narrow the experimental search of new tribological materials, thus to reduce the relative human effort and material costs. Various classical and quantum mechanical approaches have already been built up to study friction at the atomic scale, relying on ad hoc defined interatomic force formulations or parameter-free ab initio descriptions.^{24–27} The reliability of such approaches depends on the balance between the accuracy of the system-dependent parameterizations and/or the width of the simulated time-window, the latter being computationally demanding if ab initio methods are to be used.^{28–34} I therefore try here to achieve the main goal to extract information on the frictional and dissipative properties of a system from the only knowledge of its static properties at the atomic level, without the need to perform long and costly dynamic simulations; in parallel, the challenge is to develop a quantum mechanical system-independent framework which is applicable to any kind of chemistry and atomic topology. To this aim, the phonon theory represents as promising a solution as viable: its definition is universal and provides both a geometric and a dynamic description of the system. Indeed, recent discussions on the role of phonons in tribological systems seem to support this approach.^{35–40}

The sequence of geometric configurations representing the layer sliding can be decomposed in terms of the polarization vectors obtained by diagonalization of the dynamical matrix at any point of the reciprocal space.^{41,42} This allows one to recast the study of the frictional response in terms of *sliding* and *dissipative* phonon modes.⁴³ The sliding modes are associated to relative shifts of adjacent atomic layers. In terms of the classical picture, each of these modes is characterized by a harmonic restoring force $f \propto \omega^2$, where ω is the mode frequency; by lowering the mode frequency, it is then possible to lower the restoring force and hence facilitate the layer sliding. By going beyond the local harmonic description,⁴³ we observed that the layer sliding occurs as long as the energy contained in the sliding modes (i.e. their population) is above a certain threshold characteristic of the material. The dissipative modes instead are all those modes which subtract energy from the sliding modes by means of phonon recombination processes. Such processes correspond to energy dissipation, since they degrade the ordered motion (sliding) into disordered vibrations (heat); in this way, we can define the *frictional forces* as those forces corresponding to the phonon scattering events which reduce the population of the sliding modes. In the following chapters, I then discuss which are the relevant quantities at the nanoscale that determine the appearance of such forces and their related energy dissipation, and how to act to deactivate specific dissipation channels.

To summarise, in this thesis work I try to address the following questions: What is the atomic origin of friction? Is it possible to obtain a model of the nanofriction response without using long demanding dynamics simulations? Can we formulate a universal system-independent framework applicable to any tribological system, and capable to guide the design of new tribological materials with on-demand response? The answer is yes: we will do it by exploiting the information obtained from the phonon

modes of the reference structure at the quantum mechanical level. Since the phonon description is valid about small geometric displacements from the reference geometry (usually the equilibrium one), its validity might appear limited; indeed, we will see that the phonon description of the nanofriction is valid also far from the equilibrium configuration. The results of this work then represent a paradigm shift in the study of nanoscale friction: we can obtain information on out-of-equilibrium processes by means of equilibrium references. As prototypical case studies, I consider the transition metal dichalcogenides (TMDs)^{44,45} class of materials, which have been one of the main subjects of my scientific research since my first position as a postdoctoral researcher at the Advanced Materials Group.^a

^aThe “[Advanced Materials Group](#)” is part of the Department of Control Engineering, Faculty of Electrical Engineering, Czech Technical University in Prague.

Chapter 1

Common atom-scale friction models

In a recent review,⁸ we summarised the late advances in modeling and simulating tribological systems, also covering multiphysics phenomena, scale effects, and the breakdown of continuum theories at the micro- and nanoscales. If on the one hand continuum mechanics (e.g. Finite Element Method⁴⁶ or Boundary Element Method⁴⁷) allow to treat system sizes suitable for immediate engineering applications ($\sim 10^{-2} - 10^0$ m), on the other hand the development of miniaturised devices and the design of new tribological materials at large require predictive models involving matter descriptions with atomic resolution. In fact, the friction occurs when adjacent atom surfaces are forced to slide one relatively to the other: the interaction between the two surfaces generate forces which hinder the relative motion. A natural choice to model such dynamic system is to represent the sliding motion as a sequence of atom geometries (often called *snapshots*), and to study the relation among them, that is, to describe the evolution of the system response in the presence of external stimuli. The first approaches in this direction were based on the use of classical Molecular Dynamics (MD),^{48,49} with the aim to reproduce the physical, chemical and mechanical phenomena occurring in tribological conditions⁵⁰⁻⁵⁵ and for predictive purposes.⁵⁵⁻⁶⁴ The main limitation of the classical MD framework is that the interactions among a given set of atoms are defined by analytical functions parametrized according to the specific environment in which the atoms are embedded,⁶⁵ limiting the transferability of the description at varying chemical composition.⁶⁶ The MD approach is not then able to provide thorough information in terms of surface reactivity, bond formation and evolution of electronic structures; moreover, the classical picture does not take into account the quantum nature of the atoms, and is not then able to properly account for the electronic function governing the interactions or to reproduce the response of the material under external electric and/or magnetic field stimuli. The use of ab initio techniques overcomes these problems: since they rely on the Schrödinger equation, the atomic description is independent of the system, and the interatomic forces ruling the tribological response derive from the solution of the equation, instead of being an *a priori* input of the problem as in the classical picture. However, compared to the classical MD, the increased accuracy provided by the ab initio methods is paid in terms of an increased computational cost, which limits the size of the model system.

The use of classical or ab initio methods to model tribological materials is then dictated by the compromise between the kind of information that is needed, the required simulation time and the amount of computational resources at own disposal. In what

follows, we will briefly review how classical Molecular Dynamics or quantum mechanical methods have been used to study the tribological response at the nanoscale.

1.1 Molecular Dynamics

Molecular Dynamics (MD) simulation is a technique aimed to compute the physical properties of an N -atom system by integrating the Newton's equation of motion

$$m_i \ddot{\mathbf{r}}_i = \mathbf{F}_i \equiv -\nabla_i V(\mathbf{R}) \quad (1.1)$$

for each i -th atom. In this equation, m_i and $\ddot{\mathbf{r}}_i$ are the mass and the acceleration of the atom, while \mathbf{F}_i is the force acting on it due to the energy potential V , the latter depending on the position of all the atoms forming the system ($\mathbf{R} = (\mathbf{r}_1, \dots, \mathbf{r}_N)$). In classical Molecular Dynamics, V (the *force field*) is provided as an input of the simulation:⁶⁵ it depends on the atomic types and, in the majority of the cases, on the geometry of the system. An exception is represented by those formulations which allow variations of the atom topology during the time evolution of the coordinates (*reactive force fields*);⁶⁷ however, the latter are still tuned to specific chemical systems and reactions.⁶⁸ If the force field is not available in the literature, it must be developed or parameterised for the case of interest, this being a time and resource demanding procedure.⁶⁹ It is then immediately apparent that the main limitations are represented by the availability of the force field, the restricted transferability of the description and the lack of quantum effects. Nonetheless, the classical picture allows to treat up to tenth of millions of atoms, representing system sizes of the order of micrometer.⁷⁰ In the following, we review some examples on how MD simulations are used to study the friction response in systems with typical length scales of the order of hundreds of nanometers; this corresponds to model geometries including hundreds of thousands of atoms, such number being necessary to encompass most of the physical phenomena occurring in tribological conditions over long distances (e.g. Joule heating, cracks, wear, plasticity, heat transfer and roughness among others).

Molecular dynamics simulations of scanning force microscopy experiments have been performed to study the friction occurring at the sliding interface between amorphous carbon tips and diamond (Figure 1.1).⁵² In this work, the authors studied the transition from sublinear to linear dependence of the friction force as a function of the applied load, finding a detailed relation with the contact roughness. Another work investigated on the role of carbon nanotubes used as additives to nitrile-butadiene rubber.⁷¹ The simulations indicate that an increase up to 60% in shear modulus of the composites is achieved by introduction of carbon nanotubes. Moreover, the atom concentration, the peak temperature and atom movement velocities, the average cohesive energy in the friction interface region between the polymer matrix and the sliding layers, and the average friction stress of the sliding layers are all decreased, thus favouring improved tribological properties. Other studies⁷² examined the loading process among silicon substrate, silica cluster and polyurethane pad, showing that the contact status between the abrasives and pad will change from an elastic to plastic contact with increase of working pressure. From such MD simulations, they established a unified mechanical model for the single abrasive during chemical mechanical polishing under different loads. Several studies have been performed on amorphous carbon or diamond-like carbon (DLC) interfaces,⁷³ where the role of the carbon orbital hybridization has been related to the frictional properties. Si-doped DLC at different doping concentrations have been simulated to determine the sliding friction between DLC and Si-DLC films on an

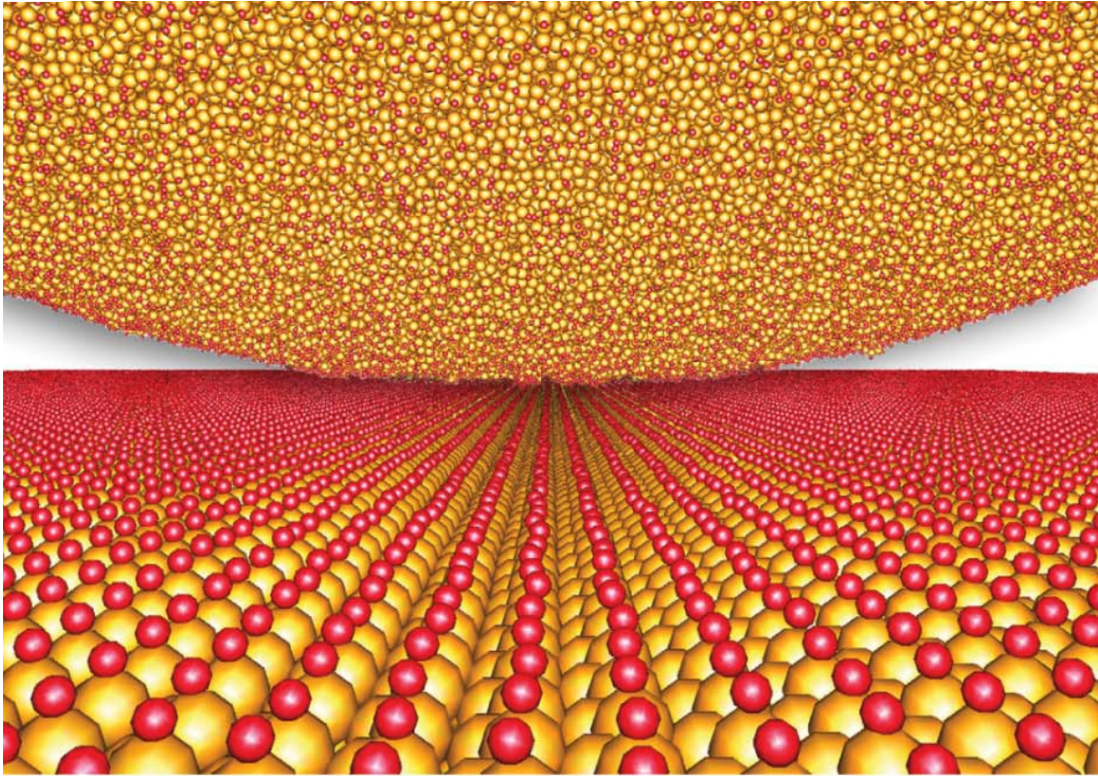


Figure 1.1: Example of model geometry used in MD simulations to study nanofriction: contact between an amorphous carbon tip and a diamond sample. Adapted from Ref. 52.

un-lubricated boundary condition.⁷⁴ The results show that addition of silicon content increases the sp^3/sp^2 ratio, determining a transfer film between the DLC and Si-DLC; this points at a friction force variation with the silicon content. In these two latter works, the orbital hybridization has been inferred from the coordination environment of the carbon atom. The influence of Cu nanoparticles on the tribological behaviour of a system has been studied as a function of the temperature, showing that temperature distribution and anti-wear properties are significantly improved by the presence of the nanoparticles.⁷⁵ The tribology behaviors of diamond and silicon dioxide nanoparticles have been investigated by considering four cases:⁷⁶ *i*) At low velocity and low load, the nanoparticles acted as ball-bearings, improving plastic deformations, temperature distribution, and friction force response; *ii*) At increased load, the SiO_2 nanoparticles crushed with a subsequent loss of the rolling effect; *iii*) Without nanoparticles, a transfer layer is observed at high velocity and low load; and *iv*) At high velocity and high load, the support effect of the nanoparticles was lost in a short sliding time.

These are examples on the advantage in using the MD technique to study nanoscale friction. However, the price to pay for such large scale simulations is to neglect quantum effects, which can be accounted only by *ab initio* simulations.

1.2 Ab initio

The term *ab initio* indicates all the simulation techniques that rely on the Schrödinger equation⁷⁷

$$i\hbar \frac{\partial \Psi(\mathbf{r}, t)}{\partial t} = \hat{H}(\mathbf{r}, t) \Psi(\mathbf{r}, t), \quad (1.2)$$

where $\hat{H}(\mathbf{r}, t)$ is the Hamiltonian representing the energy of the system and its interaction with the environment, while $\Psi(\mathbf{r}, t)$ is the solution which allows to calculate any physical observable of the system.^{78,79} The Hamiltonian is an operator which depends on the atomic types, the number of atoms and their interactions, and is free from any ad hoc parameterisation: once we select the system of our interest and the external stimuli, \hat{H} is precisely defined, and no effort is required to ensure that it is suitable for our study. It is then already apparent that the use of ab initio methods has the advantage to be able to study any tribological system, irrespective of its chemical composition, atom geometry and tribological conditions. However, the exact solution of the Schrödinger equation is possible only for the case of the hydrogen atom in which relativistic effects have been neglected; in all the other cases, including then nanotribological materials, $\Psi(\mathbf{r}, t)$ and \hat{H} must be approximated by numerical methods, requiring considerable computational resources.^{79,80} This limits the use of ab initio methods to systems of hundreds of atoms, in order to reduce the computational load and make affordable the search for the solution; the price to pay is to limit the dimensions of the system and focus on local aspects of the tribological response. Several static and dynamical approaches have been used to study tribological systems, whereas the former approaches rely on the time-independent Schrödinger equation,^{78,79} while the latter on ab initio molecular dynamics techniques;⁸¹ in what follows, we will briefly revisit such studies and what pieces of information are able to provide.

Static ab initio descriptions have been combined with high-throughput techniques to obtain the adhesion energy and the ideal interfacial shear strength,⁸² corresponding to the energy required to separate two surfaces from contact and to the static friction force per unit area, respectively. The sliding behaviour of carbon films and layered MoS₂ have been investigated in the presence of water,^{83,84} pointing at possible applications in the biomedical field. Another study⁸⁵ focuses on the frictional figures of merit of layered honeycomb nanostructures, such as graphane, fluorographene, MoS₂ and WO₂, showing that the intrinsic stiffness favours dissipationless continuous sliding. A quasi static model has been developed as an attempt to explain the microscopic origin of the nanofrictional response in dry and wearless systems.⁸⁶ Ab initio molecular dynamics simulations have been used to study the tribochemical reactions involving organophosphorus additives at iron interfaces, allowing to understand the role of phosphorus-based additives in boundary lubrication.⁸⁷ Sodium passivation of iron oxide surfaces has been studied by means of potential energy surface (PES) maps (Figure 1.2); the results show that high shear strength and lateral friction of iron oxide surface are caused by the formation of the Fe–O covalent bonds for some lateral arrangements, while the adsorption of sodium greatly reduces the lateral friction by significantly reducing the sliding barriers across the PES.⁸⁸ The static tribological properties of phosphorene have been studied by mapping the electronic response of the layers to shear stress;⁸⁹ the origin of superlubricity is ascribed to the equivalency among the localized bonds between adjacent layers, thanks to an equal charge accumulation that produces a flat PES. The nanofriction in sliding transition metal dichalcogenides have been studied by observing the evolution of the electronic distribution along selected sliding paths:⁹⁰ they reveal the dependence of

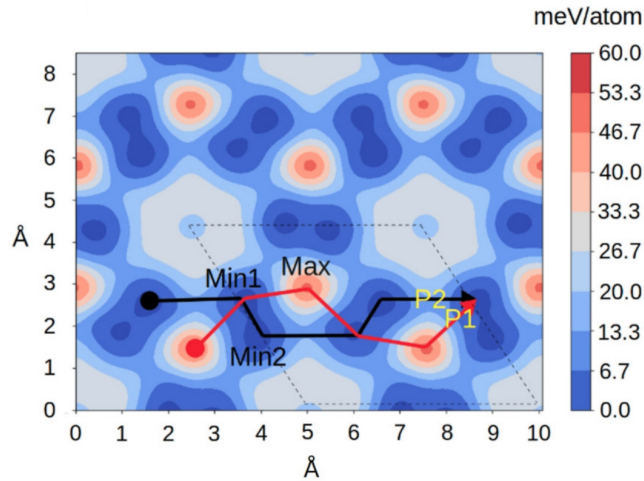


Figure 1.2: Example of static ab initio study on nanofriction: potential energy surface as a function of relative displacement of two oxide layers. The black and red solid lines indicate the minimum and maximum energy pathways, respectively, while the dashed line represents a unit cell. Adapted from Ref. 88.

shear strength on chemical composition and bilayer orientation, highlighting the role of charge accumulation in the interlayer region. Other examples can be found in a recent review,⁹¹ where the authors report theoretical works on dry friction, the role of passivation and lubricants, and the effect on photoexcitation.

1.3 So far, a common approach to model friction

All the attempts to model the frictional response at the nanoscale, including those listed above, share common features, regardless of whether they make use of classical or quantum mechanical descriptions.

As mentioned at the beginning of this chapter, the study of nanoscale friction is usually based on model geometries which represent the sequence of the atomic positions during the relative sliding of facing surfaces. Such sequence is either obtained by solving the equations of motion for a given starting atom configuration and velocity distribution, or by manually creating geometry snapshots along a configurational coordinate; an example is reported in Figure 1.3, where two adjacent WS_2 layers are displaced along one crystallographic direction. While the use of dynamics is more common within the classical description, the use of static snapshots to calculate PESs is typical of quantum mechanical studies, as the latter requires less computational effort. However, static PESs do not contain information about the effect of the temperature on the sliding energy barriers: although they might represent an average configuration at a certain temperature, the thermal motion of the atoms is completely neglected. Indeed, the temperature plays a fundamental role in the determination of the friction coefficient, as it strongly affects the potential energy, hence the sliding barriers.^{92–97}

In the attempt to distinguish the frictional forces from the remaining ones, the general tendency is to associate them to energy terms representing the interactions between the atoms forming the surfaces in relative motion. If a classical description is used, this can be done by selecting the atoms on the surfaces and collecting all the energy terms generating to the forces between such atoms. This approach suffers from

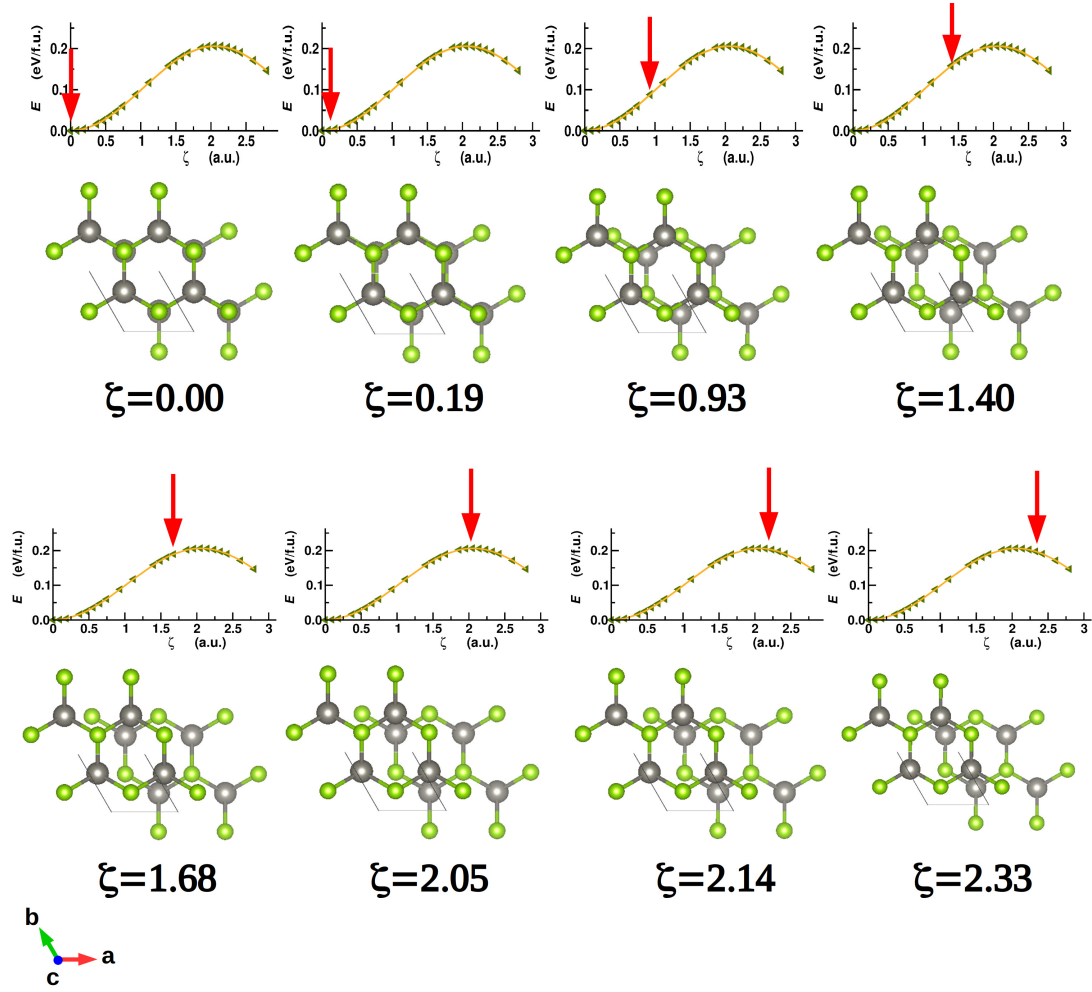


Figure 1.3: Example of geometric sequence representing the relative sliding of two facing WS_2 layers. The snapshots have been obtained by displacing the reference configuration along the \mathbf{a} crystallographic axis at increasing amplitudes of the configurational coordinate ζ . At each snapshot, the total energy is calculated in order to obtain the potential energy barrier to overcome along the sliding path.

the non-general definition of the potential energy, hence producing a system-dependent definition of the friction force; moreover, the atoms not on the surface are neglected, despite the fact that they might have an important role, especially if they are directly bonded to those forming the surface. This attempt fails if quantum mechanics is used. In this case, the forces are not obtained directly from the expression of the potential energy but are evaluated by means of the Hellmann-Feynman theorem, which relies on the wavefunction solution of the Schrödinger equation representing the whole system. In principle it is possible to partition the forces acting on the surface atoms into contributions coming from all the remaining atoms, by projecting the wavefunction onto suitable atom-centered basis sets; in this way, one can identify which atoms not lying on the surface should be included in the description. However, this is not enough to distinguish the frictional forces from the cohesive ones holding the atoms together during the sliding, the latter being responsible for the integrity of the surfaces. We must recall here that the friction force arising during the relative sliding is not due to only the atoms forming the sliding surfaces, but also due to the long-range interactions

involving also the remaining atoms, the latter also determining the properties of the surfaces. We then understand that the association of the friction force to a particular energy term or force contribution is arbitrary and system-dependent.

Therefore, it is clear that the nanoscale friction is the response of the system as a whole and the proper description of it requires a holistic approach. Ideally, the atomic interactions should be taken into account by avoiding arbitrary partitions into atomic contributions, and the definition of the friction force should arise from dynamic considerations rather than from specific energy terms. Therefore, we need a paradigm change in the study of the nanoscale friction; for this purpose, we will exploit the phonon theory. The phonon eigendisplacements represent independent collective movements of all the atoms in the structures, then capable to carry the geometric information representing the sliding; the related eigenfrequencies are instead a measure of the forces generating the eigendisplacements, therefore containing the information on the dynamics of the system. The phonon framework is not system dependent and applies to both periodic and non-periodic structures; the former are usually used to represent large contact surfaces, while the latter to study edge effects in finite systems, as in the examples mentioned in the previous sections. In the following chapters, we will see how the phonon description is able to describe the relative sliding of atomic surfaces and the corresponding frictional forces; moreover, we will see that, although the phonon description is obtained from a reference configuration, it is capable to predict the tribological response in working conditions far from the equilibrium. It is then clear that the phonon framework avoids the calculation of long dynamics simulations, then reducing the computational requirements usually needed to study the non-equilibrium processes occurring in tribological conditions.

Chapter 2

The phonon-based description of friction

As we saw in [chapter 1](#), if we want to develop a holistic and general description of the nanoscale friction, we need a paradigm change with respect to the usual modeling approaches. To this aim, we exploit the phonon theory, which is applicable to any kind of system, irrespective of the chemical composition and atom topology. We will see that the phonon-based framework that we are going to define is able to provide information on the tribological response by avoiding expensive dynamics simulations, thus considerably reducing the computational demand. In this chapter, we will describe the relative motion of facing atom surfaces in terms of phonon eigendisplacements, how to define the friction force and how to control it with atomic detail. Let us recall here that, in general, we call *friction* the macroscopic effect of a resultant force that resists the sliding or rolling of one object over another, this being the consequence of multiple microscopic phenomena. Each of such phenomena is responsible of the *microscopic friction*, which is the friction generated at the atomic scale by the relative motion of few adjacent atom layers in the presence of structural irregularities such as dislocations, layer truncations and grain boundary orientation, among others. If we consider systems without structural imperfections, the microscopic friction originates only from the atomic types and the geometric arrangement of the atoms forming a pristine compound, together with the resulting electronic features; in this case, we will then refer to it as *intrinsic friction*. The case studies presented in the following chapters are focused on the analysis of the intrinsic friction; however, the phonon-based friction description which we are about to define is general and can be applied also in the presence of any structural irregularity.

2.1 Phonons

In this section, we briefly review the mathematical derivation of the phonon modes and their physical meaning.^{98–100} Let us consider a periodic system formed by N_0 identical unit cells, each labeled by a cell index l and a vector \mathbf{r}_l pointing to its origin. Let there be N atoms per unit cell; the equilibrium positions across the whole system are written as

$$\mathbf{r}_{kl}^0 = \mathbf{r}_l + \mathbf{r}_k^0, \quad k = 1, 2, \dots, N \quad l = 1, 2, \dots, N_0 \quad (2.1)$$

where \mathbf{r}_k^0 represents the position of the k -th atom with respect to the origin of the primitive cell ([Figure 2.1](#)); the $N \times N_0$ -dimensional vector $\mathbf{r}^0 = (\mathbf{r}_{11}^0, \mathbf{r}_{21}^0, \dots, \mathbf{r}_{k1}^0, \dots, \mathbf{r}_{N1}^0)$

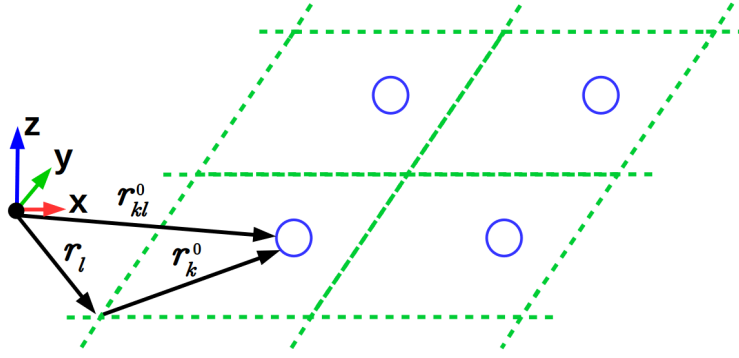


Figure 2.1: Schematic representation of the position vectors used in the formalism of the normal coordinates. The position vector \mathbf{r}_{kl}^0 of the k -th atom (blue circle) in the l -th primitive cell (green parallelogram) can be written as the sum of the position \mathbf{r}_l of the unit cell and the position \mathbf{r}_k^0 of the atom with respect to the origin of the unit cell.

then represents the structure of the lattice at the equilibrium. At a particular time t , the k -th atom within the l -th primitive cell may be found at a position $\mathbf{r}_{kl}(t)$, thanks to a time-dependent displacement of the form

$$\mathbf{u}_{kl}(t) = \mathbf{r}_{kl}(t) - \mathbf{r}_{kl}^0 = \mathbf{r}_{kl}(t) - \mathbf{r}_l - \mathbf{r}_k^0. \quad (2.2)$$

The potential energy V of the system

$$V = V(\mathbf{r}_{11}, \mathbf{r}_{21}, \dots, \mathbf{r}_{kl}, \dots, \mathbf{r}_{NN_0}) \quad (2.3)$$

is minimal if all the atoms occupy their equilibrium position, i.e. $\mathbf{r}_{kl} = \mathbf{r}_{kl}^0$. For small displacements, we can then consider the Taylor expansion of V about the equilibrium configuration with respect to $\mathbf{u}_{kl}(t)$ in the harmonic approximation, that is, by neglecting third and higher-order terms:

$$V(\mathbf{r}_{kl}(t) - \mathbf{r}_{kl}^0) = \frac{1}{2} \sum_{kl} \sum_{k'l'} \sum_{\alpha=1}^3 \sum_{\beta=1}^3 u_{kl}^{\alpha}(t) V_{\alpha\beta}(kl, k'l') u_{k'l'}^{\beta}(t) \quad (2.4)$$

where the 0-th order of the expansion has been set to zero (potential energy reference), the first order vanishes as it corresponds to the forces at the equilibrium, and $u_{kl}^{\alpha}(t)$ denotes the Cartesian component of $\mathbf{u}_{kl}(t)$ in the direction α . In order to simplify the formulae, we now drop the time dependence, keeping in mind that we are always dealing with dynamical displacements. The expansion coefficients $V_{\alpha\beta}(kl, k'l')$ in Equation 2.4 are the partial derivatives of the potential energy with respect to the atomic displacements taken at the equilibrium positions:

$$V_{\alpha\beta}(kl, k'l') = \left. \frac{\partial^2 V}{\partial u_{kl}^{\alpha} \partial u_{k'l'}^{\beta}} \right|_0. \quad (2.5)$$

Using the matrix notation

$$\mathbb{V}(kl, k'l') = \begin{pmatrix} V_{11}(kl, k'l') & V_{12}(kl, k'l') & V_{13}(kl, k'l') \\ V_{21}(kl, k'l') & V_{22}(kl, k'l') & V_{23}(kl, k'l') \\ V_{31}(kl, k'l') & V_{32}(kl, k'l') & V_{33}(kl, k'l') \end{pmatrix}, \quad (2.6)$$

Equation 2.4 reads

$$V(\mathbf{u}) = \frac{1}{2} \sum_{kl} \sum_{k'l'} \mathbf{u}_{kl} \mathbb{V}(kl, k'l') \mathbf{u}_{k'l'} \quad (2.7)$$

where $\mathbf{u} = (\mathbf{u}_{11}, \mathbf{u}_{21}, \dots, \mathbf{u}_{kl}, \dots, \mathbf{u}_{NN_0})$. The matrix $\mathbb{V}(kl, k'l')$ may be regarded as a *force constant matrix* and its elements $V_{\alpha\beta}(kl, k'l')$ as *force constants*. Within the harmonic approximation, the equation of motion for a particular atom (kl) with mass m_k is given by

$$m_k \frac{d^2 \mathbf{u}_{kl}}{dt^2} = - \sum_{k'l'} \mathbb{V}(kl, k'l') \mathbf{u}_{k'l'}. \quad (2.8)$$

Solutions of this set of coupled differential equations are of the form

$$\mathbf{u}_{kl} = \frac{1}{\sqrt{N_0 m_k}} \sum_{\mathbf{q}=\mathbf{0}}^{N_0} \sum_{j=1}^{3N} \left(Q_{\mathbf{q}j} \mathbf{e}_k(\mathbf{q}, j) e^{i\mathbf{q} \cdot \mathbf{r}_{kl}^0} + c.c. \right) \quad (2.9)$$

which are linear combinations of plane waves with wavevector \mathbf{q} and polarization vector $\mathbf{e}_{kl}(\mathbf{q}, j)$, where j is a integer label ranging from 1 to $3N$. In Equation 2.9: *i*) the coefficients $Q_{\mathbf{q}j}$ are a sinusoidal function of the time t : $Q_{\mathbf{q}j}(t) = Q_{\mathbf{q}j}^0 e^{i\omega_{\mathbf{q}j} t}$, with $\omega_{\mathbf{q}j}$ a characteristic frequency and $Q_{\mathbf{q}j}^0$ the amplitude which will be defined later; *ii*) m_k is the mass of the k -th atom; *iii*) $\mathbf{q} = (q_x, q_y, q_z)$ is a 3-dimensional wavevector of the reciprocal space written in cartesian coordinates, varying in a set of N_0 elements compatible with the periodicity of the system^a and including the null vector $\mathbf{0} = (0, 0, 0)$; *iv*) $e^{i\mathbf{q} \cdot \mathbf{r}_{kl}^0}$ is the spatial modulation of the atomic displacement, depending on the equilibrium position \mathbf{r}_{kl}^0 of the k -th atom in the l -th primitive cell; and *v*) “c.c.” denotes the complex conjugate of the first term in the parenthesis. For non periodic systems, $N_0 = 1$ and the only useful reciprocal vector is $\mathbf{q} = (0, 0, 0)$. If the ansatz Equation 2.9 is inserted into the equation of motion Equation 2.8, the following equation is obtained:

$$\omega_{\mathbf{q}j}^2 \mathbf{e}_k(\mathbf{q}, j) = \sum_{k'} \sqrt{\frac{1}{m_k m_{k'}}} \left[\sum_{l'} \mathbb{V}(kl, k'l') e^{i\mathbf{q} \cdot (\mathbf{r}_{kl} - \mathbf{r}_{k'l'})} \right] \mathbf{e}_{k'}(\mathbf{q}, j). \quad (2.10)$$

The summation over l' is the Fourier transform of the force constant matrix \mathbb{V} ,

$$\mathbb{F}_{kk'}(\mathbf{q}) = \sum_{l'} \mathbb{V}(kl, k'l') e^{i\mathbf{q} \cdot (\mathbf{r}_{kl} - \mathbf{r}_{k'l'})}, \quad (2.11)$$

which contains all the interactions between any (k, k') couple of atoms. With this notation, Equation 2.10 reduces to:

$$\omega_{\mathbf{q}j}^2 \mathbf{e}_k(\mathbf{q}, j) = \sum_{k'} \sqrt{\frac{1}{m_k m_{k'}}} \mathbb{F}_{kk'}(\mathbf{q}) \mathbf{e}_{k'}(\mathbf{q}, j). \quad (2.12)$$

^aThe complete set of \mathbf{q} vectors is made by N_0 elements, that is, as many as the number of unit cell replica, and is built consistently with the definition of the reciprocal lattice — see, for example, D. M. Wallace, *Thermodynamics of Crystals*, chapter “Lattice Dynamics”, John Wiley & Sons Inc., United States of America, ISBN: 0-471-91855-5.

For a given plane wave in Equation 2.9 characterized by (\mathbf{q}, j) , we can define a $3N$ -dimensional polarization vector $\mathbf{e}(\mathbf{q}, j)$

$$\mathbf{e}(\mathbf{q}, j) = \begin{pmatrix} \mathbf{e}_1(\mathbf{q}, j) \\ \vdots \\ \mathbf{e}_N(\mathbf{q}, j) \end{pmatrix} = \begin{pmatrix} e_1^x(\mathbf{q}, j) \\ e_1^y(\mathbf{q}, j) \\ e_1^z(\mathbf{q}, j) \\ \vdots \\ e_N^x(\mathbf{q}, j) \\ e_N^y(\mathbf{q}, j) \\ e_N^z(\mathbf{q}, j) \end{pmatrix} \quad (2.13)$$

and a $3N \times 3N$ matrix $\mathbb{F}(\mathbf{q})$

$$\mathbb{F}(\mathbf{q}) = \begin{pmatrix} F_{11}^{xx} & F_{11}^{xy} & F_{11}^{xz} & & & & F_{1N}^{xx} & F_{1N}^{xy} & F_{1N}^{xz} \\ F_{11}^{yx} & F_{11}^{yy} & F_{11}^{yz} & \dots & & & F_{1N}^{yx} & F_{1N}^{yy} & F_{1N}^{yz} \\ F_{11}^{zx} & F_{11}^{zy} & F_{11}^{zz} & & & & F_{1N}^{zx} & F_{1N}^{zy} & F_{1N}^{zz} \\ & & & F_{kk'}^{xx} & F_{kk'}^{xy} & F_{kk'}^{xz} & & & \\ & \vdots & & F_{kk'}^{yx} & F_{kk'}^{yy} & F_{kk'}^{yz} & & \vdots & \\ & & & F_{kk'}^{zx} & F_{kk'}^{zy} & F_{kk'}^{zz} & & & \\ F_{N1}^{xx} & F_{N1}^{xy} & F_{N1}^{xz} & & & & F_{NN}^{xx} & F_{NN}^{xy} & F_{NN}^{xz} \\ F_{N1}^{yx} & F_{N1}^{yy} & F_{N1}^{yz} & \dots & & & F_{NN}^{yx} & F_{NN}^{yy} & F_{NN}^{yz} \\ F_{N1}^{zx} & F_{N1}^{zy} & F_{N1}^{zz} & & & & F_{NN}^{zx} & F_{NN}^{zy} & F_{NN}^{zz} \end{pmatrix}; \quad (2.14)$$

with this definition, Equation 2.11 can be written in matrix notation as

$$\omega_{\mathbf{q}j}^2 \mathbf{e}(\mathbf{q}, j) = [\mathbb{M}\mathbb{F}(\mathbf{q})\mathbb{M}] \mathbf{e}(\mathbf{q}, j) = \mathbb{D}\mathbf{e}(\mathbf{q}, j) \quad (2.15)$$

where the diagonal matrix \mathbb{M}

$$\mathbb{M} = \begin{pmatrix} \frac{1}{\sqrt{m_1}} & 0 & 0 & & 0 & 0 & 0 \\ 0 & \frac{1}{\sqrt{m_1}} & 0 & \dots & 0 & 0 & 0 \\ 0 & 0 & \frac{1}{\sqrt{m_1}} & & 0 & 0 & 0 \\ & \vdots & & & & & \\ 0 & 0 & 0 & & \frac{1}{\sqrt{m_N}} & 0 & 0 \\ 0 & 0 & 0 & \dots & 0 & \frac{1}{\sqrt{m_N}} & 0 \\ 0 & 0 & 0 & & 0 & 0 & \frac{1}{\sqrt{m_N}} \end{pmatrix} \quad (2.16)$$

contains the masses of the atoms. Equation 2.15 is an eigenvalue-eigenvector equation for the $3N \times 3N$ matrix

$$\mathbb{D}(\mathbf{q}) = \mathbb{M}\mathbb{F}(\mathbf{q})\mathbb{M} \quad (2.17)$$

which is called the *dynamical matrix* and contains all the information about the dynamical response of the system. The crucial quantity defining \mathbb{D} is the force constant matrix \mathbb{V} (Equation 2.5), this containing essentially the first derivatives of the forces acting on the atoms. The evaluation of \mathbb{V} is done numerically from a set of displaced configurations for which the forces are calculated either classically or quantum mechanically;^{101–123} the configurations can be obtained by applying systematic or random displacements to a reference structure, or by sampling a dynamics trajectory. The frequencies $\omega_{\mathbf{q}j}^2$ and the polarization vectors $\mathbf{e}(\mathbf{q}, j)$ are the eigenvalues and the eigenvectors of the dynamical matrix, respectively, while the couple (\mathbf{q}, j) identifies the *phonon mode*. The phonon

mode is a collective harmonic (i.e. sinusoidal) vibration of the atoms of the whole system at a frequency ω_{qj} and with relative atomic displacement $\mathbf{e}(\mathbf{q}, j)$. The amplitude of the displacements is regulated by the quantity Q_{qj} , which is called *normal coordinate*, and depends on the time and on the magnitude Q_{qj}^0 , the latter being determined by the temperature or other external stimuli (e.g. electromagnetic fields). Equation 2.9 can be inverted to obtain the normal coordinate of a specific phonon mode (\mathbf{q}, j)

$$Q_{qj} = \frac{1}{\sqrt{N_0}} \sum_k^N \sum_l^{N_0} \sqrt{m_k} e^{-i\mathbf{q}\cdot\mathbf{r}_{kl}^0} \mathbf{u}_{kl} \cdot \mathbf{e}_k(\mathbf{q}, j) \quad (2.18)$$

given the displacements \mathbf{u}_{kl} at a certain time t . For a set of N atoms and N_0 unit cell replicas, the atomic displacements are described by means of $3N \times N_0$ Cartesian components forming the vector $\mathbf{u} = (\mathbf{u}_{11}, \dots, \mathbf{u}_{kl}, \dots, \mathbf{u}_{NN_0})$; correspondingly, each of the N_0 vectors $\mathbf{e}(\mathbf{q}, j)$ is formed by $3N$ Cartesian components. Therefore, there is a one-to-one correspondence between the Cartesian description \mathbf{u} and eigendisplacements description $\{\mathbf{e}(\mathbf{q}, j)\}$: in this sense, the set $\{\mathbf{e}(\mathbf{q}, j)\}$ constitutes a complete geometric basis set for the atomic positions.

The \mathbf{q} -points of the reciprocal space are in general labeled according to the symmetries of the system;¹²⁴ the origin of the reciprocal space is labeled as Γ . Following the usual convention, we label the phonon bands with progressive integer numbers, starting from the lowest associated frequency. With this convention, $(\Gamma, 1)$ is the phonon mode at $\mathbf{q} = \Gamma$ with band number equal to 1, that is, the dispersive mode with the lowest frequency $\omega_{\Gamma 1}$ at the origin of the \mathbf{q} -space; analogously, for example, $(\Gamma, 6)$ is the vibrational mode with frequency $\omega_{\Gamma 6}$ such that $\omega_{\Gamma 7} \geq \omega_{\Gamma 6} \geq \omega_{\Gamma 5}$ and so on.

2.2 Sliding and dissipative phonon modes

We already mentioned that the nanoscale friction arises due to the relative sliding of facing surfaces, which can be described by a sequence of atomic displacements. The transformation in Equation 2.9 represents the decomposition of atomic displacements \mathbf{u} in terms of the basis of the eigenvectors $\mathbf{e}(\mathbf{q}, j)$. If \mathbf{u}_{sl} is a sliding direction, then the projection^a $\Re(\mathbf{u}_{sl} \cdot \mathbf{e}(\mathbf{q}, j))$ is a measure of how large the contribution of the phonon mode (\mathbf{q}, j) to the sliding is. We can then identify which phonons are relevant for the sliding motion in this way: *i*) define a sliding direction \mathbf{d} and the set S of atoms forming the sliding surfaces; *ii*) select a phonon mode (\mathbf{q}, j) , consider the components of $\mathbf{e}(\mathbf{q}, j)$ associated to each atom of the set S and calculate the resulting displacement vector $\Delta\mathbf{r}_{qj}$ of the center of mass of S — this step provides the net relative displacement of the surfaces; *iii*) calculate the scalar product $r_{qj}^\perp = \Delta\mathbf{r}_{qj} \cdot \mathbf{d}$; *iv*) iterate *ii*)-*iii*) by considering all the eigenvectors, once at a time; and finally *v*) select the modes with the highest projection r_{qj}^\perp . We refer to the phonons identified in this way as *sliding modes* or *sliding phonons*, because they have an effective geometric contribution to the relative sliding along the direction \mathbf{d} . Therefore, the displacement vector \mathbf{u}_{sl} representing the sliding can be written as

$$\mathbf{u}_{sl} = \frac{1}{\sqrt{N_{sl}^q m_k}} \sum_{qj}^{N_{sl}} \left(Q_{qj} \mathbf{e}(\mathbf{q}, j) e^{i\mathbf{q}\cdot\mathbf{r}_{kl}^0} + c.c. \right) \quad (2.19)$$

^aAs the displacement \mathbf{u}_{sl} is a physical observable, it must be a real quantity; in fact, according to the decomposition in Equation 2.9 and its inverse relation Equation 2.18, only the real part of the scalar product^{125,126} between \mathbf{u}_{sl} and the complex vector \mathbf{e} contributes to the global displacement.

where the sum runs over the N_{sl} sliding modes and N_{sl}^q is the number of distinct \mathbf{q} vectors in the set of sliding modes. It is worthy to note here that Equation 2.19 is part of the linear combination in Equation 2.9, the latter representing the full atomic displacement also including non-sliding directions. The whole procedure can be repeated at varying \mathbf{d} in order to look for possible sliding directions on a given plane. The algorithm we just outlined is based only on geometric arguments. Indeed, at the end of this section we will see that the sliding modes play an active role in the energetics and dynamics of the sliding event: the net displacement of facing surfaces occurs until the sliding modes own enough energy (i.e. the phonon population is enough) to overcome the sliding energy barrier.

In terms of the classical picture, each phonon mode (\mathbf{q}, j) is a periodic motion of all the atoms of the system about their equilibrium position due to a harmonic restoring force \mathbf{f}_{qj}^{il} acting on the i -th atom in the l -th cell, and to which it is associated a frequency ω_{qj} such that

$$\mathbf{f}_{qj}^{il} = -m_i \omega_{qj}^2 \mathbf{u}_{il}, \quad k_{qj} = M \omega_{qj}^2 \quad (2.20)$$

where $M = \sum_i m_i$, \mathbf{u}_{il} is the displacement from the equilibrium position and k_{qj} is the equivalent force constant. The lower ω_{qj} , the weaker the restoring force, and the larger the amplitude of the corresponding atomic displacement at a fixed system energy. Therefore, if we consider the sliding modes, the lower their eigenfrequencies, the easier the surface sliding.

In tribological conditions, external intervention produces relative displacements of atomic layers forming two facing surfaces; such displacements generate an excessive overlap of the electronic densities of the facing ions, and a consequent repulsive force arising from both Coulombic interactions and Pauli's exclusion principle. Since the external forces drag the layers along directions lateral to the layer plane, the effect of the repulsive forces is to push the layers away from each other along the orthogonal direction. In the extreme case in which the orthogonal movement is not allowed, the repulsive force would act only laterally pushing the layers back, then increasing the sliding energy barrier. It is then apparent that if the forces binding the layers together are weak, the layer separation is facilitated and hence the sliding. The latter forces are mainly represented by *breathing* phonon modes. The breathing modes are associated to a restoring force which regulates the interlayer distance: a small force corresponds to a large allowed variation (compression/dilation) of the layer separation and facilitates the lateral shift. Both sliding and breathing motions then occur at the same time whenever two layers are displaced, no matter if the displacement is done slowly and in a reversible way (case of static friction) or rapidly (case of dynamic friction); in terms of the phonon description, this corresponds to the phonon coupling between both kinds of modes. Moreover, the sliding modes are also coupled with modes other than the breathing ones, all being responsible of the depopulation of the sliding modes; we will refer to the latter as *dissipative modes*. Also, we will name sliding and dissipative modes collectively as *sliding-related* modes. In order to study the dynamics of the system in tribological conditions, we must then consider anharmonic effects, that is, the phonon-phonon scattering, and how these determine the redistribution of the total energy between the sliding and the dissipative modes. The study of the frictional force is then reduced to the study of the interaction between the sliding and the dissipative modes toward which the energy of the former is transferred. All the forces producing a deceleration of the layers are of frictional kind, hindering the layer drift. Since the layer sliding is active as long as the sliding modes are populated enough, *the frictional forces are all those forces which activate dissipative processes producing a depopulation of the*

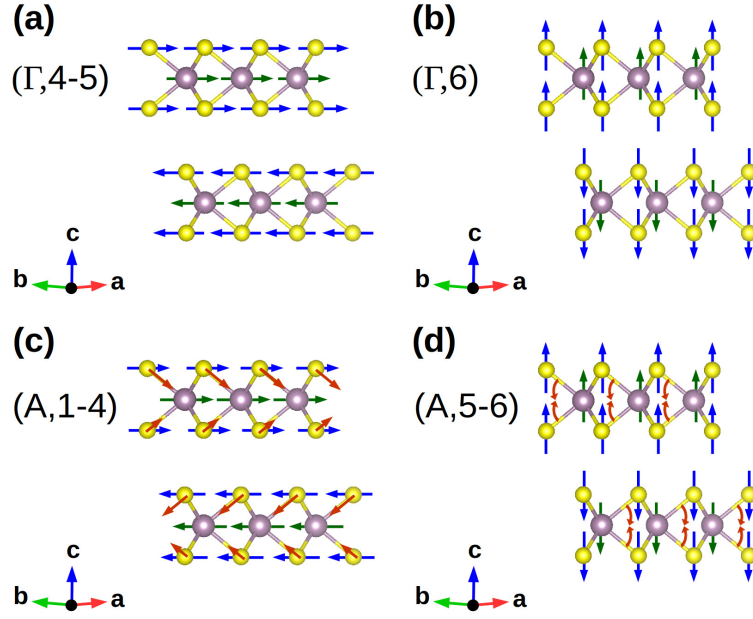


Figure 2.2: Example schematics of sliding and dissipative modes in MX_2 TMDs; purple and yellow spheres represent M and X atomic types, respectively. (a) rigid layer sliding in the ab -plane; (b) rigid layer shift along the c -axis producing a variable interlayer distance (*breathing mode*); (c) layer sliding in the ab -plane and asymmetric stretching of the X–M–X bond; (d) variable interlayer distance (*breathing*) accompanied by a flattening of the MX_6 polyhedra. Adapted from Ref. 127.

sliding modes. The variation of the energy of the sliding modes can then be considered equal to the work done by the frictional forces. In fact, the sliding modes produce an ordered motion of the system, which is downgraded into thermal vibrations by the coupling with the dissipative modes. Typical displacement patterns representing sliding and dissipative modes are displayed in Figure 2.2.

We observed a clear signature of the existence of the sliding and the dissipative modes in a series of dynamics simulations on an MoS_2 bilayer system (Figure 2.3); for a more extended discussion, see Ref. 43. In such simulations, the system is adiabatic, that is, there is no thermal bath coupled with it. In order to initiate the sliding, we imposed an initial lateral drift velocity to one of the two layers (layer A in Figure 2.3) and let the system evolve; we observed that, when the energy of the sliding modes drops below a certain threshold, the sliding terminates. We then analysed the total kinetic energy and the force acting on the layer A . The recombination processes involving the sliding and dissipative modes reveal their presence thanks to a dominant anharmonic frequency contribution identified by a Fourier analysis (Figure 2.4a). By means of a wavelet analysis,¹²⁸ we then resolved in time the frequency content of the total kinetic energy (Figure 2.4b) and the force (Figure 2.4c) acting on the A layer. The spectrograms are clearly divided into two regions: one in which the layer sliding is active and one in which it is over. The region of active sliding is dominated by the frequencies of the sliding modes and those relative to main anharmonic effects; on the contrary, once the sliding is over, the sliding and dissipative frequencies have negligible contribution to the spectrograms. We observed that the dissipation is more effective in correspondence of potential energy maxima; the time resolution of dissipative patterns then allows to identify the geometric configurations realizing critical values of the energy dissipation.

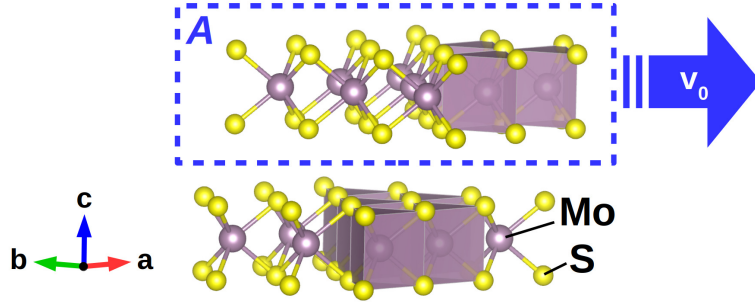


Figure 2.3: Hexagonal $P6_3/mmc$ structure of the 2H polymorph MoS_2 bulk compound. Mo-S bonds are arranged in a trigonal prismatic coordination forming MoS_2 layers that can reciprocally slide thanks to weak van der Waals interactions. An initial velocity \mathbf{v}_0 is imposed to the set of atoms forming the top layer, the latter labeled as A and indicated with a blue-dashed rectangle. Adapted from Ref. 43.

As a final remark, it is worthy to mention that this kind of analysis can be applied to characterize signals coming from any kind of experiments involving dissipative processes, like what we did for the Atomic Force Microscopy measurements presented in the cited work.

These simulations show that, although the phonon modes can be obtained from calculations on a static reference configuration, they provide a valid description of the friction response far from the equilibrium.

2.3 Phonon-phonon scattering rules and friction

The decrease of the sliding-modes population, hence the dissipative work, is regulated by the transition rate at which the scattering occurs. If we indicate a generic (\mathbf{q}, j) phonon mode as λ , the expression for the transition rate $\mathcal{P}_{\lambda\lambda'}^{\lambda''}$ of a three phonon process is⁹⁹

$$\mathcal{P}_{\lambda\lambda'}^{\lambda''} = \frac{2\pi}{\hbar} nn'(n'' + 1) |\Phi_{\lambda\lambda'\lambda''}|^2 \Delta(\mathbf{q} + \mathbf{q}' + \mathbf{q}'') \delta(\hbar\omega_\lambda - \hbar\omega_{\lambda'} - \hbar\omega_{\lambda''}) \quad (2.21)$$

where the term $\Delta(\mathbf{q} + \mathbf{q}' + \mathbf{q}'')$ ensures that the sum of the three wave vectors involved in the scattering belongs to the reciprocal lattice, while the term $\delta(\hbar\omega_\lambda - \hbar\omega_{\lambda'} - \hbar\omega_{\lambda''})$ guarantees the energy conservation. The phonon populations n , n' and n'' vary with the time and are a dynamic characteristic of the system:^a they depend from the initial conditions and from any external perturbation acting during the sliding (i.e. contact with a thermal reservoir, external forces). The third-order tensor $\Phi_{\lambda\lambda'\lambda''}$, that is the interaction strength at the third order, is instead an intrinsic characteristic of the system, since it is a function of the third order force constants, the eigenfrequencies and the

^aThe phonon population n is directly related to the amplitude $Q_{\mathbf{q}j}^0$ entering in the expression of $Q_{\mathbf{q}j}(t)$ thanks to the quantization of the phonon energy.^{98,129}

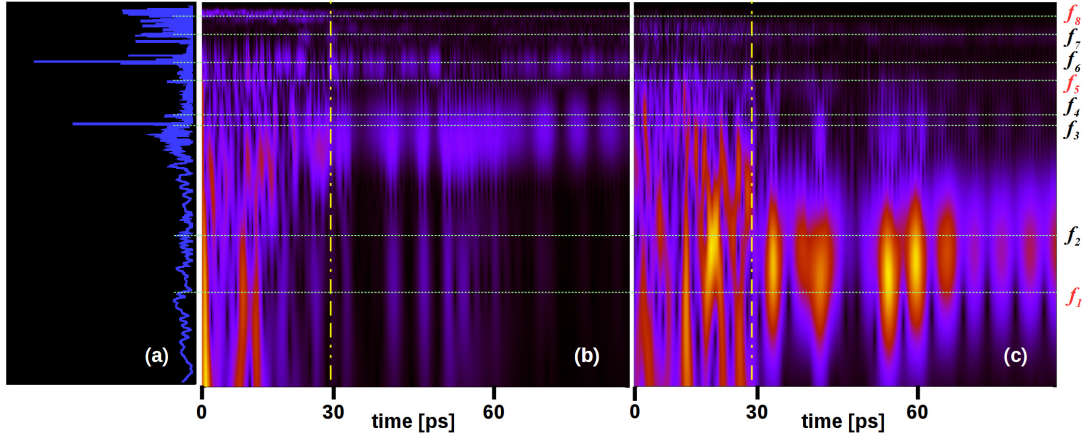


Figure 2.4: (a) Fourier transform (arbitrary units) of the total kinetic energy as calculated from the dynamics simulation; frequency range [THz] is vertically oriented in correspondence of the frequency axis of the wavelet transform of the (b) kinetic energy and (c) the force acting on the layer A . Black-blue-red-yellow color gradient indicates increasing wavelet amplitude (a.u.). The dot-dashed vertical yellow lines represent the time $t^* \approx 29.5$ ps at which the layer sliding terminates; for $0 < t < t^*$, dissipation processes involving the sliding modes are predominant. Frequency characterization is indicated with labels in correspondence of the horizontal dotted green lines as follow: $f_1 = 1.09$, $f_5 = 3.65$ and $f_8 = 26.6$ are generated by scattering processes, while the remaining ones are the harmonic frequencies of the system. Adapted from Ref. 43.

eigenvectors of the dynamical matrix:

$$\begin{aligned} \Phi_{\lambda\lambda'\lambda''} &= \sqrt{\frac{\hbar^3}{8N_0}} \frac{1}{\sqrt{\omega_\lambda \omega_{\lambda'} \omega_{\lambda''}}} \sum_{kk'k''} \frac{1}{\sqrt{m_k m_{k'} m_{k''}}} \cdot \\ &\cdot \sum_{\alpha\beta\gamma} e_\lambda^\alpha(\mathbf{r}_k) e_{\lambda'}^\beta(\mathbf{r}_{k'}) e_{\lambda''}^\gamma(\mathbf{r}_{k''}) \cdot \\ &\cdot \sum_{l'l''} e^{-i\mathbf{q}' \cdot (\mathbf{r}_{k'l'} - \mathbf{r}_k)} e^{-i\mathbf{q}'' \cdot (\mathbf{r}_{k''l''} - \mathbf{r}_k)} \mathbb{V}_{\alpha\beta\gamma}(k, k'l', k''l'') \end{aligned} \quad (2.22)$$

where

$$\mathbb{V}_{\alpha\beta\gamma}(k, k'l', k''l'') = \frac{\partial^3 V}{\partial u_{k0}^\alpha \partial u_{k'l'}^\beta \partial u_{k''l''}^\gamma} \quad (2.23)$$

is a generic element of the third order force constant matrix; a similar expression holds for all the higher-order $\Phi_{\lambda^1 \lambda^2 \dots \lambda^p}$ tensors.⁹⁸ The frictional forces therefore depend on extrinsic properties (phonon population) which vary upon external intervention, and on intrinsic properties (atomic type and geometry), which are decided once and for all when the material is built. It is therefore possible to predict the frictional response by calculating the interaction strength tensor of the stable geometry and no dynamic simulations are needed. Moreover, by finely tuning the elements of $\Phi_{\lambda^1 \lambda^2 \dots \lambda^p}$, it is possible to switch on or off selected dissipation channels, thus to regulate the phonon population of the sliding modes hence the friction force. This can be done, for example, by acting on the electronic-structure coupling, as we did in MX_2 layered systems to control the lattice thermal conductivity.¹³⁰ Another possibility is to act on the symmetries of the system. In fact, as I showed in Ref. 131, given the irreducible representations

$\Gamma^{e_{\lambda_1}}, \dots, \Gamma^{e_{\lambda_p}}$ for which the phonon eigenvectors $e_{\lambda_1}, \dots, e_{\lambda_p}$ are respectively a basis, then

$$\Phi_{\lambda^1 \lambda^2 \dots \lambda^p} \neq 0 \Rightarrow \Gamma^{e_{\lambda^1}} \otimes \dots \otimes \Gamma^{e_{\lambda^p}} \subseteq A \quad (2.24)$$

which states that if the direct product among the irreducible representations contains the totally symmetric representation A , then the $\lambda_1 + \dots + \lambda_{p-1} = \lambda_p$ scattering is allowed. By controlling the symmetries of the eigenvectors e_{λ} , it is then possible to forbid or allow selected dissipative processes. Finally, it is worthy to note that condition 2.24 is a quick guide to identify which recombination channels are active and at which order of anharmonic approximation, as it does not require any explicit calculation of the $\Phi_{\lambda^1 \lambda^2 \dots \lambda^p}$ elements.

2.4 The “Normal-Modes Transition Approximation”

The decomposition of sliding trajectories in terms of phonon eigendisplacements allows to finely tune sliding energy barriers by acting on specific phonon modes or scattering (i.e. dissipative) processes; alternatively, it may be used in a systematic way to provide possible sliding paths serving as an initial guess for transition path optimization techniques.^{132,133} We formalized this framework in a computational protocol that we named *normal-modes transition approximation* (NMTA).⁴² The NMTA has been initially applied to the study of sliding MX₂ transition metal dichalcogenides; however, the formulation is general and can be applied to any kind of system to study phase transitions or chemical reactions. As a matter of fact, the sliding event can be considered as a transition along a geometric path joining two stable configurations.

The NMTA relies on the harmonic phonon approximation. In the harmonic hypothesis, we can write the potential energy V of the system as a sum of V_{λ} contributions each coming from a single phonon mode λ as^{98,99}

$$V = \sum_{\lambda} V_{\lambda}(Q_{\lambda}) = \sum_{\lambda} \frac{1}{2} \omega_{\lambda}^2 Q_{\lambda}^2, \quad (2.25)$$

where V_{λ} is a function of the normal coordinate Q_{λ} . Let's focus our attention on an arbitrary mode λ and consider arbitrary values of the normal coordinate Q_{λ} . From now on, we will consider only those Q_{λ} value ranges for which the energy V_{λ} of the λ -mode remains bounded, varying as a continuous function between an upper (V_{λ}^{max}) and a lower (V_{λ}^{min}) limit ($-\infty < V_{\lambda}^{min} \leq V_{\lambda} \leq V_{\lambda}^{max} < +\infty$). Let's regard the normal coordinate Q_{λ} as a configurational coordinate. At the stable state, $Q_{\lambda} = Q_0$ and $V_{\lambda}(Q_0) = V_{\lambda}^{min}$; for simplicity, we can set $Q_0 = 0$ and $V_{\lambda}^{min} = 0$. Along the Q_{λ} coordinate, the energy V_{λ} is bounded by hypothesis; then there exists $Q_{\lambda}^{tr} > Q_0$ such that $V_{\lambda}(Q_{\lambda}^{tr}) = V_{\lambda}^{max} \equiv V_{\lambda}^{tr}$ is the only energy maximum in $[Q_0, Q_{\lambda}^{tr}]$. In such range, we can approximate the potential energy V_{λ} of a single λ -mode with a Fourier series truncated at the first term as

$$V_{\lambda}(Q_{\lambda}) = \frac{1}{4} \omega_{\lambda}^2 C_{\lambda}^2 \left[1 - \cos \left(\frac{\pi}{C_{\lambda}} Q_{\lambda} \right) \right], \quad (2.26)$$

being the hypotheses required by the Fourier theorem satisfied thanks to our assumptions on the $V_{\lambda}(Q_{\lambda})$ function. The geometric configuration $Q_{\lambda} = Q_{\lambda}^{tr}$, at which the maximum of the energy is realized, can then be regarded as the transition state closest to the stable state Q_0 along the Q_{λ} configurational coordinate. The $[Q_0, Q_{\lambda}^{tr}]$ range is the *transition* path along which the transition from Q_0 to Q_{λ}^{tr} is realized. Moreover, since we assumed

that $V_\lambda(Q_\lambda^{tr})$ is the only maximum in $[Q_0, Q_\lambda^{tr}]$, no metastable states are present between the stable and the closest transition state. In agreement with [Equation 2.26](#), we see that the energy V_λ^{tr} of the transition state

$$V_\lambda^{tr} = \frac{1}{2}\omega_\lambda^2(Q_\lambda^{tr})^2 = \frac{1}{2}\omega_\lambda^2(C_\lambda)^2 \quad (2.27)$$

is proportional to the square of the product between an electronic and a geometric factor: *i)* ω_λ , the frequency associated to the λ -mode, which depends on the electronic features of the atomic types; *ii)* $C_\lambda \equiv Q_\lambda^{tr}$, the normal coordinate value at which the transition is realized, which depends on the geometric features of the system and coincides with the maximum amplitude of the normal coordinate Q_λ . The smaller the frequency of the mode, the smaller the energy needed by the system to undergo a transformation from the stable configuration to the transition state. Leaving unaltered the atomic topology, the frequency of the mode can be tuned by substituting the atomic species at specific positions with suitable ones, hence tuning the energy barrier. Moreover, the transition state can be identified by inspecting how the stable geometry varies by varying the amplitude Q_λ ; in the practice, the transition state can be numerically evaluated by imposing that the interatomic distances fall in a specific range at varying Q_λ . At the transition Q_λ^{tr} , the ratios among the atomic displacements define a relation among the atomic positions that can be exploited to estimate the transition state in any system with the same atomic topology but with different chemistry.

Along a general configurational coordinate Q , the total potential energy V can be approximated as a sum of contributions from all the normal modes, by expressing V_λ in a more general form than that shown in [Equation 2.26](#):

$$V(Q) = \sum_\lambda \frac{1}{4}\omega_\lambda^2 C_\lambda^2 \left[1 - \cos\left(\frac{\pi}{C_\lambda}Q - \theta_\lambda\right) \right] \quad (2.28)$$

where some (or all) of the C_λ amplitudes and θ_λ phases can be correlated if the modes are coupled along Q ([Figure 2.5](#)).

Approximation done in [Equation 2.26](#) is reliable only if, along the $[Q_0, Q_\lambda^{tr}]$ transition path, the frequency of all the other modes vary within a small range. The wider such range, the more important the contribution of the other modes to the potential energy along the selected mode; in that case, the modes are coupled and the expression for V_λ must take into account any deviation from the harmonicity:

$$V_\lambda(Q_\lambda) = \frac{1}{4}\omega_\lambda^2 C_\lambda^2 \left[1 - \cos\left(\frac{\pi}{C_\lambda}Q_\lambda\right) \right] + f(Q_\lambda, \omega_{\lambda'}, C_{\lambda'}(C_\lambda); \lambda' \neq \lambda) \quad (2.29)$$

where $f(Q_\lambda, \omega_{\lambda'}, C_{\lambda'}(C_\lambda); \lambda' \neq \lambda)$ is a function of the amplitudes and the frequencies of all the modes other than λ' , and each amplitude $C_{\lambda'}$ of the λ' mode is a function of the C_λ amplitude of the mode λ . Using [Equation 2.28](#), the correction f can be approximated as

$$f(Q_\lambda, \omega_{\lambda'}, C_{\lambda'}(C_\lambda); \lambda' \neq \lambda) \approx \sum_{\lambda' \neq \lambda} \frac{1}{4}\omega_{\lambda'}^2 C_{\lambda'}^2 \left[1 - \cos\left(\frac{\pi}{C_{\lambda'}}Q_\lambda - \theta_{\lambda'}\right) \right], \quad (2.30)$$

which represents the anharmonic contribution to the λ -mode.

Each Q_λ normal coordinate can thus be followed to look for possible transition states. In this respect, the complete set of normal modes constitutes a finite number of

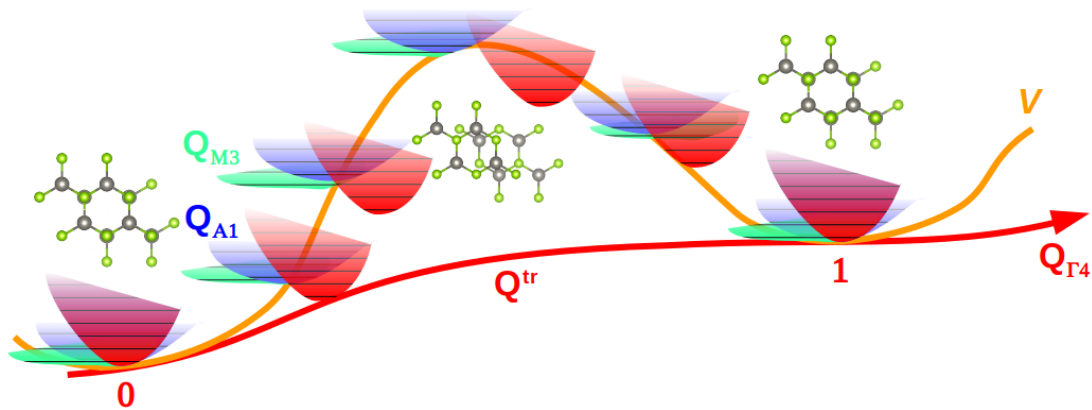


Figure 2.5: Schematic representation of phonon coupling along the normal mode $Q_{\Gamma 4}$ selected as configurational coordinate for the study of the sliding energy barrier V in a layered WSe_2 system.⁴² At the ground state “0”, the amplitude of the modes is null. By increasing the $Q_{\Gamma 4}$ amplitude, two subsequent layers slide relatively each other, causing the activation of the (A,1) and (M,3) modes until the transition state Q^{tr} is reached; a further increasing of the amplitude pushes the system towards the closest ground state “1”. The parabolae along the potential profile V represent the harmonic potential associated to each phonon mode, whereas the position relative to V represents their corresponding populations.

possible routes to explore the energy landscape in a systematic way. In the practice, a specific λ -mode is first selected, and the transition path is initially estimated using intermediate geometries connecting the stable and the transition state along the Q_λ coordinate. Subsequently, such geometries can also be modified by inducing atomic displacements according to the distortion patterns of modes other than the selected one, in order to capture different subtle and interesting features of the transition. The corresponding total potential energy is thus built as a linear superposition of all the modes considered in the transition: such superposition corresponds to the approximation done in Equation 2.28, in which only the modes participating to the transition will have significant C_λ amplitudes. In order to explore all the possible transition paths, we can then consider the entire set of the λ -modes, select one at a time, and build the transition path by considering other modes that, possibly, participate to the transition. It is worthy to note here that, the identification of possible transition paths can be performed by a numerical evaluation of geometries that requires the knowledge of only the displacement patterns of the phonon modes: once the phonon modes of the stable state have been calculated, the estimation of possible transition paths can be computed within few minutes of wallclock time on an ordinary desktop computer. Moreover, despite the number of linear superpositions to consider could be high, such number is still a finite quantity completely defined by the complete set of normal modes. This aspects of the NMTA method drastically reduces the effort to look for possible transition states of a given system, providing a systematic prescription to build possible transition paths.

Once the estimation of the transition path is built and then optimized by means of numerical techniques,^{132,133} Equation 2.28 can be used to deconvolute the calculated energy profile into contributions of single modes. By comparing the C_λ amplitudes it is possible to identify which is the mode that leads the geometric transition: the larger the C_λ value, the larger the atomic displacement induced by the λ -mode. Equation 2.28

thus constitutes a tool to identify how each mode contributes to the advancement of transitions, providing a route to finely tune reaction barriers through the adjustment of the characteristics (frequency and displacements) of single phonon modes.

As a final remark, it is worthy to stress that, while in [section 2.2](#) we used the phonon description to obtain a geometric decomposition of the sliding path, here we use it to deconvolute the energy profile along a configurational coordinate, the two descriptions being complementary.

2.5 The cophononicity metric

Each phonon mode is a complex function of all the components of the force constant tensor of all the A-B atomic pairs present in the system via the dynamical matrix ([Equation 2.15](#) and [Equation 2.11](#)); specific displacement patterns, including those representing the layer sliding, cannot be related to single components of the force constant tensor in an easy way. Therefore, the force constants alone do not represent a manageable descriptor to parametrize the interactions responsible of specific atomic displacements, the layer sliding among them. In order to obtain a simple metric, we focus on the smallest unit that produces the dynamical interactions, that is, the A-B atomic pair. Let's consider the phonon density of states¹²⁹ (phDOS) $g(\omega)$ defined in a frequency range $[\omega_0, \omega_1]$. The center mass CM^A of the atom-projected phDOS $g^A(\omega)$ of an atom A is defined as

$$CM^A = \frac{\int_{\omega_0}^{\omega_1} \omega g^A(\omega) d\omega}{\int_{\omega_0}^{\omega_1} g^A(\omega) d\omega} \quad (2.31)$$

where $g^A(\omega)$ is the contribution of the atom A to $g(\omega)$; $g(\omega)$ is the total phDOS of the solid

$$g(\omega) = \sum_i g^i(\omega) \quad (2.32)$$

obtained by summing over all the atoms in the unit cell. The integration interval $[\omega_0, \omega_1]$ in [Equation 2.31](#) is chosen in such a way that it encompasses all the phonon states relevant for the selected band. The integral at the denominator of the definition of CM^A is the contribution of the atom A to the states in the frequency range $[\omega_0, \omega_1]$; we call such quantity the *phonicity* of the A atom in that specific frequency range. The phonicity of an atom then represents the amount of phonon states that such atom contributes to form; in this respect, it can be regarded as the phonon counterpart of the atomic valence, that is the number of electrons with which an atom participates to form the electronic states of the system, counted as the integral of the atom-projected electronic density of states.¹³⁴

Let's consider a generic A-B atomic pair. The relative position $C_{ph}(A-B)$ of the center mass of $g^A(\omega)$ with respect to the center mass of $g^B(\omega)$ is given as

$$C_{ph}(A-B) = CM^A - CM^B \quad (2.33)$$

which is specified in the same units of the frequency ω . In this formalism, a positive (negative) sign of $C_{ph}(A-B)$ indicates that the A (B) atom contributes more to the high frequency modes of the specified range. The smaller $|C_{ph}(A-B)|$, the larger the mixing of the A and B contributions to the frequency band, the two atoms having very close weight

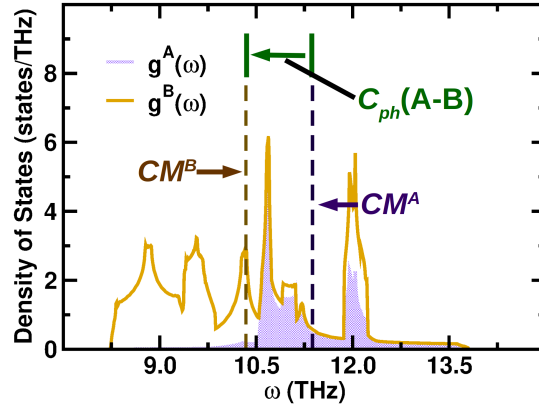


Figure 2.6: Schematic definition of the cophononicity of the A-B atomic pair: CM^A and CM^B are the center mass of the atom-projected phonon density of states of the A and B group of atoms, respectively, while $C_{ph}(A-B)$ is the cophononicity calculated as in Equation 2.33.

in the determination of the modes specific of the considered energy range. We define the quantity $C_{ph}(A-B)$ as the *cophononicity of the A-B atomic pair*,⁴¹ in analogy with the A–B bond covalency definition formulated for crystalline compounds¹³⁴ (Figure 2.6). According to the definition, positive $C_{ph}(A-B)$ values indicate that the A and B ions contribute more to higher- and lower-frequency displacements, respectively; this means that the A atoms displace faster than the B atoms in the global motion formed by the phonon eigendisplacements with frequencies in the range $[\omega_0, \omega_1]$. The opposite holds for negative values. A cophononicity value close to zero (*perfect cophononicity*) corresponds to atomic displacements in which both A and B atoms move on average at the same velocity. We initially designed the cophononicity metric to study the sliding motions in transition metal dichalcogenides; however, its formulation is general and has been applied to different kinds of materials^{135–137} irrespective of the composition and the stoichiometry. For a quick reference, I created a corresponding Wikipedia page.¹³⁸

In a given structure, a single atomic type can occupy distinct crystallographic sites. For example, in the unit cell of the 2H polymorph of MX_2 transition metal dichalcogenides,⁴⁴ the M and X crystallographic sites are unique; for this reason, if we want to calculate the A-B cophononicity in MX_2 systems, it is convenient to aggregate the contributions coming from all the M and X atoms present in the unit cell. We also note that A and B could, in principle, correspond to two ions of the same atomic species but with different properties (e.g. because sitting on distinct crystallographic sites); in this case, the definition in Equation 2.33 is still valid and represents the relative contribution of the two ions to the selected frequency band.

We emphasize that the cophononicity is a characteristic of a specific atomic pair of a system. Note that the comparison between two cophononicity values obtained from structures with different connectivity will likely be unable to provide meaningful information. For example, $C_{ph}(Mo-S)$ in MoS_2 bulk and nanoclusters would have distinct sets of vibrational modes due to the distinct topologies that, in turn, determine different electronic environments: any change of the cophononicity by means of substitutional defects could lead to non-correlated changes of the vibrational frequencies. However, if two structures with distinct topologies are connected by continuous geometric transformations, also the electronic environment of the atomic pairs, thus the vibrational

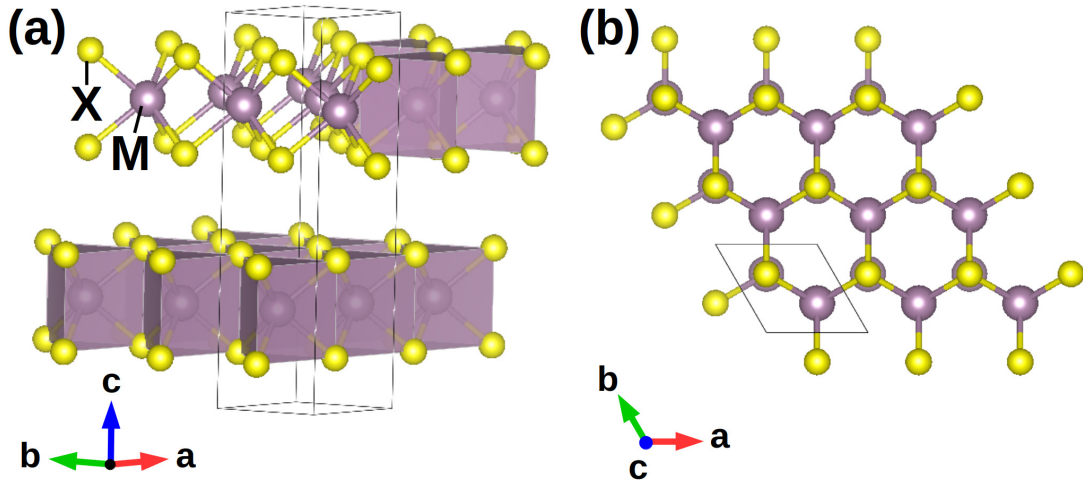


Figure 2.7: Model geometry of the hexagonal $P6_3/mmc$ structure of the MX_2 2H polymorph (M = transition metal, X = chalcogen atom). M–X bonds are arranged in a trigonal prismatic coordination forming MX_2 layers that can slide thanks to weak van der Waals interactions. The black thin lines indicate the unit cell.

frequencies and the associated modes, are related by such continuous transformations; in this case, the cophonicity of a specific atomic pair in one structure can be mapped into the cophonicity of the second one, granting the transferability of the definition, hence the reliability of the cophonicity comparison.

We will use the cophonicity as a lattice dynamics descriptor to understand the atomic type dependence of phonon frequencies related to the sliding motion. Used in combination with other electronic and geometric descriptors, it is able to provide guidelines on how to tune the system feature in order to obtain target friction properties or to design new tribological materials, as we will see in the next chapters.

2.6 Case study: MX_2 Transition Metal Dichalcogenides

As a case study for nanofriction, I mainly considered the prototypical MX_2 transition metal dichalcogenides (TMDs)^{44,45} class of materials, which have been one of the main subjects of my scientific research since I started to work at the Czech Technical University in Prague. In the next chapters, we will briefly review such study, where I applied the phonon-based friction theory that we discussed so far at varying chemical composition and load, also considering the presence of charge accumulation, external electrostatic fields and contaminants. Only the main results will be reported; for a complete discussion, the reader is referred to the respective published articles cited at the beginning of each chapter.

MX_2 transition metal dichalcogenides are layered structures, each layer made by hexagonally packed metal atoms (M) forming covalent bonds with six chalcogen anions (X) in a trigonal prismatic coordination (Figure 2.7); adjacent layers are coupled by weak van der Waals forces that allow relative sliding under tribological conditions. Several stable TMDs polymorphs and polytypes are found,⁴⁴ some transforming into each other by sliding of subsequent layers; such sliding motions include also rotations (reorientations) of one layer with respect to its two adjacent ones about an orthogonal axis. The complex atomic displacements that result into layer sliding, either commensurate or not, can be

represented as linear combinations like Equation 2.19. Our reference geometry is the 2H polymorph crystalline MX_2 structure, with $\text{M} = \text{Mo}, \text{W}$ and $\text{X} = \text{S}, \text{Se}, \text{Te}$, and hexagonal $P6_3/mmc$ symmetry (SG 194);¹³⁹ for simplicity, in general, we will refer to the model systems as “MX” by dropping the stoichiometric coefficients. The chosen 2H configuration is that in which two adjacent layers are oriented in such a way that an M atom of one layer is aligned with two X atoms of the other one along the direction orthogonal to each layer (c -axis in our setting — see Figure 2.7).

Chapter 3

Design of new tribological materials

The first work in which I applied the phonon-based friction description focuses on how to relate the phonon modes with the atomic types forming the structure and the electronic properties of the environment that they determine.⁴¹

The work considers the MX_2 hexagonal 2H polytype, with $\text{M} = \text{Mo}, \text{W}$ and $\text{X} = \text{S}, \text{Se}, \text{Te}$ (Figure 2.7). In order to disentangle the electronic from the structural contributions to determining the phonon frequencies, we first quantify the geometric distortions δ of the system by performing a group-theoretical analysis with the aid of the ISODISTORT software;¹⁴⁰ we thus decompose the MX geometries in terms of distortions of a parent phase, that we choose to be the relaxed^a MoS model (Table 3.1). We then evaluate the M–X bond covalency $C_{M,X}$ at different structural distortions, by applying the covalency metric defined in terms of atom-projected density of states.¹³⁴ We observe that the covalency is strictly decreasing with increasing distortions in MoX systems, while it has a minimum for the WTe compounds among the WX compositions [Table 3.1 and Figure 3.1(a)]. We now need to relate this electronic and structural information to the dynamical features of the system. From the analysis of the phonon eigendisplacements, we recognize that the sliding related modes are those in the six Γ –A branches with the lowest eigenfrequencies, falling in the frequency range $[0, 2]$ THz. We analyzed the trend of all the frequencies associated to the sliding-related modes against the cophonycity (section 2.5) of the system, and we find that they all have the same trend against the cophonycity metric. For simplicity, in the present analysis, we will discuss only the trend of the degenerate $\omega_{\Gamma 4-5}$ and $\omega_{A 1-4}$ frequencies, as our conclusions also apply to the other frequencies that we considered in our study: *i*) the degenerate ($\Gamma, 4$)-($\Gamma, 5$) modes correspond to rigid layer sliding in the ab -plane (Figure 2.2a), *ii*) ($\Gamma, 6$) represents a rigid layer shift along the c -axis that changes the interlayer distance (Figure 2.2b), *iii*) the degenerate (A, 1)-(A, 4) modes produce layer sliding in the ab -plane accompanied by asymmetric stretching of the X–M–X bond, maintaining constant the interlayer distance (Figure 2.2c), *iv*) the degenerate (A, 5)-(A, 6) modes correspond to a change of the interlayer distance and a flattening of the MX_6 polyhedra (Figure 2.2d).

Irrespective of the kind of phonon mode, we find that the frequency diminishes when $C_{ph}(\text{M-X})$ approaches zero [Table 3.1 and Figure 3.1(b)]. In order to capture

^aThe expressions “relaxed structure” or “optimized structure” indicate the geometric configuration which realizes a minimum of the system energy.

Table 3.1: Structural distortion δ (\AA), M–X bond covalency $C_{M,X}$ (eV), cophonycity $C_{ph}(M-X)$ (THz) of the M–X pair, sliding $\omega_{\Gamma 4-5}$ and breathing ω_{A1-4} frequencies (THz), and formation energy ΔH_f (eV) of the MX_2 model systems. MoS is the reference for calculating the δ and ΔH_f values.

System	δ	$C_{M,X}$	$C_{ph}(M-X)$	$\omega_{\Gamma 4-5}$	ω_{A1-4}	ΔH_f
MoS	0.00	-0.44	0.25	0.90	0.63	0.00
MoSe	0.06	-0.58	-1.37	0.84	0.60	2.79
MoTe	0.10	-0.75	-0.93	0.90	0.63	5.94
WS	0.02	-0.51	0.30	0.78	0.54	1.23
WSe	0.06	-0.66	0.12	0.72	0.51	4.27
WTe	0.03	-0.80	0.03	0.66	0.45	7.63
Ti:MoS	0.17	-0.76 ^a	0.14 ^b	$\omega_{\Gamma 4}$ 0.66 ^c $\omega_{\Gamma 5}$ 0.69 ^c	ω_{Z1-2} 0.45 ^c ω_{Z3-4} 0.48 ^c	0.04

^a Ti–S bond covalency value to be compared with $C_{Mo,S}$ in MoS system.

^b Global cophonycity of Ti:MoS system calculated as weighted average of the $C_{ph}(\text{Mo-S})$ and $C_{ph}(\text{Ti-S})$ cophonycities, with weights corresponding to the M stoichiometric coefficients.

^c Degeneracy of vibrational modes in MoS system is partially lifted in Ti:MoS model, having the latter a lower number of symmetries. According to the displacement patterns, the (A,1-4) modes of the MX systems correspond to the (Z,1-4) modes of Ti:MoS model.

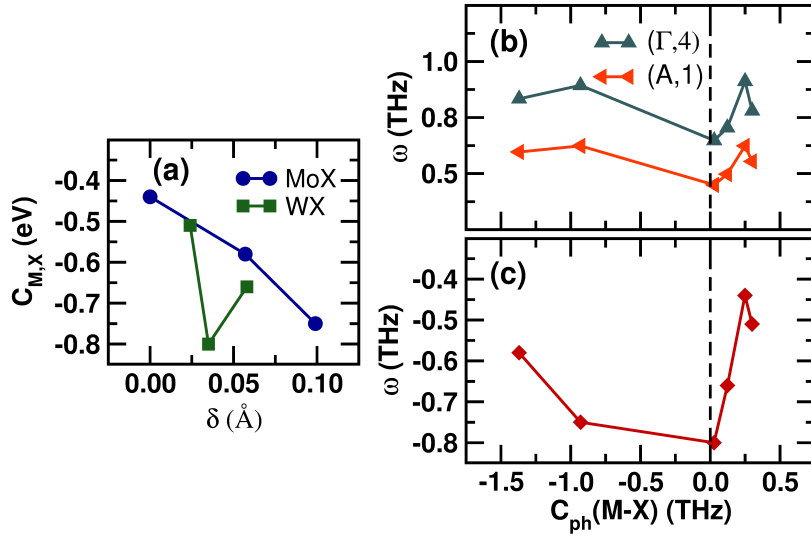


Figure 3.1: (a) M–X bond covalency as a function of structural distortions δ . Covalency can be tuned by changing the amplitude of the structural distortions. (b) Frequency of the $(\Gamma,4)$ and $(A,1)$ modes as a function of M–X pair cophonycity. Irrespective of the vibrational mode, the lowest frequency is realized for $C_{ph}(M-X) \simeq 0$. (c) Covalency of the M–X bond as a function of $C_{ph}(M-X)$. The lowest $C_{M,X}$ covalency value corresponds to a cophonycity close to zero. Adapted from Ref. 41.

the entangled electronic and structural features, we relate the change of the phonon frequency to the geometry and the atomic types forming the system by connecting

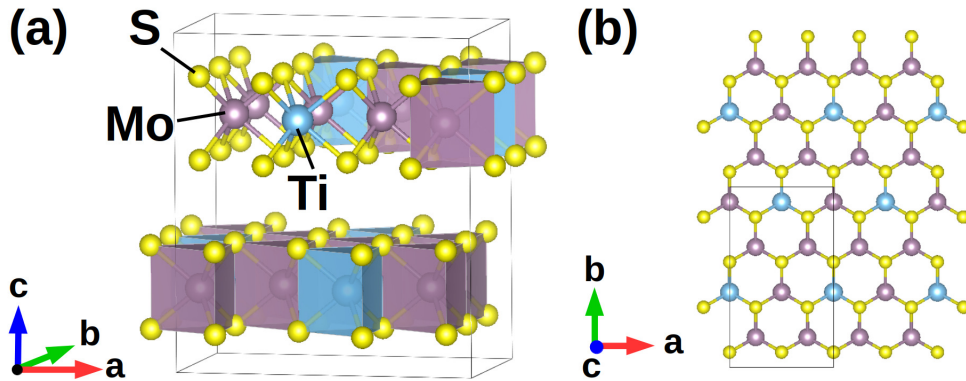


Figure 3.2: (a) Lateral and (b) c -axis view of the geometry of the orthorhombic $Cmcm$ Ti:MoS₂ model system. Within each layer, one Ti atom is surrounded by only Mo atoms in the first neighbouring cation shell. The unit cell is indicated by a thin black line.

the M-X cophonycity with the M-X bond covalency. The cophonycity is found to be minimum when the bond covalency is about -0.80 eV, that is realized in the WTe compound [Table 3.1 and Figure 3.1(c)]; on the other hand, $C_{ph}(M-X)$ shows similar trends for the MoX and WX compounds with respect to the structural distortions. According to these results, the cophonycity, hence the vibrational frequencies, can be adjusted by tuning the distortions and the covalency of the system by a proper selection of the M and X ions.

We now want to exploit the knowledge acquired so far to design a new TMD with enhanced tribological properties. In particular, according to the results discussed above, we want to find an M-X pair that realizes a low covalency value in order to minimize the M-X cophonycity, so as to lower the phonon frequencies that govern the layer drift. We focus on the MoS₂ compound, because the synthesis routes have been extensively studied and, therefore, constitutes a good candidate to easily grow derived materials. Starting from the MoS model system, we will now design a new compound by partial ion substitution. Among the chosen MoX stoichiometries, MoTe realizes the lowest covalency value; to further lower the Mo-X covalency we must increase the structural distortions [Figure 3.1(c)]. Following the series of chalcogenides, a natural choice would be polonium as X ion; since we want to avoid to use unstable elements, an other possibility is to partially substitute for the Mo cation. The substituent atom must be chosen such as to induce structural distortions that lower the covalency of the M-X bond, in order to lower the corresponding cophonycity hence the vibrational frequencies. We are thus oriented towards cations with ionic radii smaller than that of the Mo atom. Moreover, we want to choose a proper dopant concentration and geometric arrangement of the dopant to preserve the stability of the final system. To this aim, we consider the MoS optimized structure and we substitute a Mo atom with one Ti atom in such a way that, within a single layer, its first neighbouring cation shell is formed only by Mo atoms, building the Mo₃Ti₁S₈ (Ti:MoS) system with orthorhombic $Cmcm$ (SG 63) symmetry (Figure 3.2).

The calculated formation energies ΔH_f (Table 3.1), relative to the MoS system, indicate that MoS and Ti:MoS are the most stable compounds among those considered; in particular, the small difference between the MoS and Ti:MoS ΔH_f values (0.04 eV) suggests that both compounds have the same probability to be produced, especially in self-assembling tribological mixtures where both MoS₂ and TiS₂ chemical precursors are

present. The analysis on the optimized structure shows that the Mo \rightarrow Ti substitution produces a significant distortion ($\delta = 0.17 \text{ \AA}$), due to a local reduction of the M-S bond covalency that decreases from -0.44 to -0.76 eV. Such reduction produces a global lowering of the cophononicity of the system from 0.25 to 0.14 THz. The cation substitution also reduces the symmetries of the system, producing the splitting of those vibrational modes that were degenerate in the parent MoS structure. However, the displacement pattern of the modes is unvaried, and a direct comparison of the corresponding frequencies can be done without ambiguities. In the Ti:MoS system, the vibrational frequencies are found to be lower than those of the undoped counterpart, as expected according to the lower M-S cophononicity (Table 3.1); in particular, we note that the frequency values are close to those found in the WSe and WTe systems. According to the present results, the bulk contribution to the friction coefficient of the Ti:MoS, WSe and WTe systems are expected to be similar and the lowest ones among those of the TMDs compounds considered in this work.

Chapter 4

Effect of load on the sliding-related modes

In the present work,¹²⁷ we are interested into the dynamic response of the bulk in the presence of external load in the selected prototypical MX₂ TMD structures (see [section 2.6](#)) and the proposed Ti:MoS₂ phase ([chapter 3](#)). In order to identify which phonon modes are mostly affected by the application of an external load, we start by computing the mode Grüneisen parameters $\gamma_{\mathbf{q}j}$ for each (\mathbf{q}, j) mode sampled in the reciprocal space. $\gamma_{\mathbf{q}j}$ is defined as

$$\gamma_{\mathbf{q}j} = -\frac{V}{\omega_{\mathbf{q}j}} \frac{\partial \omega_{\mathbf{q}j}}{\partial V} \quad (4.1)$$

and it is a measure of how the frequency ω of the j -th mode at wave vector \mathbf{q} changes by varying the volume V of the unit cell. We find that the $\gamma_{\mathbf{q}j}$ amplitudes are the highest for the $\omega_{\Gamma 4-6}$ and ω_{A1-6} modes, that is, the sliding-related modes that we saw in [chapter 3](#). We then focus our discussion only on these modes, since all the remaining ones are less affected by a change in the unit cell volume, hence preserving the characteristic frequencies in the presence of external load.

We now want to relate the stability of the mode frequency to the chemical composition. We consider the phonon density of states of the relaxed systems and evaluate the cophononicity ([section 2.5](#)) of the M-X atomic pair in the frequency range [0,2] THz; we choose such range to be the same for all the systems because the frequencies of the modes we are focusing on fall within such integration range, irrespective of the considered chemical composition. We then relate the M-X pair cophononicity to the mode Grüneisen parameters. We find that, for rigid layer sliding ($\Gamma, 4-5$) or for those modes involving interlayer distance variation ($(\Gamma, 6)$, $(A, 5-6)$), $\gamma_{\mathbf{q}j}$ is the lowest when the lowest cophononicity is realized (MoTe system); this tells us that such modes are less affected by a change in the unit cell volume if the M and X atoms contributions show the lowest mixing. The $(A, 1-4)$ modes, instead, turn out to be more stable against volume variations when the M and X atoms equally contribute to the corresponding frequency, hence realizing $C_{ph}(M-X) \simeq 0$ (MoS system). Based on these results, among the explored chemistries, the dynamic bulk features of the MoTe system are the most stable ones against unit cell volume variations.

In tribological conditions, external load applied along the c -axis affects mainly the interlayer distances, hence producing a non-isotropic change in the unit cell volume. We therefore choose to extend our mode Grüneisen analysis to specific anisotropic variations of the volume, in order to focus on the structural response in the presence

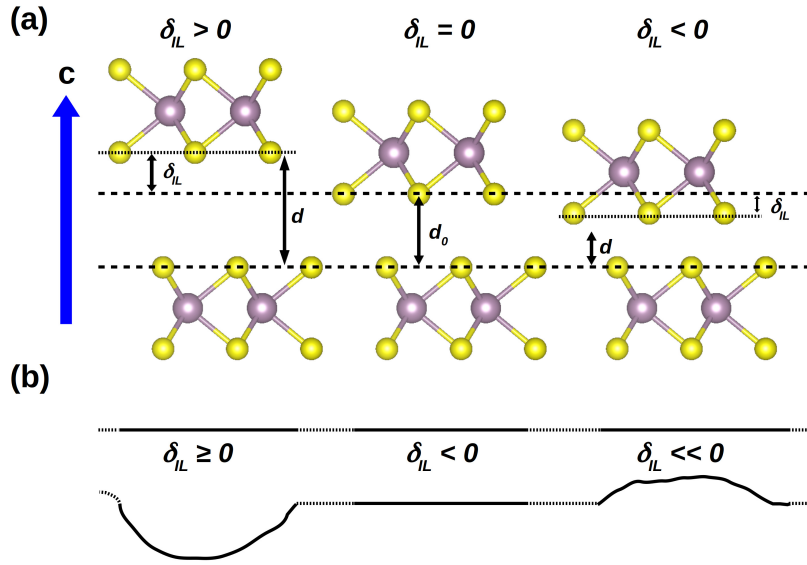


Figure 4.1: (a) The presence of external load is modeled starting from the relaxed structure and changing the optimized interlayer distance d_0 to a new value d by shifting one layer of a quantity equal to δ_{IL} along the c -axis. Purple and yellow spheres represent M and X atoms, respectively. (b) On a larger scale, positive and negative δ_{IL} values represent deviations from the parallel layer ideal configuration, due to the presence of topographic defects.

of external load. To this aim, we build new model systems by rigidly shifting two subsequent MX₂ layers to vary the interlayer distance d_0 ; calling δ_{IL} the difference $d - d_0$, where d is the distance after the rigid shift, we build 6 model geometries for each of the considered system by setting $\delta_{IL} = \pm 0.5, \pm 1.0$ and ± 1.5 Å, respectively. With this choice, a negative value of δ_{IL} represents a compression along the c -axis, which is typical for sliding of perfect crystal or TMD 2D sheets. However, topographic features can locally cause decrease in contact pressure to zero (i.e. $\delta_{IL} = 0$) or even separate two layers at the sliding interface (Figure 4.1a). Such scenario occurs when TMD sheets are bended during sliding, as illustrated in Figure 4.1b. It is worthy to note here that, in our simulations, $\delta_{IL} = -1.5$ Å correspond to an external pressure greater than 80 GPa for all the considered chemistries. We then analyze the variation of $\omega_{\Gamma 4-\Gamma 6}$ and $\omega_{A 4-A 6}$ with δ_{IL} . We find that decreasing the interlayer distance d reduces the frequency of: *i*) the sliding modes ($\Gamma, 4-5$) and ($A, 1-4$), reducing the bulk contribution to the layer sliding; *ii*) the breathing modes changing the interlayer distance d , making the bulk less prone to a further compression along the c -axis.

To understand how the vibrational frequencies variation is coupled to the electronic structure, we need to analyse the electronic density distribution in detail. The analysis of the Bader charges¹⁴¹⁻¹⁴⁵ show no charge variation for Ti atom in the entire δ_{IL} range; indeed, irrespective of the composition, at decreasing δ_{IL} , we observe an increase of the Mo or W atomic charge at the expenses of the X anion, indicative of charge transfer from X to M ion. To better understand how the electronic charge is rearranged after variations of the interlayer distance, we measure the *orbital polarization*^{146,147} of the X and M atomic species as a function of δ_{IL} . Let's recall here that the orbital polarization

\mathcal{P} of the m_{l_1} orbital relative to the m_{l_2} orbital is defined as

$$\mathcal{P}_{l_1 m_{l_1}, l_2 m_{l_2}} = \frac{n_{l_1 m_{l_1}} - n_{l_2 m_{l_2}}}{n_{l_1 m_{l_1}} + n_{l_2 m_{l_2}}}, \quad (4.2)$$

where $n_{l_1 m_{l_1}}$ and $n_{l_2 m_{l_2}}$ are the occupancies of $|l_1 m_{l_1}\rangle$ and $|l_2 m_{l_2}\rangle$ orbitals, with orbital quantum number l_i and magnetic quantum number m_{l_i} , respectively. It is an effective measure of the charge excess in the former orbital with respect to the latter: positive values indicate that m_{l_1} is more populated than m_{l_2} , while the opposite holds for negative values. Using real-space atomic orbital projections, it is possible to partition the electronic density into distinct atomic and interatomic regions, so as to isolate the single contributions hence identifying the electron transfer path. In detail, for each studied system, we calculate \mathcal{P}_{px-py} , \mathcal{P}_{px-pz} and \mathcal{P}_{py-pz} of the X atom, $\mathcal{P}_{t_{2g}-e_g}$ and $\mathcal{P}_{d_{x^2-y^2}-d_{z^2}}$ of Mo and W cations, \mathcal{P}_{d-s} and \mathcal{P}_{d-p} of the Ti atom in the Ti:MoS model. Irrespective of the chemical composition, positive values of δ_{IL} do not affect any orbital population in a significant way; moreover, orbital polarization of the Ti atom are nearly constant within the considered δ_{IL} range, their average values $\mathcal{P}_{d-s} = 85.1\%$ and $\mathcal{P}_{d-p} = 77.2\%$ changing about 1%. At increasing load ($\delta_{IL} < 0$), we observe that: *i*) X p_x and p_y population are almost unvaried while p_z orbital population decreases, *ii*) M e_g orbital population increases, and *iii*) M d_{z^2} population increases at the expenses of $d_{x^2-z^2}$. This indicates that reducing the interlayer distance induces a flow of charge from the interlayer region, described by the p_z orbitals, towards the intralayer region. Charge tends to accumulate on each M atom, in particular along an axis orthogonal to the plane containing the M atoms belonging to the same MX_2 layer (Figure 4.2). We can then conclude that interactions among layers are mediated by the p_z orbitals of X anions belonging to two adjacent layers and facing the same interlayer region. Finally, we can argue that the charge distribution in the inner part of each layer can be controlled by proper perturbations of the electronic density at the surface of the layer.

Orbital polarization is a fine partition of the electronic density, providing a real-space picture of the charge redistribution after alteration of the system geometry in the presence of external load. However, to understand how the redistribution of the electronic charge affects the atomic motions (electro-vibrational coupling), we need to recollect the fragmented information provided by the orbital polarization into a simple electronic descriptor. To this aim, we now analyse the $C_{M,X}$ M–X bond covalency at each of the considered δ_{IL} values, defined in terms of atomic orbital contributions to the electronic density of states.¹³⁴ In the first instance, for $\delta \geq 0.0$ Å we note that the M–X bond covalency can be considered as constant; this result is difficult to extrapolate from the orbital polarizations due to the fluctuations found in the same δ_{IL} range, and shows how the covalency metric $C_{M,X}$ acts as a collective descriptor of the details of the electronic structure. As we already observed about the mode frequencies, the constant trend of $C_{M,X}$ for $\delta > 0$ can be explained considering that, at large interlayer distances, only intralayer interactions are relevant, and they are the only ones that determine the electronic distribution. On the other hand, irrespective of the chemical composition, we find that the covalency is monotonically decreasing with increasing load. We understand this in this way: the charge accumulation in the intralayer region increases the electronic repulsion due to the Pauli's exclusion principle, inducing a localization of the electronic charge onto the M cation, making the M–X bond more ionic. Such charge localization, and the consequent reduction of the covalency, is responsible of the hardening of the (Γ 4-6) and (A,1-6) modes; this means that the less covalent the M–X bond, the less favorable the bulk contribution to the layer shift along the c -axis ((Γ ,6) and (A,5-6) modes) and to the layer sliding ((Γ ,4-5) and (A,1-4) modes). This last aspect suggests

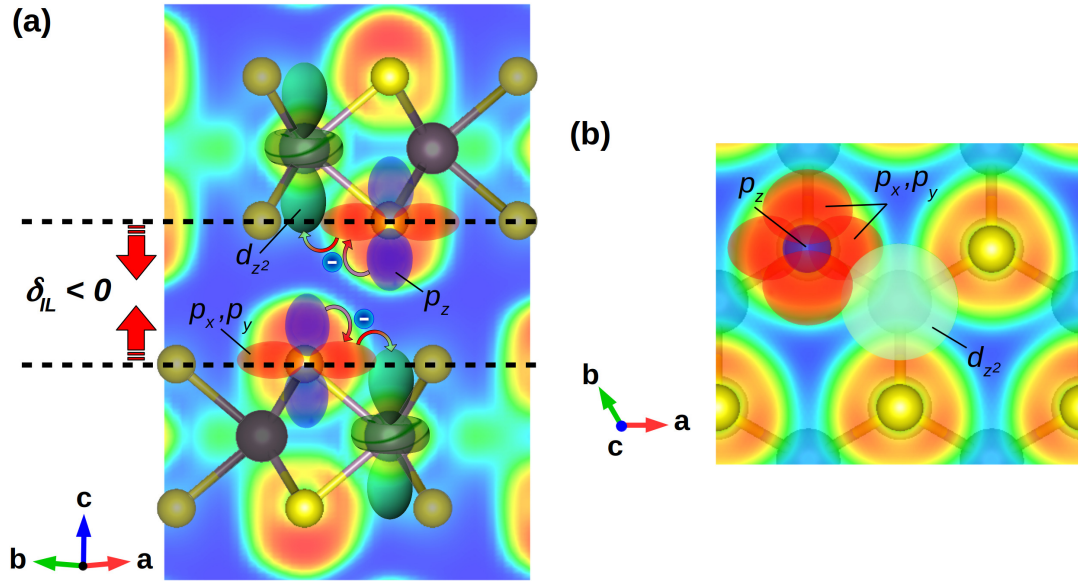


Figure 4.2: Schematic representations of the charge density and the inter-to-intralayer charge flow mechanism: RGB gradient indicates decreasing charge density (red=highest, blue=lowest) while shaded atoms and bonds are out of the sections showing the charge distribution. Color code for atoms is the same as in Figure 4.1; the generic M cation here represents Mo or W atom, since no variation of the orbital polarization of Ti atom has been observed in the Ti:MoS system. (a) Electronic density on a plane parallel to the c -axis and containing two X–M–X bonds, each belonging to two subsequent MX_2 layers. Upon interlayer distance reduction, charge flows from the inter- to the intralayer region, thanks to electron transfer from X p_z to M e_g orbitals via an intermediate step involving the p_x and p_y orbitals of the X atom; charge thus accumulates onto an axis containing the M cation and orthogonal to the layers. (b) Electronic charge distribution on a plane orthogonal to the c -axis and containing the X anions facing the same interlayer region. The hybridization of the d_{z^2} orbital of the M cation with the p_x and p_y orbitals of the X atom allows the X→M charge transfer. Adapted from Ref. 127.

that, at increasing load, the macroscopic friction coefficient is expected to increase; exceptions are found for those systems with instabilities at $\delta_{IL} = -1.5 \text{ \AA}$, which, at very high loads, are expected to show improved frictional properties.

To further disentangle the atomic contributions to the vibrational response, we now calculate the M-X pair cophonycity at the considered δ_{IL} values, in order to understand how the relative M/X atomic composition of the vibrational bands is affected by the interlayer distance (Figure 4.3b). Interestingly, we find an abrupt variation of $C_{ph}(\text{M-X})$ at $\delta_{IL} = -1.5 \text{ \AA}$, supporting the idea that significant electro-structural coupling effects arise at high load; on the other hand, irrespective of the atomic types, $C_{ph}(\text{M-X})$ can be considered constant for $\delta_{IL} \geq -1.0 \text{ \AA}$. This last result tells us that once the chemical composition and the M-X connectivity are fixed, the M-X pair cophonycity is a feature of the systems, which is preserved if the external load is not extremely high.

The variability of the structural response can be quantified in terms of the amplitude of the interval within which each mode frequency variates: the higher such amplitude, the higher the variation of a specific frequency with the external load. We define the

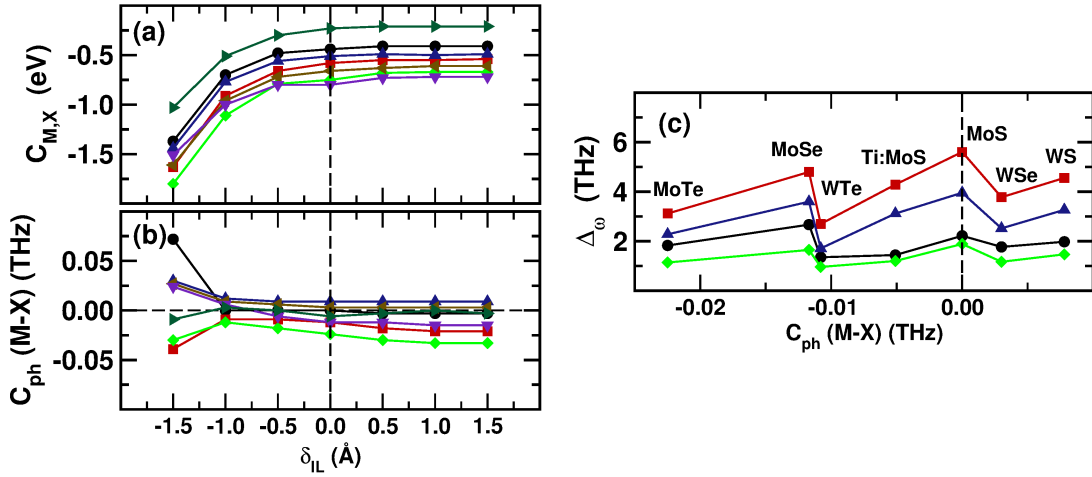


Figure 4.3: (a) M–X bond covalency and (b) M–X pair cophonicity as a function of the interlayer distance variation δ_{IL} ; covalency is found to be a monotonic function of δ_{IL} while cophonicity is nearly constant for $\delta_{IL} \geq -1.0$ Å. (c) Amplitude of the variation interval of $\Gamma(4-6)$ and $A(1-6)$ mode frequencies as a function of $C_{ph}(M-X)$; $C_{ph}(M-X)$ values here used are those calculated at $\delta_{IL} = 0.0$ Å. The smallest variation interval of the considered frequencies is realized at $C_{ph}(M-X) \approx -0.01$ THz, corresponding to the WTe system. Adapted from Ref. 127.

variation amplitude $\Delta\omega_{qj}$ of the frequency ω associated to the \mathbf{q} reciprocal vector as

$$\Delta\omega_{qj} = \max_{\omega_{qj}} [\omega] - \min_{\omega_{qj}} [\omega] \quad (4.3)$$

evaluated among all the calculated ω_{qj} frequencies at varying load. The smaller $\Delta\omega$, the smaller the change of the vibrational frequency; a system with small $\Delta\omega$ shows bulk properties that are less affected by the external load. We find that, irrespective of the mode, the minimum $\Delta\omega$ is realized at $C_{ph}(M-X) \approx -0.01$ THz, corresponding to the WTe system (Figure 4.3b). Moreover, concerning the $(\Gamma,4-5)$ and $(A,1-4)$ sliding modes, the Ti:MoS system shows a small $\Delta\omega$ value similarly to WTe. These outcomes suggest that, in the presence of external load, the Ti:MoS and WTe bulk contributions to the sliding are expected to be the least affected among the studied systems.

Chapter 5

The role of charge accumulation in the nanofriction response

In tribological conditions, non-null net charges can arise^{148–151} and redistribute in the neighbourhood of the volume where they originated; this corresponds to a charge injection across several layers, and to a perturbation of their charge neutrality. Such perturbation influences the intrinsic frictional properties, the latter being highly relevant in the micromanipulation of free-standing atomic layers,¹⁵² hence in the final design of TMD-based nanostructured materials. Charges may be free to move through the material or may localize in the local environment of specific atomic sites. As a consequence, attractive or repulsive Coulombic forces may arise, either hindering or facilitating relative layer gliding, depending on several factors such as sliding velocity, temperature and atomic types forming the structure. In the light of such observations, in the work reported in Ref. 153 and summarised in this chapter, we focus on how the presence of non-null charge affects the sliding-related modes in the prototypical MX₂ TMDs.

We consider neutral as well as charged systems, with charge $q = 0, \pm 0.01, \pm 0.03 \pm 0.05, \pm 0.1, \pm 0.2, \pm 0.3, \pm 0.5, \pm 0.7, \pm 1.0$ $|e|/\text{cell}$. We do not find unstable displacements, with the exception of the MoS systems with $q = -0.5, -0.7, -1.0$ $|e|/\text{cell}$; the careful search of the stable states we performed on the latter cases, indeed, suggests that such instabilities cannot be removed unless the charge content is varied. For this reason, we will exclude these cases from our present analysis. Perturbation of the charge neutrality induces a reduction of the system symmetries, from hexagonal to orthorhombic, monoclinic or triclinic; among the charged systems, we notice that the MoTe, WSe and WTe models maintain the geometry with the highest symmetry ($Cmcm$) at very different charge amounts. This can be qualitatively ascribed to the fact that larger ions can accommodate charge variations better than smaller ones, limiting possible symmetry reductions. At $q = \pm 0.05$ $|e|/\text{cell}$, the symmetry is lowered from hexagonal to orthorhombic, monoclinic (WS at $q = -0.05$ $|e|/\text{cell}$), or triclinic (MoS at $q = 0.05$ $|e|/\text{cell}$), with space group number ranging between 194 and 1; correspondingly, a variation of the c -axis is observed. In all the charged systems, at fixed X anion the c -axis is found longer when $M = \text{Mo}$. Considering that the c -axis variation range is wider than that of the a -axis, we can infer that the charge alteration is mostly accommodated along the direction orthogonal to the layer planes, producing a volume increase at increasing charge content.

We then proceed with the phonon analysis. At $q = 0$, the sliding modes are ($\Gamma, 4-7$), ($\Gamma, 8-9$), ($A, 1-4$), ($A, 7-10$), while the compressive (breathing) modes are ($\Gamma, 10-11$), ($\Gamma, 12$),

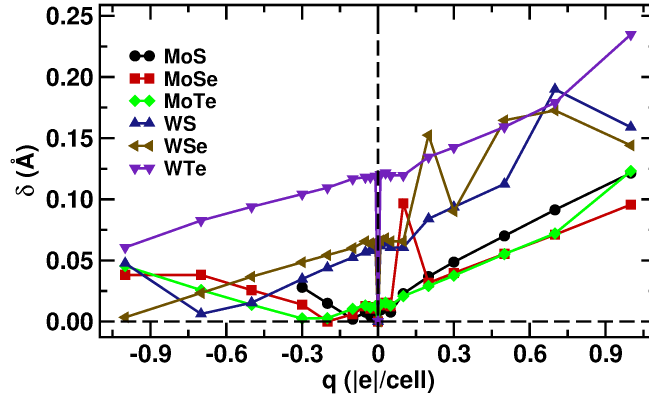


Figure 5.1: Overall structural distortion δ as a function of the charge content q . Lines are a guide for the eye. Adapted from Ref. 153.

(A,5-6), (A,11-12), where we grouped the modes with degenerate frequencies.^a We want here to notice that, according to the usual convention, the A point relative to the hexagonal space group 194 corresponds to the Z point relative to the space groups 63, 40, 15, 8, 5, 2 and 1, and to the Y point relative to the space groups 12 and 6; all the three A, Y and Z high symmetry points correspond to the direction $(0,0,1/2)$ of the respective reciprocal lattices. However, the displacement pattern of the (A,1-12) modes is equivalent to that of the (Z,1-12) and (Y,1-12) modes; for this reason, we will simplify the notation by referring to the (Z,1-12) and (Y,1-12) modes as (A,1-12) modes without any ambiguities. As expected, the loss of charge neutrality and the consequent symmetry reduction produce, in general, the split of some degenerate modes. Irrespective of the chemical composition, the frequencies of the considered modes are globally increasing at increasing q . However, the frequency-charge relation is not symmetric about $q = 0$: while for $q < 0$ the trend is smooth, for $q > 0$ sudden jumps are observed. Some of the jumps are expected due to a change in the space group; in other cases, frequency jumps are observed despite no variation of the system symmetries occurs. In this respect, the frequency-charge-structure relation is not trivial and other descriptors must be considered to harness the frequency change at variable charge content.

Interplay between charges and structural distortions have already been observed in several classes of materials.^{44,154,155} To analyse the details of the symmetry reduction upon removal of charge neutrality, we perform a group theoretical analysis by decomposing the ground state geometries into irreducible representations of the corresponding high symmetry hexagonal $P6_3/mmc$ phase, aided by the ISODISTORT software.¹⁴⁰ Strain distortions are mainly accounted by the variation of the c -axis length discussed above; thus, from now on, we will only consider the overall structural distortion δ generated by pure atomic displacement (Figure 5.1). The main kind of distortion is $\Gamma 1+$, corresponding to the bending of the X-M-X intralayer angle (Figure 5.2a); other distortions have negligible values, being 3 order of magnitude smaller. In few particular cases, the latter are not negligible and contribute to the overall atomic displacements in such a way to produce sudden variations of the atomic displacements (Figure 5.1). Such cases are: *i*) $\Gamma 5+$, relative rigid sliding of adjacent MX_2 layers in MoSe at $q = 0.1$, WSe at $q = 0.2, 0.5, 0.7$, MoTe and WTe at $q = 1.0$ (Figure 5.2b); *ii*) $\Gamma 6+$, intralayer rigid

^aUnlike the models considered in the other chapters, the geometries used for the present study are obtained as supercells of the respective primitive ones; accordingly, the mode labels are different.

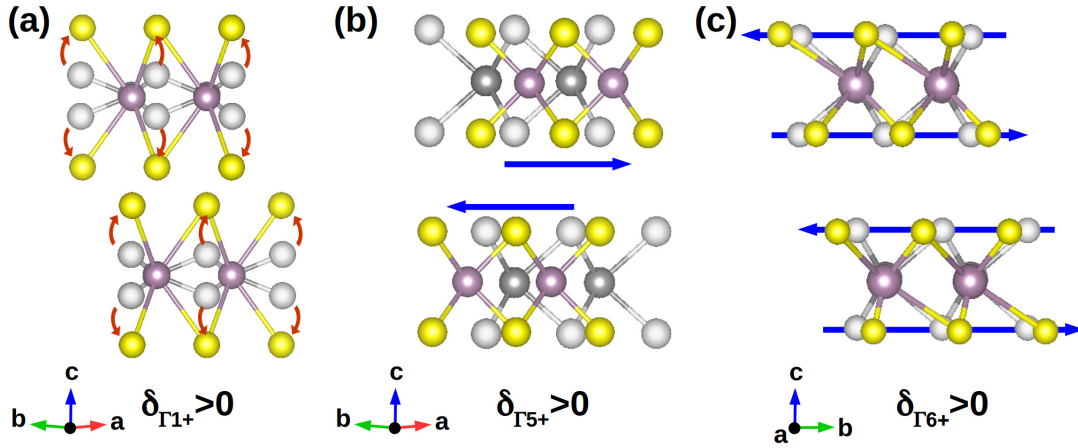


Figure 5.2: Schematics of (a) Γ_{1+} , (b) Γ_{5+} and (c) Γ_{6+} distortion modes corresponding to the bending of the X-M-X intralayer angle, rigid interlayer sliding, and intralayer rigid sliding of X planes relative M planes, respectively; positive distortion $\delta_{\Gamma_{1+}}$, $\delta_{\Gamma_{5+}}$ and $\delta_{\Gamma_{6+}}$ amplitudes indicate displacements along the directions shown by the arrows. Γ_{1+} distortion is dominant in all the examined cases. Atom color legend is the same as in Figure 2.7; grey spheres represent undistorted atomic positions. Displacements are magnified for clarity. Adapted from Ref. 153.

sliding of S planes with respect to W planes in WS system at $q = 0.7$ (Figure 5.2c).

At fixed X anion, δ is larger in WX than in MoX compounds, with some exceptions at specific q values of the MSe models. This means that MoX systems are able to accommodate charge variations better than WX systems, limiting the atomic displacements to the minimum. Similarly to what observed in the frequency-charge relation, δ values are not symmetric about $q = 0$. Distortions at $-|q|$ are lower than the corresponding ones at $+|q|$, and increase for $q > 0$; for $q < 0$, the distortions decrease at increasing charge content in WX systems, while they increase at a lower rate in MoX systems. This outcome is a further example of the non-trivial charge-structure relation, and point out that multiple descriptors must be used to control the electro-structural coupling and its effect on the sliding-related vibrational modes of the system.

We now proceed with the study of the details of the electronic distribution. To this aim, we first perform a Bader charge analysis and consider the difference $q_B = q_M - q_X$, where q_M and q_X are the Bader charges of the X and M atomic species, respectively (Figure 5.3a); we then calculate the $C_{M,X}$ bond covalency¹³⁴ and the $C_{ph}(M-X)$ cophononicity (section 2.5) of the M-X pair, in the range $[-10, 0]$ eV and $[0, 2.25]$ THz, respectively (Figure 5.3b-c). We observe that the variation range of q_B is wider in WX systems, and can be put in correspondence with a larger variation of the structural distortions with the charge content (Figure 5.1). Bond covalency is slightly decreasing upon charge injection, displaying a general linear trend with the system charge; however, by comparing Figure 5.3b) and c), it is immediately apparent that the covalent character of the bond is not strictly related to q_B , nor directly connected with δ (Figure 5.1). Similar observation can be applied to the cophononicity data: in a good approximation, $C_{ph}(M-X)$ is linear with the charge content, after neglecting few local minima/maxima due to more subtle electronic features which we will discuss later on. We also compute the electron localization function^{156,157} (ELF) of all the considered systems: irrespective of the chemistry and the charge content, no localization of the

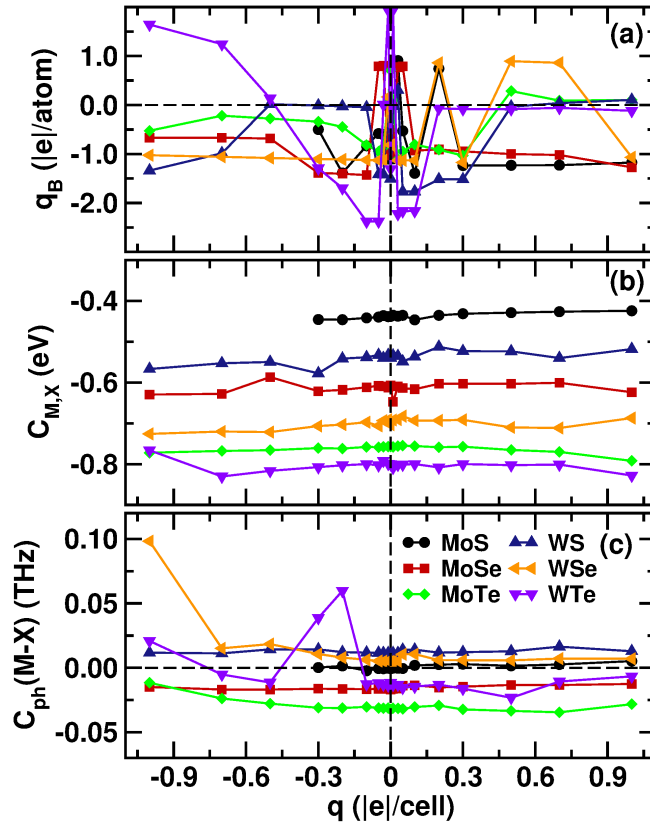


Figure 5.3: (a) q_B Bader charge difference ($|e|/atom$), (b) $C_{M,X}$ M-X bond covalency (eV) and (c) $C_{ph}(M-X)$ cophonicity (THz) of the M-X pair as a function of the system charge q . Lines are a guide for the eye. Adapted from Ref. 153.

extra charge q occurs in any specific volume of the system cell. These last outcomes suggest that the electronic and dynamic features of the ionic environment are the result of a delicate balance between local rearrangements of the electron density, structural distortions and overall charge neutrality perturbation. For this reason, we now focus on the subtle details of the electronic density spatial distribution by analysing the orbital polarization.

The charge density can be partitioned in atom-centered hydrogen-like orbitals, so as to uncover the features of electronic flows through the structure at variable charge content q .¹⁵⁸ We then measure the orbital polarization (Equation 4.2) of the X and M atomic species in each of the relaxed systems. In all the charged systems, X p_x and p_y orbitals are almost equally populated, with an exception at $q = \pm 0.03$ for all the systems and at $q = 0.01$ for the MoSe system, where p_x orbital is more populated than the p_y one. On the other hand, p_z orbital displays an excess of population with respect to both p_x and p_y orbitals. At fixed M cation, \mathcal{P}_{p_x,p_z} and \mathcal{P}_{p_y,p_z} polarizations increase as $MTe < MS < MSe$, assuming higher values if $M = W$. The t_{2g} orbitals are more populated than the e_g ones, with $d_{3z^2-r^2}$ orbital bearing an excess of charge with respect to the $d_{x^2-y^2}$ orbital. In general, at fixed M cation and charge content q , the $d_{3z^2-r^2}$ population decreases with the X species as $S > Se > Te$, whereas higher population is found in WX systems. The amount with which the $d_{3z^2-r^2}$ orbital can accommodate a specific amount of charge is therefore determined by both the M and X atomic types. We can then state that, upon charge injection, a flow of charge occurs from the t_{2g} to

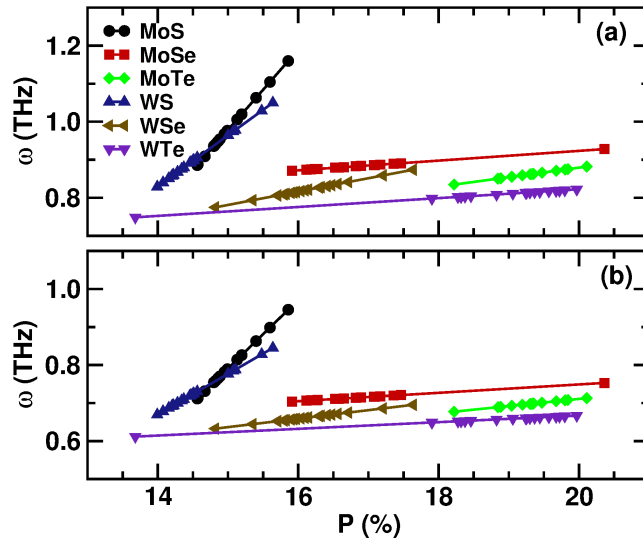


Figure 5.4: Linear interpolation of the average frequency ω as a function of the $\mathcal{P}_{t2g,eg}$ orbital polarization of the considered (a) $\Gamma(4-12)$ and (b) $A(1-12)$ phonon modes, respectively. Irrespective of the chemical composition, mode frequencies are overall increasing with increasing $\mathcal{P}_{t2g,eg}$ orbital polarization. Adapted from Ref. 153.

the e_g orbitals, in particular towards the $d_{3z^2-r^2}$ one, which results to be more prone to accommodate the incoming electrons. This mechanism accounts for the c -axis variation with the system charge q , as the $d_{3z^2-r^2}$ orbital extends along the \hat{c} direction. In fact, ion substitution regulates the charge transfer from the planes parallel to the xy -plane and containing the X anions towards an axis parallel to \hat{c} , with the $\mathcal{P}_{t2g,eg}$ orbital polarization being the quantity controlling such transfer. Moreover, $\mathcal{P}_{t2g,eg}$ regulates the M-X interaction, hence the lattice dynamics. Following these results, we first focus on the ($\Gamma,4-12$) modes and calculate the average frequency ω at fixed $\mathcal{P}_{t2g,eg}$ value, thus obtaining a $\{\omega, \mathcal{P}_{t2g,eg}\}$ data set for each MX system; we then evaluate the linear interpolation of such data sets and report the results in Figure 5.4a. We repeat the same procedure on the ($A,1-12$) modes and show the interpolated data in Figure 5.4b. An inspection of the figures clearly show that the mode frequencies overall increase with the $\mathcal{P}_{t2g,eg}$ orbital polarization. By controlling the $\mathcal{P}_{t2g,eg}$ orbital polarization, it is then possible to finely tune the phonon modes relative to layer sliding; to this aim, we will exploit the connection between $\mathcal{P}_{t2g,eg}$ with the M-X bond covalency and cophonycity. Irrespective of the chemical composition, at a fixed charge, $\mathcal{P}_{t2g,eg}$ is decreasing with increasing $C_{M,X}$ and $C_{ph}(M-X)$, the latter two descriptors being connected with the atomic type, the structural distortions and the electronic density distribution, as we have already shown in previous studies.^{41,127,158}

Chemical composition and stoichiometry can be chosen in such a way that they induce specific structural distortions that alter the electronic distribution and are more suitable to accommodate a specific amount of charge in the structure; at the same time, they alter the interatomic interactions that determine the vibrational motions of the system. We can thus conclude that covalency and cophonycity can be used as a knob to control the $\mathcal{P}_{t2g,eg}$ orbital polarization, and hence low-frequency phonons contributing to the intrinsic friction in charged MX_2 systems.

Chapter 6

The electrostatic field as an external knob to tune nanoscale friction

Previous studies already pointed out that load can be used as an external knob to control the nanoscale friction,^{52,159,160} although it may induce unwanted permanent changes to the atomic geometry.^{161–164} On the other hand, electrical fields induce charge movements which may alter the frictional properties temporarily, while allowing to revert to the original structure once the field is suppressed.^{21,22,153} Some theoretical studies have already dealt with the effect of electric fields on the coupling between the electronic and dynamic (i.e. phonon) features in low-dimensional materials;^{165,166} interestingly, such coupling has been found to be effective in altering the lateral frictional force in MoS₂ and graphene bilayer systems.^{167,168} Recent experimental studies showed how to manipulate free-standing atomic layers by in-plane potential gradients with an Atomic Force Microscopy tip,^{152,169} while the friction between the tip and the layer decreases with the field.²¹ Motivated by this findings, in the work reported in Ref. 170 we study the microscopic mechanisms governing the intrinsic friction at the nanoscale in the presence of electrostatic fields. We here summarise the main results of that work, together with the methodology to obtain them.

As a case study, we consider the six prototypical van der Waals transition metal dichalcogenides that we already analysed in the previous chapters. Following the formulation of Nunes and Gonze,^{171,172} we apply an external electrostatic field \mathbf{E} along a direction parallel to the \mathbf{c} lattice vector (perpendicular to the sliding plane), the magnitude of which varies in the range $[0, 2.5] \times 10^{-3}$ a.u.^a Apart the largest values of 2.0 and 2.5×10^{-3} a.u. which we consider as extreme cases, the remaining values are representative of the electric fields typically used in MEMS/NEMS devices.^{173–177}

According to the classical picture (chapter 2), at a constant system energy, the lower the frequency of the sliding modes, the larger the amplitude of the corresponding atomic displacements, this corresponding to facilitated sliding. If the frequency of a sliding mode becomes negative^b due to external stimuli, the geometry becomes unstable against the distortion represented by the eigendisplacement of such mode, and the atomic

^a1 a.u. of electric field corresponds to 514220624373.482 V/m, as $1 \text{ a.u.} = e/(4\pi\epsilon_0 a_0^2)$, where e is the electron charge, ϵ_0 is the vacuum permittivity and a_0 is the Bohr radius.

^bWhen the eigendisplacement of a phonon mode is unstable, the corresponding eigenfrequency is an imaginary number; however, it is instead usually indicated by a negative real number for convenience of representation.

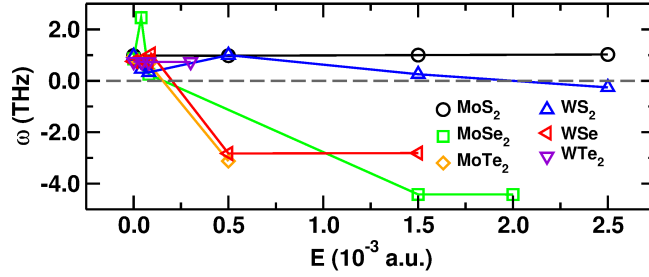


Figure 6.1: Average frequency as a function of the applied electric field. Instabilities arise when the field magnitude is above a critical value depending on the chemical composition. Lines are a guide for the eye. Adapted from Ref. 170.

configuration does not realize a minimum of the energy any more. This means that a very small perturbation of the geometry is enough to activate the sliding motion along the direction of the mode eigenvector; as a consequence, a new minimum of the energy is realized. The latter corresponds to a new geometric configuration with new sliding mode frequencies which, in principle, can be larger than the initial ones. To obtain easy sliding over long distances, it is then necessary to lower the frequencies of the sliding modes at each local minimum of the energy landscape; indeed, it has been found that layered compounds display several energy minima with different curvatures.^{90,178–181} Nevertheless, the present discussion is general and does not depend on the specific atomic topology. For this reason, we here focus on the structural configurations corresponding to one of the possible energy local minima of the considered compounds; the same analysis can then be repeated on the geometries corresponding to any other minimum. If an approximate evaluation of the frequencies is required, it is possible to reduce the computational load by exploiting the *normal-modes transition approximation*⁴² (section 2.4).

We want to avoid the fragmentation of information into several parameters; instead, we use global quantities in order to obtain a unified description of the physics of the system. To this aim, we consider the mean frequency ω which is calculated as

$$\omega = \frac{1}{N} \sum_j^N \omega_j \quad (6.1)$$

where N is the number of the considered sliding and breathing modes and ω_j is the frequency of the j -th mode. It is worthy to note here that ω can assume positive values despite the fact that some of the ω_j can be negative, that is, also in the presence of unstable modes. In this respect, a positive value of ω indicates that the amount of instabilities, that is the number of unstable modes and the magnitude of the relative frequencies, is null or negligible; in the latter case, the structure can be considered “globally” stable. The phonons relevant to our discussion are mainly located at the Γ and A points of the irreducible Brillouin zone; we will then focus on this portion of the reciprocal space in our phonon analysis.

We start our investigation from the effect of the electric field on the geometry. At non-null fields, we observe the largest volume variation in the MoSe₂, MoTe₂ and WSe₂ systems, mainly due to the change in the length of the c lattice vector; this is expected, since such crystallographic axis is parallel to the direction of the applied field \mathbf{E} . Some structure becomes unstable for field values beyond a certain threshold which depends on the atomic types; for those values, the lattice parameters

correspond to a transient configuration which belongs to a geometric path connecting two stable states. Such transient configuration can be detected by time-resolved crystallography techniques, capable to monitor structural changes occurring in very short time scales.^{182–184} Concerning the phonon structure, we observe that an increase of the field produces a general hardening of the Γ –A modes together with a softening of some sliding branches, which may become unstable beyond some critical E ($E = |\mathbf{E}|$) value specific of the system. This is apparent when we consider the average frequency ω as a function of E (Figure 6.1): the MoS₂, WS₂ and WTe₂ systems appear to be the most stable against large field perturbations while, in the remaining compounds, some of the sliding modes become unstable already at $E = 0.5 \times 10^{-3}$ a.u. This suggests that the sliding can already be facilitated in MoSe₂, MoTe₂ and WSe₂ pristine TMDs by means of the application of small electric fields.

To quantify how the electronic charge redistributes across the structure under the effect of the field we make use of the orbital polarization analysis (Equation 4.2). We consider the p_x , p_y and p_z orbitals centered at the anion sites, and the t_{2g} and the e_g orbitals centered at the cation sites, in order to calculate the following polarizations: \mathcal{P}_{p_x,p_y} , \mathcal{P}_{p_x,p_z} , \mathcal{P}_{p_y,p_z} , \mathcal{P}_{t_{2g},e_g} , $\mathcal{P}_{d_{x^2-y^2},d_{z^2}}$. We notice that the presence of the field does not induce any significant change in the relative occupation of the p_x with respect to the p_y orbital; the fluctuation around zero of \mathcal{P}_{p_x,p_y} indicates that the electrons are equally distributed between the two orbitals. This is an expected behaviour thanks to the symmetries present in the a, b plane; for the same reason, both \mathcal{P}_{p_x,p_z} and \mathcal{P}_{p_y,p_z} orbital polarizations show the same trend. The negative values of \mathcal{P}_{p_x,p_z} and \mathcal{P}_{p_y,p_z} indicate an excess of electrons along an axis orthogonal to the layers at the anion site, such excess remaining nearly constant irrespective of the applied field. Concerning the relative occupation of the t_{2g} and e_g orbitals, in the MoSe₂, MoTe₂ and WSe₂ systems we notice that an increase of the field induces a transfer of electrons towards the e_g orbitals and, correspondingly, an electron flow from the $d_{x^2-y^2}$ to the d_{z^2} orbital. This points at a charge transfer along an axis orthogonal to the a, b plane and passing through the cation sites. Differently, in the MoS₂, WS₂ and WTe₂ systems the variation of the field leaves almost unaltered both the \mathcal{P}_{t_{2g},e_g} and $\mathcal{P}_{d_{x^2-y^2},d_{z^2}}$ polarizations. This analysis then suggests that the applied field induces an accumulation of charge along the \hat{c} direction in the MoSe₂, MoTe₂ and WSe₂ systems, which accounts for a significant variation of the c lattice constant and the consequent instability of the sliding modes (Figure 6.1).

In order to connect the charge redistribution to the dynamic response (i.e. phonons), we calculate the cophononicity (section 2.5) $C_{ph}(\text{M-X})$ of the M-X pairs. We observe that the cophononicity is nearly constant for low values of the electric field (Figure 6.2); in this respect, it can be regarded as an intrinsic characteristic of the stable system. For each system, there is a critical electric field beyond which the cophononicity deviates significantly from the value at zero field. Correspondingly, the structure becomes highly unstable against the sliding and breathing distortions, that is, the relative layer motion is promoted in a more significant amount than what is observed for the cases at low field. Interestingly, in general, the sliding and breathing displacements are stable when perfect cophononicity is realized ($C_{ph}(\text{M-X}) \approx 0$), while become prevalently unstable when $C_{ph}(\text{M-X})$ significantly deviates from zero; how far from zero it must be to have unstable modes depends on the system. This means that if the overall layer displacement is formed by atomic motions in which the M and X atoms move in average at the same velocity, the sliding is favoured at low electric field values; on the contrary, larger field values require that cations and anions move at a very different velocity in order to

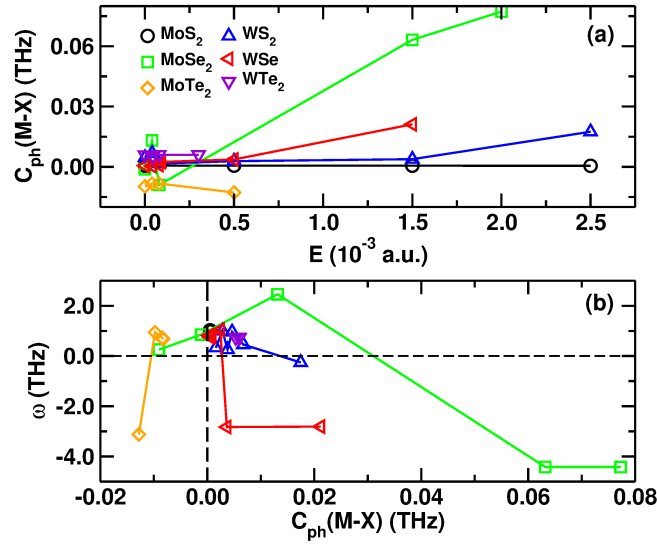


Figure 6.2: (a) Cophonicity of the M-X pair as a function of the electric field. (b) Average frequency as a function of the cophonicity. Legend is common to both subfigures; lines are a guide for the eye. Adapted from Ref. 170.

produce easy gliding of the layers. In passing, we notice that the cophonicity values here reported are similar to those realized in finite n -layered TMDs, where the orbital polarization and the consequent interlayer charge distribution play a relevant role in the determination of the sliding-related frequencies.¹⁵⁸

The presented case study can be extended by considering geometric configurations corresponding to local energy minima other than those considered in the present work; in this way, it is possible to obtain a more complete overview of the set of electric field values suitable for the selected atomic types. Moreover, atomic species and geometries other than those pertaining the here examined TMD prototypes can be the subject of future studies. To this aim, it is possible to use the cophonicity to parameterize the nanoscale frictional response to external electric fields in large databases of chemical moieties and atomic topologies. Such parametrization can be used in machine learning engines¹⁸⁵ for automated research of proper combination of atomic species and geometries, to ultimately design novel tribological materials with targeted frictional response under electric field stimuli. Finally, the observed relation between the charge flow and the electric field may guide the probe and control of metal-to-insulator transition in nanomechanical motions,^{186,187} since the transition is generally determined by subtle anisotropic rearrangements of the electronic density.^{146,188,189}

Chapter 7

Inert intercalant as friction modifier

The fundamental starting point to build 2D TMD-based systems is to obtain mono or few-layered TMD films. The crucial aspect involved in harnessing layer exfoliation is understanding the interlayer environment. In bulk TMD structures, the weak van der Waals forces allow relative sliding of adjacent layers and ease layer separation under external solicitations. Individual layers of TMDs can be isolated from the bulk parent via mechanical cleavage,^{190–192} liquid exfoliation,^{193,194} or ion intercalation.^{195–198} The most promising method would seem to be the intercalation of inert rather than ionic species in order to prevent unwanted interactions.

Computational investigations on exfoliation of layered materials have mainly focused on interlayer adhesion energies also in the presence of exfoliation assisting molecules,^{199–203} and very few of them dealt with TMD compounds.²⁰⁴ Adhesion indeed is the main force resisting the layer peeling and is then one of the main structural responses to harness in order to facilitate the exfoliation process. However, adhesion is inevitably accompanied by the resistance that adjacent atomic layers develop to prevent the relative parallel shift, this occurring because the exfoliation is initiated and carried out by mechanical stress tangent to the layer surface.^{205–208} layer sliding and separation are the two main phenomena that must be controlled in order to obtain a facile exfoliation of the lamellar structure. Nanotribological properties of TMD layers play therefore a fundamental role in the exfoliation process. Following the perspective outlined above, we here review our work²⁰⁹ focusing on how inert molecules change the tribological properties of TMD layers when intercalated in the interlayer gap.

The exfoliation process occurs thanks to the combined action of external forces acting along the shear and vertical directions with respect to the layer plane;^{205–208} such forces are capable to overcome the internal forces which bind the layers together. This can be visualized in the following way. If an external macroscopic force acts on the system with a non-null component tangent to the material surface, the atomic layers slide upon shearing. As a response, internal forces opposing the shift develop, and the relative motion is realized as long as the external tangent force is active and larger than these internal ones; such internal forces manifest as friction. Both sliding and breathing modes are then active whenever two subsequent layers are laterally displaced to be separated (section 2.2); if the separation occurs thanks to only vertical forces, then solely the breathing modes are active and are hindering the exfoliation. The control of both sliding and breathing frequencies is then desirable to optimize the exfoliation process. To this aim, we will focus on the frequencies of both the sliding and the breathing

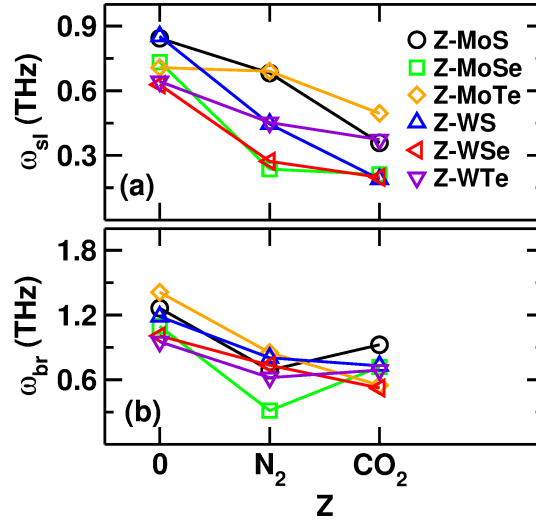


Figure 7.1: Average frequency of (a) sliding and (b) breathing modes at the considered molecular moieties; $Z=0$ indicates the pristine compounds. Legend is common to all the subfigures. Adapted from Ref. 209.

modes. In order to reduce the number of parameters and facilitate the analysis, we consider the mean sliding frequency ω_{sl} which reads

$$\omega_{sl} = \frac{1}{N} \sum_j^N \omega_j \quad (7.1)$$

where ω_j is the frequency of the j -th sliding mode and N is the total number of the considered sliding modes; the mean breathing frequency ω_{br} is defined in an analogous way. Let us here recall that, in the practice, the distinction into breathing and sliding modes is done by considering reference vectors parallel and perpendicular to the layer surface. The modes with large scalar projections along the parallel or perpendicular reference vectors are labeled as sliding and breathing modes, respectively (section 2.2).

We consider the six prototypical MX₂ TMDs, with $M = \text{Mo, W}$ and $X = \text{S, Se, Te}$; we select $Z = \text{N}_2, \text{CO}_2$ as inert intercalant molecules, whereas $Z = 0$ indicates the pristine structure. In general, the presence of a molecule induces a lowering of ω_{sl} and ω_{br} with respect to the pristine case ($Z = 0$), irrespective of the chemical composition of the layers; this is expected, because the presence of the molecule increases the separation between the layers and screens the interaction between them, making the sliding (friction) and breathing (adhesion) restoring forces weaker. However, although the steric hindrance of the CO₂ molecule is larger than the N₂ one, the effect on the mean sliding and breathing frequencies is peculiar of the system (Figure 7.1): while the mean sliding frequency decreases as in the sequence $0 > \text{N}_2 > \text{CO}_2$, the mean breathing frequency increases in Z-MoS, Z-MoSe and Z-WTe systems when Z changes from N₂ to CO₂. There is no direct relation between the cell volume and the frequency shift: ω_{sl} and ω_{br} increase or decrease with the volume according to the specific chemical composition. The frequency shift is not then a mere result of the change in the geometry of the system but arises from the subtle interplay between the electronic and the dynamic features. In fact, the phonon frequencies are obtained from the diagonalization of the dynamical matrix which, in turn, is the normalized Fourier transform of the interatomic force constants (section 2.1);^{98,99} these latter depend on the atomic types forming the system

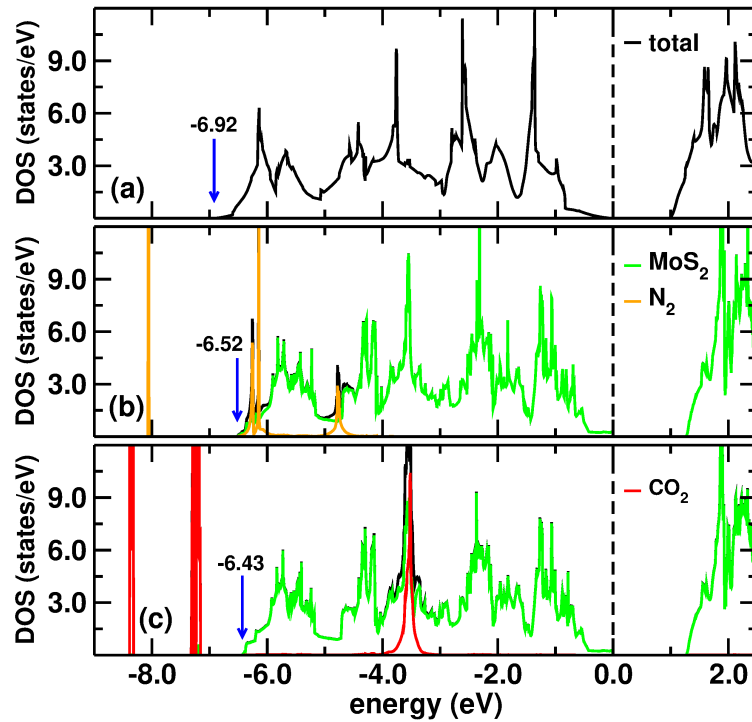


Figure 7.2: Density of states of the (a) 0-MoS, (b) N₂-MoS and (c) CO₂-MoS systems. The DOS values are normalized by a factor chosen to optimize the visualization. In each plot, the Fermi level has been set to 0 eV and is marked by a vertical dashed line, while the blue arrow indicates the position of the bottom of the valence band with the corresponding value reported right above. Legend is common to all the subfigures. Adapted from Ref. 209.

and determining the electronic environment in which they are embedded. Any change induced in the electronic distribution of the pristine material is therefore reflected into a change of the atomic interactions and the corresponding phonon frequencies. For this reason, we continue our analysis by focusing on the electronic density of states (DOS).

A typical profile of Z-MX electronic DOS is reported in Figure 7.2, where we show the case of the Z-MoS systems. The valence band of the pristine material covers the energy range $[-6.92, 0]$ eV (Figure 7.2a); once a molecule is inserted into the interlayer gap, the width of the valence band is narrowed by an amount that depends on the kind of molecule (Figure 7.2b-c). The atom-projected DOS reveals that the molecule contributes with its own states to the valence band; however, no hybridization occurs between the atomic-like wavefunctions centered on the molecule and those centered on each surrounding X anions. This is an expected behavior because N₂ and CO₂ are known to be inert gases and any non-null wavefunction overlap would indicate an interaction between the molecule and the layers. This is apparent from the analysis of the partial electronic density generated by considering the energy range which includes the Z-states in the valence band (Figure 7.3): the partial electronic distribution is localized on the molecule and around the cation within the layer, while no density shared between the layers and the molecule is found. The effect of the molecule orbitals is then to change the width of the valence band by contributing to the whole system wavefunction without interacting with the MX₂ layer orbitals, but yet determining the relative position of the latter within the valence band. We find that the valence-band width does not correlate

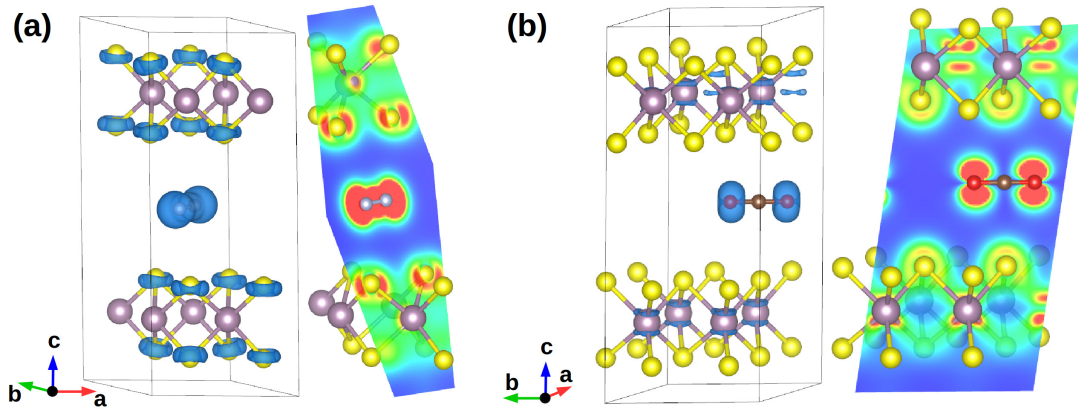


Figure 7.3: Isosurface (blue) and plane projection of the partial charge density in (a) N₂-MoS and (b) CO₂-MoS, obtained by selecting the electronic bands in the range $[-6.5, -6.0] \cup [-5.0, -4.5]$ and $[-4.0, -3.2]$ eV, respectively, each including the corresponding Z-states (see Figure 7.2). No significant charge is found in the region between the molecule and the sulphur atoms, this showing that no hybridization occurs between the S-centered and molecule-centered atomic orbitals. The Red-Green-Blue color gradient indicates decreasing charge density values. Adapted from Ref. 209.

with the lattice vectors length nor with the system volume; interestingly, the width decreases as in the sequence $0 > \text{N}_2 > \text{CO}_2$ irrespective of the chemical composition of the layers (Figure 7.4a). Such behavior is similar to that found for the sliding and breathing frequencies (Figure 7.1); in fact, ω_{sl} and ω_{br} seem to correlate with the width of the valence band (Figure 7.4b-c). In general, we observe that an increase of the valence-band width favor higher sliding and breathing frequencies; this result suggests that it is beneficial to narrow the valence band in order to reduce the lateral friction and the layer adhesion, hence in order to promote the layer exfoliation. In passing, we note that the variation range of the valence-band width depends on the specific atomic type forming the layers; for practical applications, it can be pre-evaluated in high-throughput calculations preliminary to the experimental validation of the selected exfoliation-assisting species.

The covalency and orbital polarization analysis show no clear connection between the Z species and the charge arrangement within the layer; accordingly, no clear relation is found between the charge distribution and the sliding and breathing frequencies. This result is different than what we found in the pristine MX₂ systems under different stimuli, in which the orbital polarization plays instead a fundamental role in determining the nanoscale frictional behavior.^{127,153,170} We then conclude that the molecule suppresses the effect of the details of the electronic distribution inside the layer on the sliding-related modes.

In our analysis so far, we used the properties of the equilibrium geometry to estimate the response of the system during the layer sliding and separation, that is, to predict the system behavior far from the equilibrium. We now want to check the reliability of such prediction. As a first step, for each of the considered systems, we create a *sliding path* along the M-X bond (Figure 7.5a). A sliding path is a sequence of configurations (atom positions and lattice parameters) which represent the relative parallel shift of two subsequent MX₂ layers. The initial guess of the paths have been obtained by considering linear combinations of eigenvectors corresponding to the sliding modes, according to the

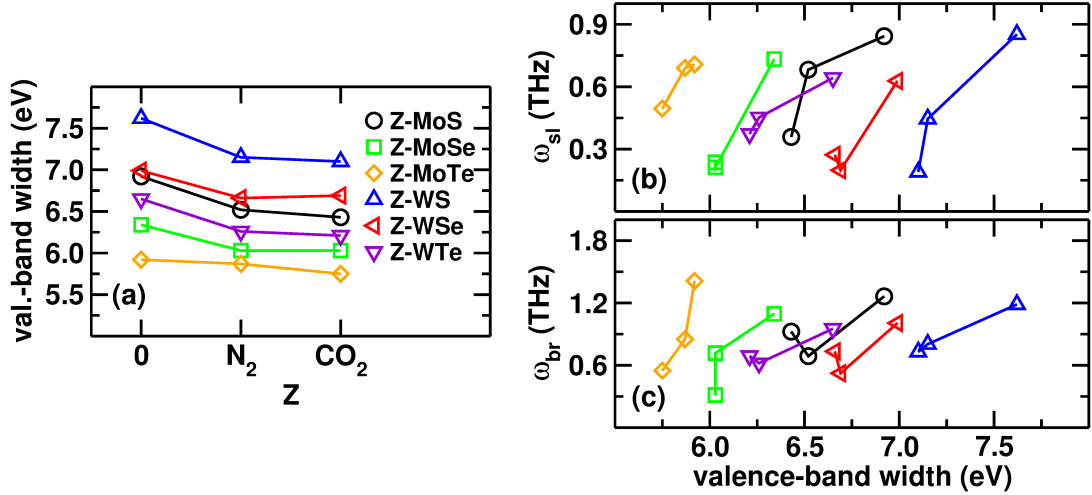


Figure 7.4: (a) Width of the valence band as a function of the intercalated moiety. Average frequency of (b) sliding and (c) breathing modes as a function of the width of the valence band. Legend is common to all the subfigures. Adapted from Ref. 209.

prescription of the *normal-modes transition approximation*;⁴² in this way, we created a total of 11 configurations for each sliding path. We then performed a Climbing-Image Nudged Elastic Band (CI-NEB)^{133,210} full relaxation (atom positions and lattice vectors) of the paths. As a result of the CI-NEB calculations, we obtain the potential energy barrier ΔE_{bar} associated to the relative layer sliding. We can then define the average friction force f_{fr} as

$$f_{fr} = \frac{\Delta E_{bar}}{\Delta R_{NEB}}; \quad (7.2)$$

ΔE_{bar} is the difference between the energy of the ground state and the maximum energy value realized along the path while

$$\Delta R_{NEB} = \sqrt{\sum_{i=1}^N |\mathbf{R}_{bar}^i - \mathbf{R}_0^i|}, \quad (7.3)$$

with \mathbf{R}_{bar}^i being the position of the i -th atom in the configuration realizing the energy maximum and \mathbf{R}_0^i the position of the same atom in the equilibrium geometry. With this definition, ΔR_{NEB} is a measure of the displacement covered by the atoms during the sliding. As a second step, we estimate the adhesion force. Starting from the equilibrium geometry, we consider 11 geometric configurations in which the two layers are progressively shifted along the c -axis direction until the interlayer distance is 15 Å (Figure 7.5b). For each configuration, we fix the lattice parameters and the positions of the M cations, and finally optimize the coordinates of the remaining atoms. By tracking the evolution of the system energy as a function of the interlayer distance, we observe an asymptotic behaviour; this assures us that the last configuration corresponds to non-interacting (separated) layers. Analogously to the definition of the average friction force f_{fr} (Equation 7.2), we then define the average adhesion force f_{ad} as

$$f_{ad} = \frac{\Delta E_{sep}}{\Delta R_{sep}} \quad (7.4)$$

where ΔE_{sep} is the difference between the energy of the ground state and the last configuration, while ΔR_{sep} is the layer-layer distance. Similarly to what we observed for

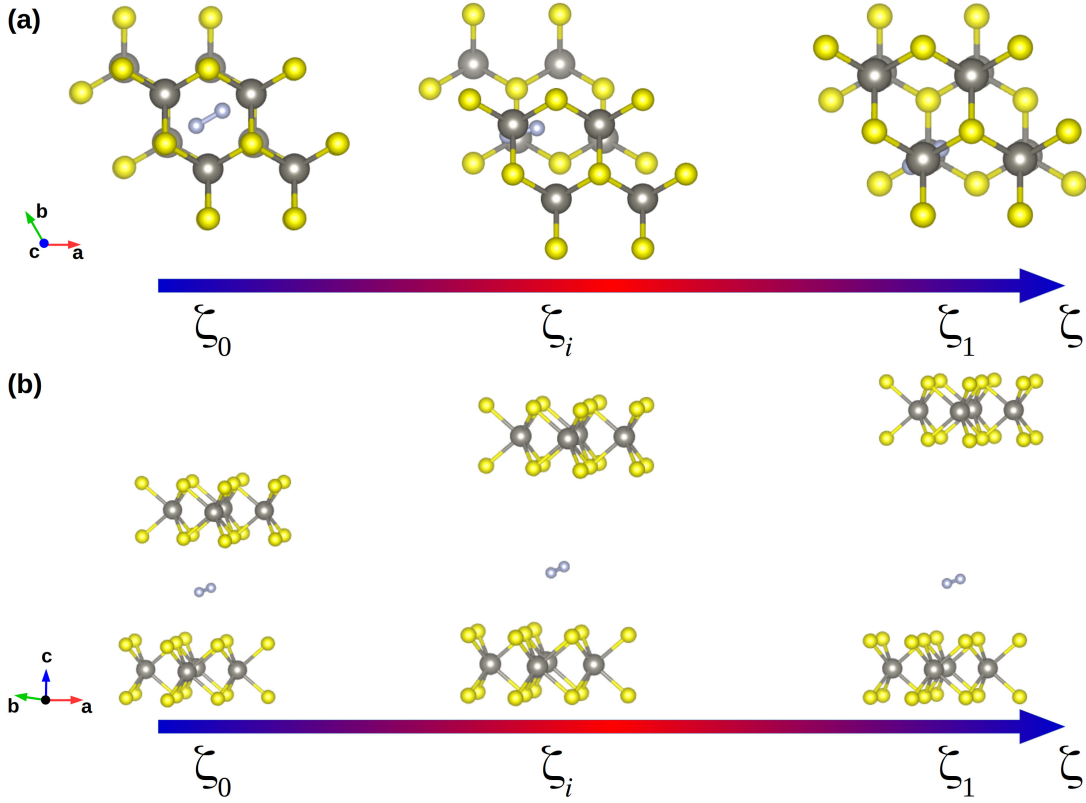


Figure 7.5: Example of (a) sliding path and (b) layer separation. Along the configurational coordinate ζ , the initial, an intermediate and the final states are indicated with ζ_0 , ζ_i and ζ_1 , respectively. Adapted from Ref. 209.

the sliding and breathing mode frequencies, the frictional and adhesion forces display large values in correspondence with large values of the band width (Figure 7.6). Moreover, we notice that the adhesion forces are larger than the frictional ones, as the breathing frequencies are larger than the sliding ones; this supports the harmonic representation of the two forces discussed in section 2.2. In the same section, we examined how both lateral friction and adhesion forces appear during the exfoliation process. This suggests us to consider an average force $f_{ave} = (f_{fr} + f_{ad})/2$ arising during the exfoliation; analogously, we consider the average frequency $\omega_{ave} = (\omega_{sl} + \omega_{br})/2$. In general, we notice that both quantities increase with increasing values of the valence-band width (Figure 7.7). These results suggest us that from the analysis of the equilibrium geometry (electronic structure, phonon spectrum) we may infer the response of the system far from the equilibrium (layer sliding and separation); in this respect, the width of the valence band seems to be a useful descriptor to parametrize the forces opposing the layer exfoliation in the presence of inert intercalated molecules.

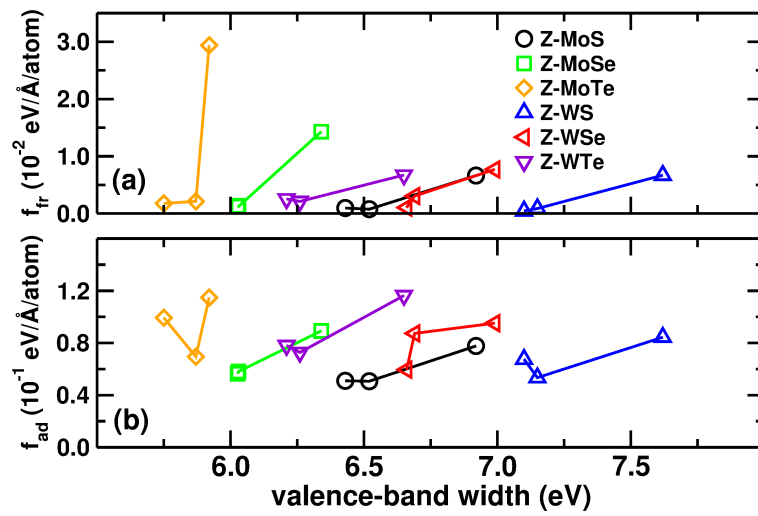


Figure 7.6: (a) Lateral frictional force and (b) adhesion force as a function of the width of the valence band. Legend is common to all the subfigures. Adapted from Ref. 209.

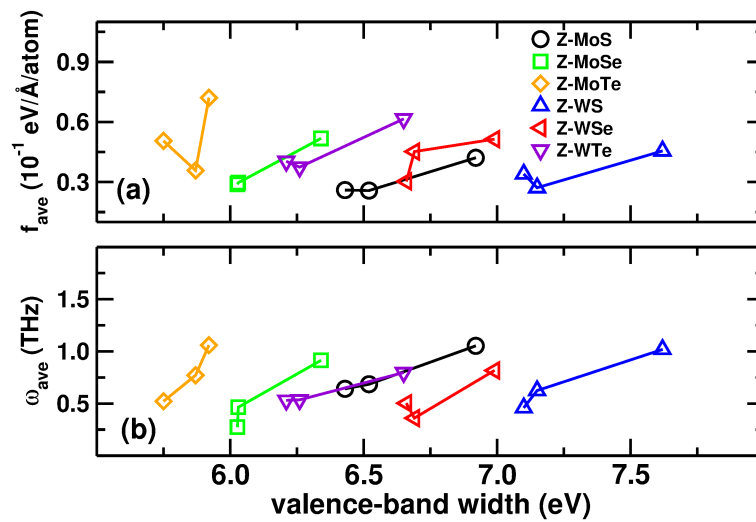


Figure 7.7: (a) Average force and (b) average mode frequency as a function of the width of the valence band. Legend is common to all the subfigures. Adapted from Ref. 209.

Chapter 8

Nanofriction in thin films

Moving parts during nanodevices fabrication and operation are subject to non-conservative forces active during the relative motion of the involved surfaces; those forces limit the output efficiency by producing heat, fatigue and wear up until compromising the correct construction or functioning of the device. Indeed, the comprehension of mechanisms governing friction in thin films is a forefront challenge to save energy and increase the lifetime and sustainability of miniaturised devices, besides improving their performance.⁸ To this aim, we applied the phonon-based description of the nanoscale friction to few-layer prototypical TMDs,^{158,211} in order to study the sliding-related modes and the relative dissipative processes generated by frictional forces occurring during relative motions of few atomic layers. In what follows, we briefly review the results of that work.

We already saw (section 2.2) that the decomposition of sliding trajectories into phonon modes allows one to distinguish between *sliding* and *dissipative* modes: the former are those who have an effective geometric contribution to the layer drift, while the latter reduce the population of the sliding ones via phonon-phonon recombination processes. Layer sliding is active as long as the sliding modes own enough energy. The frictional forces are then all those forces which activate recombination processes involving sliding and dissipative modes, producing a depopulation of the former. By indicating with $\lambda = (\mathbf{q}, j)$ a phonon mode with wave vector \mathbf{q} and band index j , the decrease of the population of the sliding mode λ occurs at a transition rate $\mathcal{P}_{\lambda, \lambda'}^{\lambda''}$ involving the λ' and λ'' dissipative modes, and is proportional to the square of the interaction strength $\Phi_{\lambda \lambda' \lambda''}$ ⁹⁹ (Equation 2.21):

$$\mathcal{P}_{\lambda, \lambda'}^{\lambda''} \propto nn'(n'' + 1)|\Phi_{\lambda \lambda' \lambda''}|^2 \quad (8.1)$$

where n , n' and n'' are the phonon populations depending on the environment (e.g. presence of thermal bath, irradiation, external forces), while $\Phi_{\lambda \lambda' \lambda''}$ is a characteristic of the system. A fine tune of the interaction strength tensor $\Phi_{\lambda \lambda' \lambda''}$ then allows to design tribological materials with controlled frictional response: as $|\Phi_{\lambda \lambda' \lambda''}|^2$ becomes smaller and smaller, the $\lambda + \lambda' = \lambda''$ scattering becomes less probable and the lifetime of the sliding phonon λ increases. This implies that the magnitude of an external drift force needed to keep the sliding active is small when low values of $|\Phi_{\lambda \lambda' \lambda''}|^2$ are realized. The interaction strength tensor $\Phi_{\lambda \lambda' \lambda''}$ is an intrinsic property of the material: it is determined by the atomic kinds and geometry forming the system which, in turn, determine the eigenvectors, eigenfrequencies and interatomic force constants. We already observed¹³¹ (section 2.3) that it is possible to switch off or on any $\lambda + \lambda' = \lambda''$ scattering process by controlling the symmetries of the system; in what follows, we show that an

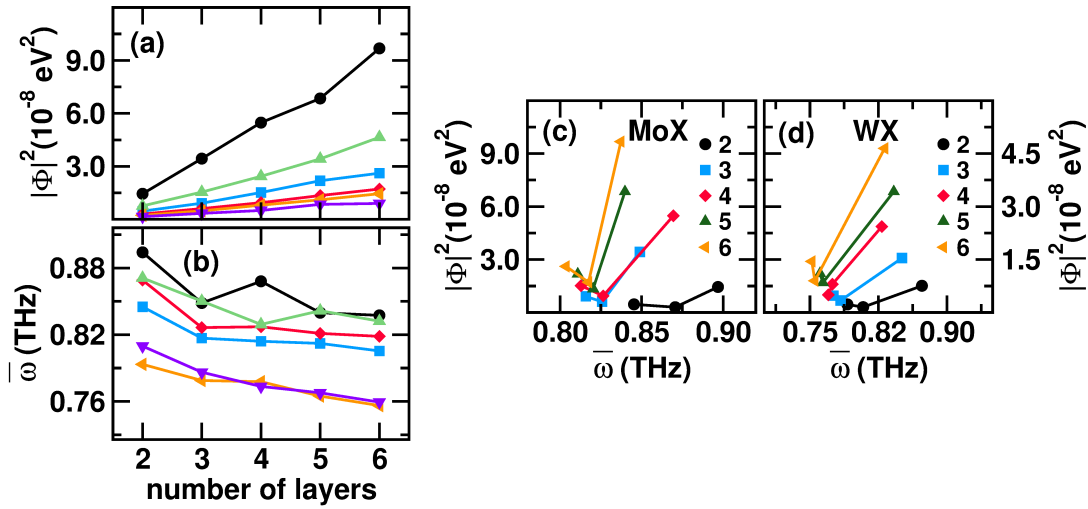


Figure 8.1: (a) Sum of the square modulus of the interaction strengths involving both sliding and dissipative modes against the number of layers: the number of dissipation channels increases with n , producing an increase of the dissipated energy. (b) Average frequency of the sliding-related modes against the number of layers: at fixed composition the trend is not monotonic with n , showing the non-trivial relation between electronic and dynamic features of the systems; symbols are the same as in (a). (c-d) $|\Phi|^2$ values of MoX- n L and WX- n L systems against eigenfrequency average comprising both sliding and dissipative modes; the value of n is indicated by the different symbols as shown in the legend. Lines are a guide for the eye. Adapted from Ref. 211.

other way to control the value of $\Phi_{\lambda\lambda'\lambda''}$ is to act on the subtle relation between the electronic density and the dynamic properties of the system.

Starting from the six prototypical TMDs, we truncate the periodic image repetition along the c axis by setting the c lattice parameter at 65 \AA , and consider only 2, 3, 4, 5 and 6 MX₂ subsequent layers. In this way, for each considered compound, we build 5 model systems that we name MX- n L, where M and X specify the kind of transition metal and chalcogen atom, respectively, while n corresponds to the number of MX₂ layers forming the unit cell. The number of sliding modes depends on the number of layers: the higher n , the higher the number of modes effectively contributing to the sliding, the higher the number of dissipative modes and corresponding dissipation channels. To track all the dissipative processes, we then consider the quantity $|\Phi|^2$, which we define as the sum of the squared modulus of all the $\Phi_{\lambda\lambda'\lambda''}$ elements involving both λ sliding and λ', λ'' dissipative modes. By controlling $|\Phi|^2$, we can then control the energy dissipation in tribological conditions at the nanoscale. A quick inspection of Equation 2.22 shows that $\Phi_{\lambda\lambda'\lambda''}$ can be decreased by simply choosing atoms with higher atomic masses m_k via isotope substitution: however, this would cause a decrease of the eigenfrequencies ω_λ , the two quantities being related by a relation of the kind $\omega \propto 1/\sqrt{m}$. Instead, we will focus on the choice of the atomic type, which is the most adopted solution in practical applications. The crucial quantity that determines $\Phi_{\lambda\lambda'\lambda''}$ is the third order tensor of the anharmonic force constants; therefore, the geometry and the consequent electronic distribution determine concurrently the final $\Phi_{\lambda\lambda'\lambda''}$ values in a non trivial way. Since it is not simple to map the behaviour of $\Phi_{\lambda\lambda'\lambda''}$ against the atomic kind, we need to identify proper collective descriptors to guide us through the complex interplay between the electronic structure and the dynamic features of the

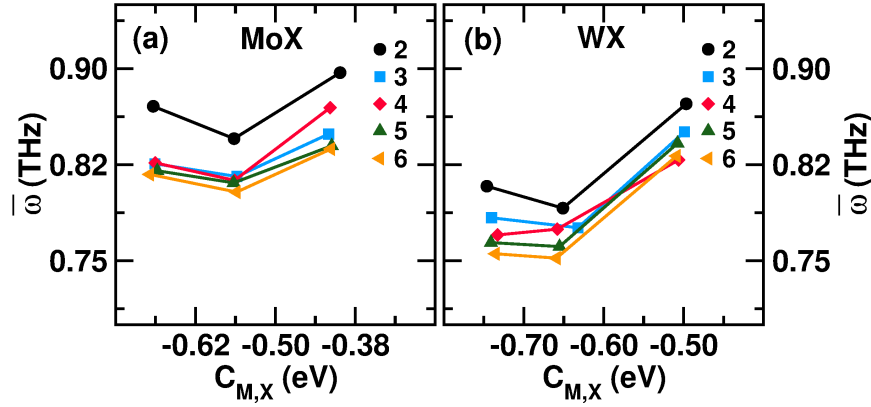


Figure 8.2: Average frequency values of (a) MoX- n L and (b) WX- n L systems against the M-X bond covalency: higher frequencies are realized at increased values of the bond covalency. Lines are a guide for the eye. Adapted from Ref. 211.

system. To this aim, we will investigate the relations among phononic states, electronic density, and phonon-phonon interactions. We observe that, irrespective of the atomic type of the M and X ions, $|\Phi|^2$ monotonically increases with increasing n (Figure 8.1a), in correspondence with the increase of the number of active dissipation channels. We then define $\bar{\omega}$ as the average frequency of the sliding-related modes, with the aim to capture how the eigenfrequencies determine the value of $|\Phi|^2$ at different number of layers. We observe that $\bar{\omega}$ is globally decreasing with n but the trend is not monotonic (Figure 8.1b); indeed, at a fixed number of layers, higher $|\Phi|^2$ is realized at higher frequencies (Figure 8.1c-d), against the intuitive trend suggested by Equation 2.22, where the eigenfrequencies appear at the denominator of the expression of $\Phi_{\lambda\lambda'\lambda''}$. Since by fixing n we are making a comparison at a fixed topology, the e_λ vectors do not change significantly; the anharmonic force constants have then a key role in governing $\Phi_{\lambda\lambda'\lambda''}$, since in this case they depend only on the atomic kinds and how these determine the electronic density. In order to get more insight on how to control $|\Phi|^2$, we then need to analyse in detail the subtleties of the electronic distribution.

We first calculate the M-X bond covalency. We observe that the covalency can be considered constant with the number of layers; the same result is obtained when we consider the difference among the atomic charges obtained either by integration of the atom-projected density of states or by performing a Bader analysis.^{141–145} Irrespective of chemical composition and number of layers, we find that the more covalent the M-X bond, the higher the $|\Phi|^2$ values hence the higher is the energy dissipation during layer sliding. Concerning the dynamic aspect, at fixed n the highest M-X bond covalency realizes the highest average frequencies $\bar{\omega}$ (Figure 8.2); however, as we already observed, an increase of the M-X bond covalency produces an increase of the dissipation (Figure 8.1b-c), against the fact that the eigenfrequencies ω_λ appear at the denominator of the expression of $\Phi_{\lambda\lambda'\lambda''}$ (Equation 2.22). This then confirms that the dominant contributions to the $\Phi_{\lambda\lambda'\lambda''}$ values are represented by the third-order force constants. Analysis of the electron localization functions^{156,157} does not show any strong evidence of charge redistribution along the M-X bond at varying chemical composition. This is the result of the subtle interplay between geometry, atomic kind and electronic distribution, which can be uncovered by a deeper investigation. To this aim, we consider the orbital polarization (Equation 4.2) of the d and p orbital projections of the M and X ions, respectively.

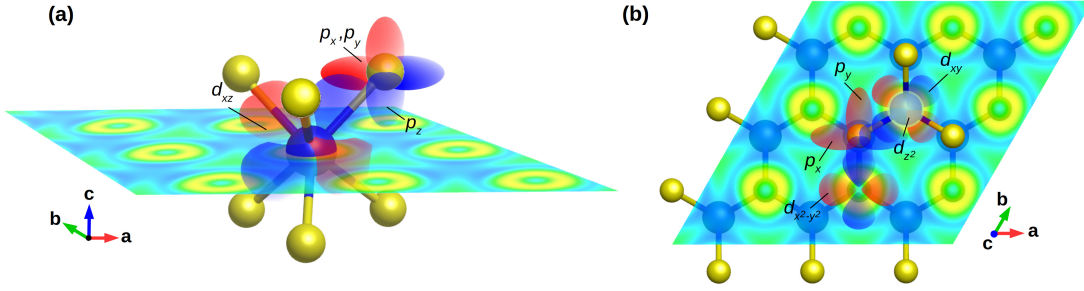


Figure 8.3: Schematic of the electronic density projected on t_{2g} and p orbitals, depicted as red and blue lobes and centered on the M and X atoms respectively; the plane containing the M cations is represented as a section of the electronic density, with RGB gradient showing density isovalues (red = highest, blue = lowest). The t_{2g} and p overlap is small, since the most of the t_{2g} orbitals extend into the region outside the M–X bond axis; a charge shift towards the t_{2g} orbitals then makes the M–X bond character more ionic. (a) Overlap among d_{xz} (and d_{yz} not shown for clarity), p_x and p_y is realized only by partial interpenetration of the orbital boundaries; (b) the same holds for the d_{xy} and p orbitals. The $d_{x^2-y^2}$ and p_y overlap is more effective and an increase of their population makes the bond character more covalent. The d_{z^2} orbital does not participate to the bond formation. Adapted from Ref. 211.

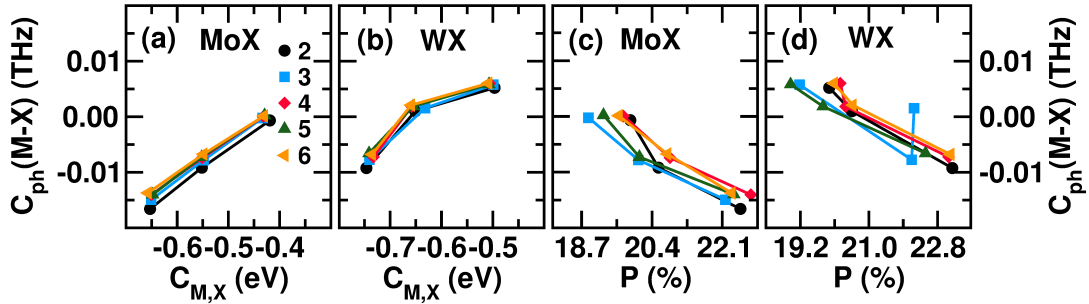


Figure 8.4: (a-b) Cophonicity of the M–X pair of the $\text{MoX-}n\text{L}$ and $\text{WX-}n\text{L}$ systems as a function of the M–X bond covalency: more covalent bond characters favour an increase of the M–X cophonicity. (c-d) Cophonicity of the M–X pair as a function of the \mathcal{P}_{t_{2g},e_g} orbital polarization: an excess of electrons in the t_{2g} orbitals favour a decrease of the cophonicity values. Lines are a guide for the eye. Adapted from Ref. 211.

We already observed that the relative occupation of t_{2g} and e_g orbitals plays an important role in the determination of the sliding dynamics in TMDs^{127,153} (chapter 4 and chapter 5); indeed, we find that an excess of electrons in the t_{2g} orbitals reduces the $|\Phi|^2$ values hence the energy dissipation during layer sliding. The delicate balance among the orbital populations determine the value of the covalency: we find that high values of \mathcal{P}_{p_x,p_y} and \mathcal{P}_{t_{2g},e_g} determine the formation of more ionic M–X bonds (Figure 8.3) which lower the energy dissipation during sliding.

We now want to characterize the atomic types and their contribution to the sliding dynamics of the system; to this aim, we use the cophonicity metric (section 2.5). We observe that, at a fixed number of layers, low cophonicity realises low $|\Phi|^2$ values at fixed cation type, suggesting that when anions displace faster than cations, the frictional force and the corresponding energy dissipation is lower. This dynamical effect

is connected to the spatial extent and directionality of the electronic distribution. In fact, at fixed n , $C_{ph}(M-X)$ is monotonically increasing with $C_{M,X}$ (Figure 8.4a-b); at the same time, $C_{ph}(M-X)$ decreases with \mathcal{P}_{t_{2g},e_g} becoming negative, indicating that a charge transfer towards t_{2g} orbitals favours a faster motion of the X ions with respect to the M cations when forming the global sliding motion (Figure 8.4c-d). In other words, a higher t_{2g} population changes the character of the sliding motion from M-dominant to X-dominant contributions to the overall layer shift. In our previous works^{41,153,158} we already used the cophononicity descriptor to parameterize the atomic type and relate it to local harmonic forces which might contribute to the frictional response; here we can instead recognize that cophononicity can also be used to tune the anharmonic interactions which produce energy dissipation due to friction, hence going beyond the harmonic description.

Conclusions

In this thesis, I summarise my work at the Czech Technical University in Prague on the nanoscale friction. The goal was to answer to the following questions: What is the origin of friction? Is it possible to obtain a model of the nanofriction response without using long demanding dynamics simulations? Can we formulate a universal system-independent framework applicable to any tribological system, and capable to guide the design of new tribological materials with on-demand response?

In order to develop an experimental model of the nanoscale friction, it is common practice to obtain the relevant parameters from a trial and error approach at varying tribological conditions (e.g. pressure, load, temperature and sliding velocity among others); similarly, conventional atomistic simulations usually describe the friction response in terms of sequences of model geometries aimed to represent the sliding events in working regime. As we saw, in both cases, the attempt to distinguish the frictional forces from the remaining ones responsible for the integrity of the material is not general and is system-dependent. We then understood that the nanoscale friction is the response of the system as a whole and the proper description of it requires a holistic approach; to this aim, we exploited the phonon theory and the quantum mechanics, which provide a universal system-independent framework.

The phonon eigendisplacements are a complete basis set for the geometric representation of the whole system, then capable to carry the structural information representing the sliding; the related eigenfrequencies are instead a measure of the forces generating the eigendisplacements, therefore containing the information on the dynamics of the system. The atomic motions determining the relative slide of facing surfaces can then be decomposed as linear combinations of suitable phonon displacement patterns; we named the latter as *sliding modes*. In terms of the classical picture, the frequency of the sliding modes is a measure of the restoring force hindering the sliding: the lower the frequency, the weaker the restoring force, and the larger the amplitude of the relative displacement at a fixed system energy.

The layer sliding is active as long as the sliding modes own enough energy to overcome the sliding energy barriers. In fact, the interaction with other modes (i.e. phonon scattering) causes a decrease of the sliding mode population and a deceleration of the relative shift of the surfaces, hence manifesting as friction force; accordingly, we named these other modes as *dissipative modes*. We then understood that the frictional forces are all those forces which activate dissipative processes producing a depopulation of the sliding modes. The variation of the energy of the sliding modes can then be considered equal to the work done by the frictional forces: while the sliding modes produce an ordered motion of the system, the dissipative modes downgrade it into thermal vibrations thanks to the phonon-phonon coupling.

We therefore recast the control of the friction response in terms of phonon frequencies and scattering tensor elements. We saw that, in the first place, the sliding-related

frequencies can be adjusted by choosing suitable atomic types or inert intercalant species, in order to obtain a target response against external stimuli like shear forces or applied load. We also learned that the sliding frequencies can be tuned on-demand by means of external electric fields. Moreover, the atomic species and geometric arrangement determine the anharmonic force constants and the activation/deactivation of specific dissipation channels thanks to the scattering selection rules: with a suitable choice, we can then control the energy dissipation during the sliding.

The phonon-based description of friction that I propose in my work then appears to be capable to predict the system response in tribological conditions (i.e. far from the equilibrium) thanks to the information extracted from a reference configuration (i.e. equilibrium geometry). This avoids the use of demanding dynamics simulations, while providing guidelines on how to design tribological materials with targeted friction response. I am confident that this work opens the way towards a phonon friction theory which can tackle one of the biggest challenges in the field of nanotribology: the calculation of the friction coefficient of two surfaces in contact based on the sole knowledge of the atom types and their geometric arrangement. Indeed, this will be one of my research topics in the next future.

Acknowledgements

This work would not have been possible without the support of the head of our group, Tomáš Polcar: I gratefully acknowledge his trust in my scientific initiative and his professional effort in assisting my work.

I will never get tired to thank my wife Francesca, who patiently supported me in every moment, and to thank my parents, my brother Vincenzo and my dears who always believed in all my choices and who always have been able to find words of comfort for the most difficult moments.

No words are enough to say thanks to my friend Martin Sedlák and all the friends that I met thanks to him, for making me feel home since I moved to Czech Republic. Each of them is unique and irreplaceable.

Last but not least, I thank the CGB family and my old dear friends met thanks to it: they are always next to me and push me to move forward.

Bibliography

- [1] P. Varotsos and M. Lazaridou, A review on friction, in *Earthquake Source Asymmetry, Structural Media and Rotation Effects*, edited by R. Teisseyre, E. Majewski, and M. Takeo (Springer Berlin Heidelberg, Berlin, Heidelberg, 2006) pp. 91–111.
- [2] G. S. Chen, *Handbook of Friction-Vibration Interactions (Woodhead Publishing in Mechanical Engineering)*, edited by Elsevier (Woodhead Publishing, 2014).
- [3] K. Holmberg and A. Erdemir, *FME Transactions* **43**, 181 (2015).
- [4] World Commission On Environment and Development, *Our Common Future*, edited by O. U. Press (Oxford University Press, 1987).
- [5] I. M. Hutchings, *Wear* **360-361**, 51 (2016).
- [6] E. Popova and V. L. Popov, *Friction* **3**, 183 (2015).
- [7] S. Hsu, C. Ying, and F. Zhao, *Friction* **2**, 1 (2014).
- [8] A. Vakis, V. Yastrebov, J. Scheibert, L. Nicola, D. Dini, C. Minfray, A. Almqvist, M. Paggi, S. Lee, G. Limbert, J. Molinari, G. Anciaux, R. Aghababaei, S. Echeverri Restrepo, A. Papangelo, A. Cammarata, P. Nicolini, C. Putignano, G. Carbone, S. Stupkiewicz, J. Lengiewicz, G. Costagliola, F. Bosia, R. Guarino, N. Pugno, M. Müser, and M. Ciavarella, *Tribol. Int.* **125**, 169 (2018).
- [9] E. Gnecco and E. Meyer, *Fundamentals of Friction and Wear on the Nanoscale*, 2nd ed., NanoScience and Technology (Springer International Publishing, Switzerland, 2015) p. 704.
- [10] A. I. Vakis, C. N. Hadjicostis, and A. A. Polycarpou, *J. Phys. D Appl. Phys.* **45**, 135402 (2012).
- [11] S. V. Canchi and D. B. Bogy, *J. Tribol. T. ASME* **133**, 021902 (2011).
- [12] I. Tzanakis, M. Hadfield, B. Thomas, S. Noya, I. Henshaw, and S. Austen, *Renewable and Sustainable Energy Reviews* **16**, 4126 (2012).
- [13] P. Cann and M. Wimmer, *Biotribology* **1-2**, 1 (2015).
- [14] J. van Kuilenburg, M. A. Masen, and E. van der Heide, *Proc. Mech. Eng. J.-J Eng.* **229**, 243 (2015).
- [15] S. Ma, M. Scaraggi, D. Wang, X. Wang, Y. Liang, W. Liu, D. Dini, and F. Zhou, *Adv. Func. Mater.* **25**, 7366 (2015).
- [16] H. Rashid, *Eur. J. Dent.* **8**, 571 (2014).

- [17] J. Scheibert, S. Leurent, A. Prevost, and G. Debrégeas, *Science* **323**, 1503 (2009).
- [18] V. Hayward, *Phil. Trans. R. Soc. B* **366**, 3115 (2011).
- [19] A. Klöcker, M. Wiertlewski, V. Théate, V. Hayward, and J.-L. Thonnard, *PLOS ONE* **8**, 1 (2013).
- [20] T. J. Prescott, M. E. Diamond, and A. M. Wing, *Phil. Trans. R. Soc. B* **366**, 2989 (2011).
- [21] F. He, X. Yang, Z. Bian, G. Xie, D. Guo, and J. Luo, *Small* **15**, 1904613 (2019).
- [22] H. Wang, C.-C. Huang, and T. Polcar, *Sci. Rep.* **9**, 334 (2019).
- [23] B. L. Perotti, A. Cammarata, F. Cemin, S. R. Sales de Mello, L. M. Leidens, F. G. Echeverrigaray, T. Minea, F. Alvarez, A. F. Michels, T. Polcar, and C. A. Figueroa, *ACS Appl. Mater. Interfaces* **13**, 43746 (2021).
- [24] A. Vanossi, N. Manini, M. Urbakh, S. Zapperi, and E. Tosatti, *Rev. Mod. Phys.* **85**, 529 (2013).
- [25] T. A. Sharp, L. Pastewka, and M. O. Robbins, *Phys. Rev. B* **93**, 121402(R) (2016).
- [26] D. Dietzel, J. Brndiar, I. Štich, and A. Schirmeisen, *ACS Nano* **11**, 7642 (2017).
- [27] A. Vanossi, D. Dietzel, A. Schirmeisen, E. Meyer, R. Pawlak, T. Glatzel, M. Kisiel, S. Kawai, and N. Manini, *Beil. J. Nanotech.* **9**, 1995 (2018).
- [28] M. Igarashi, A. Natori, and J. Nakamura, *Phys. Rev. B* **78**, 165427 (2008).
- [29] W. K. Kim and M. L. Falk, *Phys. Rev. B* **80**, 235428 (2009).
- [30] P. Steiner, R. Roth, E. Gnecco, A. Baratoff, S. Maier, T. Glatzel, and E. Meyer, *Phys. Rev. B* **79**, 045414 (2009).
- [31] D. Perez, Y. Dong, A. Martini, and A. F. Voter, *Phys. Rev. B* **81**, 245415 (2010).
- [32] E. Cihan, S. Ipek, E. Durgun, and M. Z. Baykara, *Nat. Commun.* **7**, 12055 (2016).
- [33] M. Z. Baykara, M. R. Vazirisereshk, and A. Martini, *Appl. Phys. Rev.* **5**, 041102 (2018).
- [34] Z. Wei, Z. Duan, Y. Kan, Y. Zhang, and Y. Chen, *J. Appl. Phys.* **127**, 015105 (2020).
- [35] S. R. S. de Mello, M. E. H. M. da Costa, C. M. Menezes, C. D. Boeira, F. L. Freire Jr, F. Alvarez, and C. A. Figueroa, *Sci. Rep.* **7**, 3242 (2017).
- [36] E. Panizon, G. E. Santoro, E. Tosatti, G. Riva, and N. Manini, *Phys. Rev. B* **97**, 104104 (2018).
- [37] R. Hu, S. Y. Krylov, and J. W. M. Frenken, *Tribol. Lett.* **68**, 8 (2019).
- [38] J. L. Streater, *Front. Mech. Eng.* **5**, 23 (2019).
- [39] Y. Dong, Y. Tao, R. Feng, Y. Zhang, Z. Duan, and H. Cao, *Nanotechnology* **31**, 285711 (2020).

- [40] M. Lee, R. L. C. Vink, C. A. Volkert, and M. Krüger, *Phys. Rev. B* **104**, 174309 (2021).
- [41] A. Cammarata and T. Polcar, *Inorg. Chem.* **54**, 5739 (2015).
- [42] A. Cammarata and T. Polcar, *Phys. Rev. B* **96**, 085406 (2017).
- [43] A. Cammarata, P. Nicolini, K. Simonovic, E. Ukraintsev, and T. Polcar, *Phys. Rev. B* **99**, 094309 (2019).
- [44] M. Chhowalla, H. S. Shin, G. Eda, L.-J. Li, K. P. Loh, and H. Zhang, *Nat. Chem.* **5**, 263 (2013).
- [45] A. K. Geim and I. V. Grigorieva, *Nature* **499**, 419 (2013).
- [46] O. C. Zienkiewicz, R. L. Taylor, R. L. Taylor, and R. L. Taylor, *The finite element method: solid mechanics*, Vol. 2 (Butterworth-heinemann, 2000).
- [47] P. K. Banerjee, P. K. Banerjee, and R. Butterfield, *Boundary element methods in engineering science* (McGraw-Hill (UK), 1981).
- [48] B. J. Alder and T. E. Wainwright, *J. Chem. Phys.* **31**, 459 (1959).
- [49] M. P. Allen, Introduction to molecular dynamics simulation, in *NIC Series Volume 23 : Computational Soft Matter: From Synthetic Polymers to Proteins, Lecture Notes, edited by Norbert Attig, Kurt Binder, Helmut Grubmüller, Kurt Kremer, chapter 1, p. 1-28, Jülich : John von Neumann Institute for Computing, 2004. ISBN: 3-00-012641-4*, NIC series, Vol. 23 (John von Neumann Institute for Computing, Jülich, 2004) pp. 1–28.
- [50] R. Komanduri, N. Chandrasekaran, and L. Raff, *Wear* **240**, 113 (2000).
- [51] M. J. Brukman, G. Gao, R. J. Nemanich, and J. A. Harrison, *J. Phys. Chem. C* **112**, 9358 (2008).
- [52] Y. Mo, K. T. Turner, and I. Szlufarska, *Nature* **457**, 1116 (2009).
- [53] T. Onodera, Y. Morita, R. Nagumo, R. Miura, A. Suzuki, H. Tsuboi, N. Hatakeyama, A. Endou, H. Takaba, F. Dassenoy, C. Minfray, L. Joly-Pottuz, M. Kubo, J.-M. Martin, and A. Miyamoto, *J. Phys. Chem. B* **114**, 15832 (2010).
- [54] J. D. Schall, G. Gao, and J. A. Harrison, *J. Phys. Chem. C* **114**, 5321 (2010).
- [55] Y. Zhu, Y. Zhang, Y. Shi, X. Lu, J. Li, and L. Lu, *J. Chem. Eng. Data* **61**, 4023 (2016).
- [56] J. A. Harrison, C. T. White, R. J. Colton, and D. W. Brenner, *Phys. Rev. B* **46**, 9700 (1992).
- [57] M. H. Müser, L. Wenning, and M. O. Robbins, *Phys. Rev. Lett.* **86**, 1295 (2001).
- [58] M. Chandross, E. B. Webb, M. J. Stevens, G. S. Grest, and S. H. Garofalini, *Phys. Rev. Lett.* **93**, 166103 (2004).
- [59] D. Mulliah, S. D. Kenny, and R. Smith, *Phys. Rev. B* **69**, 205407 (2004).
- [60] P. Tangney, S. G. Louie, and M. L. Cohen, *Phys. Rev. Lett.* **93**, 065503 (2004).

- [61] J. P. Ewen, C. Gattinoni, F. M. Thakkar, N. Morgan, H. A. Spikes, and D. Dini, *Tribol. Lett.* **63**, 38 (2016).
- [62] S. Nakaoka, Y. Yamaguchi, T. Omori, and L. Joly, *J. Chem. Phys.* **146**, 174702 (2017).
- [63] J. A. Harrison, C. T. White, R. J. Colton, and D. W. Brenner, *Thin Solid Films* **260**, 205 (1995).
- [64] B. Bhattacharya, G. Dinesh Kumar, A. Agarwal, Şakir Erkoç, A. Singh, and N. Chakraborti, *Comp. Mater. Sci.* **46**, 821 (2009).
- [65] D. Frenkel and B. Smit, *Understanding molecular simulation: from algorithms to applications* (Academic Press, San Diego, California, USA, 1996).
- [66] H. Heinz and H. Ramezani-Dakhel, *Chem. Soc. Rev.* **45**, 412 (2016).
- [67] K. Farah, F. Müller-Plathe, and M. C. Böhm, *ChemPhysChem* **13**, 1127 (2012).
- [68] B. Hartke and S. Grimme, *Phys. Chem. Chem. Phys.* **17**, 16715 (2015).
- [69] J. A. Harrison, J. D. Schall, S. Maskey, P. T. Mikulski, M. T. Knippenberg, and B. H. Morrow, *Appl. Phys. Rev.* **5**, 031104 (2018).
- [70] G. Xiao, M. Ren, and H. Hong, *Adv. Eng. Softw.* **124**, 66 (2018).
- [71] Y. Li, S. Wang, B. Arash, and Q. Wang, *Carbon* **100**, 145 (2016).
- [72] R. Chen, S. Li, Z. Wang, and X. Lu, *Tribol. Int.* **133**, 40 (2019).
- [73] J. D. Schall, P. T. Mikulski, G. M. Chateauneuf, G. Gao, and J. A. Harrison, in *Superlubricity*, edited by A. Erdemir and J.-M. Martin (Elsevier Science B.V., Amsterdam, 2007) pp. 79–102.
- [74] H. Lan, T. Kato, and C. Liu, *Tribol. Int.* **44**, 1329 (2011).
- [75] C. Hu, J. Lv, M. Bai, X. Zhang, and D. Tang, *Friction* **8**, 531 (2020).
- [76] C. Hu, M. Bai, J. Lv, Z. Kou, and X. Li, *Tribol. Int.* **90**, 297 (2015).
- [77] E. Schrödinger, *Phys. Rev.* **28**, 1049 (1926).
- [78] C. Cohen-Tannoudji, B. Diu, and F. Laloe, *Quantum Mechanics, Volume 1*, 2nd ed. (Wiley-VCH Verlag, Weinheim, Germany, 2020).
- [79] I. N. Levine, *Quantum Chemistry* (Allyn & Bacon, Old Tappan, NJ, 1991).
- [80] R. A. Friesner, *Proc. Natl. Acad. Sci. USA* **102**, 6648 (2005).
- [81] D. Marx and J. Hutter, *Ab initio molecular dynamics* (Cambridge University Press, Cambridge, England, 2009).
- [82] P. Restuccia, G. Levita, M. Wolloch, G. Losi, G. Fatti, M. Ferrario, and M. Righi, *Comp. Mater. Sci.* **154**, 517 (2018).
- [83] S. Kajita and M. Righi, *Carbon* **103**, 193 (2016).
- [84] G. Levita and M. C. Righi, *ChemPhysChem* **18**, 1475 (2017).

- [85] S. Cahangirov, C. Ataca, M. Topsakal, H. Sahin, and S. Ciraci, [Phys. Rev. Lett.](#) **108**, 126103 (2012).
- [86] M. Wolloch, G. Feldbauer, P. Mohn, J. Redinger, and A. Vernes, [Phys. Rev. B](#) **90**, 195418 (2014).
- [87] M. Dienwiebel and M.-I. De Barros Bouchet, eds., *Advanced Analytical Methods in Tribology*, 1st ed., Microtechnology and MEMS (Springer International Publishing, Cham, Switzerland, 2018).
- [88] N. V. Tran, A. K. Tieu, H. Zhu, H. T. T. Ta, H. M. Le, and T. D. Ta, [J. Appl. Phys.](#) **127**, 065305 (2020).
- [89] G. Losi, P. Restuccia, and M. C. Righi, [2D Materials](#) **7**, 025033 (2020).
- [90] B. J. Irving, P. Nicolini, and T. Polcar, [Nanoscale](#) **9**, 5597 (2017).
- [91] H. Ustunel and D. Toffoli, [Electronic Structure](#) **4**, 023002 (2022).
- [92] Y. Sang, M. Dubé, and M. Grant, [Phys. Rev. Lett.](#) **87**, 174301 (2001).
- [93] J. F. Curry, A. R. Hinkle, T. F. Babuska, M. A. Wilson, M. T. Dugger, B. A. Krick, N. Argibay, and M. Chandross, [ACS Appl. Nano Mater.](#) **1**, 5401 (2018).
- [94] W. Wang, D. Dietzel, and A. Schirmeisen, [Sci. Adv.](#) **6**, eaay0165 (2020).
- [95] W. Wang, A. Wang, and L. Zeng, [AIP Adv.](#) **10**, 085322 (2020).
- [96] P. R. Barry, P. Y. Chiu, S. S. Perry, W. G. Sawyer, S. B. Sinnott, and S. R. Phillpot, [Tribol. Lett.](#) **58**, 50 (2015).
- [97] M. Antonov, H. Afshari, J. Baronins, E. Adoberg, T. Raadik, and I. Hussainova, [Tribol. Int.](#) **118**, 500 (2018).
- [98] D. M. Wallace, *Thermodynamics of Crystals* (John Wiley & Sons Inc, United States of America, 1972).
- [99] J. M. Ziman, *Electrons and Phonons: The Theory of Transport Phenomena in Solids* (Oxford University Press, 2001).
- [100] International tables for crystallography (2006).
- [101] P. Souvatzis, O. Eriksson, M. I. Katsnelson, and S. P. Rudin, [Phys. Rev. Lett.](#) **100**, 095901 (2008).
- [102] P. Souvatzis and S. P. Rudin, [Phys. Rev. B](#) **78**, 184304 (2008).
- [103] W. Luo, B. Johansson, O. Eriksson, S. Arapan, P. Souvatzis, M. I. Katsnelson, and R. Ahuja, [P. Natl. Acad. Sci. USA](#) **107**, 9962 (2010).
- [104] A. Togo, F. Oba, and I. Tanaka, [Phys. Rev. B](#) **78**, 134106 (2008).
- [105] A. Togo and I. Tanaka, [Scripta Mater.](#) **108**, 1 (2015).
- [106] L. Chaput, A. Togo, I. Tanaka, and G. Hug, [Phys. Rev. B](#) **84**, 094302 (2011).
- [107] K. Parlinski, Z. Q. Li, and Y. Kawazoe, [Phys. Rev. Lett.](#) **78**, 4063 (1997).

- [108] A. Carreras, A. Togo, and I. Tanaka, *Comput. Phys. Commun.* **221**, 221 (2017).
- [109] T. Tadano and S. Tsuneyuki, *J. Phys. Soc. Jpn.* **87**, 041015 (2018).
- [110] I. Errea, M. Calandra, and F. Mauri, *Phys. Rev. Lett.* **111**, 177002 (2013).
- [111] I. Errea, M. Calandra, and F. Mauri, *Phys. Rev. B* **89**, 064302 (2014).
- [112] L. Paulatto, I. Errea, M. Calandra, and F. Mauri, *Phys. Rev. B* **91**, 054304 (2015).
- [113] M. Borinaga, I. Errea, M. Calandra, F. Mauri, and A. Bergara, *Phys. Rev. B* **93**, 174308 (2016).
- [114] R. Bianco, I. Errea, L. Paulatto, M. Calandra, and F. Mauri, *Phys. Rev. B* **96**, 014111 (2017).
- [115] L. J. Nelson, G. L. W. Hart, F. Zhou, and V. Ozoliņš, *Phys. Rev. B* **87**, 035125 (2013).
- [116] F. Zhou, W. Nielson, Y. Xia, and V. Ozoliņš, *Phys. Rev. Lett.* **113**, 185501 (2014).
- [117] A. Glensk, B. Grabowski, T. Hickel, and J. Neugebauer, *Phys. Rev. X* **4**, 011018 (2014).
- [118] A. Glensk, B. Grabowski, T. Hickel, and J. Neugebauer, *Phys. Rev. Lett.* **114**, 195901 (2015).
- [119] A. I. Duff, T. Davey, D. Korbmacher, A. Glensk, B. Grabowski, J. Neugebauer, and M. W. Finnis, *Phys. Rev. B* **91**, 214311 (2015).
- [120] K. Esfarjani and H. T. Stokes, *Phys. Rev. B* **77**, 144112 (2008).
- [121] K. Esfarjani, G. Chen, and H. T. Stokes, *Phys. Rev. B* **84**, 085204 (2011).
- [122] J. Shiomi, K. Esfarjani, and G. Chen, *Phys. Rev. B* **84**, 104302 (2011).
- [123] F. Eriksson, E. Fransson, and P. Erhart, *Advanced Theory and Simulations* **2**, 1800184 (2019).
- [124] W. Setyawan and S. Curtarolo, *Comput. Mater. Sci.* **49**, 299 (2010).
- [125] S. Lipschutz and M. Lipson, *Schaum's Outline of Linear Algebra*, 4th ed., Schaums' Outline Series (Schaum Outline Series, New York, NY, 2008).
- [126] S. K. Berberian, *Linear Algebra*, Dover Books on Mathematics (Dover Publications, Mineola, NY, 2014).
- [127] A. Cammarata and T. Polcar, *RSC Adv.* **5**, 106809 (2015).
- [128] M. Stéphane, in *A Wavelet Tour of Signal Processing* (Elsevier, 2009) pp. 59–88.
- [129] C. Kittel, *Introduction to solid state physics*, 8th ed. (John Wiley & Sons, Nashville, TN, 2004).
- [130] A. Cammarata and T. Polcar, *Phys. Rev. B* **103**, 035406 (2021).
- [131] A. Cammarata, *RSC Adv.* **9**, 37491 (2019).

- [132] C. Dellago, P. G. Bolhuis, and D. Chandler, *J. Chem. Phys.* **110**, 6617 (1999).
- [133] G. Henkelman and H. Jónsson, *J. Chem. Phys.* **113**, 9978 (2000).
- [134] A. Cammarata and J. M. Rondinelli, *J. Chem. Phys.* **141**, 114704 (2014).
- [135] R. Fei, W. Kang, and L. Yang, *Phys. Rev. Lett.* **117**, 097601 (2016).
- [136] T. Hu, M. Hu, Z. Li, H. Zhang, C. Zhang, J. Wang, and X. Wang, *J. Phys. Chem. A* **119**, 12977 (2015).
- [137] Y. Fan, X. Liu, J. Wang, H. Ai, and M. Zhao, *Phys. Chem. Chem. Phys.* **20**, 11369 (2018).
- [138] Wikipedia contributors, [Cophonycity — Wikipedia, the free encyclopedia](#) (2022), [Online; accessed 22-August-2022].
- [139] B. Schönfeld, J. J. Huang, and S. C. Moss, *Acta Crystallogr. B* **39**, 404 (1983).
- [140] B. J. Campbell, H. T. Stokes, D. E. Tanner, and D. M. Hatch, *J. Appl. Cryst.* **39**, 607 (2006).
- [141] R. F. V. Bader, *Atoms in Molecules: a Quantum Theory* (Oxford University Press, New York, 1990).
- [142] W. Tang, E. Sanville, and G. Henkelman, *J. Phys. Condens. Mat.* **21**, 084204 (2009).
- [143] E. Sanville, S. D. Kenny, R. Smith, and G. Henkelman, *J. Comp. Chem.* **28**, 899 (2007).
- [144] G. Henkelman, A. Arnaldsson, and H. Jónsson, *Comp. Mater. Sci.* **36**, 354 (2006).
- [145] M. Yu and D. Trinkle, *J. Chem. Phys.* **134**, 064111 (2011).
- [146] A. Cammarata and J. M. Rondinelli, *Phys. Rev. B* **87**, 155135 (2013).
- [147] M. J. Han, C. A. Marianetti, and A. J. Millis, *Phys. Rev. B* **82**, 134408 (2010).
- [148] L. B. Loeb, *Science* **102**, 573 (1945).
- [149] T. A. L. Burgo, C. A. Silva, L. B. S. Balestrin, and F. Galembeck, *Sci. Rep.* **3**, 2384 (2013).
- [150] A. Diaz and R. Felix-Navarro, *J. Electrostat.* **62**, 277 (2004).
- [151] F. R. Fan, W. Tang, and Z. L. Wang, *Adv. Mater.* **28**, 4283 (2016).
- [152] J. P. Oviedo, S. KC, N. Lu, J. Wang, K. Cho, R. M. Wallace, and M. J. Kim, *ACS Nano* **9**, 1543 (2015).
- [153] A. Cammarata and T. Polcar, *Nanoscale* **9**, 11488 (2017).
- [154] F. Flicker and J. van Wezel, *Nat Commun* **6**, 7034 (2015).
- [155] A. Cammarata and J. M. Rondinelli, *Appl. Phys. Lett.* **108**, 213109 (2016).
- [156] A. D. Becke and K. E. Edgecombe, *J. Chem. Phys.* **92**, 5397 (1990).

- [157] A. Savin, O. Jepsen, J. Flad, O. K. Andersen, H. Preuss, and H. G. von Schnering, *Angew. Chem. Int. Edit.* **31**, 187 (1992).
- [158] A. Cammarata and T. Polcar, *Phys. Chem. Chem. Phys.* **18**, 4807 (2016).
- [159] E. Serpini, A. Rota, S. Valeri, E. Ukraintsev, B. Rezek, T. Polcar, and P. Nicolini, *Tribol. Int.* **136**, 67 (2019).
- [160] G. Levita, A. Cavaleiro, E. Molinari, T. Polcar, and M. Righi, *J. Phys. Chem. C* **118**, 13809 (2014).
- [161] J.-U. Lee, S. Woo, J. Park, H. C. Park, Y.-W. Son, and H. Cheong, *Nat. Commun.* **8**, 1370 (2017).
- [162] H. Bao, Y. Huang, Z. Yang, Y. Miao, P. K. Chu, K. Xu, and F. Ma, *Appl. Surf. Sci.* **404**, 180 (2017).
- [163] B. Mortazavi, A. Ostadhossein, T. Rabczuk, and A. C. T. van Duin, *Phys. Chem. Chem. Phys.* **18**, 23695 (2016).
- [164] A. Kumar, T. Staedler, and X. Jiang, *Beil. J. Nanotech.* **4**, 66 (2013).
- [165] Q. Liu, L. Li, Y. Li, Z. Gao, Z. Chen, and J. Lu, *J. Phys. Chem. C* **116**, 21556 (2012).
- [166] R. Rani, N. Jena, A. Kundu, A. De Sarkar, and K. S. Hazra, *J. Appl. Phys.* **127**, 145101 (2020).
- [167] C. Wang, W. Chen, Y. Zhang, and Q. Sun, *Tribol. Lett.* **59** (2015).
- [168] J. Wang, J. Li, C. Li, X. Cai, W. Zhu, and Y. Jia, *Tribol. Lett.* **61**, 1 (2016).
- [169] Y. J. Yun, C. S. Ah, S. Kim, W. S. Yun, B. C. Park, and D. H. Ha, *Nanotechnology* **18**, 505304 (2007).
- [170] F. Belviso, A. Cammarata, J. Missaoui, and T. Polcar, *Phys. Rev. B* **102**, 155433 (2020).
- [171] R. W. Nunes and X. Gonze, *Phys. Rev. B* **63**, 155107 (2001).
- [172] R. W. Nunes and D. Vanderbilt, *Phys. Rev. Lett.* **73**, 712 (1994).
- [173] M. Mehregany, S. Senturia, J. Lang, and P. Nagarkar, *IEEE T. Electron. Dev.* **39**, 2060 (1992).
- [174] G. Meng, Y. Cheng, L. Chen, Y. Chen, and K. Wu, in *2013 IEEE International Conference on Solid Dielectrics ICSD2013 : Bologna, Italy, 30 June - 4 July 2013 ; Vol. 1, IEEE International Conference on Solid Dielectrics ; 11* (IEEE, Piscataway, NJ, 2013) pp. 662–665.
- [175] J. Guo, J. Gallegos, A. Tom, and D. Fan, *ACS Nano* **12**, 1179 (2018).
- [176] Y. Yoshizumi, T. Honegger, K. Berton, H. Suzuki, and D. Peyrade, *Small* **11**, 5630 (2015).
- [177] L. Zhang, Z. Xiao, X. Chen, J. Chen, and W. Wang, *ACS Nano* **13**, 8842 (2019).

- [178] S. Zhou, J. Han, S. Dai, J. Sun, and D. J. Srolovitz, *Phys. Rev. B* **92**, 155438 (2015).
- [179] T. Liang, W. G. Sawyer, S. S. Perry, S. B. Sinnott, and S. R. Phillpot, *Phys. Rev. B* **77**, 104105 (2008).
- [180] G. Levita, E. Molinari, T. Polcar, and M. C. Righi, *Phys. Rev. B* **92**, 085434 (2015).
- [181] A. V. Lebedev, I. V. Lebedeva, A. M. Popov, A. A. Knizhnik, N. A. Poklonski, and S. A. Vyrko, *Phys. Rev. B* **102**, 045418 (2020).
- [182] W. Jo, I. Eom, E. C. Landahl, S. Lee, and C.-J. Yu, *Rev. Sci. Instrum.* **87**, 035107 (2016).
- [183] N. Casaretto, D. Schaniel, P. Alle, E. Wenger, P. Parois, B. Fournier, E.-E. Bendeif, C. Palin, and S. Pillet, *Acta Cryst. B* **73**, 696 (2017).
- [184] T. Ors, N. Ranc, M. Pelerin, V. Michel, V. Favier, O. Castelnaud, C. Mocuta, and D. Thiaudière, *J. Synchrotron Radiat.* **26**, 1660 (2019).
- [185] F. Belviso, V. E. P. Claerbout, A. Comas-Vives, N. S. Dalal, F.-R. Fan, A. Filippetti, V. Fiorentini, L. Foppa, C. Franchini, B. Geisler, L. M. Ghiringhelli, A. Groß, S. Hu, J. Íñiguez, S. K. Kauwe, J. L. Musfeldt, P. Nicolini, R. Pentcheva, T. Polcar, W. Ren, F. Ricci, F. Ricci, H. S. Sen, J. M. Skelton, T. D. Sparks, A. Stroppa, A. Urru, M. Vandichel, P. Vavassori, H. Wu, K. Yang, H. J. Zhao, D. Puggioni, R. Cortese, and A. Cammarata, *Inorg. Chem.* **58**, 14939 (2019).
- [186] J. Wei, Z. Wang, W. Chen, and D. H. Cobden, *Nat. Nanotechnol.* **4**, 420 (2009).
- [187] D. Singh and B. Viswanath, *J. Mater. Sci.* **52**, 5589 (2017).
- [188] S. Lv, H. Li, Z. Wang, L. Han, Y. Liu, X. Liu, and J. Meng, *Appl. Phys. Lett.* **99**, 202110 (2011).
- [189] A. I. Poteryaev, M. Ferrero, A. Georges, and O. Parcollet, *Phys. Rev. B* **78**, 045115 (2008).
- [190] A. Splendiani, L. Sun, Y. Zhang, T. Li, J. Kim, C.-Y. Chim, G. Galli, and F. Wang, *Nano Lett.* **10**, 1271 (2010).
- [191] S. Bertolazzi, J. Brivio, and A. Kis, *ACS Nano* **5**, 9703 (2011).
- [192] B. Radisavljevic, A. Radenovic, J. Brivio, V. Giacometti, and A. Kis, *Nat. Nano* **6**, 147 (2011).
- [193] J. N. Coleman, M. Lotya, A. O'Neill, S. D. Bergin, P. J. King, U. Khan, K. Young, A. Gaucher, S. De, R. J. Smith, I. V. Shvets, S. K. Arora, G. Stanton, H.-Y. Kim, K. Lee, G. T. Kim, G. S. Duesberg, T. Hallam, J. J. Boland, J. J. Wang, J. F. Donegan, J. C. Grunlan, G. Moriarty, A. Shmeliov, R. J. Nicholls, J. M. Perkins, E. M. Grievson, K. Theuwissen, D. W. McComb, P. D. Nellist, and V. Nicolosi, *Science* **331**, 568 (2011).
- [194] K.-G. Zhou, N.-N. Mao, H.-X. Wang, Y. Peng, and H.-L. Zhang, *Angew. Chem. Int. Edit.* **50**, 10839 (2011).

- [195] M. Osada and T. Sasaki, *J. Mater. Chem.* **19**, 2503 (2009).
- [196] Z. Zeng, Z. Yin, X. Huang, H. Li, Q. He, G. Lu, F. Boey, and H. Zhang, *Angew. Chem. Int. Edit.* **50**, 11093 (2011).
- [197] M. B. Dines, *Mater. Res. Bull.* **10**, 287 (1975).
- [198] G. Eda, H. Yamaguchi, D. Voiry, T. Fujita, M. Chen, and M. Chhowalla, *Nano Lett.* **11**, 5111 (2011).
- [199] G. Yoon, D.-H. Seo, K. Ku, J. Kim, S. Jeon, and K. Kang, *Chem. Mater.* **27**, 2067 (2015).
- [200] R. Rasuli and A. I. zad, *Appl. Surf. Sci.* **256**, 7596 (2010).
- [201] G. Garcia, M. Atilhan, and S. Aparicio, *Phys. Chem. Chem. Phys.* **18**, 1212 (2016).
- [202] Y. Miyamoto, H. Zhang, and D. Tománek, *Phys. Rev. Lett.* **104**, 208302 (2010).
- [203] N. I. Kovtyukhova, Y. Wang, A. Berkdemir, R. Cruz-Silva, M. Terrones, V. H. Crespi, and T. E. Mallouk, *Nat. Chem.* **6**, 957 (2014), article.
- [204] G. Guan, S. Zhang, S. Liu, Y. Cai, M. Low, C. P. Teng, I. Y. Phang, Y. Cheng, K. L. Duei, B. M. Srinivasan, Y. Zheng, Y.-W. Zhang, and M.-Y. Han, *J. Am. Chem. Soc.* **137**, 6152 (2015).
- [205] J. R. Brent, N. Savjani, and P. O'Brien, *Prog. Mater. Sci.* **89**, 411 (2017).
- [206] X. Yin, Y. Li, W. Wu, G. Chu, Y. Luo, and H. Meng, *Ind. Eng. Chem. Res.* **56**, 4736 (2017).
- [207] Q. Zhang, L. Mei, X. Cao, Y. Tang, and Z. Zeng, *J. Mater. Chem. A* **8**, 15417 (2020).
- [208] L. Zhang, C. Chen, J. Zhou, G. Yang, J. Wang, D. Liu, Z. Chen, and W. Lei, *Adv. Func. Mater.* **30**, 2004139 (2020).
- [209] J. Missaoui, A. Cammarata, F. Belviso, and T. Polcar, *Phys. Rev. Appl.* **15**, 064041 (2021).
- [210] G. Henkelman, B. P. Uberuaga, and H. Jónsson, *J. Chem. Phys.* **113**, 9901 (2000).
- [211] A. Cammarata and T. Polcar, *Phys. Rev. B* **102**, 085409 (2020).

Copy of selected published papers

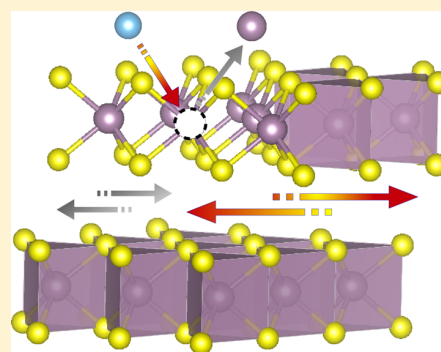
In the next pages, I provide a copy of the articles which I briefly describe in this thesis work. The list of such articles is here reported together with the corresponding chapter where the study is summarised:

- **A. Cammarata** and T. Polcar, *Tailoring Nanoscale Friction in MX₂ Transition Metal Dichalcogenides*, *Inorg. Chem.* **54**, 5739 (2015), [chapter 3](#).
- **A. Cammarata*** and T. Polcar, *Electro-vibrational Coupling Effects on “Intrinsic Friction” in Transition Metal Dichalcogenides*, *RSC Adv.* **5**, 106809 (2015), [chapter 4](#).
- **A. Cammarata*** and T. Polcar, *Vibrational Contributions to Intrinsic Friction in Charged Transition Metal Dichalcogenides*, *Nanoscale* **9**, 11488 (2017), [chapter 5](#).
- F. Belviso*, **A. Cammarata***, J. Missaoui, T. Polcar, *Effect of electric fields in low-dimensional materials: Nanofrictional response as a case study*, *Phys. Rev. B* **102**, 155433 (2020), [chapter 6](#).
- J. Missaoui*, **A. Cammarata***, F. Belviso, T. Polcar, *Effect of Noninteracting Intercalants on Layer Exfoliation in Transition-Metal Dichalcogenides*, *Phys. Rev. Applied* **14**, 064041 (2021), [chapter 7](#).
- **A. Cammarata***, T. Polcar, *Control of energy dissipation in sliding low-dimensional materials*, *Phys. Rev. B* **102**, 085409 (2020), [chapter 8](#).

Tailoring Nanoscale Friction in MX₂ Transition Metal DichalcogenidesAntonio Cammarata^{*,†} and Tomáš Polcar^{†,‡}[†]Department of Control Engineering, Czech Technical University in Prague, Technická 2, 16627 Prague 6, Czech Republic[‡]Engineering Materials & nCATS, FEE, University of Southampton, SO17 1BJ Southampton, United Kingdom

Supporting Information

ABSTRACT: Lattice dynamics of MX₂ transition metal dichalcogenides (M = Mo, W; X = S, Se, Te) have been studied with density functional theory techniques to control the macroscopic tribological behavior. Long-range van der Waals forces have been modeled with Grimme correction to capture the interlayer interactions. A new lattice dynamic metric, named *cophoncity*, is proposed and used in combination with electronic and geometric descriptors to relate the stability of the lattice distortions with the electro-structural features of the system. The cophoncity analysis shows that the distortion modes relevant to the microscopic friction can be controlled by tuning the relative M/X atomic contributions to the phonon density of states. Guidelines on how to engineer macroscopic friction at nanoscale are formulated, and finally applied to design a new Ti-doped MoS₂ phase with enhanced tribologic properties.



INTRODUCTION

The control of friction by lubricants is a great issue in automotive or aerospace industrial applications, that strongly addresses research efforts toward the comprehension of the mechanisms underlying friction, wear, and lubrication.^{1,2} Great attention has been directed to transition metal dichalcogenides (TMDs) because of their close features with graphene and their highly versatile chemical composition.³ They find tribologic applications in all those situations in which liquid lubricants cannot be used, such as in a vacuum, in extreme-temperature conditions, or for facile expulsion from the gaps between moving parts in a device.

Numerous studies have been devoted mainly to the electronic properties,^{4–6} while only a few theoretical papers have dealt with the tribologic aspects;^{7–11} most of them have been devoted solely to the study of the MoS₂ compound. The atomic description of friction is usually provided in terms of the atom arrangement forming the sliding surfaces and the lubricant in between them; Newtonian (or Langevin) equations of motion are solved in the presence of an external load and a drift force pulling the sliding surfaces. In this way, it is possible to sample the evolution of the geometry of the system in order to obtain information on friction, adhesion, and wear.² This represents a standard example of how MD simulations are used to model the tribological properties at the atomic scale; despite their capability to simulate thousand-atom systems, their results can hardly be transferred across the stoichiometries, since they rely on force fields designed *ad hoc* for the studied system. Moreover, a deeper insight of the local electronic and geometric characteristics is required to capture subtleties that a molecular mechanic description cannot represent; indeed, quantum mechanical approaches have been used to this aim,¹² focusing

on the theoretical modeling of a specific stoichiometry and chemical composition.

The selection of the proper chemical composition, stoichiometry, and geometry to obtain a TMD compound with reduced friction coefficient has been, so far, based mainly on experimental data, while theoretical works have had the role to model the selected material to uncover peculiar properties. A broader theoretical framework encompassing all the compounds of the TMD family would help researchers to focus the experimental exploration on only those materials that are promising candidates with enhanced frictional properties. However, to the best of our knowledge, a unified description of the electronic and structural features common to all the MX₂ compounds and relevant to the tribological properties is missing at the quantum mechanical level. In the present work, our goal is to identify how the electronic and structural features of MX₂ TMDs determine the macroscopic friction, in order to engineer the tribological properties at the atomic scale. Using density functional theory based techniques, we formulate a new lattice dynamics descriptor, that we denote as *cophoncity*, based on the dynamic properties of the M and X atomic species; with such a descriptor, we are able to disentangle the atomic electro-structural contributions to the lattice vibrations affecting the layer sliding. Our approach enables us to capture the electronic and geometric features that are common to the MX₂ TMDs systems and responsible for the frictional properties; in this way, we formulate a protocol to properly choose and modify the MX₂ stoichiometry, geometry, and chemical composition to obtain TMD compounds with improved frictional response. Finally, we apply such a protocol to suggest a particular Ti-

Received: February 22, 2015

Published: May 22, 2015

doped MoS₂ phase as new material with enhanced tribologic characteristics.

COMPUTATIONAL DETAILS

MX₂ transition metal dichalcogenides are layered structures, with each layer formed by hexagonally packed metal atoms (M) forming covalent bonds with six chalcogen anions (X) in a trigonal prismatic coordination (Figure 1); adjacent layers are coupled by weak van der

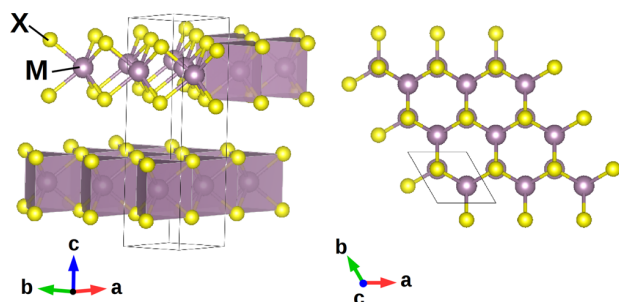


Figure 1. Hexagonal $P6_3/mmc$ structure of 2H polymorph MX₂ model geometries (M = transition metal, X = chalcogen atom). M–X bonds are arranged in a trigonal prismatic coordination forming MX₂ layers that can slide thanks to weak van der Waals interactions.

Waals forces that allow relative sliding under tribological conditions. Several stable TMD polymorphs and polytypes are found,³ with some transforming into each other by sliding of subsequent layers; such sliding motions include also rotations (reorientations) of one layer with respect to its two adjacent ones about an orthogonal axis. The complex atomic displacements that result into layer sliding, either commensurate or not, can be represented as linear combinations of collective atomic motions, e.g., phonon or vibrational modes, of two adjacent layers of the most stable configuration. We will thus focus on model systems with two layers in the unit cell, and we choose 2H polymorph crystalline MX₂ structures as model geometries, with M = Mo, W and X = S, Se, Te, and hexagonal $P6_3/mmc$ symmetry (SG 194); for simplicity, we will refer to them as MX by dropping the stoichiometric coefficients. We choose the 2H configuration in which two adjacent layers are oriented in such a way that an M atom of one layer is aligned with two X atoms of the other one along the direction orthogonal to each layer (*c*-axis in our setting, see Figure 1); this choice is motivated by a recent *ab initio* study on the MoS₂ compound,¹² where it has been shown that this configuration corresponds to the lowest energy value found for several arrangements of two subsequent MoS₂ layers.

Our density functional theory (DFT) calculations are performed using the projector-augmented wave (PAW) formalism and the Perdew–Burke–Ernzerhof (PBE) energy functional¹³ with van der Waals correction as implemented in the most recent version of VASP¹⁴ package. Particular attention has been paid to the choice of the description of the van der Waals interactions, that are known to play an important role in determining the static and dynamic properties of TMDs;¹⁵ after preliminary benchmarks, we chose the Grimme correction,¹⁶ that is able to capture the structural features. The Brillouin zone is sampled with a minimum of a $5 \times 5 \times 3$ *k*-point mesh and plane wave cutoff of 550 eV. Full structural (atoms and lattice) relaxations are initiated from diffraction data^{17–22} and the forces minimized to a 0.5 meV Å⁻¹ tolerance. We computed the phonon band structure of each considered system using the fully relaxed geometries, aided by the PHONOPY software.²³

RESULTS AND DISCUSSION

The goal of our study is to identify and control the bulk features that contribute to the macroscopic friction. To this aim, we start with the characterization of the atomic motions

that produce a global slide of adjacent layers. All the possible sliding directions can be represented as suitable linear combinations of vibrational modes; for this reason, no assumption is done on the layer drift, and our conclusions will be valid irrespective of the sliding direction. To investigate the electron–lattice effect on the macroscopic tribological properties, we need first to identify the phonon modes directly related to the sliding of adjacent layers. We thus compute each phonon band structure (Figure 2) along a linear path joining the high-symmetry points of the irreducible Brillouin zone (IBZ); we do not find any unstable displacements, confirming that the considered geometries represent stable configurations. We then characterize each vibrational mode at a fixed *k*-point by analyzing the corresponding atomic displacements. Since all six compounds have the same geometry and the same set of structural symmetries, they share the same set of vibrational modes, with frequencies depending only on the atomic types. We observe that a variation of the atomic species produces a shift of the vibrational frequencies and a variation of the M/X relative contribution (pDOS in Figure 2) to the vibrational bands.

Only a few modes are related to sliding motion, corresponding to pure rigid layer translations or to layer shifts combined with intralayer motions, like stretching and/or bending of atomic bonds or flattening of coordination polyhedra (top of Figure 2). Our goal is to lower the frequency of those vibrational modes that are relevant to the layer sliding, in order to facilitate those kinds of atomic displacements that correspond to a global shift of one layer with respect to its two adjacent ones. This can be understood in terms of the classical picture, where the frequency represents the curvature of the system energy hypersurface as a function of the atomic coordinates. In modeling tribological conditions, at the working regime of the tribological material, the system energy can be considered as constant; at fixed system energy, the lower the frequency of a mode is, the higher the amplitude of the corresponding atomic displacement is. Concerning the phonon modes that are associated with the layer sliding, a higher amplitude of the atomic displacements corresponds to an enhanced shift of one layer with respect to its adjacent ones, hence favoring the sliding of the layers.

The frequencies of the sliding-related modes are found to be highest for MoS₂ and lowest for WTe₂, following the ordering MoS₂ > MoTe₂ > MoSe₂ > WS₂ > WSe₂ > WTe₂; such ordering is expected to be the same for the bulk contribution to the macroscopic friction coefficients of the corresponding materials. It is worth noting here that a direct comparison with available experimental data is not straightforward, since this is not fully comparable due to the different experimental conditions.^{24–30} Moreover, our models are aimed at studying the resistance of layer shearing in the bulk of the structure, while experimentally measured macroscopic friction is almost inevitably related also to wear and surface effects due to exfoliation, absorption of small molecules, presence of oxidizing agents, and elastic effects related to the number of layers.²⁴

In order to quantify how the chemical composition determines the mode frequency, we need to relate the electronic and geometric properties of the structure to the frequency shift. We recall that the vibrational frequencies of the lattice are determined by the atomic types involved in the formation of the structure, their geometric arrangement, and the symmetries that the latter determines. Once the atomic topology (atom coordination shells) is fixed, the kinds of

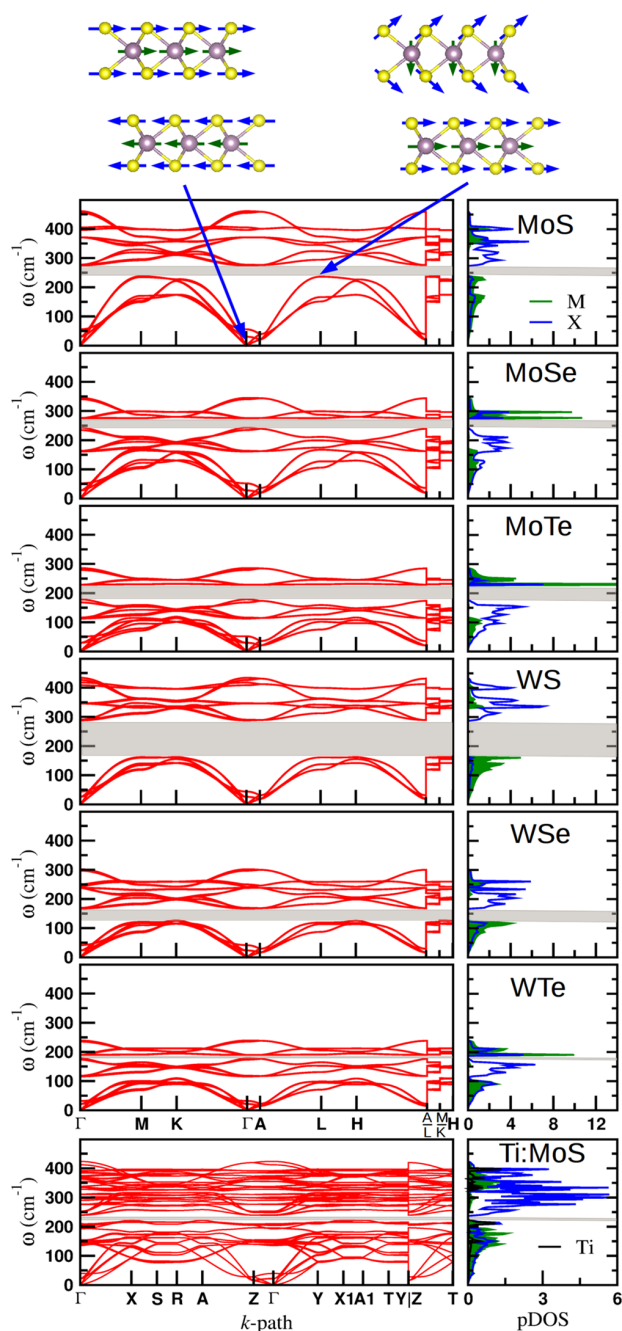


Figure 2. Computed phonon band structures (left panels) and phonon-DOS (right panels) of MX_2 compounds; the gray area in each plot indicates the energy gap separating the low- from the high-frequency band. In the inset, examples of vibrational modes relevant to the macroscopic friction are shown: pure layer sliding (top left) and layer sliding combined with intralayer asymmetric M–X–M bond stretching (top right).

atomic displacements, that is, the vibrational modes, and hence the corresponding phonon band structure, are determined. A specific vibrational mode is the result of the collective motion of ions of distinct atomic type; each ion contributes to the collective motion in an amount that depends on the electronic structure of the environment where it is embedded that, in turn, depends on the electronic characteristics of the nearest

neighboring atoms. For this reason, at a fixed topology, the atomic type determines the vibrational frequency of the modes.

To disentangle the electronic from the structural contributions to the determination of the phonon frequencies, we first quantify the geometric distortions δ^{31} of the system by performing a group-theoretical analysis with the aid of the ISODISTORT software;³² we thus decompose the MX geometries in terms of distortions of a parent phase, that we choose to be the relaxed MoS structure (Table 1). We then evaluate the M–X bond covalency $C_{\text{M,X}}$ at different structural distortions, applying the covalency metric (see Supporting Information), designed for crystalline materials,³³ in the energy range of the valence band. The $C_{\text{M,X}}$ bond covalency is a measure of the electronic density distributed along the M–X bond; it is determined by the cooperative effect of the electronic structure of the M and X atoms and the structural distortions of the system, as has been already observed in a theoretical study on perovskite oxides.³³ We observe that covalency is strictly decreasing with distortions in MoX systems, while it has a minimum for the WTe compounds among the WX compositions (Table 1 and Figure 3a).

We now need a metric to quantify how changing the atomic type affects specific vibration frequencies. Each phonon mode is a complex function of all the components of the force constant tensors of all the atomic pairs present in the system,³⁴ a particular displacement pattern, including those representing the layer sliding, cannot be related to single components of the force constant tensors in a unique way. Therefore, the force constants alone do not represent a manageable descriptor to parameterize the interactions responsible of specific atomic displacements, the layer sliding among them. To obtain a simple metric, we focus on the smallest unit that produces the dynamical interactions, that is, the M–X atomic pair. We call this metric *cophonycity of the M–X atomic pair* $C_{\text{ph}}(\text{M–X})$, and we use it as a lattice dynamics descriptor to understand the atomic type dependence of phonon frequencies. The complete mathematical implementation is described in the Supporting Information together with a discussion on its validity and limitations.

We thus use the cophonycity metric to relate the vibrational frequency to the atomic types that generate the corresponding distortion mode. All the computed pDOSs show two distinct energy bands, corresponding to low- and high-frequency ranges, respectively, separated by a gap. Following the usual convention, we label phonon bands with progressive integer numbers, starting from the lowest associated frequency. With this convention, $\Gamma(1)$ represents the vibrational mode associated with band number 1, that is, the dispersive mode associated with the lowest frequency $\omega(\Gamma)_1$ at the Γ point of the IBZ; analogously, $\Gamma(2)$ is associated with the vibrational mode with frequency $\omega(\Gamma)_2$ such that $\omega(\Gamma)_3 \geq \omega(\Gamma)_2 \geq \omega(\Gamma)_1$ and so on. We analyzed the trend of all the frequencies associated with the sliding-related modes against the cophonycity of the system, and we find that they all have the same trend against the cophonycity metric. For simplicity, in the present analysis, we will discuss only the trend of the degenerate $\omega(\Gamma)_{4-5}$ and $\omega(\text{A})_{1-4}$ frequencies, as our conclusions also apply to the other frequencies that we considered in our study. Irrespective of the kind of phonon mode, we find that the frequency diminishes when $C_{\text{ph}}(\text{M–X})$ approaches zero (Table 1 and Figure 3b). If $C_{\text{ph}}(\text{M–X}) = 0$, we will say that perfect cophonycity is realized (see Supporting Information).

Table 1. Structural Distortion δ (Å), M–X Bond Covalency $C_{M,X}$ (eV), Cophonycity $C_{ph}(M-X)$ (cm^{-1}) of the M–X Pair, Selected Vibrational Frequencies $\omega(k)_i$ (cm^{-1}), and Formation Energy ΔH_f (eV) of the MX_2 Model Systems with MoS System as Reference for Calculating δ and ΔH_f Values

system	δ	$C_{M,X}$	$C_{ph}(M-X)$	$\omega(\Gamma)_{4-5}$	$\omega(A)_{1-4}$	ΔH_f
MoS	0.00	−0.44	8.3	30	21	0.00
MoSe	0.06	−0.58	−45.7	28	20	2.79
MoTe	0.10	−0.75	−31.0	30	21	5.94
WS	0.02	−0.51	10.0	26	18	1.23
WSe	0.06	−0.66	4.1	24	17	4.27
WTe	0.03	−0.80	0.9	22	15	7.63
Ti:MoS	0.17	−0.76 ^a	4.6 ^b	$\omega(\Gamma)_4$ 22 ^c $\omega(\Gamma)_5$ 23 ^c	$\omega(Z)_{1-2}$ 15 ^c $\omega(Z)_{3-4}$ 16 ^c	0.04

^aTi–S bond covalency value to be compared with $C_{Mo,S}$ in the MoS system. ^bGlobal cophonycity of Ti:MoS system calculated as weighted average of the $C_{ph}(Mo-S)$ and $C_{ph}(Ti-S)$ cophonycities, with weights corresponding to the M stoichiometric coefficients. ^cDegeneracy of vibrational modes in MoS system is partially lifted in Ti:MoS model, having the latter a lower number of symmetries. According to the displacement patterns, A(1–4) modes of MoS system correspond to Z(1–4) modes of Ti:MoS model.

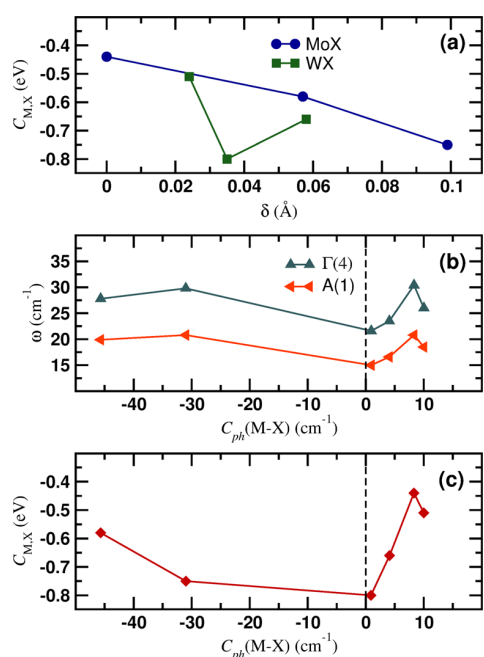


Figure 3. (a) M–X bond covalency as a function of structural distortions δ . Covalency can be tuned by changing the amplitude of the structural distortions. (b) Frequency of the $\Gamma(4)$ and $A(1)$ modes as a function of M–X pair cophonycity. Irrespective of the vibrational mode, the lowest frequency is realized for $C_{ph}(M-X) \approx 0$. (c) Covalency of the M–X bond as a function of $C_{ph}(M-X)$. The lowest $C_{M,X}$ covalency value corresponds to a cophonycity close to zero.

As we discussed above, the $C_{M,X}$ covalency metric captures the entangled electronic and structural features into a single descriptor; thanks to this characteristic, we can relate the change of the phonon frequency to the geometry and the atomic types forming the system by connecting cophonycity with M–X bond covalency. Cophonycity is found to be minimal when $C_{M,X}$ bond covalency is about -0.80 eV, that is realized in the WTe compound (Table 1 and Figure 3c); on the other hand, $C_{ph}(M-X)$ shows similar trends for the MoX and WX compounds with respect to the structural distortions. According to these results, cophonycity, and hence vibrational frequencies, can be adjusted by tuning the distortions and the covalency of the system by a proper selection of the M and X ions.

We now want to exploit the knowledge acquired so far to design a new TMD with enhanced tribological properties. In particular, according to the results discussed above, we want to find an M–X pair that realizes a low covalency value in order to minimize the M–X cophonycity, so as to lower the phonon frequencies that govern the layer drift. We focus on the MoS_2 compound, because the synthesis routes have been extensively studied, and therefore, it constitutes a good candidate to easily grow derived materials. Starting from the MoS model system, we will now design a new compound by partial ion substitution. Among the chosen MoX stoichiometries, MoTe realizes the lowest covalency value; to further lower the Mo–X covalency we must increase the structural distortions (Figure 3c). Following the series of chalcogenides, a natural choice would be polonium as X ion; since we want to avoid to use unstable elements, another possibility is to partially substitute for the Mo cation. The substituent atom must be chosen so as to induce structural distortions that lower the covalency of the cation structural site, in order to lower the corresponding cophonycity and hence the vibrational frequencies. We are thus oriented toward cations with ionic radii smaller than that of the Mo atom. Moreover, we want to choose a proper dopant concentration and geometric arrangement of the dopant to preserve the stability of the final system. To this aim, we consider the MoS optimized structure, and we substitute a Mo atom with one Ti atom in such a way that, within a single layer, its first neighboring cation shell is formed only by Mo atoms, building the $Mo_3Ti_1S_8$ (Ti:MoS) system with orthorhombic $Cmcm$ (SG 63) symmetry (Figure 4). We then fully optimize the geometry³⁵ and compare the relative properties with those of the unsubstituted MoS system.

The calculated formation energies ΔH_f (Table 1), relative to those of the MoS system, indicate that MoS and Ti:MoS are the most stable compounds among those considered; in particular, the small difference between MoS and Ti:MoS ΔH_f values (0.04 eV) suggests that both compounds have the same probability to be produced, especially in self-assembling tribological mixtures where both MoS_2 and TiS_2 chemical precursors are present. The Mo→Ti substitution produces a significant distortion of the structure ($\delta = 0.17$ Å), due to a local reduction of the M–S bond covalency that decreases from -0.44 to -0.76 eV. Such a local decrease of the covalency produces a global lowering of the cophonycity of the system, that decreases from 8.3 to 5.9 cm^{-1} . The cation substitution also reduces the symmetries of the system, producing the

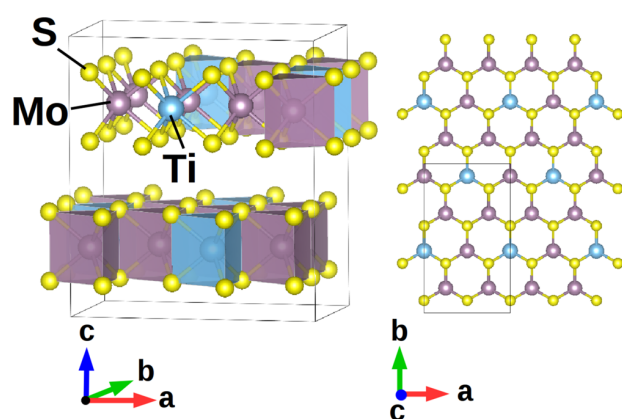


Figure 4. Geometry of the orthorhombic $Cmc21$ Ti:MoS₂ model system. Within each layer, one Ti atom is surrounded by only Mo atoms in the first neighboring cation shell.

splitting of those vibrational modes that were degenerate in the parent MoS structure. However, the displacement pattern of those modes that are relevant to the tribological properties is unvaried, and a direct comparison of the corresponding frequencies can be done without ambiguities. In the Ti:MoS system, the vibrational frequencies are found to be lower than those of the undoped counterpart, as expected according to the lower M–S cophoncity (Table 1); in particular, we note that the frequency values are close to those found in the WSe and WTe systems. According to the present results, the bulk contribution to the friction coefficient of the Ti:MoS, WSe, and WTe systems are expected to be similar and the lowest among those of the TMDs compounds considered in this work.

CONCLUSIONS

Six transition metal dichalcogenides with general stoichiometry MX₂ have been studied by means of ab initio techniques. The frequency analysis suggests that the WSe and WTe compounds are expected to display the lowest bulk contribution to the friction coefficient among those of the considered systems. A new lattice dynamic metric, named cophoncity, has been proposed, to capture the effect of the electronic features of the ion environment on the stability of the lattice distortions. We find that cophoncity of the M–X pair in MX₂ TMDs is related to the vibrational frequencies of the distortion modes relevant to the microscopic friction. In particular, we find that, as cophoncity tends to zero, the stability of layer sliding modes is lowered, favoring the relative shift of two subsequent MX₂ layers; in correspondence, a lower macroscopic friction coefficient is expected.

Cophoncity in the studied TMDs is found to be related to the covalency of the M–X bond. Increasing structural distortions in MoX systems induces a lowering of the Mo–X bond covalency, and the Mo–X pair approaches the perfect cophoncity. Following these outcomes, we design the Ti:MoS compound, a new material derived from the MoS₂ TMD by partial Mo→Ti substitution. The analysis of the vibrational frequencies suggests that the Ti:MoS system is expected to have a bulk contribution to the friction coefficient comparable to that of the WSe and WTe compounds.

The cophoncity metric here proposed, combined with electro-structural analyses, constitutes a new tool to finely tune the dynamic properties of a system at the atomic scale; thanks to the generality of its definition, this new lattice dynamic

descriptor can be universally applied to any A–B atomic pair, irrespective of the geometric environment in which the pair is embedded.

ASSOCIATED CONTENT

Supporting Information

Covalency metric and the mathematical definition of the cophoncity metric. The Supporting Information is available free of charge on the ACS Publications website at DOI: 10.1021/acs.inorgchem.5b00431.

AUTHOR INFORMATION

Corresponding Author

*E-mail: cammaant@fel.cvut.cz.

Notes

The authors declare no competing financial interest.

ACKNOWLEDGMENTS

This work has been done with the support of intersectoral mobility and quality enhancement of research teams at Czech Technical University in Prague, CZ.1.07/2.3.00/30.0034. This work was supported by the IT4Innovations Centre of Excellence project (CZ.1.05/1.1.00/02.0070), funded by the European Regional Development Fund and the national budget of the Czech Republic via the Research and Development for Innovations Operational Programme, as well as Czech Ministry of Education, Youth and Sports via the project Large Research, Development and Innovations Infrastructures (LM2011033). The use of VESTA³⁶ software is also acknowledged.

REFERENCES

- Pereira, G.; Lachenwitzer, A.; Kasrai, M.; Norton, P.; Capehart, T.; Perry, T.; Cheng, Y.-T.; Frazer, B.; Gilbert, P. *Tribol. Lett.* **2007**, *26*, 103–117.
- Vanossi, A.; Manini, N.; Urbakh, M.; Zapperi, S.; Tosatti, E. *Rev. Mod. Phys.* **2013**, *85*, 529–552.
- Chhowalla, M.; Shin, H. S.; Eda, G.; Li, L.-J.; Loh, K. P.; Zhang, H. *Nat. Chem.* **2013**, *5*, 263–275.
- Wang, Q. H.; Kalantar-Zadeh, K.; Kis, A.; Coleman, J. N.; Strano, M. S. *Nat. Nanotechnol.* **2012**, *7*, 699–712.
- Yin, Z.; Li, H.; Li, H.; Jiang, L.; Shi, Y.; Sun, Y.; Lu, G.; Zhang, Q.; Chen, X.; Zhang, H. *ACS Nano* **2012**, *6*, 74–80.
- Mak, K. F.; Lee, C.; Hone, J.; Shan, J.; Heinz, T. F. *Phys. Rev. Lett.* **2010**, *105*, 136805.
- Cahangirov, S.; Ataca, C.; Topsakal, M.; Sahin, H.; Ciraci, S. *Phys. Rev. Lett.* **2012**, *108*, 126103.
- Onodera, T.; Morita, Y.; Suzuki, A.; Koyama, M.; Tsuboi, H.; Hatakeyama, N.; Endou, A.; Takaba, H.; Kubo, M.; Dassenoy, F.; Minfray, C.; Joly-Pottuz, L.; Martin, J.-M.; Miyamoto, A. *J. Phys. Chem. B* **2009**, *113*, 16526–16536.
- Onodera, T.; Morita, Y.; Nagumo, R.; Miura, R.; Suzuki, A.; Tsuboi, H.; Hatakeyama, N.; Endou, A.; Takaba, H.; Dassenoy, F.; Minfray, C.; Joly-Pottuz, L.; Kubo, M.; Martin, J.-M.; Miyamoto, A. *J. Phys. Chem. B* **2010**, *114*, 15832.
- Liang, T.; Sawyer, W. G.; Perry, S. S.; Sinnott, S. B.; Phillpot, S. R. *Phys. Rev. B* **2008**, *77*, 104105.
- Morita, Y.; Onodera, T.; Suzuki, A.; Sahnoun, R.; Koyama, M.; Tsuboi, H.; Hatakeyama, N.; Endou, A.; Takaba, H.; Kubo, M.; Carpio, C. A. D.; Shin-yoshi, T.; Nishino, N.; Suzuki, A.; Miyamoto, A. *Appl. Surf. Sci.* **2008**, *254*, 7618–7621.
- Levita, G.; Cavaleiro, A.; Molinari, E.; Polcar, T.; Righi, M. C. *J. Phys. Chem. C* **2014**, *118*, 13809–13816.
- Perdew, J. P.; Burke, K.; Ernzerhof, M. *Phys. Rev. Lett.* **1996**, *77*, 3865–3868.

- (14) (a) Kresse, G.; Furthmüller, J. *Comput. Mater. Sci.* **1996**, *6*, 15–50; (b) Kresse, G.; Joubert, D. *Phys. Rev. B* **1999**, *59*, 1758–1775.
- (15) Geim, A. K.; Grigorieva, I. V. *Nature* **2013**, *499*, 419–425.
- (16) Grimme, S. J. *Comput. Chem.* **2006**, *27*, 1787–1799.
- (17) Schönfeld, B.; Huang, J. J.; Moss, S. C. *Acta Crystallogr., Sect. B* **1983**, *39*, 404–407.
- (18) Kalikhman, V. *Inorg. Mater.* **1983**, *19*, 957–962.
- (19) Brixner, L. J. *Inorg. Nucl. Chem.* **1962**, *24*, 257–263.
- (20) Schutte, W.; Boer, J. D.; Jellinek, F. J. *Solid State Chem.* **1987**, *70*, 207–209.
- (21) Kalikhman, V. L. *Neorg. Mater.* **1983**, *19*, 1060–1065.
- (22) Yanaki, A. A.; Obolonchik, V. A. *Inorg. Mater.* **1973**, *9*, 1855–1858.
- (23) Togo, A.; Oba, F.; Tanaka, I. *Phys. Rev. B* **2008**, *78*, 134106.
- (24) Lee, C.; Li, Q.; Kalb, W.; Liu, X.-Z.; Berger, H.; Carpick, R. W.; Hone, J. *Science* **2010**, *328*, 76–80.
- (25) Kim, Y.; Huang, J.; Lieber, C. M. *Appl. Phys. Lett.* **1991**, *59*, 3404–3406.
- (26) Cao, K.; Li, C.; Yonghua, C.; Tang, H.; Yan, F.; Song, H.; Yang, X. *Tribol. Trans.* **2012**, *55*, 297–301.
- (27) Oviedo, J. P.; KC, S.; Lu, N.; Wang, J.; Cho, K.; Wallace, R. M.; Kim, M. J. *ACS Nano* **2015**, *9*, 1543–1551.
- (28) Chhowalla, M.; Amaratunga, G. A. J. *Nature* **2000**, *407*, 164–167.
- (29) Dominguez-Meister, S.; Justo, A.; Sanchez-Lopez, J. *Mater. Chem. Phys.* **2013**, *142*, 186–194.
- (30) Cohen, S.; Rapoport, L.; Ponomarev, E.; Cohen, H.; Tsirlina, T.; Tenne, R.; Lévy-Clément, C. *Thin Solid Films* **1998**, *324*, 190–197.
- (31) The geometric distortion δ is defined as

$$\delta = \sqrt{\frac{A_s}{A_p} \sum_{i,j} (r_{i,j} - x_{i,j})^2} \quad (1)$$

where A_p and A_s are the volume of the parent and distorted structure, respectively, while $r_{i,j}$ and $x_{i,j}$ are the j -th Cartesian components of the i -th atom of the parent and distorted structure, respectively. Distorted structures are from the corresponding ones in the parent phase. The complete mathematical derivation is described in ref 32.

(32) Campbell, B. J.; Stokes, H. T.; Tanner, D. E.; Hatch, D. M. *J. Appl. Crystallogr.* **2006**, *39*, 607–614.

(33) Cammarata, A.; Rondinelli, J. M. *J. Chem. Phys.* **2014**, *141*, 114704.

(34) Parlinski, K.; Li, Z. Q.; Kawazoe, Y. *Phys. Rev. Lett.* **1997**, *78*, 4063–4066.

(35) Optimized parameters of the orthorhombic $Cmcm$ Ti:MoS model are the following: (i) lattice parameters (Å), $a = 6.463\ 21$, $b = 11.194\ 61$, $c = 12.567\ 47$; (ii) Wyckoff positions, Mo 4c (0, -0.082 43, $\frac{1}{4}$), Ti 4c (0, 0.417 44, $\frac{1}{4}$) Mo 8g ($\frac{1}{4}$, 0.167 67, $\frac{1}{4}$), S 8f (0, 0.584 87, 0.128 45), S 8f (0, 0.084 24, 0.126 85), S 16h (0.748 66, 0.333 85, 0.128 31).

(36) Momma, K.; Izumi, F. *J. Appl. Crystallogr.* **2008**, *41*, 653–658.



Cite this: *RSC Adv.*, 2015, 5, 106809

Received 23rd November 2015
Accepted 1st December 2015

DOI: 10.1039/c5ra24837j

www.rsc.org/advances

Electro-vibrational coupling effects on “intrinsic friction” in transition metal dichalcogenides†

Antonio Cammarata^{*a} and Tomas Polcar^{ab}

We propose a protocol to disentangle the electro-vibrational structural coupling contributing to the intrinsic tribologic properties of layered MX_2 transition metal dichalcogenides ($\text{M} = \text{Mo}, \text{W}; \text{X} = \text{S}, \text{Se}, \text{Te}$) under load. We employ *ab initio* techniques to model how changing the interlayer distance affects the electronic distribution and the vibrational properties of the system. We analyze the electro-vibrational coupling features by combining orbital polarization and mode Grüneisen parameters analyses with the recently developed bond covalency descriptor and the lattice dynamic metric named *cophoncity*. We find that intralayer charge distribution depends on the interlayer distance, determining, in turn, a shift of specific vibrational frequencies. We finally suggest a route to control the frequency shift, thus the bulk response to the load, in transition metal dichalcogenides through a proper selection of the atomic type.

1 Introduction

Transition metal dichalcogenides (TMDs) are van der Waals structures with general MX_2 stoichiometry ($\text{M} =$ transition metal cation, $\text{X} =$ chalcogen anion); they have attracted great interests because of their close features with graphene and their highly versatile stoichiometry.¹ They find tribologic applications whereas liquid lubricants cannot be used, such as in extreme temperature-pressure conditions or possibility to be expelled from the gaps separating moving parts in a device. Numerous studies have dealt mainly with the electronic properties;^{2–4} indeed, only few theoretical works investigated on the tribologic aspects,^{5–9} and, to the best of our knowledge, there are no theoretical studies about the electron–phonon coupling effects on the frictional properties. Tribological properties are usually modeled at the atomic scale by molecular dynamics simulations, the results of which, unfortunately, can hardly be transferred across the chemical compositions, since they rely on mathematical expressions of atomic interactions calibrated ad hoc on the studied system. Quantum mechanical approaches have also been used to this aim,¹⁰ focusing on a specific stoichiometry and chemical composition.

Theoretical works have had the role to model specific tribologic materials, while experimental data has been so far the guide to select the proper stoichiometry, chemical composition and geometry of the system to design a TMD compound with improved frictional properties. A broader theoretical approach

encompassing all the compositions of the TMDs family would help to narrow the experimental exploration to only those materials that are promising candidates. In this perspective, we now want to go beyond the construction of models that explain the experimental data, and will thus formulate new guidelines to design novel tribologic materials.

In a previous computational investigation,¹¹ we understood that the dynamic properties of the MX_2 compounds can be tuned by proper adjustment of M–X bond covalency, structural distortions, and M/X atomic participation to the vibrational properties of the system with no applied load. We then found a route to select the proper atomic species and geometry; we thus individuated Ti as optimal substituent for Mo in MoS_2 and suggested a new Ti-doped MoS_2 phase as promising tribological material.

Indeed, substitution of Mo in MoS_2 with Nb,¹² Cr,¹³ Mn¹⁴ and Ti¹⁵ have been recently reported, showing that transition metal doping in the Mo crystallographic site is quite common practice and is experimentally feasible. We now study the coupling of the electronic and dynamic properties in the presence of external load; in particular, we want to understand how to control the dynamic features of the system *via* a fine control of the electronic structure. The mechanism governing such coupling would also contribute to the comprehension of the strain-induced shifts of the Raman-active modes observed in TMDs under uniaxial strain.^{16–18}

In the present work, we study the *intrinsic friction* in MX_2 TMDs in the presence of external load. The term *microscopic friction* refers to the friction generated by the relative motion of few adjacent atom layers; it is the result of the local electronic and structural features of the material at the atomic level, originating from the atomic type and the geometric arrangement of the atoms. When microscopic friction involves only

^aDepartment of Control Engineering, Czech Technical University in Prague, Technicka 2, 16627 Prague 6, Czech Republic. E-mail: cammaant@fel.cvut.cz; Fax: +420 224 91 8646; Tel: +420 224 35 7598

^bnCATS, FEE, University of Southampton, SO17 1BJ Southampton, UK

† Electronic supplementary information (ESI) available: Mathematical definition of cophoncity metric. See DOI: 10.1039/c5ra24837j

atomic layers of the bulk structure with no structural irregularities (dislocations, layer truncations *etc.*), we can name it as *intrinsic friction*, since it can be considered as a property peculiar of the pure compound without imperfections. In consequence, all tribological properties originating from intrinsic friction, will be referred as *intrinsic* of the considered system. The knowledge of the intrinsic tribological properties is nowadays becoming mandatory with the advance of the experimental techniques, now capable to micromanipulate free-standing atomic layers.¹⁹

We here propose a protocol to disentangle the electro-vibrational coupling contributions to the atomic motions that may facilitate interlayer slip, hence affecting intrinsic friction. Thanks to its universal applicability, our approach can be promptly exploited to engineer the lattice dynamic properties and the electronic distribution in materials for diverse applications other than tribology, like in optical or electronic devices. We also extend the present analysis to the specific Ti-doped MoS₂ phase that we already identified as promising TMD-based candidate. To this aim, we will disentangle the electronic from the structural features of MX₂ TMDs that determine the bulk contribution to intrinsic friction at the quantum mechanical level, using density functional theory based techniques. We will exploit the recently developed lattice dynamics descriptor, named *cophoncity*,¹¹ to capture how each atomic species contributes to a specific vibrational band (see ESI†). With such descriptor, we are able to disentangle the atomic electro-structural contributions to the lattice vibrations affecting the layer sliding. Our approach enables us to capture the electronic and geometric features that are common to the MX₂ systems and responsible of the intrinsic frictional properties under external load. Finally, we suggest a route to select and modify the MX₂ stoichiometry and geometry to obtain TMD compounds with improved intrinsic tribological response under load.

2 Methods

MX₂ transition metal dichalcogenides are formed by layers coupled by weak van der Waals forces that allow relative sliding under tribological conditions. Each layer is formed by hexagonally packed metal atoms (M) forming covalent bonds with six chalcogen anions (X) in a trigonal prismatic coordination (Fig. 1). Several stable TMDs polymorphs and polytypes are found,¹ some transforming into each other by sliding of subsequent layers. Sliding motions include reorientations of one layer with respect to its two adjacent ones by means of rotations about an orthogonal axis. The complex atomic displacements that result into layer sliding, either commensurate or not, can be represented as linear combinations of displacement patterns, *e.g.* vibrational modes, of two adjacent layers of the most stable configuration. We focus on model systems with two layers in the unit cell and we choose 2H polymorph crystalline MX₂ structures as model geometries, with M = Mo, W and X = S, Se, Te, and hexagonal *P6₃/mmc* symmetry (SG 194); for simplicity, we will refer to them as MX by dropping the stoichiometric coefficients. We choose the 2H

configuration in which two adjacent layers are oriented in such a way that an M atom of one layer is aligned with two X atoms of the other one along the direction orthogonal to each layer (*c*-axis in our setting—see Fig. 1a); we make this choice following the outcomes of a recent *ab initio* study on the MoS₂ compound:¹⁰ in this, authors show that this configuration is the most stable one among those considering several arrangements of two subsequent MoS₂ layers. We also consider the MoS optimized structure and we substitute a Mo atom with one Ti atom in such a way that, within a single layer, its first neighbouring cation shell is formed only by Mo atoms, building the Mo₃Ti₁S₈ (Ti:MoS) system with orthorhombic *Cmcm* (SG 63) symmetry (Fig. 1b).

Our calculations are performed on 2 × 2 × 2 supercells of the MX₂ and Mo₃Ti₁S₈ unit cells, within the framework of the density functional theory (DFT), using the projector-augmented wave (PAW) formalism and the Perdew–Burke–Ernzerhof (PBE) energy functional²⁰ with van der Waals correction as implemented in VASP.²¹ We paid particular attention to the choice of the description of the van der Waals interactions, since it is recognized they play an important role in determining the static and dynamic properties of TMDs;²² after preliminary benchmarks, we chose the Grimme correction,²³ that is able to capture the structural features. The Brillouin zone is sampled with a minimum of a 5 × 5 × 3 *k*-point mesh and plane wave cutoff of 550 eV. Full structural (atoms and lattice) relaxations are initiated from diffraction data^{24–29} and the forces minimized to a 0.5 meV Å⁻¹ tolerance. We computed the phonon band structure and the mode Grüneisen parameters of each considered system with the aid of the phonopy software.³⁰

3 Results and discussion

We are here interested into the dynamic response of the bulk in the presence of external load. We are going to focus on the atomic motions that affect a global slide of adjacent layers, in order to study the intrinsic friction of the systems. Such motions can be represented by means of linear combinations of vibrational modes, each having an associated vibrational frequency that depends on the atomic species; the lower is the frequency, the easier the sliding motion can be promoted. In terms of the classical picture, we understand this by recalling that the frequency represents the curvature of the system energy hypersurface as a function of the atomic coordinates. At a constant energy of the system, the lower is the frequency of a mode, the higher is the amplitude of the corresponding atomic displacements; if such displacements are associated to layer sliding, higher amplitudes correspond to enhanced shift of one layer with respect to its adjacent ones, hence promoting the sliding of the layers. The study of how the mode frequencies change at different external load and what is the role of electro-vibrational coupling tells us how the bulk contributions to the macroscopic frictional properties are affected; at the same time, we will learn how to tune such contributions, in order to design new TMDs with enhanced frictional response.

We first relax the system geometries and compute the corresponding phonon band structure along a standard³¹ linear

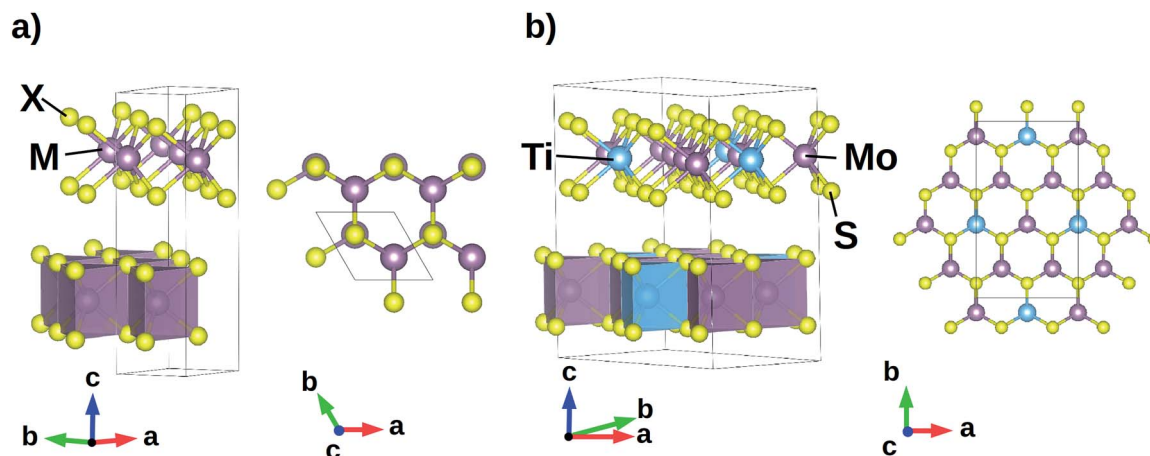


Fig. 1 (a) Hexagonal $P6_3/mmc$ structure of 2H polymorph MX_2 model geometries (M = transition metal, X = chalcogen atom); M–X bonds are arranged in a trigonal prismatic coordination forming MX_2 layers that can slide thanks to weak van der Waals interactions. (b) Orthorhombic Cmc Ti:MoS₂ model system: within each layer, one Ti atom is surrounded by only Mo atoms in the first neighbouring cation shell.

path joining the high-symmetry points of the irreducible Brillouin zone (IBZ); we do not find unstable displacements, confirming that atomic positions are in a stable configuration. We label phonon bands with progressive integer numbers according to standard convention, starting from the lowest associated frequency. In such description, $\Gamma(1)$ represents the vibrational mode relative to the band number 1, that is the displacive mode associated to the lowest frequency $\omega(\Gamma)_1$ at the Γ point of the IBZ; analogously, $\Gamma(2)$ is associated to the vibrational mode with frequency $\omega(\Gamma)_2$ such that $\omega(\Gamma)_3 \geq \omega(\Gamma)_2 \geq \omega(\Gamma)_1$ and so on. We here recall that degeneracy of vibrational modes in MoS system is partially lifted in Ti:MoS model, having the latter a lower number of symmetries. According to the displacement patterns, A(1–4) degenerate modes of MX systems correspond to Z(1–2) and Z(3–4) degenerate modes of Ti:MoS model, respectively, while A(5–6) degenerate modes correspond to Z(5–6) degenerate modes, respectively; however, for brevity, we will still call the Z(1–6) modes as A(1–6), without affecting the clarity of our discussion.

The presence of external load determines a change in the volume of the unit cell. To study how the load affects the mode frequency, we start by computing the mode Grüneisen parameters $\gamma_i(\vec{q})$ for each i -th mode at each point \vec{q} of the selected IBZ path; $\gamma_i(\vec{q})$ is defined as

$$\gamma_i(\vec{q}) = -\frac{V}{\omega_i(\vec{q})} \frac{\partial \omega_i(\vec{q})}{\partial V} \quad (1)$$

and it is a measure of how the frequency ω of the i -th mode at wave vector \vec{q} changes with the volume V of the unit cell. We find that the $\gamma_i(\vec{q})$ amplitudes are highest for $\omega(\Gamma)_{4-6}$ and $\omega(A)_{1-6}$ (Table 1), while all the remaining mode frequencies show $|\gamma_i(\vec{q})| \approx 1$. This means that the modes that are mostly affected by a change of the unit cell volumes are: (i) the degenerate $\Gamma(4-5)$ modes, corresponding to rigid layer sliding in the ab -plane (Fig. 2a), (ii) $\Gamma(6)$, representing a rigid layer shift along the c -axis that changes the interlayer distance (Fig. 2b), (iii) the

degenerate A(1–4) modes, producing layer sliding in the ab -plane accompanied by asymmetric stretching of the X–M–X bond, maintaining constant the interlayer distance (Fig. 2c), (iv) the degenerate A(5–6) modes, corresponding to a change of the interlayer distance and a flattening of the MX_6 polyhedra (Fig. 2d). We will focus our discussion only on the modes that we just described since all the remaining modes are less affected by a change in the unit cell volume, hence preserving the characteristic frequencies in the presence of external load.

We now want to relate the stability of the mode frequency to the chemical composition. We consider the phonon density of states of the relaxed systems and evaluate the cophononicity of the M–X atomic pair (Table 1) in the frequency range $[0, 70] \text{ cm}^{-1}$; we choose such range to be the same for all the systems because the frequencies of the modes we are focusing on fall within such integration range, irrespective of the considered chemical composition. We then relate the M–X pair cophononicity to the mode Grüneisen parameters. We find that, for rigid layer sliding ($\Gamma(4-5)$) or for those modes involving interlayer distance

Table 1 Mode Grüneisen parameters $\gamma_i(\vec{q})$ of the $\omega_{4-5}(\Gamma)$, $\omega_6(\Gamma)$, $\omega_{1-4}(A)$ and $\omega_{5-6}(A)$ mode frequencies, and $C_{\text{ph}}(\text{M-X})$ cophononicity (cm^{-1}) of the M–X atomic pair of the MX and Ti:MoS systems

System	$\gamma_{4-5}(\Gamma)$	$\gamma_6(\Gamma)$	$\gamma_{1-4}(A)$	$\gamma_{5-6}(A)$	$C_{\text{ph}}(\text{M-X})$
MoS	3.7	5.3	2.6	4.9	0.00
MoSe	4.1	5.1	4.4	4.9	−0.39
MoTe	3.0	3.9	3.4	3.7	−0.75
WS	3.9	5.7	3.0	5.6	0.26
WSe	4.1	5.3	3.7	5.2	0.10
WTe	4.9	9.3	4.9	9.2	−0.36
Ti:MoS	5.5	8.7	5.9 ^a	8.3 ^a	−0.17 ^b

^a Z(1–6) modes of Ti:MoS model correspond to A(1–6) modes of MX systems. ^b Global cophononicity of Ti:MoS system calculated as weighted average of the $C_{\text{ph}}(\text{Mo-S})$ and $C_{\text{ph}}(\text{Ti-S})$ cophononicities, with weights corresponding to the M stoichiometric coefficients.

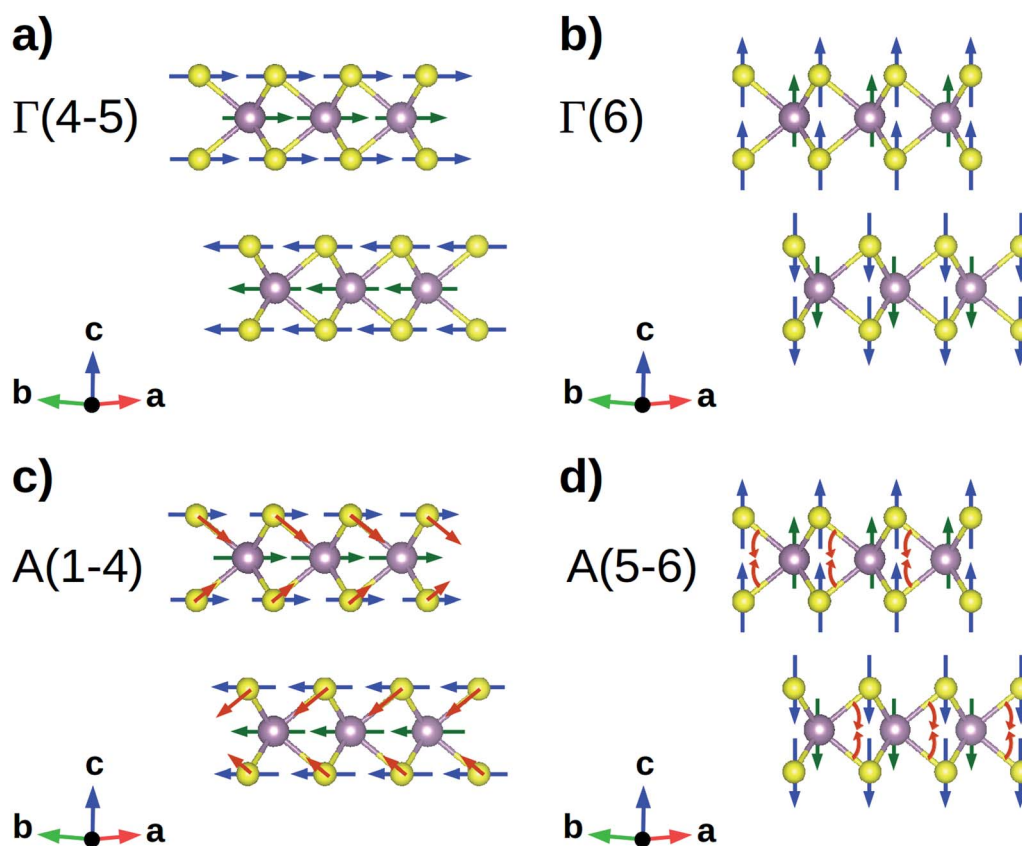


Fig. 2 Schematics of the modes with the highest associated mode Grüneisen parameters: (a) rigid layer sliding in the ab -plane; (b) rigid layer shift along the c -axis producing a variable interlayer distance; (c) layer sliding in the ab -plane and asymmetric stretching of the X–M–X bond; (d) variable interlayer distance accompanied by a flattening of the MX_6 polyhedra. Color code for atoms is the same as in Fig. 1.

variation ($\Gamma(6)$, $A(5-6)$), $\gamma_i(\vec{q})$ is the lowest when the lowest cophonycity is realized (MoTe system); this tells us that such modes are less affected by a change in the unit cell volume if the M and X atoms contributions to the corresponding energy band show the lowest mixing. The $A(1-4)$ modes, instead, turn out to be more stable against volume variations when the M and X atoms equally contribute to the corresponding frequency, hence realizing $C_{\text{ph}}(\text{M-X}) \approx 0$ (MoS system). Based on these results, among the explored chemistries, the dynamic bulk features of the MoTe system are the most stable ones against unit cell volume variations.

The evaluation of the mode Grüneisen parameters is done within the approximation of isotropic variations of the relaxed volume. However, thanks to the presence of interlayer gaps determining the layered structure of the studied TMDs, the X–X distances across the gap can be affected more easily than the intralayer atomic spacing, where stronger atomic bonds make the M–X coordination more rigid. For this reason, in tribological conditions, external load applied along the c -axis affects mainly the interlayer distances, hence producing a non-isotropic change in the unit cell volume. We therefore choose to extend our mode Grüneisen analysis to specific anisotropic variations of the volume, in order to focus on the structural response in the presence of external load. We want to compare the results at particular structure configurations; for this

reason, instead of fixing the value of the load along the c -axis, we will model the presence of load in this way: starting from the relaxed structures, we will build new model systems by rigidly shifting two subsequent MX_2 layers to vary the interlayer distance d_0 ; calling δ_{IL} the difference $d - d_0$, where d is the distance after the rigid shift, we build 6 model geometries for each of the considered system by setting $\delta_{\text{IL}} = \pm 0.5, \pm 1.0$ and ± 1.5 Å, respectively. With this choice, a negative value of δ_{IL} represents a compression along the c -axis, which is typical for sliding of perfect crystal or TMD 2D sheets. However, topographic features can locally cause decrease in contact pressure to zero (*i.e.* $\delta_{\text{IL}} = 0$) or even separate two layers at the sliding interface (Fig. 3a). Such scenario occurs when TMD sheets are bended during sliding, as illustrated in Fig. 3b. It is worthy to note here that, in our simulations, $\delta_{\text{IL}} = -1.5$ Å correspond to an external pressure greater than 80 GPa for all the considered chemistries. We are aware that an isostructural phase transition from $2H_c$ to $2H_a$ polytype is observed for MoS_2 between 20 and 29 GPa;^{32–34} on the other hand, experiments performed in the presence of high pressure have been reported only for few of the considered systems other than MoS_2 , and no phase transitions have been found for them nor are expected.^{35,36} For this reason, to make a complete comparison at different δ_{IL} among the calculated quantities of all the systems, we do not consider the MoS_2 phase transition at high pressure.

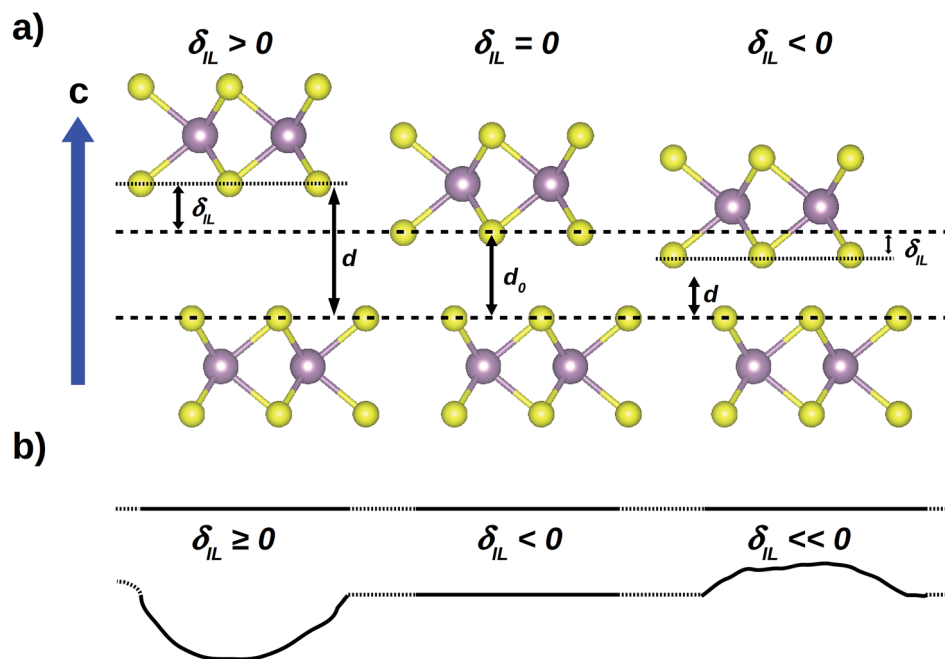


Fig. 3 (a) The presence of external load is modeled starting from the relaxed structure and changing the optimized interlayer distance d_0 to a new value d by shifting one layer of a quantity equal to δ_{IL} along the c -axis. (b) On a larger scale, positive and negative δ_{IL} values represent deviations from the parallel layer ideal configuration, due to the presence of topographic defects.

We then analyze the variation of $\omega(\Gamma)_{4-6}$ and $\omega(A)_{1-6}$ with δ_{IL} (Fig. 4). Irrespective of the atomic types, increasing the interlayer distance ($\delta_{IL} > 0$) reduces the vibrational frequencies, tending to similar asymptotic values. This is an expected result because the displacement patterns of the considered modes involve interlayer interactions that depend on the specific atomic type; at high δ_{IL} values, such interactions tend to vanish and the relative position of the layers does not affect the intralayer atomic motions. On the other hand, negative δ_{IL} values increase ω , reducing the population of the corresponding modes at fixed system energy, hence disfavoring the corresponding displacement patterns, with exceptions at $\delta_{IL} = -1.5$ Å, where some instabilities arise. The origin of such exceptions could be sought in the peculiar accommodation of the electronic cloud due to the highly reduced interlayer distance; this requires a more detailed study of the electro-structural coupling, but is out of the scope of the present work. Specifically, we find that decreasing the interlayer distance d reduces the population of: (i) the sliding modes $\Gamma(4-5)$ and $A(1-4)$, reducing the bulk contribution to the layer sliding; (ii) the modes that change the interlayer distance d , making the bulk less prone to a further compression along the c -axis.

To understand how the vibrational frequencies variation is coupled to the electronic structure, we now focus on the electronic density distribution. We start by evaluating the evolution of the atomic charge with δ_{IL} using two approaches: Bader analysis,³⁷ based on zero flux surfaces, and integration of the atom-site projected electronic density of states up to the Fermi level. Comparing the two methods helps us to address the ambiguity in assigning charges to atoms. Interestingly, both methods point at same conclusions. No charge variation is

found for Ti atom in the entire δ_{IL} range; indeed, irrespective of the composition, at decreasing δ_{IL} , we observe an increase of the Mo or W atomic charge at the expenses of the X anion, indicative of charge transfer from X to M ion. To better understand how the electronic charge is rearranged after variations of the interlayer distance, we measure the orbital polarization^{38,39} of the X and M atomic species as a function of δ_{IL} . Let's recall here that the orbital polarization \mathcal{P} of m_{l_1} orbital relative to m_{l_2} orbital is defined as

$$\mathcal{P}_{l_1 m_{l_1}, l_2 m_{l_2}} = \frac{n_{l_1 m_{l_1}} - n_{l_2 m_{l_2}}}{n_{l_1 m_{l_1}} + n_{l_2 m_{l_2}}}, \quad (2)$$

where $n_{l_1 m_{l_1}}$ and $n_{l_2 m_{l_2}}$ are the occupancies of $|l_1 m_{l_1}\rangle$ and $|l_2 m_{l_2}\rangle$ orbitals, with orbital quantum number l_i and magnetic quantum number m_{l_i} , respectively. It is an effective measure of the charge excess in the former orbital with respect to the latter: positive values indicate that m_{l_1} orbital is more populated than m_{l_2} , while opposite holds for negative values. Using real-space atomic orbital projections, it is possible to partition the electronic density into distinct atomic and interatomic regions, so as to isolate the single contributions hence identifying the electron transfer path. In detail, for each studied system, we calculate $\mathcal{P}_{p_x-p_y}$, $\mathcal{P}_{p_x-p_z}$ and $\mathcal{P}_{p_y-p_z}$ of the X atom, $\mathcal{P}_{t_{2g}-e_g}$ and $\mathcal{P}_{d_{x^2-y^2}-d_{z^2}}$ of Mo and W cations, \mathcal{P}_{d-s} and \mathcal{P}_{d-p} of the Ti atom in the Ti:MoS model. Irrespective of the chemical composition, positive values of δ_{IL} do not affect any orbital population in a significant way; moreover, orbital polarization of the Ti atom are nearly constant within the considered δ_{IL} range, their average values $\mathcal{P}_{d-s} = 85.1\%$ and $\mathcal{P}_{d-p} = 77.2\%$ changing about 1%. Increasing the load ($\delta_{IL} < 0$), we observe that: (i) X p_x and p_y population are almost unvaried while p_z orbital population

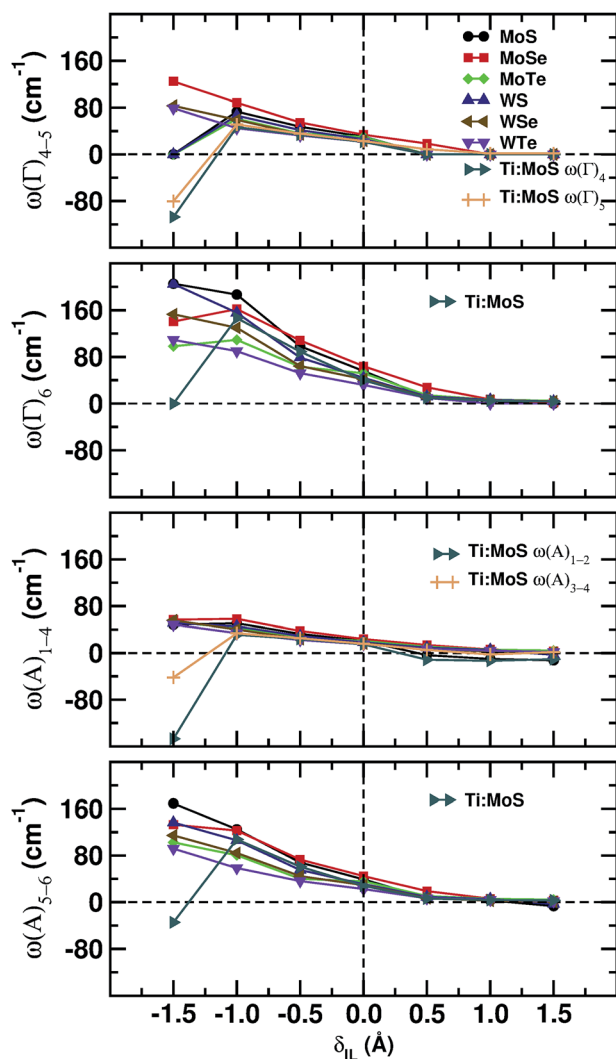


Fig. 4 Frequencies of $\Gamma(4-6)$ and $A(1-6)$ modes as a function of the interlayer distance variation δ_{IL} . Irrespective of the M and X atomic types, increasing the interlayer distance lowers the vibrational frequencies, while increasing the load is expected to disfavor sliding, with exceptions at $\delta_{\text{IL}} = -1.5$ Å.

decreases (Fig. 5a–c), (ii) M e_g orbital population increases (Fig. 5d) and (iii) M d_{z^2} population increases at the expenses of $d_{x^2-z^2}$ (Fig. 5e). This indicates that reducing the interlayer distance induces flow of charge from the interlayer region, described by the p_z orbitals, towards the intralayer region. Charge tends to accumulate on each M atom, in particular along an axis orthogonal to the plane containing the M atoms belonging to the same MX_2 layer (Fig. 6). We can then conclude that interactions among layers are mediated by the p_z orbitals of X anions belonging to two adjacent layers and facing the same interlayer region. Finally, we can argue that the charge distribution in the inner part of each layer can be controlled by proper perturbations of the electronic density at the surface of the layer.

Orbital polarization is a fine partition of the electronic density, providing a real-space picture of the charge

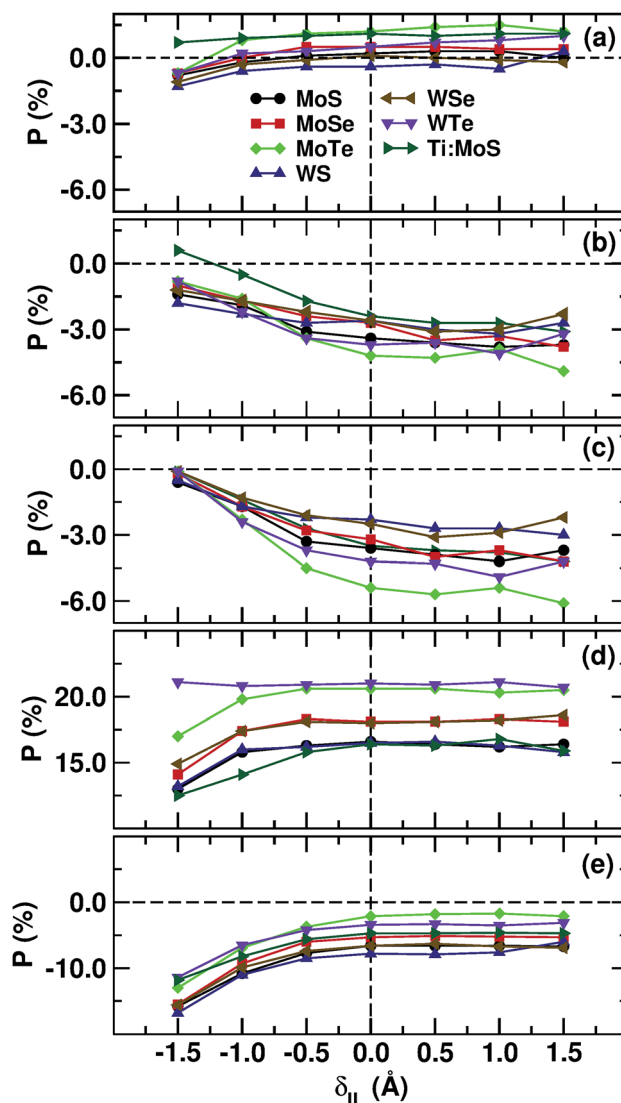


Fig. 5 Orbital polarization of MX and Ti:MoS systems as a function of δ_{IL} : (a) $X P_{p_x-p_y}$, (b) $X P_{p_x-p_z}$, (c) $X P_{p_y-p_z}$, (d) $M P_{t_{2g}-e_g}$, (e) $M P_{d_{z^2}-d_{x^2-z^2}}$; M = Mo for the data relative to the Ti:MoS system in panels (d) and (e). Reducing the interlayer distance induces charge accumulation towards the intralayer region, along an axis orthogonal to the plane containing the M atoms belonging to the same MX_2 layer.

redistribution after alteration of the system geometry in the presence of external load. However, to understand how the redistribution of the electronic charge affects the atomic motions (electro-vibrational coupling), we need to recollect the fragmented information provided by the orbital polarization into a simple electronic descriptor. To this aim, we now analyse the $C_{\text{M,X}}$ M–X bond covalency at each of the considered δ_{IL} values, making use of the bond covalency metric that has already been defined by means of atomic orbital contributions to the electronic density of states.⁴⁰ M–X bond covalency is determined by the cooperative effect of the electronic structure of the M and X atoms and the structural distortions of the system, as it has already been observed in a theoretical study on perovskite oxides,⁴⁰ optically active telluro-molybdates⁴¹ and

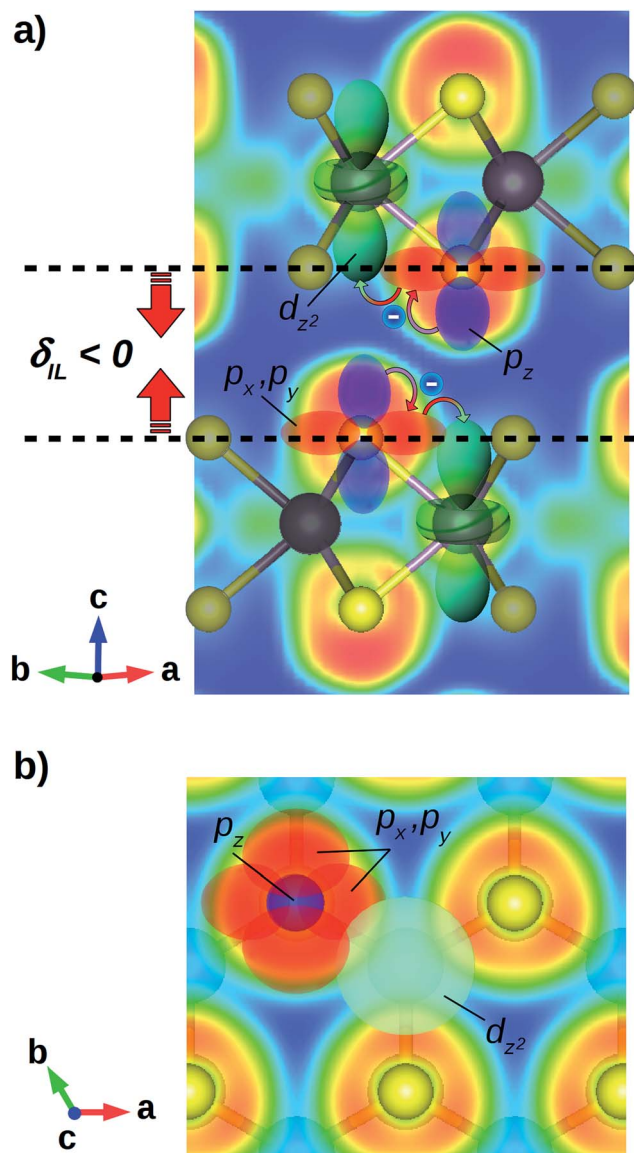


Fig. 6 Schematic representations of the charge density and the inter-to-intralayer charge flow mechanism: RGB gradient indicates decreasing charge density (red = highest, blue = lowest) while shaded atoms and bonds are out of the sections showing the charge distribution. Color code for atoms is the same as in Fig. 1; the generic M cation here represents Mo or W atom, since no variation of the orbital polarization of Ti atom has been observed in the Ti:MoS system. (a) Electronic density on a plane parallel to the c -axis and containing two X–M–X bonds, each belonging to two subsequent MX₂ layers. Upon interlayer distance reduction, charge flows from the inter- to the intralayer region, thanks to electron transfer from X p_z orbital to M e_g orbital via an intermediate step involving the p_x and p_y orbitals of the X atom; charge thus accumulates onto an axis containing the M cation and orthogonal to the layers. (b) Electronic charge distribution on a plane orthogonal to the c axis and containing the X anions facing the same interlayer region. The hybridization of the d_{z^2} orbital of the M cation with the p_x and p_y orbitals of the X atom allows the X \rightarrow M charge transfer.

tribologic TMD materials.¹¹ We evaluate $C_{M,X}$ as a function of δ_{IL} by considering the energy range $[-10.0, 0.0]$ eV, corresponding to the electronic valence band, where the Fermi level has been

set to 0.0 eV (Fig. 7a). In the first instance, we note that, for $\delta \geq 0.0$ Å, M–X bond covalency can be considered as constant; this result is difficult to extrapolate from the orbital polarizations due to the fluctuations found in the same δ_{IL} range (Fig. 5), and shows how the covalency metric $C_{M,X}$ acts as a collective descriptor of the details of the electronic structure. As we already observed about the mode frequencies, the constant trend of $C_{M,X}$ for $\delta > 0$ can be explained considering that at high interlayer distances only intralayer interactions are relevant, and they are the only ones that determine the electronic distribution. On the other hand, irrespective of the chemical composition, we find that M–X covalency is monotonically decreasing with increasing load. We understand this in this way: the charge accumulation in the intralayer region increases the electronic repulsion due to the Pauli's exclusion principle, inducing a localization of the electronic charge onto the M cation, making the M–X bond more ionic. Such charge localization, and the consequent reduction of M–X bond covalency, is responsible of the hardening of the $\Gamma(4-6)$ and A(1-6) modes; this means that the less covalent the M–X bond is, the less favorable the bulk contribution is to the layer shift along the c -axis ($\Gamma(6)$ and A(5-6) modes) and to the layer sliding ($\Gamma(4-5)$ and A(1-4) modes). This last aspect suggests that, at increasing load,

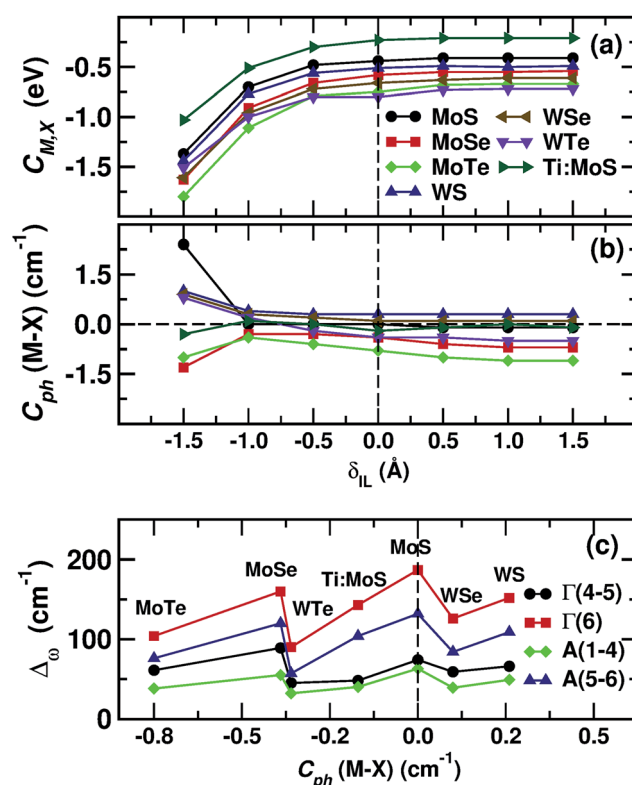


Fig. 7 (a) M–X bond covalency and (b) M–X pair cophonicity as a function of the interlayer distance variation δ_{IL} ; covalency is found to be a monotonic function of δ_{IL} while cophonicity is nearly constant for $\delta_{IL} \geq -1.0$ Å. (c) Amplitude of the variation interval of $\Gamma(4-6)$ and A(1-6) mode frequencies as a function of $C_{ph}(M-X)$; $C_{ph}(M-X)$ values here used are those calculated at $\delta_{IL} = 0.0$ Å. The smallest variation interval of the considered frequencies is realized at $C_{ph}(M-X) = -0.36$ cm⁻¹, corresponding to the WTe system.

the macroscopic friction coefficient is expected to increase; exceptions are found for those systems with instabilities at $\delta_{\text{IL}} = -1.5 \text{ \AA}$, which, at very high loads, are expected to show improved frictional properties.

So far we have shown that the frequencies of those modes that are mainly affected by a change in the unit cell volume, *e.g.* $\Gamma(4-6)$ and $A(1-6)$ modes, generally increase at increasing external load ($\delta_{\text{IL}} < 0$); we found some exceptions that are expected to have bulk contributions favoring the layer sliding at high load ($\delta_{\text{IL}} = -1.5 \text{ \AA}$). We explained the hardening of the modes in terms of localization of the electronic density on the M cation and a consequent reduced M–X bond covalency; the latter turned out to be a convenient descriptor to understand the origin of the vibrational behavior of the system in the presence of external load. To further disentangle the atomic contributions to the vibrational response, we now calculate the M–X pair cophonycity at the considered δ_{IL} values, in order to understand how the relative M/X atomic contribution to the vibrational bands is affected by the interlayer distance (Fig. 7b). Interestingly, we find an abrupt variation of $C_{\text{ph}}(\text{M-X})$ at $\delta_{\text{IL}} = -1.5 \text{ \AA}$, supporting the idea that significant electro-structural coupling effects arise at high load; on the other hand, irrespective of the atomic types, $C_{\text{ph}}(\text{M-X})$ can be considered constant for $\delta_{\text{IL}} \geq -1.0 \text{ \AA}$. This last result tells us that once the chemical composition and the M–X connectivity are fixed, M–X pair cophonycity is a feature of the MX and Ti:MoS systems, that is preserved if the external load is not extremely high. We can therefore use the M–X cophonycity calculated at zero load to characterize the system and its response under load.

The variability of the structural response can be quantified in terms of the amplitude of the interval within which each mode frequency changes: the higher is such amplitude, the higher is the variation of a specific frequency with the external load. We define the variation amplitude $\Delta_{\omega}(\vec{q})$ of the frequency ω associated to the \vec{q} point of the IBZ as

$$\Delta_{\omega}(\vec{q}) = \max_{\omega} [\omega(\vec{q})] - \min_{\omega} [\omega(\vec{q})] \quad (3)$$

where $\max_{\omega}[\omega(\vec{q})]$ and $\min_{\omega}[\omega(\vec{q})]$ are the highest and the lowest frequency ω at fixed \vec{q} point of the IBZ. The smaller $\Delta_{\omega}(\vec{q})$ is, the smaller the variation amplitude of the vibrational frequency is; a system with small $\Delta_{\omega}(\vec{q})$ shows bulk properties that are less affected by the external load. We calculate Δ_{ω} for the $\Gamma(4-5)$, $\Gamma(6)$, $A(1-4)$ and $A(5-6)$ modes, respectively. The variability of the structural response is strictly connected to the chemical composition; we then connect the frequency variation amplitude to the M–X cophonycity by evaluating Δ_{ω} for $\delta \in [-1.0, 1.5] \text{ \AA}$, where $C_{\text{ph}}(\text{M-X})$ can be considered constant. We find that, irrespective of the mode, the minimum Δ_{ω} is realized at $C_{\text{ph}}(\text{M-X}) = -0.36 \text{ cm}^{-1}$, corresponding to the WTe system (Fig. 7b). Moreover, concerning the $\Gamma(4-5)$ and $A(1-4)$ sliding modes, Ti:MoS system shows a small Δ_{ω} value similarly to WTe. These outcomes suggest that, in the presence of external load, the Ti:MoS and WTe bulk contributions to the sliding are expected to be the least affected among the studied systems. We here note that in our previous study on MX_2 TMDs,¹¹ we already discussed how, in absence of load, the Ti:MoS bulk contribution

to the macroscopic friction is expected to be the same as that of WTe compound.

We want to know how to tune Δ_{ω} in order to determine how prone the material is to change its response under load; to this aim, we prefer to rely on properties that are characteristic of the system with no load, in order to reduce the number of parameters to consider to build our models. We showed how the variation of the frequencies, those associated to the modes mostly affected by unit cell volume changes, is due to charge flow between the interlayer and intralayer region, induced by variations of the interlayer distance; such charge redistribution affects the M–X bond covalency, being thus a function variable with the load. On the other hand, we observed that $C_{\text{ph}}(\text{M-X})$ can be considered as constant in almost all the explored δ_{IL}

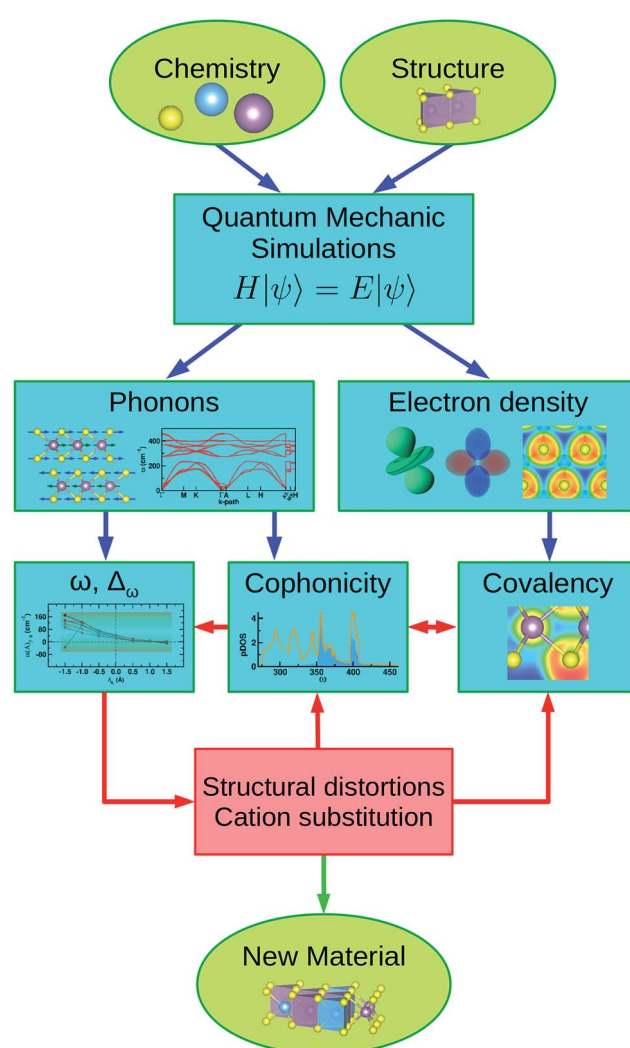


Fig. 8 Schematic diagram showing the investigation protocol applied in this work. *Ab initio* simulations are employed to calculate the electronic and dynamic properties of the selected system; cophonycity and covalency determine the vibrational frequencies and their variation against variable load. By proper cation substitutions and/or induced structural distortions it is possible to tune the electro-dynamic coupling, producing a new material with enhanced tribologic properties.

range; we can thus exploit this fact to use the cophononicity of the system to control the phonon frequencies variation amplitude $\Delta\omega$. M–X pair cophononicity is a measure of the M/X relative contribution to a selected frequency interval; it depends on the M and X atomic masses, the geometry of the system and the electronic density distribution, thus the M–X bond covalency, this latter determined in turn by both atomic types and the geometry of the system. This easily shows how cophononicity captures several entangled properties into one unique descriptor and what are the parameters that can be adjusted to finely tune the cophononicity value. For example, structural distortions can be induced by selective cation substitution, inducing in turn variations to covalency, hence to cophononicity (for a complete discussion see ref. 11). Moreover, the electronic distribution, hence the cophononicity, can be tuned by external electric fields, as is the case of particular applications of TMDs in which they are used to reduce friction between electrically conducting contacts in motion. In this last respect, the protocol detailed in this work will be beneficial for future studies on how to engineer the electronic distribution so as to tune the electronic gap in TMDs to favor the electric conductivity. In future works, we will discuss how to selectively tune the charge transfer for optimal frictional properties; nevertheless, the related outcomes will outline a general approach that can be promptly extended to broad classes of materials with diverse applications other than tribology.

4 Conclusions

In the present work, we study the electronic and vibrational contributions to the intrinsic friction of MX_2 transition metal dichalcogenides by applying the investigation protocol outlined in Fig. 8.

We first analyze the distortion patterns to characterize the phonon modes calculated in the IBZ; we then compute the mode Grüneisen parameters to isolate those modes that are mainly affected by a change in the unit cell volume and studied how the associated vibrational frequencies change by changing the interlayer distance.

We individuate the electronic origin of the frequency shift by analyzing the electronic charge distribution about the atomic species at different interlayer distances. We find that compressing the system along an axis orthogonal to parallel layers induce charge flow from the interlayer to the intralayer region. Specifically, we observe that the M cation accommodates the excess of electronic charge *via* a change in the e_g orbital population; this corresponds to charge accumulation along an axis orthogonal to the layer and containing the M cation.

The fragmented information provided by the orbital polarization analysis is recollected by means of the covalency descriptor. The M–X bond becomes more ionic after charge accumulation on the M cation, while it preserves its covalent character at increased interlayer distance. Covalency is thus varying with variable load; on the other hand, we find that the M–X pair cophononicity can be considered constant in a wide load range. We therefore choose the cophononicity, calculated at null load, to characterize the system and its response.

We then parameterize the variability of the structural response by quantifying the variation amplitude of the frequency modes and we relate it to the cophononicity. We find that, irrespective of the mode, small variation amplitude values associated to the sliding modes are realized for WTe and Ti:MoS systems, that are thus expected to be the least affected systems among those here studied.

The variation amplitude can be adjusted by controlling the M–X pair cophononicity; the latter, in turn, can be tuned by selective cation substitution inducing variations of the covalency and the structural distortions, or by external applied fields.

The investigation protocol used in the present work can also be applied to the study of the electron–vibrational coupling effects in electronic materials, as alternative to standard methodologies.^{42–45}

5 Acknowledgements

This work has been done with the support of inter-sectoral mobility and quality enhancement of research teams at Czech Technical University in Prague, CZ.1.07/2.3.00/30.0034. This work was supported by the IT4Innovations Centre of Excellence project (CZ.1.05/1.1.00/02.0070), funded by the European Regional Development Fund and the national budget of the Czech Republic *via* the Research and Development for Innovations Operational Programme, as well as Czech Ministry of Education, Youth and Sports *via* the project Large Research, Development and Innovations Infrastructures (LM2011033). The use of vesta⁴⁶ software is also acknowledged.

References

- 1 M. Chhowalla, H. S. Shin, G. Eda, L.-J. Li, K. P. Loh and H. Zhang, *Nat. Chem.*, 2013, 5, 263–275.
- 2 Q. H. Wang, K. Kalantar-Zadeh, A. Kis, J. N. Coleman and M. S. Strano, *Nat. Nanotechnol.*, 2012, 7, 699–712.
- 3 Z. Yin, H. Li, H. Li, L. Jiang, Y. Shi, Y. Sun, G. Lu, Q. Zhang, X. Chen and H. Zhang, *ACS Nano*, 2012, 6, 74–80.
- 4 K. F. Mak, C. Lee, J. Hone, J. Shan and T. F. Heinz, *Phys. Rev. Lett.*, 2010, 105, 136805.
- 5 S. Cahangirov, C. Ataca, M. Topsakal, H. Sahin and S. Ciraci, *Phys. Rev. Lett.*, 2012, 108, 126103.
- 6 T. Onodera, Y. Morita, A. Suzuki, M. Koyama, H. Tsuboi, N. Hatakeyama, A. Endou, H. Takaba, M. Kubo, F. Dassenoy, C. Minfray, L. Joly-Pottuz, J.-M. Martin and A. Miyamoto, *J. Phys. Chem. B*, 2009, 113, 16526–16536.
- 7 T. Onodera, Y. Morita, R. Nagumo, R. Miura, A. Suzuki, H. Tsuboi, N. Hatakeyama, A. Endou, H. Takaba, F. Dassenoy, C. Minfray, L. Joly-Pottuz, M. Kubo, J.-M. Martin and A. Miyamoto, *J. Phys. Chem. B*, 2010, 114, 15832.
- 8 T. Liang, W. G. Sawyer, S. S. Perry, S. B. Sinnott and S. R. Phillpot, *Phys. Rev. B: Condens. Matter Mater. Phys.*, 2008, 77, 104105.
- 9 Y. Morita, T. Onodera, A. Suzuki, R. Sahnoun, M. Koyama, H. Tsuboi, N. Hatakeyama, A. Endou, H. Takaba, M. Kubo,

- C. A. D. Carpio, T. Shin-yoshi, N. Nishino, A. Suzuki and A. Miyamoto, *Appl. Surf. Sci.*, 2008, **254**, 7618–7621.
- 10 G. Levita, A. Cavaleiro, E. Molinari, T. Polcar and M. C. Righi, *J. Phys. Chem. C*, 2014, **118**, 13809–13816.
- 11 A. Cammarata and T. Polcar, *Inorg. Chem.*, 2015, **54**, 5739–5744.
- 12 M. R. Laskar, D. N. Nath, L. Ma, E. W. Lee, C. H. Lee, T. Kent, Z. Yang, R. Mishra, M. A. Roldan, J.-C. Idrobo, S. T. Pantelides, S. J. Pennycook, R. C. Myers, Y. Wu and S. Rajan, *Appl. Phys. Lett.*, 2014, **104**, 092104.
- 13 D. J. Lewis, A. A. Tedstone, X. L. Zhong, E. A. Lewis, A. Rooney, N. Savjani, J. R. Brent, S. J. Haigh, M. G. Burke, C. A. Muryn, J. M. Raftery, C. Warrens, K. West, S. Gaemers and P. O’Brien, *Chem. Mater.*, 2015, **27**, 1367–1374.
- 14 K. Zhang, S. Feng, J. Wang, A. Azcatl, N. Lu, R. Addou, N. Wang, C. Zhou, J. Lerach, V. Bojan, M. J. Kim, L.-Q. Chen, R. M. Wallace, M. Terrones, J. Zhu and J. A. Robinson, *Nano Lett.*, 2015, **15**(10), 6586–6591.
- 15 (a) D. Teer, *Wear*, 2001, **251**, 1068–1074; (b) N. Renevier, V. Fox, D. Teer and J. Hampshire, *Surf. Coat. Technol.*, 2000, **127**, 24–37; (c) N. Renevier, J. Hampshire, V. Fox, J. Witts, T. Allen and D. Teer, *Surf. Coat. Technol.*, 2001, **142**–**144**, 67–77.
- 16 C. Rice, R. J. Young, R. Zan, U. Bangert, D. Wolverson, T. Georgiou, R. Jalil and K. S. Novoselov, *Phys. Rev. B: Condens. Matter Mater. Phys.*, 2013, **87**, 081307.
- 17 X. Zhang, X.-F. Qiao, W. Shi, J.-B. Wu, D.-S. Jiang and P.-H. Tan, *Chem. Soc. Rev.*, 2015, **44**, 2757–2785.
- 18 H. Sahin, S. Tongay, S. Horzum, W. Fan, J. Zhou, J. Li, J. Wu and F. M. Peeters, *Phys. Rev. B: Condens. Matter Mater. Phys.*, 2013, **87**, 165409.
- 19 J. P. Oviedo, S. KC, N. Lu, J. Wang, K. Cho, R. M. Wallace and M. J. Kim, *ACS Nano*, 2015, **9**, 1543–1551.
- 20 J. P. Perdew, K. Burke and M. Ernzerhof, *Phys. Rev. Lett.*, 1996, **77**, 3865–3868.
- 21 (a) G. Kresse and J. Furthmüller, *Comput. Mater. Sci.*, 1996, **6**, 15–50; (b) G. Kresse and D. Joubert, *Phys. Rev. B: Condens. Matter Mater. Phys.*, 1999, **59**, 1758–1775.
- 22 A. K. Geim and I. V. Grigorieva, *Nature*, 2013, **499**, 419–425.
- 23 S. Grimme, *J. Comput. Chem.*, 2006, **27**, 1787–1799.
- 24 B. Schönfeld, J. J. Huang and S. C. Moss, *Acta Crystallogr., Sect. B: Struct. Sci.*, 1983, **39**, 404–407.
- 25 V. Kalikhman, *Inorg. Mater.*, 1983, **19**, 957–962.
- 26 L. Brixner, *J. Inorg. Nucl. Chem.*, 1962, **24**, 257–263.
- 27 W. Schutte, J. D. Boer and F. Jellinek, *J. Solid State Chem.*, 1987, **70**, 207–209.
- 28 V. L. Kalikhman, *Neorg. Mater.*, 1983, **19**, 1060–1065.
- 29 A. A. Yanaki and V. A. Obolonchik, *Inorg. Mater.*, 1973, **9**, 1855–1858.
- 30 A. Togo, F. Oba and I. Tanaka, *Phys. Rev. B: Condens. Matter Mater. Phys.*, 2008, **78**, 134106.
- 31 W. Setyawan and S. Curtarolo, *Comput. Mater. Sci.*, 2010, **49**, 299–312.
- 32 R. Aksoy, Y. Ma, E. Selvi, M. C. Chyu, A. Ertas and A. White, *J. Phys. Chem. Solids*, 2006, **67**, 1914–1917.
- 33 Z.-H. Chi, X.-M. Zhao, H. Zhang, A. F. Goncharov, S. S. Lobanov, T. Kagayama, M. Sakata and X.-J. Chen, *Phys. Rev. Lett.*, 2014, **113**, 036802.
- 34 T. Livneh and E. Sterer, *Phys. Rev. B: Condens. Matter Mater. Phys.*, 2010, **81**, 195209.
- 35 A. P. Nayak, Z. Yuan, B. Cao, J. Liu, J. Wu, S. T. Moran, T. Li, D. Akinwande, C. Jin and J.-F. Lin, *ACS Nano*, 2015, **9**(9), 9117–9123.
- 36 Z. Zhao, H. Zhang, H. Yuan, S. Wang, Y. Lin, Q. Zeng, G. Xu, Z. Liu, G. K. Solanki, K. D. Patel, Y. Cui, H. Y. Hwang and W. L. Mao, *Nat. Commun.*, 2015, **6**, 7312.
- 37 (a) R. F. V. Bader, *Atoms in Molecules: a Quantum Theory*, Oxford University Press, New York, 1990; (b) W. Tang, E. Sanville and G. Henkelman, *J. Phys.: Condens. Matter*, 2009, **21**, 084204.
- 38 A. Cammarata and J. M. Rondinelli, *Phys. Rev. B: Condens. Matter Mater. Phys.*, 2013, **87**, 155135.
- 39 M. J. Han, C. A. Marianetti and A. J. Millis, *Phys. Rev. B: Condens. Matter Mater. Phys.*, 2010, **82**, 134408.
- 40 A. Cammarata and J. M. Rondinelli, *J. Chem. Phys.*, 2014, **141**, 114704.
- 41 A. Cammarata, W. Zhang, P. S. Halasyamani and J. M. Rondinelli, *Chem. Mater.*, 2014, **26**, 5773–5781.
- 42 C. Attaccalite, L. Wirtz, M. Lazzeri, F. Mauri and A. Rubio, *Nano Lett.*, 2010, **10**, 1172–1176.
- 43 F. Flicker and J. van Wezel, *Nat. Commun.*, 2015, **6**, 7034.
- 44 N. Zarifi, H. Liu and J. S. Tse, *Sci. Rep.*, 2015, **5**, 10458.
- 45 C. Chen, Z. Xie, Y. Feng, H. Yi, A. Liang, S. He, D. Mou, J. He, Y. Peng, X. Liu, Y. Liu, L. Zhao, G. Liu, X. Dong, J. Zhang, L. Yu, X. Wang, Q. Peng, Z. Wang, S. Zhang, F. Yang, C. Chen, Z. Xu and X. J. Zhou, *Sci. Rep.*, 2013, **2**, 2411.
- 46 K. Momma and F. Izumi, *J. Appl. Crystallogr.*, 2008, **41**, 653–658.



Cite this: *Nanoscale*, 2017, **9**, 11488

Vibrational contributions to intrinsic friction in charged transition metal dichalcogenides

Antonio Cammarata * and Tomas Polcar 

Vibrational contributions to intrinsic friction in layered transition metal dichalcogenides (TMDs) have been studied at different charge contents. We find that any deviation from charge neutrality produces complex rearrangements of atomic positions and electronic distributions, and consequent phase transitions. Upon charge injection, cell volume expansion is observed, due to charge accumulation along an axis orthogonal to the layer planes. Such accumulation is accounted for by the $d_{3z^2-r^2}$ orbital of the transition metal and it is regulated by the \mathcal{P}_{t_{2g},e_g} orbital polarization. The latter, in turn, determines the frequency of the phonon modes related to the intrinsic friction through non-trivial electro-vibrational coupling. The bond covalency and atom pair cophononicity can be exploited as a knob to control such coupling, ruling subtle charge flows through atomic orbitals hence determining vibrational frequencies at a specific charge content. The results can be exploited to finely tune vibrational contributions to intrinsic friction in TMD structures, in order to facilitate assembly and operation of nanoelectromechanical systems and, ultimately, to govern electronic charge distribution in TMD-based devices for applications beyond nanoscale tribology.

Received 6th June 2017,

Accepted 7th July 2017

DOI: 10.1039/c7nr04034b

rsc.li/nanoscale

Introduction

Layered transition metal dichalcogenides (TMDs) attract great technological attention owing to their highly versatile stoichiometry and their close features to graphene. Production of advanced TMD-based nanostructured materials mainly relies on the comprehension of local frictional forces. Lubricants are able to reduce friction at the macroscopic scale, but assembly and functionality of micro- or nanoelectromechanical systems (NEMSs) require a deep knowledge of the mechanisms governing friction at the atomic scale. The fundamental processes at the basis of macroscopic friction have been a subject of theoretical and experimental interest in tribology for a long time.^{1,2} Several attempts to model friction have been made so far,³ and only a few theoretical studies took into account the explicit atomic structure of the tribological contacts;^{4–10} a deep investigation of the electron–phonon coupling effects on the intrinsic frictional properties is, however, still required. We call intrinsic friction the friction generated by the relative motion of a few subsequent atom layers in the absence of structural imperfections (dislocations, layer truncations *etc.*); it then originates from the atomic type and the geometric arrangement of the atoms forming a pristine compound, together with the result-

ing electronic features. Under tribological conditions, non-null net charges can arise^{11–14} and redistribute in the neighbourhood of the volume where they originated; this corresponds to a charge injection across several layers, and to a perturbation of their charge neutrality. Such perturbation influences the intrinsic frictional properties, the latter being highly relevant in the micromanipulation of free-standing atomic layers,¹⁵ hence in the final design of TMD-based nanostructured materials. Charges may be free to move through the material or may localize in the local environment of specific atomic sites. As a consequence, attractive or repulsive Coulombic forces may arise, either hindering or facilitating relative layer gliding, depending on several factors such as sliding velocity, temperature and atomic types forming the structure. However, these latter aspects are out of the scope of the present study and will be investigated in future studies.

In the present manuscript, we will focus on how the presence of non-null charge affects the frequency of the phonon modes which are relevant to the layer sliding phenomenon. The lower the frequency of such modes, the easier the sliding motion, the lower their contribution to the intrinsic friction. This can be understood in terms of the classical picture. At a constant energy of the system, the lower the frequency of a mode, the higher the amplitude of the corresponding atomic displacements; ample displacements, corresponding to relative layer shifts, promote layer sliding. Our goal is to understand which electronic and structural features determine the frequency of such modes and how the presence of non-null

Department of Control Engineering, Czech Technical University in Prague, Technicka 2, 16627 Prague 6, Czech Republic. E-mail: cammaat@fel.cvut.cz; Fax: +420 224 91 8646; Tel: +420 224 35 7598

charge influences them; at the same time, we want to learn how to tune such features, in order to find guidance to design new TMDs with an enhanced intrinsic frictional response.

We will show that there is no trivial relationship between the net charge of the system and the mode frequencies of the latter; however, by exploiting electronic and structural descriptors, we are able to identify guidelines to control subtle features of the electronic density, hence the frequency of the sliding-related phonon modes.

Computational details

Transition metal dichalcogenides have a layered structure with the general stoichiometry MX_2 , where M is a transition metal and X is a chalcogen. Each MX_2 layer is formed by hexagonally packed metal atoms coordinating six chalcogen anions in a trigonal prismatic fashion (Fig. 1); adjacent layers are bound by weak van der Waals forces which allow relative sliding under tribological conditions. Among the several stable TMD polymorphs and polytypes that are found,¹⁶ we consider $2 \times 2 \times 2$ supercells of the 2H polymorph crystalline MX_2 compounds as reference structures, with M = Mo, W and X = S, Se, Te, and hexagonal $P6_3/mmc$ symmetry (SG 194); for simplicity, we will refer to them as MX by dropping the stoichiometric coefficients. The 2H configuration consists of two adjacent layers arranged in such a way that a metal atom of one layer is aligned with two anions of the other one along the direction orthogonal to each layer (c -axis in our setting—see Fig. 1).

We perform density functional theory (DFT) calculations using the projector-augmented wave (PAW) formalism and the Perdew–Burke–Ernzerhof (PBE) energy functional¹⁷ as implemented in VASP.¹⁸ We also take into account van der Waals interactions using the Grimme correction,¹⁹ which is able to reproduce the structural features, as we reported in previous studies and references therein.^{20–22} The Brillouin zone is

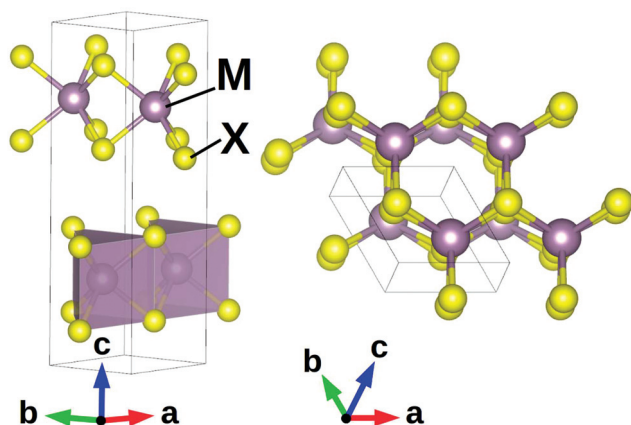


Fig. 1 Model structure of the hexagonal $P6_3/mmc$ 2H polymorph of the MX_2 TMD crystal. M–X bonds form trigonal prisms arranged in parallel layers which can reciprocally slide due to weak van der Waals interactions.

sampled with a minimum of a $5 \times 5 \times 3$ k -point mesh and a plane wave cutoff of 550 eV. We consider neutral as well as charged systems, with charges $q = 0, \pm 0.01, \pm 0.03, \pm 0.05, \pm 0.1, \pm 0.2, \pm 0.3, \pm 0.5, \pm 0.7, \pm 1.0|e|$ per cell, where one “cell” is a $2 \times 2 \times 2$ supercell of the reference unit cell. Full structural (atoms and lattice) relaxations are initiated from diffraction data^{23–28} and the forces are minimized to a $0.5 \text{ meV } \text{\AA}^{-1}$ tolerance. We computed phonon band structures with the aid of the PHONOPY software.²⁹

Results and discussion

In our previous studies,^{20–22} we already pointed out how few low-frequency phonon modes are directly connected with the relative sliding of the adjacent layers. These consist of relative layer glides and out-of-phase vertical (parallel to \hat{c}) shifts of subsequent layers, eventually combined with intralayer motions (Fig. 2); we will refer to such modes as *sliding* and *compressive* modes. Following the standard convention, we label them with increasing integers corresponding to dispersion branches with relatively increasing frequency; for example, the $\Gamma(5)$ mode is the mode corresponding to the fifth branch at the Γ point of the reciprocal lattice, the frequency of which is higher (or equal in the case of degeneracy) than that associated with the $\Gamma(4)$ mode, and lower (or equal) than that relative to the $\Gamma(6)$ mode.

Lattice parameters

We first relax the model geometries and compute the corresponding phonon band structure along a standard³⁰ path joining the high-symmetry points of the irreducible Brillouin zone (IBZ). We do not find unstable displacements, with the exception of the MoS systems with $q = -0.5, -0.7, -1.0|e|$ per cell; the careful search for the stable states we performed in the latter cases, indeed, suggests that such instabilities cannot be removed unless the charge content is varied. For this reason, we will exclude these cases from our present analysis.

Perturbation of the charge neutrality induces reduction of system symmetries, from hexagonal to orthorhombic, monoclinic or triclinic (Table 1); among the charged systems, we

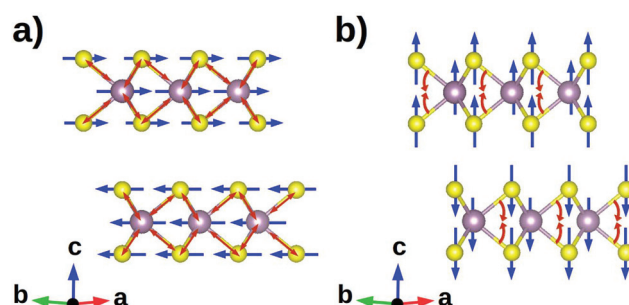


Fig. 2 Schematics of (a) relative layer sliding and (b) out-of-phase vertical shifts. Red arrows indicate eventual intralayer motions which overlap with interlayer displacements (blue arrows). The atom color legend is the same as in Fig. 1.

Table 1 Crystallographic space group of the fully relaxed TMD systems at the considered charge content q (|e| per cell). MoS systems with $q = -0.5, -0.7, -1.0$ |e| per cell are not considered due to the presence of structural instabilities

System	q																		
	-1.0	-0.7	-0.5	-0.3	-0.2	-0.1	-0.05	-0.03	-0.01	0.0	0.01	0.03	0.05	0.1	0.2	0.3	0.5	0.7	1.0
MoS	—	—	—	1	6	40	40	40	194	194	194	1	1	63	6	1	5	1	1
MoSe	1	1	1	1	1	63	63	63	194	194	63	63	63	63	2	1	1	1	1
MoTe	63	63	63	63	63	63	63	63	194	194	63	63	63	63	1	1	6	12	12
WS	15	15	15	15	15	15	15	15	194	194	63	63	63	63	1	1	1	2	2
WSe	1	1	1	1	1	63	63	63	194	194	63	63	63	63	63	63	63	63	63
WTe	63	63	63	63	63	63	63	63	194	194	63	63	63	63	63	63	63	63	63

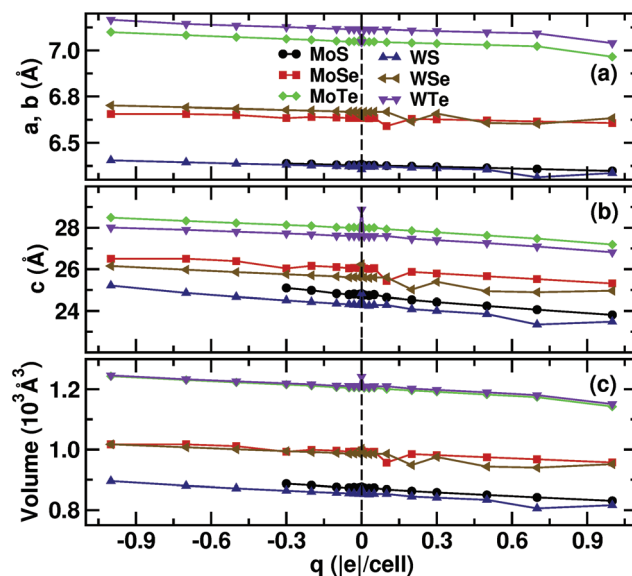


Fig. 3 Lattice parameters (a, b) and volume (c) of the considered MX models as a function of the system charge q . Lines are a guide to the eye.

notice that MoTe, WSe and WTe models maintain the geometry with the highest symmetry ($Cmcm$) at very different charge contents. This can be qualitatively ascribed to the fact that larger ions can accommodate charge variations better than the smaller ones, limiting eventual symmetry reduction.

Concerning the lattice vectors, at each MX composition, $a = b$ irrespective of the charge content (Fig. 3a); a (b) globally increases with increasing q , the variation range being about 0.1 Å. At $q = 0$, the a -axis has a local maximum for the MoX compounds, while it has a local minimum for the WX compounds; on the other hand, the c -axis has a local maximum at $q = 0$ irrespective of the composition although more pronounced in WX compounds, and its variation range is about 1.5 Å throughout the entire charge range (Fig. 3b). The behaviour of crystallographic axes about $q = 0$ indicates that a small perturbation of the charge neutrality is enough to induce structural transitions: at $q = \pm 0.05|e|$ per cell, the symmetry is lowered from hexagonal to orthorhombic, monoclinic (WS at $q = -0.05|e|$ per cell), or triclinic (MoS at $q = 0.05|e|$ per cell). In all the charged systems, with a fixed X anion, the c -axis is longer when $M = \text{Mo}$. Considering that the c -axis variation range is wider than that of the a -axis, we can infer that the charge variation is mostly accommodated along the direction orthogonal to the layer planes, producing a volume increase at increasing charge content (Fig. 3c).

Mode frequencies

We now analyse how the frequencies associated with the sliding and compressive modes vary with different charge contents (Fig. 4 and 5). At $q = 0$, the sliding modes are $\Gamma(4-7)$, $\Gamma(8-9)$, $A(1-4)$, and $A(7-10)$, while the compressive modes are $\Gamma(10-11)$, $\Gamma(12)$, $A(5-6)$, and $A(11-12)$, where we grouped the

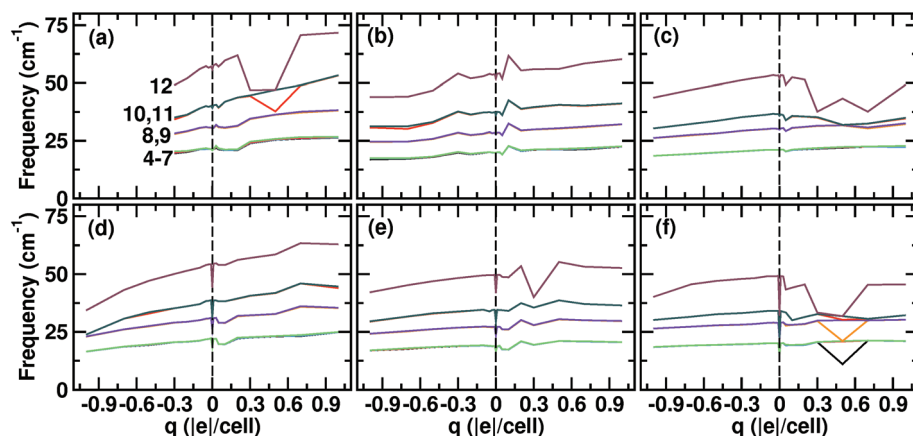


Fig. 4 Frequency of the phonon modes in branches 4–12 at the IBZ Γ point as a function of the system charge: (a) MoS, (b) MoSe, (c) MoTe, (d) WS, (e) WSe and (f) WTe systems. For clarity, we only show the lines connecting the data points, and omit the corresponding symbols.

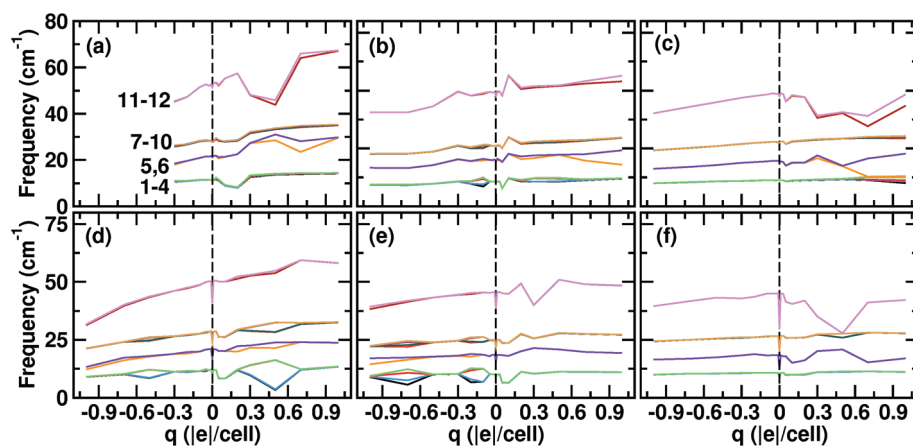


Fig. 5 Frequency of the phonon modes in branches 1–12 at the IBZ A point as a function of the system charge: (a) MoS, (b) MoSe, (c) MoTe, (d) WS, (e) WSe and (f) WTe systems. For clarity, we only show the lines connecting the data points, and omit the corresponding symbols.

modes with degenerate frequencies. We want here to note that, according to the usual convention, the IBZ A point relative to the hexagonal space group 194 corresponds to the Z point of the IBZ relative to the space groups 63, 40, 15, 8, 5, 2 and 1, and to the Y point of the IBZ relative to the space groups 12 and 6; all the three A , Y and Z high symmetry points correspond to the direction $(0,0,1/2)$ of the respective reciprocal lattice. However, the displacement pattern of the $A(1-12)$ modes is equivalent to that of the $Z(1-12)$ and $Y(1-12)$ modes; for this reason, we will simplify the notation by referring to the $Z(1-12)$ and $Y(1-12)$ modes as $A(1-12)$ modes without any ambiguities. As expected, the loss of charge neutrality and the consequent symmetry reduction cause, in general, the split of some degenerate modes. Irrespective of the chemical composition, the frequencies of the considered modes are globally increasing with increasing q . However, the frequency–charge relationship is not symmetric about $q = 0$: while for $q < 0$ the trend is smooth, for $q > 0$ sudden jumps are observed. Some of the jumps are expected due to a change in the space group; in

other cases, frequency jumps are observed even if no variation in the system symmetries occurs. In this respect, the frequency–charge–structure relationship is not trivial and other descriptors must be considered to harness the frequency change at a variable charge content.

Distortion mode analysis

Interplay between charges and structural distortions has already been observed in several classes of materials.^{16,31,32} To analyse the details of symmetry reduction upon removal of charge neutrality, we perform a group theoretical analysis of the charged structures by decomposing the ground state geometries into irreducible representations of the corresponding high symmetry hexagonal $P6_3mmc$ phase, aided by the ISODISTORT software.³³ Strain distortions are mainly due to the variation of the c axis length, which we discussed above; thus, from now on, we will discuss only the overall structural distortion δ generated by pure atomic displacement (Fig. 6). The main kind of distortion is $\Gamma 1+$, corresponding to the

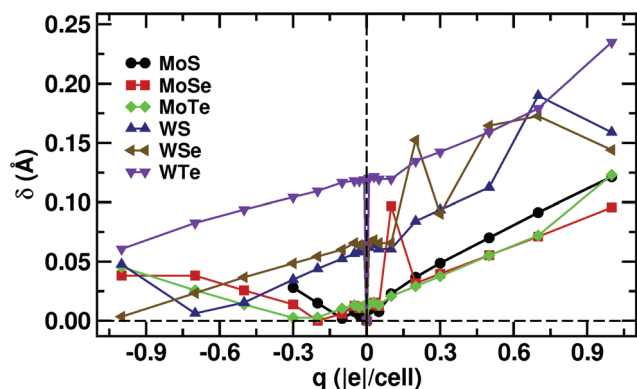


Fig. 6 Overall structural distortion δ as a function of the charge content q . Lines are a guide to the eye.

bending of the X–M–X intralayer angle (Fig. 7a); other distortions have negligible values, being 3 orders of magnitude smaller. In few particular cases, such smaller distortions are not negligible and contribute to the overall atomic displacements in such a way to produce sudden variations of the atomic displacements (Fig. 6). Such cases are: (i) $\Gamma 5+$, relative rigid sliding of adjacent MX_2 layers in MoSe at $q = 0.1$, WSe at $q = 0.2, 0.5, 0.7$, MoTe and WTe at $q = 1.0$ (Fig. 7b); (ii) $\Gamma 6+$, intralayer rigid sliding of S planes with respect to W planes in the WS system at $q = 0.7$ (Fig. 7c).

Comparing Fig. 6 with Fig. 3c, it is possible to note that such smaller distortions produce local minima in the volume–charge relationship. Interestingly, the appearance of such extra distortions, then of sudden jumps in the $\delta(q)$ trend, does not induce a change in the crystallographic space group (see Table 1). For this reason, the analysis of the electronic structure is needed in order to clarify the relationship between the charge content and the structural distortions, hence the frequency of the modes.

In a fixed X anion, structural distortions are larger in WX than in MoX compounds, with some exceptions at specific

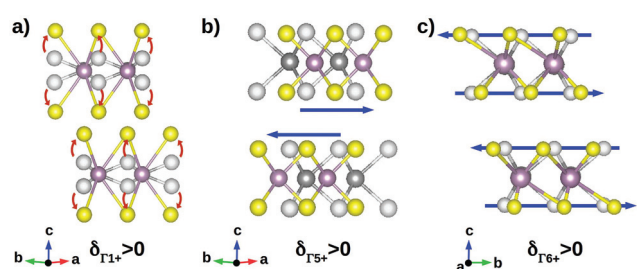


Fig. 7 Schematics of (a) $\Gamma 1+$, (b) $\Gamma 5+$ and (c) $\Gamma 6+$ distortion modes corresponding to the bending of the X–M–X intralayer angle, rigid interlayer sliding, and intralayer rigid sliding of X planes relative to M planes, respectively; positive distortion $\delta_{\Gamma 1+}$, $\delta_{\Gamma 5+}$ and $\delta_{\Gamma 6+}$ amplitudes indicate displacements along the directions shown by the arrows. $\Gamma 1+$ distortion is dominant in all the examined cases. The atom color legend is the same as in Fig. 1; grey spheres represent undistorted atomic positions. Displacements are magnified for clarity.

q values of the MSe systems. This means that MoX systems are able to accommodate charge variations better than WX systems, limiting atomic displacements at the minimum. Similarly to what was observed in the frequency–charge relationship, δ values are not symmetric about $q = 0$. Distortions at $-|q|$ are lower than the corresponding ones at $+|q|$, and they increase for $q > 0$; for $q < 0$, structural distortions decrease with an increasing charge content in WX systems, while they increase at a lower rate in MoX systems. This outcome is a further example of the non-trivial charge–structure relationship, and it points out that multiple descriptors must be used to control the electro-structural coupling and its effect on the sliding-related vibrational modes of the system.

Electro-structural coupling

We now proceed with the study of the details of the electronic distribution. To this aim, we first perform a charge Bader analysis in all the considered systems, and consider the difference $q_B = q_M - q_X$, where q_M and q_X are the Bader charges of the X and M atomic species, respectively (Fig. 8a); we then calculate the $C_{M,X}$ M–X bond covalency³⁴ and the $C_{\text{ph}}(\text{M-X})$ cophononicity²⁰ of the M–X pair, in the range $[-10, 0]$ eV and $[0, 75]$ cm^{-1} , respectively (Fig. 8b and c). The M–X pair cophononicity is a

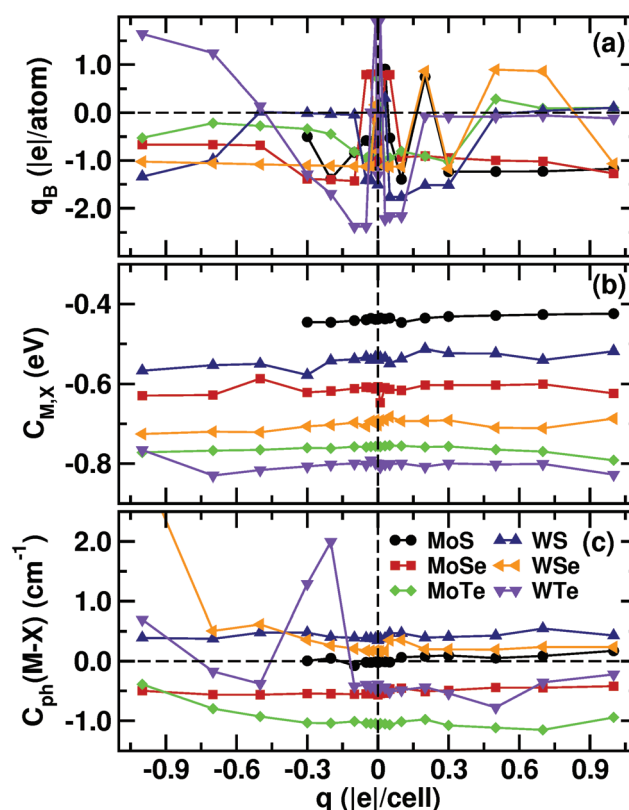


Fig. 8 (a) q_B Bader charge difference (e/atom), (b) $C_{M,X}$ M–X bond covalency (eV) and (c) $C_{\text{ph}}(\text{M-X})$ cophononicity (cm^{-1}) of the M–X pair as a function of the system charge q . For clarity, in plot (c) we do not show the $C_{\text{ph}}(\text{W-Se}) = 3.28 \text{ cm}^{-1}$ value at $q = -1.0$. Lines are a guide to the eye.

measure of how the M and X atomic species contribute to form the phonon states in the considered range, and has been applied to the study of the electro-structural coupling in distinct classes of materials.^{35–37} We observe that the variation range of q_B is wider in WX systems, and can be put into correspondence with a larger variation of the structural distortions with the charge content (Fig. 6). Bond covalency slightly decreases upon charge injection, displaying a general linear trend with the system charge; however, by comparing Fig. 8(b) and (c), it is immediately apparent that the covalent character of the bond is not strictly related to the q_B charge difference, nor directly connected with the structural distortions δ (Fig. 6). A similar observation can be applied to the cophononicity data: in a good approximation, $C_{\text{ph}}(\text{M-X})$ is linear with the charge content, after neglecting few local minima/maxima due to more subtle electronic features we will discuss later on. We also compute the electron localization function^{38,39} (ELF) of all the considered systems. Irrespective of the chemistry and the charge content, no localization of the extra charge q occurs in any specific volume of the cell system; this can be immediately appreciated by inspecting Fig. 9, where we report the ELF of the selected WTe systems, as an example. These last outcomes suggest that the electronic and dynamic features of the ionic environment are the result of a delicate balance between the local rearrangements of the electron density, structural distortions and overall charge neutrality perturbation. In this respect, we now focus on the subtle details of the electronic density spatial distribution by analysing the atomic orbital polarization.

Orbital polarization

The charge density can be partitioned in atom-centered hydrogen-like orbitals, so as to uncover the features of electronic flows through the structure at a variable charge content q .²² We then measure the orbital polarization^{40,41} of the X and M atomic species in each of the relaxed systems. Orbital polarization $\mathcal{P}_{l_1 m_{l_1}, l_2 m_{l_2}}$ of the $|l_1 m_{l_1}\rangle$ orbital relative to the $|l_2 m_{l_2}\rangle$ orbital is defined as

$$\mathcal{P}_{l_1 m_{l_1}, l_2 m_{l_2}} = \frac{n_{l_1 m_{l_1}} - n_{l_2 m_{l_2}}}{n_{l_1 m_{l_1}} + n_{l_2 m_{l_2}}}, \quad (1)$$

where $n_{l_1 m_{l_1}}$ and $n_{l_2 m_{l_2}}$ are the occupancies of $|l_1 m_{l_1}\rangle$ and $|l_2 m_{l_2}\rangle$ orbitals, with the orbital quantum number l_i and the magnetic quantum number m_{li} , respectively. It measures the charge excess of the former orbital with respect to the latter: positive (negative) values indicate that the m_{l_1} orbital is more (less) populated than the m_{l_2} orbital. In the considered cases, the observed local maxima and minima of $\mathcal{P}(q)$ do not appear to be related to a change in the space group, the latter, instead, determining the frequency split/degeneracy (Fig. 10).

In all charged systems, X p_x and p_y orbitals are almost equally populated (Fig. 10a), with an exception at $q = \pm 0.03$ for all the systems and at $q = 0.01$ for the MoSe system, where the p_x orbital is more populated than the p_y one. On the other hand, the p_z orbital displays an excess of population with respect to both p_x and p_y orbitals (Fig. 10b and c). In a fixed M cation, \mathcal{P}_{p_x, p_x} and \mathcal{P}_{p_y, p_y} polarizations increase as $\text{MTe} < \text{MS} < \text{MSe}$, assuming higher values if $\text{M} = \text{W}$. The t_{2g} orbitals are

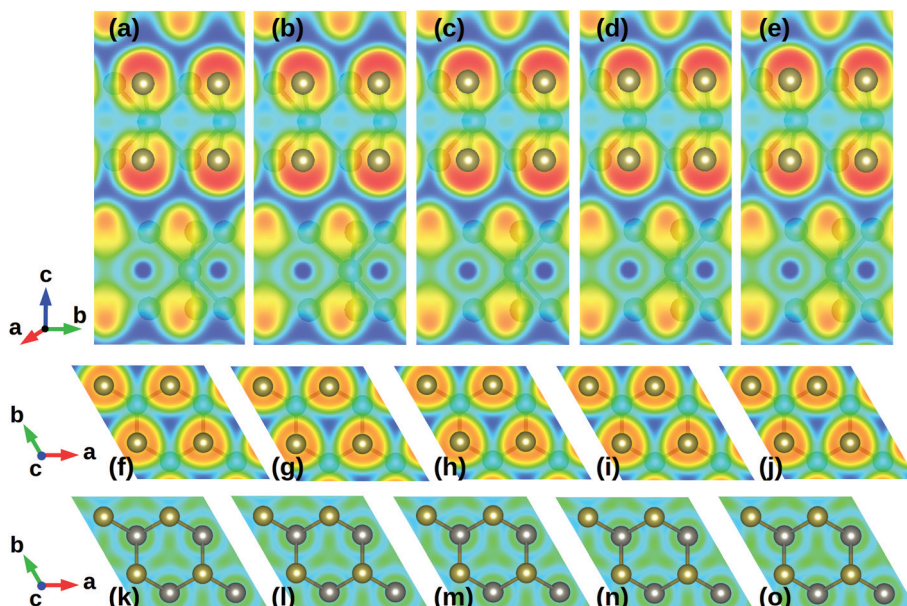


Fig. 9 Electron localization function (ELF) surfaces of the WTe systems calculated at (a, f, k) $q = -1.0$, (b, g, l) $q = -0.5$, (c, h, m) $q = 0.0$, (d, i, n) $q = 0.5$, and (e, j, o) $q = 1.0|e|$ per atom, respectively. Surfaces have been obtained by projecting the corresponding ELF's onto (a–e) the (100) plane containing Te atoms, (f–j) the (001) plane containing Te atoms, and (k–o) the (001) plane containing W cations, respectively. The RGB gradient represents the charge localization, where red color corresponds to the highest ELF value. Orientation of the crystallographic axes, reported on the left side of the figure, is shared among the (a–e), (f–j) and (k–o) subfigures, respectively.

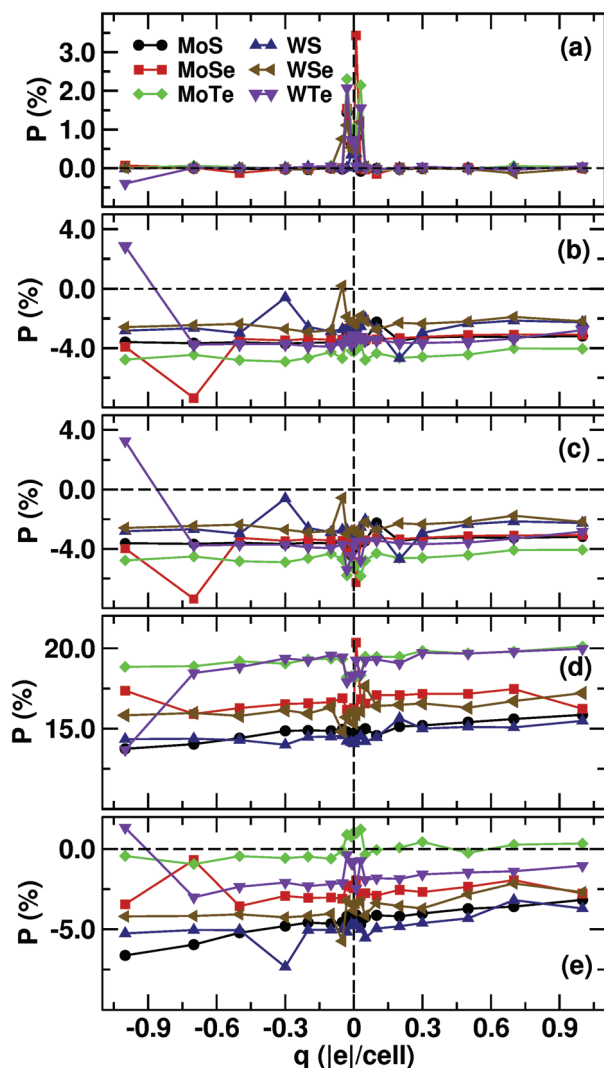


Fig. 10 Orbital polarization as a function of the system charge q : (a) $X \mathcal{P}_{P_x, P_y}$, (b) $X \mathcal{P}_{P_x, P_z}$, (c) $X \mathcal{P}_{P_y, P_z}$, (d) $M \mathcal{P}_{d_{3z^2-r^2}}$ and (e) $M \mathcal{P}_{d_{x^2-y^2}}$. Upon charge injection, the population of the M $d_{3z^2-r^2}$ orbital increases, accounting for the variation of the c lattice parameter. Lines are a guide to the eye.

more populated than the e_g ones (Fig. 10d), with the $d_{3z^2-r^2}$ orbital bearing an excess of charge with respect to the $d_{x^2-y^2}$ orbital (Fig. 10e). In general, in the fixed M cation and charge content q , the $d_{3z^2-r^2}$ population decreases with the X species as $S > Se > Te$, whereas higher population is found in WX systems (Fig. 10e). The amount with which the $d_{3z^2-r^2}$ orbital can accommodate a specific amount of charge is therefore determined by both the M and X atomic types. By comparing Fig. 10(d) and (e), it is possible to appreciate that, upon charge injection, a flow of charge occurs from the t_{2g} orbital to the e_g orbital, in particular towards the $d_{3z^2-r^2}$ one, which results to be more prone to accommodate the incoming electrons. We can therefore infer that this mechanism accounts for the c -axis variation with the system charge q . In this respect, ion substitution regulates the charge transfer from the planes parallel to the xy -plane and containing the X anions towards an axis parallel to the \hat{c} direction, with the $\mathcal{P}_{t_{2g}, e_g}$ orbital polarization being the quantity controlling such transfer. Moreover, $\mathcal{P}_{t_{2g}, e_g}$ regulates the M-X interaction, hence the lattice dynamics. Following these results, we continue our analysis by relating the frequency of the considered Γ and A modes to the $\mathcal{P}_{t_{2g}, e_g}$ orbital polarization values calculated at the same system charge (Fig. 11 and 12).

In order to better understand what is the relationship between the frequencies and the orbital polarization, we first focus on the considered $\Gamma(4-12)$ modes (Fig. 11) and calculate the average frequency ω at a fixed $\mathcal{P}_{t_{2g}, e_g}$ value, thus obtaining a $\{\omega, \mathcal{P}_{t_{2g}, e_g}\}$ data set for each MX system; we then evaluate the linear interpolation of such data sets and report the results in Fig. 13a. We repeat the same procedure on the A(1-12) modes and show the interpolated data in Fig. 13b. An inspection of the aforementioned figures clearly shows that the mode frequencies overall increase with the $\mathcal{P}_{t_{2g}, e_g}$ orbital polarization. By controlling the $\mathcal{P}_{t_{2g}, e_g}$ orbital polarization, it is then possible to finely tune the considered phonon modes relative to layer sliding; to this aim, we will exploit the connection between $\mathcal{P}_{t_{2g}, e_g}$ with the M-X bond covalency and cophonicity. Irrespective of the chemical composition, at a fixed charge, $\mathcal{P}_{t_{2g}, e_g}$ decreases with increasing $C_{M,X}$ and $C_{ph}(M-X)$ (Fig. 14),

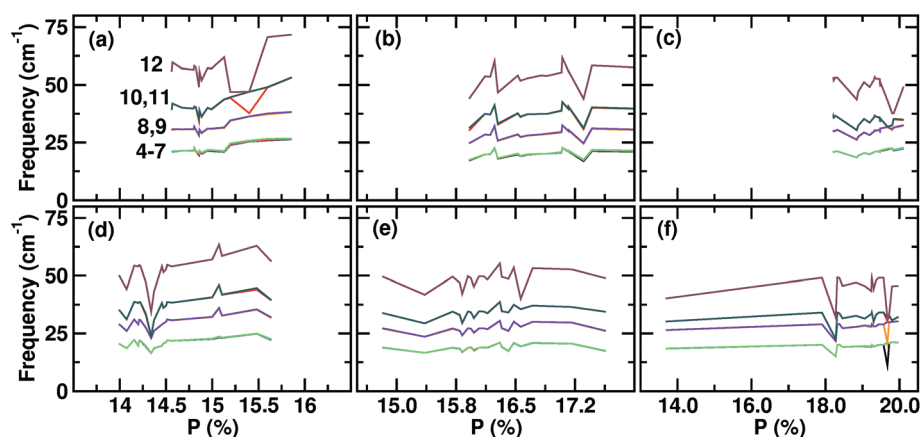


Fig. 11 Frequency of the phonon modes in branches 4–12 at the IBZ Γ point as a function of M $\mathcal{P}_{t_{2g}, e_g}$ orbital polarization of (a) MoS, (b) MoSe, (c) MoTe, (d) WS, (e) WSe and (f) WTe systems. For clarity, we only show the lines connecting the data points, and omit the corresponding symbols.

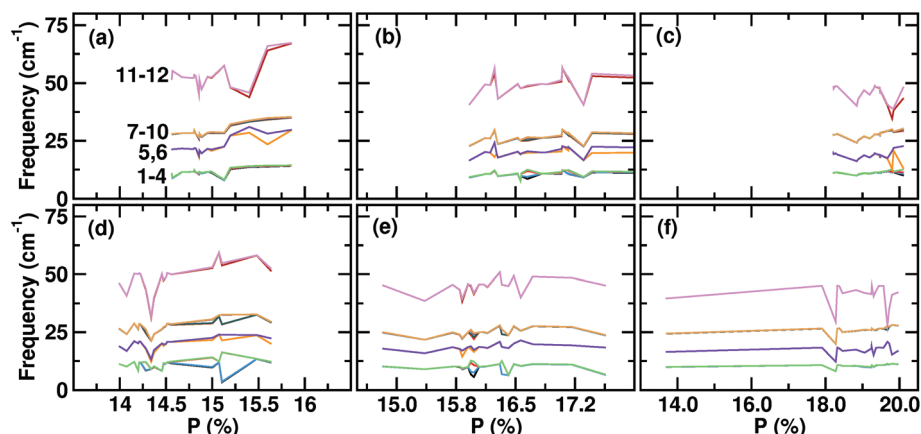


Fig. 12 Frequency of the phonon modes in branches 1–12 at the IBZ A point as a function of M \mathcal{P}_{t_{2g},e_g} orbital polarization of (a) MoS, (b) MoSe, (c) MoTe, (d) WS, (e) WSe and (f) WTe systems. For clarity, we only show the lines connecting the data points, and omit the corresponding symbols.

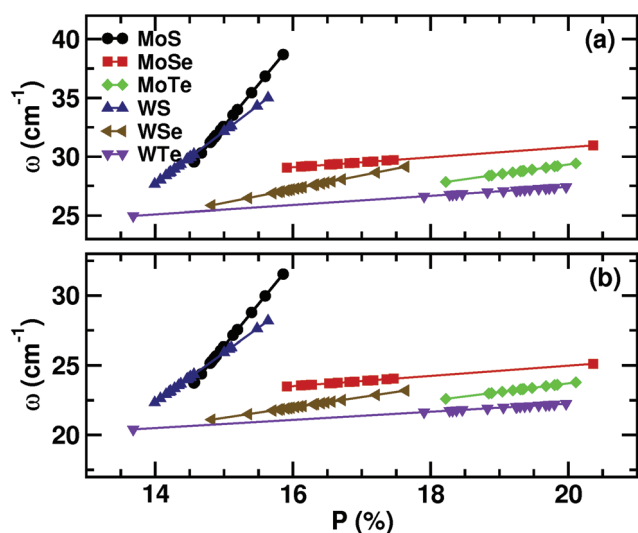


Fig. 13 Linear interpolation of the average frequency ω as a function of the \mathcal{P}_{t_{2g},e_g} orbital polarization of the considered (a) $\Gamma(4-12)$ and (b) $A(1-12)$ phonon modes, respectively. Irrespective of the chemical composition, mode frequencies increase overall with increasing \mathcal{P}_{t_{2g},e_g} orbital polarization.

the latter two descriptors being connected with the atomic type, the structural distortions and the electronic density distribution, as we have already shown in previous studies.^{21–23} In this respect, such quantities capture several entangled properties that can be singularly adjusted to finely tune the covalency and cophononicity values. The chemical composition and stoichiometry can be chosen in such a way so as to induce specific structural distortions that alter the electronic distribution and are more suitable for accommodating a specific amount of charge in the structure; at the same time, they alter the interatomic interactions that determine the vibrational motions of the system. We can thus conclude that covalency and cophononicity can be used as a knob to control the \mathcal{P}_{t_{2g},e_g} orbital polarization, and hence low-frequency phonons contributing to intrinsic friction in charged MX_2 systems.

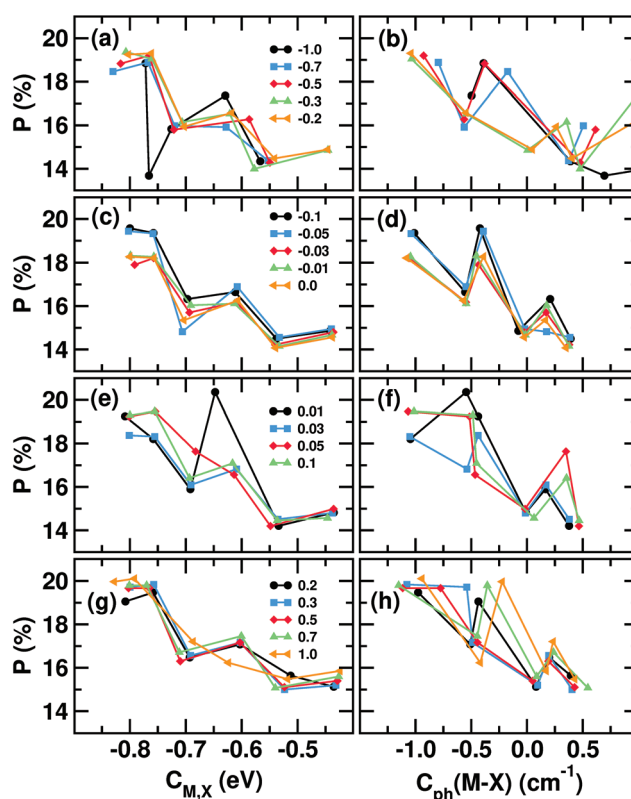


Fig. 14 M cation \mathcal{P}_{t_{2g},e_g} orbital polarization as a function of (a, c, e, g) M–X bond covalency and (b, d, f, h) M–X pair cophononicity. Plots (a) and (b), (c) and (d), (e) and (f), and (g) and (h) share the same legend which refers to the charge content of the system. In plot (b), values at $C_{\text{ph}}(\text{M-X}) > 0.5 \text{ cm}^{-1}$ are not shown for clarity. Lines are a guide to the eye.

Conclusions

We studied how the presence of non-null electronic charge affects the low-frequency modes influencing intrinsic friction in layered transition metal dichalcogenides. We find that any deviation from charge neutrality results in complex rearrange-

ments of the electronic density and atomic positions, inducing electronic and structural transitions. Charge injection determines an expansion of the cell volume due to the accumulation of charge along an axis orthogonal to the MX_2 layers. Such accumulation is accounted for by the $d_{3z^2-r^2}$ orbital of the transition metal and it is regulated by the \mathcal{P}_{t_{2g},e_g} orbital polarization; the latter also determines the M–X interactions, hence the modes affecting the intrinsic friction. The frequencies of such modes increase with the \mathcal{P}_{t_{2g},e_g} orbital polarization. In turn, increasing bond covalency and cophoncity induce a decrease of the \mathcal{P}_{t_{2g},e_g} orbital polarization at a fixed charge content. With the proper choice of the atomic type, it is possible to control such electro-structural descriptors, then the orbital polarization and the mode frequency. Such relationships are the result of subtle electro-vibrational coupling. Electron–phonon coupling can thus be exploited to control the vibrational frequencies of the system: by tuning the cophoncity and covalency values, we can finely control charge flow through atomic orbitals hence the vibrational frequencies at a specific charge content. This feature can be exploited to finely tune intrinsic friction to facilitate assembly and operation of nanoelectromechanical systems and, ultimately, to control the electronic charge distribution in TMD-based devices for application beyond nanoscale tribology. The information gained in the present study will be extended in future studies, where we will investigate the role of Coulombic forces arising from charge displacement and localization under tribological conditions.

Conflict of interest

There are no conflicts of interest to declare.





Acknowledgements

This work has been done with the support of the Czech Science Foundation, project 17-24164Y. This work was supported by the IT4Innovations Centre of Excellence project (CZ.1.05/1.1.00/02.0070), funded by the European Regional Development Fund and the national budget of the Czech Republic via the Research and Development for Innovations Operational Programme, as well as Czech Ministry of Education, Youth and Sports via the project Large Research, Development and Innovations Infrastructures (LM2011033).

References

- 1 B. Persson, *Sliding Friction: Physical Principles and Applications*, Springer-Verlag, Berlin Heidelberg, 2000.
- 2 E. Gneco, R. Bennewitz, T. Gyalog and E. Meyer, *J. Phys.: Condens. Matter*, 2001, **13**, R619.
- 3 A. Vanossi, N. Manini, M. Urbakh, S. Zapperi and E. Tosatti, *Rev. Mod. Phys.*, 2013, **85**, 529–552.
- 4 S. Cahangirov, C. Ataca, M. Topsakal, H. Sahin and S. Ciraci, *Phys. Rev. Lett.*, 2012, **108**, 126103.
- 5 T. Onodera, Y. Morita, A. Suzuki, M. Koyama, H. Tsuboi, N. Hatakeyama, A. Endou, H. Takaba, M. Kubo, F. Dassenoy, C. Minfray, L. Joly-Pottuz, J.-M. Martin and A. Miyamoto, *J. Phys. Chem. B*, 2009, **113**, 16526–16536.
- 6 T. Onodera, Y. Morita, R. Nagumo, R. Miura, A. Suzuki, H. Tsuboi, N. Hatakeyama, A. Endou, H. Takaba, F. Dassenoy, C. Minfray, L. Joly-Pottuz, M. Kubo, J.-M. Martin and A. Miyamoto, *J. Phys. Chem. B*, 2010, **114**, 15832.
- 7 T. Liang, W. G. Sawyer, S. S. Perry, S. B. Sinnott and S. R. Phillpot, *Phys. Rev. B: Condens. Matter*, 2008, **77**, 104105.
- 8 Y. Morita, T. Onodera, A. Suzuki, R. Sahnoun, M. Koyama, H. Tsuboi, N. Hatakeyama, A. Endou, H. Takaba, M. Kubo, C. A. D. Carpio, T. Shin-yoshi, N. Nishino, A. Suzuki and A. Miyamoto, *Appl. Surf. Sci.*, 2008, **254**, 7618–7621.
- 9 B. J. Irving, P. Nicolini and T. Polcar, *Nanoscale*, 2017, **9**, 5597–5607.
- 10 P. Nicolini and T. Polcar, *Comput. Mater. Sci.*, 2016, **115**, 158–169.
- 11 L. B. Loeb, *Science*, 1945, **102**, 573–576.
- 12 T. A. L. Burgo, C. A. Silva, L. B. S. Balestrin and F. Galembeck, *Sci. Rep.*, 2013, **3**, 2384.
- 13 A. Diaz and R. Felix-Navarro, *J. Electrostat.*, 2004, **62**, 277–290.
- 14 F. R. Fan, W. Tang and Z. L. Wang, *Adv. Mater.*, 2016, **28**, 4283–4305.
- 15 J. P. Oviedo, S. Kc, N. Lu, J. Wang, K. Cho, R. M. Wallace and M. J. Kim, *ACS Nano*, 2015, **9**, 1543–1551.
- 16 M. Chhowalla, H. S. Shin, G. Eda, L.-J. Li, K. P. Loh and H. Zhang, *Nat. Chem.*, 2013, **5**, 263–275.
- 17 J. P. Perdew, K. Burke and M. Ernzerhof, *Phys. Rev. Lett.*, 1996, **77**, 3865–3868.
- 18 (a) G. Kresse and J. Furthmüller, *Comput. Mater. Sci.*, 1996, **6**, 15–50; (b) G. Kresse and D. Joubert, *Phys. Rev. B: Condens. Matter*, 1999, **59**, 1758–1775.
- 19 S. Grimme, *J. Comput. Chem.*, 2006, **27**, 1787–1799.
- 20 A. Cammarata and T. Polcar, *Inorg. Chem.*, 2015, **54**, 5739–5744.
- 21 A. Cammarata and T. Polcar, *RSC Adv.*, 2015, **5**, 106809–106818.
- 22 A. Cammarata and T. Polcar, *Phys. Chem. Chem. Phys.*, 2016, **18**, 4807–4813.
- 23 B. Schönfeld, J. J. Huang and S. C. Moss, *Acta Crystallogr., Sect. B: Struct. Sci.*, 1983, **39**, 404–407.
- 24 V. Kalikhman, *Inorg. Mater.*, 1983, **19**, 957–962.
- 25 L. Brixner, *J. Inorg. Nucl. Chem.*, 1962, **24**, 257–263.
- 26 W. Schutte, J. D. Boer and F. Jellinek, *J. Solid State Chem.*, 1987, **70**, 207–209.
- 27 V. L. Kalikhman, *Neorg. Mater.*, 1983, **19**, 1060–1065.
- 28 A. A. Yanaki and V. A. Obolonchik, *Inorg. Mater.*, 1973, **9**, 1855–1858.
- 29 A. Togo, F. Oba and I. Tanaka, *Phys. Rev. B: Condens. Matter*, 2008, **78**, 134106.
- 30 W. Setyawan and S. Curtarolo, *Comput. Mater. Sci.*, 2010, **49**, 299–312.

- 31 F. Flicker and J. van Wezel, *Nat. Commun.*, 2015, **6**, 7034.
- 32 A. Cammarata and J. M. Rondinelli, *Appl. Phys. Lett.*, 2016, **108**, 213109.
- 33 B. J. Campbell, H. T. Stokes, D. E. Tanner and D. M. Hatch, *J. Appl. Crystallogr.*, 2006, **39**, 607–614.
- 34 A. Cammarata and J. M. Rondinelli, *J. Chem. Phys.*, 2014, **141**, 114704.
- 35 Z. Lu, C. Chen, Z. M. Baiyee, X. Chen, C. Niu and F. Ciucci, *Phys. Chem. Chem. Phys.*, 2015, **17**, 32547–32555.
- 36 T. Hu, M. Hu, Z. Li, H. Zhang, C. Zhang, J. Wang and X. Wang, *J. Phys. Chem. A*, 2015, **119**, 12977–12984.
- 37 R. Fei, W. Kang and L. Yang, *Phys. Rev. Lett.*, 2016, **117**, 097601.
- 38 A. D. Becke and K. E. Edgecombe, *J. Chem. Phys.*, 1990, **92**, 5397–5403.
- 39 A. Savin, O. Jepsen, J. Flad, O. K. Andersen, H. Preuss and H. G. von Schnering, *Angew. Chem., Int. Ed. Engl.*, 1992, **31**, 187–188.
- 40 A. Cammarata and J. M. Rondinelli, *Phys. Rev. B: Condens. Matter*, 2013, **87**, 155135.
- 41 M. J. Han, C. A. Marianetti and A. J. Millis, *Phys. Rev. B: Condens. Matter*, 2010, **82**, 134408.

Effect of electric fields in low-dimensional materials: Nanofrictional response as a case studyFlorian Belviso ^{*}, Antonio Cammarata [†] and Jamil Missaoui *Department of Control Engineering, Faculty of Electrical Engineering,
Czech Technical University in Prague, Technicka 2, 16627 Prague 6, Czech Republic*Tomas Polcar *Engineering Materials & nCATS, FEE, University of Southampton, SO17 1BJ Southampton, United Kingdom* (Received 28 August 2020; revised 11 October 2020; accepted 12 October 2020; published 29 October 2020)

A proper control of nanoscale friction is mandatory for the fabrication and operation of optimal nanoengineered devices. In this respect, the use of electric fields looks to be promising, since they are able to alter the frictional response without imprinting permanent deformations into the structure. To this aim, we perform *ab initio* simulations to study the microscopic mechanisms governing friction in low-dimensional materials in the presence of electrostatic fields. We consider MX_2 transition metal dichalcogenides as a case study. By applying an electric field along an axis orthogonal to the atom layers, we induce a transfer of charge along the same axis; this transfer modifies the interatomic forces, leading, in general, to easier relative layer motion. The reported outcomes constitute a starting point to study the effect of the field direction on the intrinsic friction in future investigations. Finally, the present results can be used to predict the preferential electronic redistribution in nanostructured devices where metal-to-insulator transitions may occur in working conditions.

DOI: [10.1103/PhysRevB.102.155433](https://doi.org/10.1103/PhysRevB.102.155433)**I. INTRODUCTION**

Low-dimensional materials have found vast use in nanoengineered devices thanks to their properties with wide applicability such as in photovoltaics, lithium ion batteries, hydrogen evolution catalysis, transistors, photodetectors, DNA detection, memory devices, and tribology [1–5]. Fabrication of such devices requires micromanipulation of free standing atomic layers, and a thorough knowledge and control of the frictional properties at the nanoscale is then mandatory [6,7]. Moreover, their frictional properties are of particular interest in micro- and nanoelectromechanical devices [8,9] (MEMS, NEMS) or in energy harvesters, where nanoscale layers are in relative motion [9,10]. Previous studies already pointed out that load can be used as an external knob to control the nanoscale friction [11–13], although it may induce unwanted permanent changes to the atomic geometry [14–17]. On the other hand, electrical fields induce charge movements which may alter the frictional properties temporarily, while allowing them to revert to the original structure once the external field is suppressed [18–20]. Some theoretical studies have already dealt with the effect of electric fields on the coupling between the electronic and dynamic (i.e., phonon) features in low-dimensional materials [21,22]; interestingly, such coupling has been found to be effective in altering the lateral frictional force in MoS_2 and graphene bilayer systems [23,24]. Recent experimental studies showed how to manipulate free-standing atomic layers by in-plane

potential gradients with an atomic force microscopy tip [6,25], while the friction between the tip and the layer decreases with the field [20].

Motivated by this findings, in the present work we study the microscopic mechanisms governing the intrinsic friction at the nanoscale in the presence of electrostatic fields. As a case study, we consider van der Waals transition metal dichalcogenides (TMDs), which are of great interest in diverse fields where nanoengineering is the fundamental used technique [2]. We use quantum mechanical simulations to uncover the electronic response to an external field; we then show how this determines the atomic participation to the relative motion of few TMD layers and hence the intrinsic friction. The outcomes constitute a theoretical tool for future studies on the effect of the field direction on the layer motions. Among other applications, we finally discuss how the present results can be exploited in machine learning engines aimed to design nanotribological materials with targeted frictional response.

II. METHODS**A. Computational details**

The bulk structure of MX_2 transition metal dichalcogenides consists of hexagonally-ordered planes of M cations, inserted between two planes of X anions arranged in a similar fashion. This layered motif produces X-M-X “sandwiches” held together by van der Waals forces and yielding a lamellar structure. Such forces are weak enough to allow easy relative sliding of neighboring layers, manifesting as macroscopic lubricating effect. Among the possible polymorphs [1], we consider the 2H phase with space group symmetry $P6_3/mmc$,

^{*}belviflo@fel.cvut.cz[†]cammaant@fel.cvut.cz

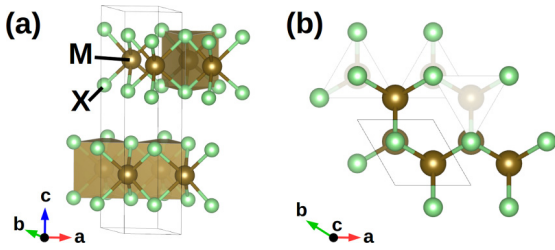


FIG. 1. Model geometry of the hexagonal $P6_3/mmc$ 2H polymorph of prototypical TMD compounds; the unit cell is indicated by a fine-line box. The a , b , c vectors forming the reference frame at the bottom left of each subfigure represent the crystallographic axes in our settings and the orientation of the unit cell with respect to the reader's view. Adjacent MX_2 layers are bound together by weak van der Waals forces which allow relative gliding.

in which the anions are aligned with the cations along a direction orthogonal to the layer surface (Fig. 1). We select $M = Mo, W$ and $X = S, Se, Te$; in our settings, the layers are able to slide in parallel with the a, b plane.

We perform density functional theory calculations by means of the ABINIT software [26–32]. The plane-wave energy cutoff is set to a minimum of 18.4 Ha and the Brillouin zone is sampled with a minimum of $7 \times 7 \times 5$ k -mesh divisions; the convergence of the electronic distribution is considered to be achieved when the difference of the total energy calculated between two subsequent self-consistent field cycles occurs twice in a row to be less than 10^{-12} Ha. Structural relaxations are initiated from diffraction data [33–38]; the lattice parameters and atomic positions are considered to be optimized when the maximum component of the total force acting on each atom is less than 10^{-7} Ha/Bohr.

After a preliminary benchmark, [39] we select the PBE functional [40] together with the vdW-DFT-D3(BJ) correction [41] to account for the van der Waals interactions. Following the formulation of Nunes and Gonze [42,43], we apply an external electrostatic field E along a direction parallel to the c lattice vector (perpendicular to the sliding plane), the magnitude of which varies in the range $[0, 2.5] \times 10^{-3}$ a.u. Apart from the largest values of 2.0 and 2.5×10^{-3} a.u. which we consider as extreme cases, the remaining values are representative of the electric fields typically used in MEMS/NEMS devices [44–48]. We observe the presence of structural instabilities beyond certain field values depending on the atomic types forming the structure; for this reason, the maximum field value is chosen differently for each system in order to minimize the number of unstable displacements. We finally calculate eigendisplacements and eigenfrequencies of the dynamical matrix of the structures by using the PHONOPY software [49].

B. Sliding and breathing modes

Microscopic friction is defined as the friction appearing due to the relative motion of adjacent atom layers in the presence of structural irregularities (e.g., dislocations, layer truncations, wrinkles). If such irregularities are absent, friction is still occurring due to the interatomic forces arising from the electronic (type of atom) and structural arrangement

(geometry); in this case, we call it *intrinsic friction* as it is an intrinsic characteristic of the system [50]. In the present work, we focus on the latter by considering pristine compounds lacking in irregularities or defects. We already observed that relative atomic motions can be geometrically described by linear combination of phonon eigendisplacements [51,52]; those with the largest coefficients in the combination are named *sliding modes* and keep active the layer sliding as long as they own enough energy [53,54]. The sliding modes can be classically seen as restoring forces which prevent the layer to displace from the equilibrium position, such forces being proportional to the square of the mode frequency. Therefore, at a constant system energy, the lower the frequency of the sliding modes, the larger the amplitude of the corresponding atomic displacements, this corresponding to facilitated sliding. If the frequency of a sliding mode becomes negative [55] due to external stimuli, the geometry becomes unstable against the distortion represented by the eigendisplacement of such a mode, and the atomic configuration does not realize a minimum of the energy anymore. This means that a very small perturbation of the geometry is enough to activate the sliding motion along the direction of the mode eigenvector; as a consequence, a new minimum of the energy is realized. The latter corresponds to a new geometric configuration with new sliding mode frequencies which, in principle, can be larger than the initial ones. To obtain easy sliding over long distances, it is then necessary to lower the frequencies of the sliding modes at each local minimum of the energy landscape; indeed, it has been found that layered compounds display several energy minima with different curvatures [56–60]. Nevertheless, the present discussion is general and does not depend on the specific atomic topology. For this reason, we here focus on the structural configurations corresponding to one of the possible energy local minima of the considered compounds; the same analysis can then be repeated on the geometries corresponding to any other local energy minimum. If an approximate evaluation of the frequencies is required, it is possible to reduce the computational load by exploiting the *normal-modes transition approximation* [52]: Starting from the knowledge of the phonon modes of one of the stable structures, the approximation allows us to estimate the eigenfrequencies of neighboring energy minima, thus avoiding the time-consuming diagonalization of the corresponding dynamical matrices.

In tribological conditions, external intervention produces displacements of a layer with respect to the adjacent ones; such displacements generate an excessive overlap of the electronic densities of the facing anions, and a consequent repulsive force arising from both Coulombic interactions and Pauli's exclusion principle. Since the external forces drag the layers along directions parallel to the a, b plane, the effect of the repulsive forces is to push the layers away from each other along the c direction orthogonal to the layer plane. In the extreme case in which the orthogonal movement is not allowed, the repulsive force would act only laterally pushing the layer back, then increasing the sliding energy barrier. It is then apparent that if the forces binding the layers together are weak, the layer separation is facilitated and hence the sliding. The latter forces mainly arise from the van der Waals interactions and are represented by the *breathing* phonon modes. The breathing modes are associated to a restoring force which

regulates the interlayer distance: A small force corresponds to a large allowed variation (compression/dilation) of the layer separation and facilitates the lateral shift. Both sliding and breathing motions then occur at the same time whenever two layers are displaced, no matter if the displacement is done slowly and in a reversible way (case of static friction) or rapidly (case of dynamic friction); in terms of the phonon description, this corresponds to the phonon coupling between both kind of modes, leading to dissipative processes which are active until the relative layer displacement occurs [53,54]. By tuning the phonon frequency we can then control the intrinsic frictional response; to this aim, in what follows, we will focus on both the sliding and the breathing modes. A schematic representation of the displacements associated to such modes is reported, for example, in the freely available Supplemental Material of Ref. [50] and in Ref. [19].

We want to avoid the fragmentation of information into several parameters; instead, we use global quantities in order to obtain a unified description of the physics of the system. To this aim, we consider the mean frequency ω which is calculated as

$$\omega = \frac{1}{N} \sum_j^N \omega_j, \quad (1)$$

where N is the number of the considered sliding and breathing modes and ω_j is the frequency of the j th mode. It is worth noting here that ω can assume positive values despite the fact that some of the ω_j can be negative, that is, also in the presence of unstable modes. In this respect, a positive value of ω indicates that the amount of instabilities, that is the number of unstable modes and the magnitude of the relative frequencies, is null or negligible; in the latter case, the structure can be considered “globally” stable. The phonons relevant to our discussion are mainly located at the Γ and A points of the irreducible Brillouin zone; we will then focus on this portion of the reciprocal space in our phonon analysis.

III. RESULTS AND DISCUSSION

We start our investigation from the effect of the electric field on the geometry. At non-null fields, we observe the largest volume variation in the MoSe₂, MoTe₂, and WSe₂ systems, mainly due to the change in the length of the c lattice vector (Fig. 2); this is expected, since such a crystallographic axis is parallel to the direction of the applied field \mathbf{E} . As we discuss later on, some structure becomes unstable for field values beyond a certain threshold which depends on the material; for those values, the lattice parameters correspond to a transient configuration which belongs to a geometric path connecting two stable states. Such transient configuration can be detected by time-resolved crystallography techniques, capable to monitor structural changes occurring in very short time scales [61–63]. Concerning the phonon structure, we observe that an increase of the field produces a general hardening of the $\Gamma - A$ modes together with a softening of some sliding branches, which may become unstable beyond some critical E ($E = |\mathbf{E}|$) value specific of the system. This is apparent when we consider the average frequency ω as a function of E (Fig. 3): The MoS₂, WS₂, and WTe₂ systems appear to

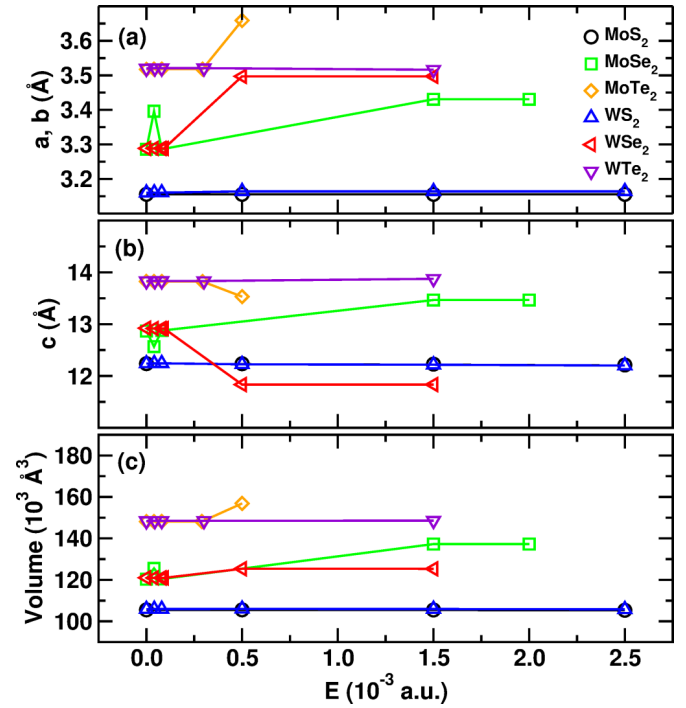


FIG. 2. Effect of the electric field on the lattice parameters of the model systems: (a) lattice constants a and b , (b) lattice constant c , (c) cell volume. Values relative to MoS₂ and WS₂ systems are close. Lines are a guide for the eye.

be the most stable against large field perturbations while, in the remaining compounds, some of the sliding modes become unstable already at $E = 0.5 \times 10^{-3}$ a.u. (the dependency of each sliding and breathing mode frequency as a function of the field is reported in the Supplemental Material [39]). This suggests that the sliding can already be facilitated in MoSe₂, MoTe₂, and WSe₂ pristine TMDs by means of the application of small electric fields; however, the critical electric fields to obtain easy sliding are the lowest required to realize negative average frequencies and depend on the chemical composition. To estimate the effect of the field on the nanoscale friction, we recall that we are here describing friction as a harmonic restoring force

$$f = -kx = m\omega^2\ddot{x}, \quad (2)$$

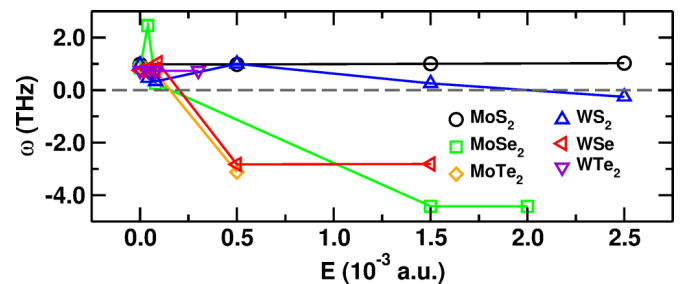


FIG. 3. Average frequency as a function of the applied electric field. Instabilities arise when the field magnitude is above a critical value depending on the chemical composition. Lines are a guide for the eye.

where x is the relative layer displacement, m is the mass of the system, and $k(\omega)$ is an effective force constant (frequency) resulting from the sliding and breathing modes. From Eq. (2) we can infer that, if the effect of the electric field is to halve the frequency, the resulting frictional force is four times smaller than the initial one. We are aware that this is an approximation because phonon coupling should be taken into account explicitly [52–54,64]. A rigorous derivation of the frictional force in terms of phonon contributions requires the explicit expression of the energy in terms of single phonons and the relative coupling, also including the effect of the temperature; however, this falls out of the scope of the present discussion and we plan to investigate it in a future work. By inspecting Fig. 3, it is apparent that there is no clear relation between the magnitude of the field, the phonon frequency, and the atomic types. This relation is the result of the coupling between the electronic structure and the dynamical response of the system; understanding and controlling such coupling is indeed the goal of the present work. To this aim, we proceed with the analysis of the subtle features of the electronic density. To quantify how the electronic charge redistributes across the structure under the effect of the field we make use of the orbital polarization [65] defined as

$$\mathcal{P}_{a,b} = \frac{n_a - n_b}{n_a + n_b}, \quad (3)$$

where n_i is the occupation of a given i orbital; in this way, we measure the excess of population of the a with respect to the b orbital. Since the atomic orbitals provide a partition of the electronic density into regions with specific spatial orientations, by comparing different kind of polarizations we can determine the preferential distribution of the electrons at specific field magnitudes. We consider the p_x , p_y , and p_z orbitals centered at the anion sites, and the t_{2g} and the e_g orbitals centered at the cation sites, in order to calculate the following polarizations: \mathcal{P}_{p_x,p_y} , \mathcal{P}_{p_x,p_z} , \mathcal{P}_{p_y,p_z} , \mathcal{P}_{t_{2g},e_g} , $\mathcal{P}_{d_{x^2-y^2},d_{z^2}}$. We notice that the presence of the field does not induce any significant change in the relative occupation of the p_x with respect to the p_y orbital [Fig. 4(a)]; the fluctuation around zero of \mathcal{P}_{p_x,p_y} indicates that the electrons are equally distributed between the two orbitals. This is an expected behavior thanks to the symmetries present in the a, b plane; for the same reason, both \mathcal{P}_{p_x,p_z} and \mathcal{P}_{p_y,p_z} orbital polarizations show the same trend [Figs. 4(b) and 4(c)]. The negative values of \mathcal{P}_{p_x,p_z} and \mathcal{P}_{p_y,p_z} indicate an excess of electrons along an axis orthogonal to the layers at the anion site, such excess remaining nearly constant irrespective of the applied field. Concerning the relative occupation of the t_{2g} and e_g orbitals, in the MoSe₂, MoTe₂, and WSe₂ systems we notice that an increase of the field induces a transfer of electrons towards the e_g orbitals [Fig. 4(d)] and, correspondingly, an electron flow from the $d_{x^2-y^2}$ to the d_{z^2} orbital [Fig. 4(e)]. This points at a charge transfer along an axis orthogonal to the a, b plane and passing through the cation sites. Differently, in the MoS₂, WS₂, and WTe₂ systems the variation of the field leaves almost unaltered both the \mathcal{P}_{t_{2g},e_g} and $\mathcal{P}_{d_{x^2-y^2},d_{z^2}}$ polarizations. This analysis then suggests that the applied field induces an accumulation of charge along the c direction in the MoSe₂, MoTe₂, and WSe₂ systems, which accounts for a significant variation of the c lattice constant (Fig. 2) and the consequent instability

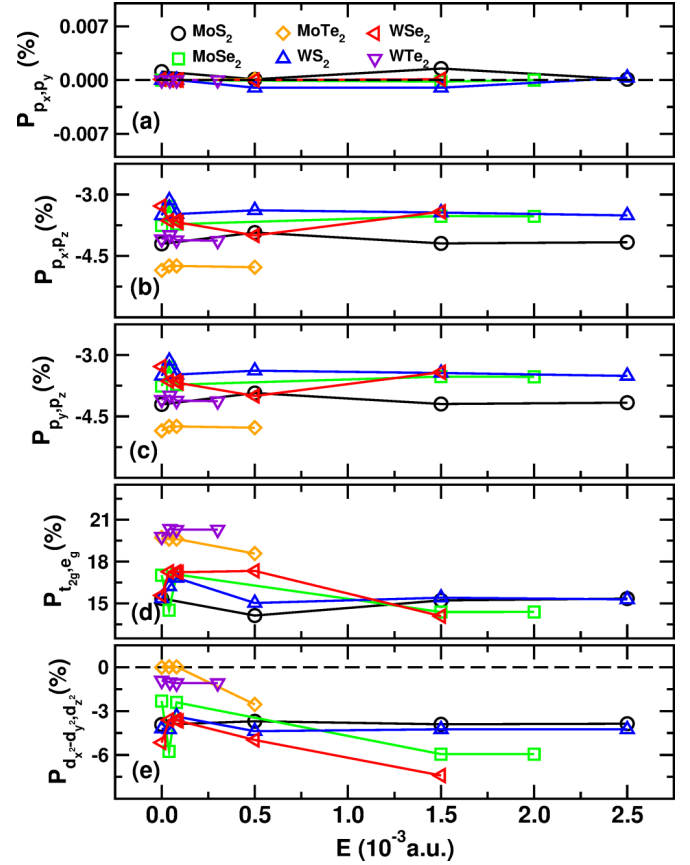


FIG. 4. Orbital polarization of the MX₂ systems as a function of the electric field. An increase of the field magnitude induces a charge transfer along the direction orthogonal to the lattice planes. Legend is common to all the subplots; lines are a guide for the eye.

of the sliding modes (Fig. 3). For a convenient visualization of this effect, we report the projections of selected charge density differences in the Supplemental Material [39]. The charge redistribution may affect the M-X bond covalency, as it has already been observed in TMD-based systems [54]. In order to quantify this effect, we calculate the bond covalency $C_{M,X}$ in terms of atomic participation to the electronic density of states [66]; we then consider the relation among $C_{M,X}$ and the polarizations involving the d orbitals (Fig. 5). In MoS₂, MoSe₂, and MoTe₂ systems, the bond covalency is nearly constant despite the large variation of the orbital polarizations; on the contrary, the covalent character of the bond is more sensitive to the charge rearrangement in WS₂ and WSe₂ systems. In the case of the WTe₂ compound, the variation of the orbital polarization is too small to induce significant changes in the bond covalency. Correspondingly, no clear trend is observed for ω as a function of $C_{M,X}$ (not shown). This shows that the relation among the atomic motions (i.e., mode eigendisplacements and their frequency), the covalency, the orbital polarizations, and the atomic types forming the structure is not trivial. Indeed, the atomic types and the electronic environment in which they are embedded rule the interatomic forces which, in turn, dictate the dynamic response. In fact, the interatomic force constant tensor enters in the definition of the dynamical matrix and determines the values of the

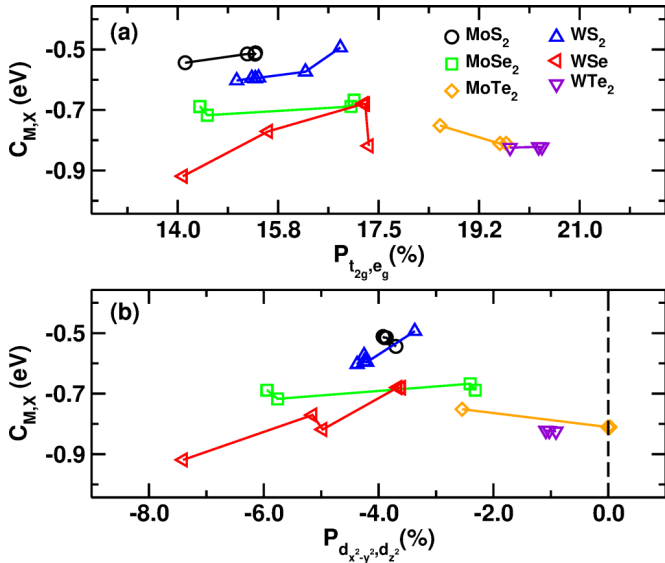


FIG. 5. M-X bond covalency as a function of the (a) P_{t_{2g}, e_g} and (b) $P_{d_{x^2-y^2}, d_{z^2}}$ orbital polarizations. Depending on the system, the charge rearrangement does not affect the covalent character of the bond. Legend is common to both subplots; lines are a guide for the eye.

mode frequencies of the system [67,68]. This leads us to consider the cophonycity [51] metric as a general descriptor able to parametrize the effect of the atomic type on such entangled electro-dynamical coupling, as already observed for other physical phenomena [69–73]. The cophonycity metric $C_{ph}(M-X)$ is a measure of the relative atomic contributions to a specific range of phonon eigenfrequencies, whereas the contribution of a single atom is quantified by the atom-projected phonon density of states. To calculate $C_{ph}(M-X)$ for each compound, we select the frequency range corresponding to the sliding and breathing modes [39]. According to the definition, positive $C_{ph}(M-X)$ values indicate that the M and X ions contribute more to higher- and lower-frequency displacements, respectively; in this case, M cations displace faster than X anions when forming the global layer sliding motion. The opposite holds for negative values. A cophonycity value close to zero (*perfect cophonycity*) corresponds to atomic displacements in which both M and X atoms move on average at the same velocity. We observe that the cophonycity is nearly constant for low values of the electric field (Fig. 6); in this respect, it can be regarded as an intrinsic characteristic of the stable system. For each system, there is a critical electric field beyond which the cophonycity deviates significantly from the value at zero field. Correspondingly, the structure becomes highly unstable against the sliding and breathing distortions, that is, the relative layer motion is promoted in a more significant amount than what is observed for the cases at low field. Interestingly, in general, the sliding and breathing displacements are stable when perfect cophonycity is realized ($C_{ph}(M-X) \approx 0$), while they become prevalently unstable when $C_{ph}(M-X)$ significantly deviates from zero; how far from zero it must be to have unstable modes depends on the system. This means that if the overall layer displacement is formed by atomic motions in which the M and X atoms move on

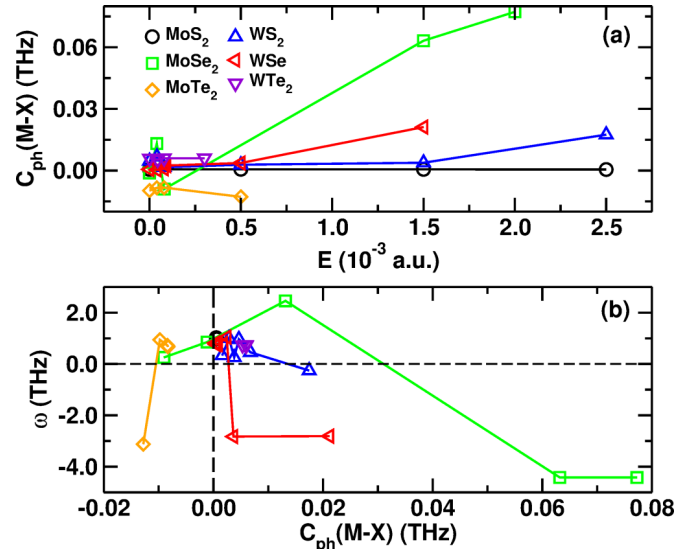


FIG. 6. (a) Cophonycity of the M-X pair as a function of the electric field. (b) Average frequency as a function of the cophonycity. Legend is common to both subplots; lines are a guide for the eye.

average at the same velocity, the sliding is favored at low electric field values; on the contrary, larger field values require that cations and anions move at a very different velocity in order to produce easy gliding of the layers. In passing, we notice that the cophonycity values here reported are similar to those realized in finite n -layered TMDs, where the orbital polarization and the consequent interlayer charge distribution play a relevant role in the determination of the sliding-related frequencies [50].

The presented case study can be extended by considering geometric configurations corresponding to local energy minima other than those considered in the present work; in this way, it is possible to obtain a more complete overview of the set of electric field values suitable for the selected atomic types. Moreover, atomic species and geometries other than those pertaining to the here examined TMD prototypes can be the subject of future studies. To this aim, it is possible to use the cophonycity to parametrize the nanoscale frictional response to external electric fields in large databases of chemical moieties and atomic topologies. Such parametrization can be used in machine learning engines [9] for automated research of proper combination of atomic species and geometries, to ultimately design novel tribological materials with targeted frictional response under electric field stimuli. Finally, the observed relation between the charge flow and the electric field may guide the probe and control of metal-to-insulator transition in nanomechanical motions [74,75], since the transition is generally determined by subtle anisotropic rearrangements of the electronic density [65,76,77].

IV. CONCLUSIONS

We studied the effect of an electrostatic field on the nanoscale frictional properties of lamellar materials, by considering prototypical layered transition metal dichalcogenides as a case study. By applying an electric field along an axis orthogonal to the atom layers, we induce a transfer of charge

along the same axis; this transfer does not affect significantly the covalent character of the bond, while it modifies the interatomic forces. Such modification determines the softening of the sliding modes until they become unstable above a certain critical field specific of the system. This effect is quantified by the cophononicity metric: The larger the module of the cophononicity, the more different the cation and anion velocity when forming the overall sliding motion, leading to strongly unstable phonon modes and lower friction. The present outcomes are therefore a theoretical tool for future investigations aimed to parametrize the triboresponse to electric fields against the atomic types forming the compound. The reported results also represent a starting point for further studies where different directions of the field other than that orthogonal to atomic layers are considered, in order to elucidate the effect of the field orientation on the intrinsic friction. Finally, the present study can help to predict the preferential electronic

redistribution in nanomechanical devices, where local metal-to-insulator transitions may occur in working conditions.

ACKNOWLEDGMENTS

This project has received funding from the European Union's Horizon2020 research and innovation programme under Grant agreement No. 721642: SOLUTION. This work has been done with the support of the Czech Science Foundation (Project No. 17-24164Y), and by the project "Novel nanostructures for engineering applications" No. CZ.02.1.01/0.0/0.0/16_026/0008396. This work was supported by The Ministry of Education, Youth and Sports from the Large Infrastructures for Research, Experimental Development and Innovations project "e-Infrastructure CZ—LM2018140."


-
- [1] M. Chhowalla, H. Shin, G. Eda, L. Li, K. Loh, and H. Zhang, *Nat. Chem.* **5**, 263 (2013).
- [2] W. Choi, N. Choudhary, G. H. Han, J. Park, D. Akinwande, and Y. H. Lee, *Materials Today* **20**, 116 (2017).
- [3] H. Schmidt, F. Giustiniano, and G. Eda, *Chem. Soc. Rev.* **44**, 7715 (2015).
- [4] W. Guo, J. Yin, H. Qiu, Y. Guo, H. Wu, and M. Xue, *Friction* **2**, 209 (2014).
- [5] J. Cumings and A. Zettl, *Science* **289**, 602 (2000).
- [6] J. P. Oviedo, S. KC, N. Lu, J. Wang, K. Cho, R. M. Wallace, and M. J. Kim, *ACS Nano* **9**, 1543 (2015).
- [7] H. Li, J. Wu, Z. Yin, and H. Zhang, *Acc. Chem. Res.* **47**, 1067 (2014).
- [8] D. Young, C. Zorman, and M. Mehregany, "Mems/nems devices and applications," in *Springer Handbook of Nanotechnology*, edited by B. Bhushan (Springer Berlin Heidelberg, Berlin, Heidelberg, 2007), pp. 415–442.
- [9] F. Belviso, V. E. P. Claerbout, A. Comas-Vives, N. S. Dalal, F.-R. Fan, A. Filippetti, V. Fiorentini, L. Foppa, C. Franchini, B. Geisler, L. M. Ghiringhelli, A. Groß, S. Hu, J. Íñiguez, S. K. Kauwe, J. L. Musfeldt, P. Nicolini, R. Pentcheva, T. Polcar, W. Ren, F. Ricci, F. Ricci, H. S. Sen, J. M. Skelton, T. D. Sparks, A. Stroppa, A. Urru, M. Vandichel, P. Vavassori, H. Wu, K. Yang, H. J. Zhao, D. Puggioni, R. Cortese, and A. Cammarata, *Inorg. Chem.* **58**, 14939 (2019).
- [10] E. Gnecco and E. Meyer, *Fundamentals of Friction and Wear on the Nanoscale*, 2nd ed., NanoScience and Technology (Springer International Publishing, 2015), p. 704.
- [11] E. Serpini, A. Rota, S. Valeri, E. Ukraintsev, B. Rezek, T. Polcar, and P. Nicolini, *Tribol. Int.* **136**, 67 (2019).
- [12] G. Levita, A. Cavaleiro, E. Molinari, T. Polcar, and M. Righi, *J. Phys. Chem. C* **118**, 13809 (2014).
- [13] Y. Mo, K. Turner, and I. Szlufarska, *Nature (London)* **457**, 1116 (2009).
- [14] J.-U. Lee, S. Woo, J. Park, H. C. Park, Y.-W. Son, and H. Cheong, *Nat. Commun.* **8**, 1370 (2017).
- [15] H. Bao, Y. Huang, Z. Yang, Y. Miao, P. K. Chu, K. Xu, and F. Ma, *Appl. Surf. Sci.* **404**, 180 (2017).
- [16] B. Mortazavi, A. Ostadhossein, T. Rabczuk, and A. C. T. van Duin, *Phys. Chem. Chem. Phys.* **18**, 23695 (2016).
- [17] A. Kumar, T. Staedler, and X. Jiang, *Beilstein J. Nanotechnol.* **4**, 66 (2013).
- [18] H. Wang, K. C.-C. Huang, and T. Polcar, *Sci. Rep.* **9**, 334 (2019).
- [19] A. Cammarata and T. Polcar, *Nanoscale* **9**, 11488 (2017).
- [20] F. He, X. Yang, Z. Bian, G. Xie, D. Guo, and J. Luo, *Small* **15**, 1904613 (2019).
- [21] Q. Liu, L. Li, Y. Li, Z. Gao, Z. Chen, and J. Lu, *J. Phys. Chem. C* **116**, 21556 (2012).
- [22] R. Rani, N. Jena, A. Kundu, A. De Sarkar, and K. S. Hazra, *J. Appl. Phys.* **127**, 145101 (2020).
- [23] C. Wang, W. Chen, Y. Zhang, and Q. Sun, *Tribol. Lett.* **59**, 48 (2015).
- [24] J. Wang, J. Li, C. Li, X. Cai, W. Zhu, and Y. Jia, *Tribol. Lett.* **61**, 1 (2016).
- [25] Y. J. Yun, C. S. Ah, S. Kim, W. S. Yun, B. C. Park, and D. H. Ha, *Nanotechnology* **18**, 505304 (2007).
- [26] X. Gonze, B. Amadon, G. Antonius, F. Arnardi, L. Baguet, J.-M. Beuken, J. Bieder, F. Bottin, J. Bouchet, E. Bousquet, N. Brouwer, F. Bruneval, G. Brunin, T. Cavignac, J.-B. Charraud, W. Chen, M. Côté, S. Cottenier, J. Denier, G. Geneste, P. Ghosez, M. Giantomassi, Y. Gillet, O. Gingras, D. R. Hamann, G. Hautier, X. He, N. Helbig, N. Holzwarth, Y. Jia, F. Jollet, W. Lafargue-Dit-Hauret, K. Lejaeghere, M. A. L. Marques, A. Martin, C. Martins, H. P. C. Miranda, F. Naccarato, K. Persson, G. Petretto, V. Planes, Y. Pouillon, S. Prokhorenko, F. Ricci, G.-M. Rignanese, A. H. Romero, M. M. Schmitt, M. Torrent, M. J. van Setten, B. V. Troeye, M. J. Verstraete, G. Zérah, and J. W. Zwanziger, *Comput. Phys. Commun.* **248**, 107042 (2020).
- [27] A. H. Romero, D. C. Allan, B. Amadon, G. Antonius, T. Applencourt, L. Baguet, J. Bieder, F. Bottin, J. Bouchet, E. Bousquet, F. Bruneval, G. Brunin, D. Caliste, M. Côté, J. Denier, C. Dreyer, P. Ghosez, M. Giantomassi, Y. Gillet, O. Gingras, D. R. Hamann, G. Hautier, F. Jollet, G. Jomard, A. Martin, H. P. C. Miranda, F. Naccarato, G. Petretto, N. A. Pike, V. Planes, S. Prokhorenko, T. Rangel, F. Ricci, G.-M. Rignanese, M. Royo, M. Stengel, M. Torrent, M. J. van Setten, B. V. Troeye, M. J. Verstraete, J. Wiktor, J. W. Zwanziger, and X. Gonze, *J. Chem. Phys.* **152**, 124102 (2020).

- [28] M. Torrent, F. Jollet, F. Bottin, G. Zerah, and X. Gonze, *Comput. Mater. Sci.* **42**, 337 (2008).
- [29] D. R. Hamann, *Phys. Rev. B* **88**, 085117 (2013).
- [30] X. Gonze, B. Amadon, P.-M. Anglade, J.-M. Beuken, F. Bottin, P. Boulanger, F. Bruneval, D. Caliste, R. Caracas, M. Côté, T. Deutsch, L. Genovese, P. Ghosez, M. Giantomassi, S. Goedecker, D. Hamann, P. Hermet, F. Jollet, G. Jomard, S. Leroux, M. Mancini, S. Mazevet, M. Oliveira, G. Onida, Y. Pouillon, T. Rangel, G.-M. Rignanese, D. Sangalli, R. Shaltaf, M. Torrent, M. Verstraete, G. Zerah, and J. Zwanziger, *Comput. Phys. Commun.* **180**, 2582 (2009).
- [31] X. Gonze, G.-M. Rignanese, M. Verstraete, J.-M. Beuken, Y. Pouillon, R. Caracas, F. Jollet, M. Torrent, G. Zerah, M. Mikami, P. Ghosez, M. Veithen, J.-Y. Raty, V. Olevano, F. Bruneval, L. Reining, R. Godby, G. Onida, and D. H. D.C. Allan, *Z. Kristallogr. - Cryst. Mater.* **220**, 558 (2005).
- [32] X. Gonze, *Z. Kristallogr. - Cryst. Mater.* **220**, 558 (2005).
- [33] B. Schönfeld, J. J. Huang, and S. C. Moss, *Acta Crystallogr. B* **39**, 404 (1983).
- [34] V. Kalikhman, *Inorg. Mater.* **19**, 957 (1983).
- [35] L. Brixner, *J. Inorg. Nucl. Chem.* **24**, 257 (1962).
- [36] W. Schutte, J. D. Boer, and F. Jellinek, *J. Solid State Chem.* **70**, 207 (1987).
- [37] V. L. Kalikhman, *Neorganicheskie Materialy* **19**, 1060 (1983).
- [38] A. A. Yanaki and V. A. Obolonchik, *Inorg. Mater.* **9**, 1855 (1973).
- [39] See Supplemental Material at <http://link.aps.org/supplemental/10.1103/PhysRevB.102.155433>, section “Benchmark of van der Waals corrections” which includes Refs. [78–82], section “ Γ – A Phonon Band Dispersion in the MX_2 model systems,” section “Sliding and breathing mode frequencies as a function of the applied field,” section “Charge density difference projections, and section “Integration intervals for the calculation of the cophonicity.”
- [40] J. P. Perdew, K. Burke, and M. Ernzerhof, *Phys. Rev. Lett* **77**, 3865 (1996).
- [41] A. D. Becke and E. R. Johnson, *J. Chem. Phys.* **124**, 221101 (2006).
- [42] R. W. Nunes and X. Gonze, *Phys. Rev. B* **63**, 155107 (2001).
- [43] R. W. Nunes and D. Vanderbilt, *Phys. Rev. Lett.* **73**, 712 (1994).
- [44] M. Mehregany, S. Senturia, J. Lang, and P. Nagarkar, *IEEE Trans. Electron Devices* **39**, 2060 (1992).
- [45] G. Meng, Y. Cheng, L. Chen, Y. Chen, and K. Wu, in *2013 IEEE International Conference on Solid Dielectrics ICSD 2013: Bologna, Italy, 30 June - 4 July 2013; Vol. 1, IEEE International Conference on Solid Dielectrics; 11* (IEEE, Piscataway, NJ, 2013), pp. 662–665.
- [46] J. Guo, J. Gallegos, A. Tom, and D. Fan, *ACS Nano* **12**, 1179 (2018).
- [47] Y. Yoshizumi, T. Honegger, K. Berton, H. Suzuki, and D. Peyrade, *Small* **11**, 5630 (2015).
- [48] L. Zhang, Z. Xiao, X. Chen, J. Chen, and W. Wang, *ACS Nano* **13**, 8842 (2019).
- [49] A. Togo and I. Tanaka, *Scr. Mater.* **108**, 1 (2015).
- [50] A. Cammarata and T. Polcar, *Phys. Chem. Chem. Phys.* **18**, 4807 (2016).
- [51] A. Cammarata and T. Polcar, *Inorg. Chem.* **54**, 5739 (2015).
- [52] A. Cammarata and T. Polcar, *Phys. Rev. B* **96**, 085406 (2017).
- [53] A. Cammarata, P. Nicolini, K. Simonovic, E. Ukraintsev, and T. Polcar, *Phys. Rev. B* **99**, 094309 (2019).
- [54] A. Cammarata and T. Polcar, *Phys. Rev. B* **102**, 085409 (2020).
- [55] When the eigendisplacement of a phonon mode is unstable, the corresponding eigenfrequency is an imaginary number; however, it is instead usually indicated by a negative real number for convenience of representation.
- [56] S. Zhou, J. Han, S. Dai, J. Sun, and D. J. Srolovitz, *Phys. Rev. B* **92**, 155438 (2015).
- [57] T. Liang, W. G. Sawyer, S. S. Perry, S. B. Sinnott, and S. R. Phillpot, *Phys. Rev. B* **77**, 104105 (2008).
- [58] G. Levita, E. Molinari, T. Polcar, and M. C. Righi, *Phys. Rev. B* **92**, 085434 (2015).
- [59] A. V. Lebedev, I. V. Lebedeva, A. M. Popov, A. A. Knizhnik, N. A. Poklonski, and S. A. Vyrko, *Phys. Rev. B* **102**, 045418 (2020).
- [60] B. J. Irving, P. Nicolini, and T. Polcar, *Nanoscale* **9**, 5597 (2017).
- [61] W. Jo, I. Eom, E. C. Landahl, S. Lee, and C.-J. Yu, *Rev. Sci. Instrum.* **87**, 035107 (2016).
- [62] N. Casaretto, D. Schaniel, P. Alle, E. Wenger, P. Parois, B. Fournier, E.-E. Bendeif, C. Palin, and S. Pillet, *Crystallogr. Sect.* **73**, 696 (2017).
- [63] T. Ors, N. Ranc, M. Pelerin, V. Michel, V. Favier, O. Castelnaud, C. Mocuta, and D. Thiaudière, *J. Synchrotron Radiat.* **26**, 1660 (2019).
- [64] A. Cammarata, *RSC Adv.* **9**, 37491 (2019).
- [65] A. Cammarata and J. M. Rondinelli, *Phys. Rev. B* **87**, 155135 (2013).
- [66] A. Cammarata and J. M. Rondinelli, *J. Chem. Phys.* **141**, 114704 (2014).
- [67] D. M. Wallace, *Thermodynamics of Crystals* (John Wiley & Sons Inc, 1972).
- [68] J. M. Ziman, *Electrons and Phonons: The Theory of Transport Phenomena in Solids* (Oxford University Press, 2001).
- [69] T. Hu, M. Hu, Z. Li, H. Zhang, C. Zhang, J. Wang, and X. Wang, *J. Phys. Chem. A* **119**, 12977 (2015).
- [70] Z. Lu, C. Chen, Z. M. Baiyee, X. Chen, C. Niu, and F. Ciucci, *Phys. Chem. Chem. Phys.* **17**, 32547 (2015).
- [71] R. Fei, W. Kang, and L. Yang, *Phys. Rev. Lett.* **117**, 097601 (2016).
- [72] Z. Hu, Y. Ding, X. Hu, W. Zhou, X. Yu, and S. Zhang, *Nanotechnology* **30**, 252001 (2019).
- [73] Y. Fan, X. Liu, J. Wang, H. Ai, and M. Zhao, *Phys. Chem. Chem. Phys.* **20**, 11369 (2018).
- [74] J. Wei, Z. Wang, W. Chen, and D. H. Cobden, *Nat. Nanotechnol.* **4**, 420 (2009).
- [75] D. Singh and B. Viswanath, *J. Mater. Sci.* **52**, 5589 (2017).
- [76] S. Lv, H. Li, Z. Wang, L. Han, Y. Liu, X. Liu, and J. Meng, *Appl. Phys. Lett.* **99**, 202110 (2011).
- [77] A. I. Poteryaev, M. Ferrero, A. Georges, and O. Parcollet, *Phys. Rev. B* **78**, 045115 (2008).
- [78] S. Grimme, *J. Comput. Chem.* **25**, 1463 (2004).
- [79] I. V. Lebedeva, A. V. Lebedev, A. M. Popov, and A. A. Knizhnik, *Comput. Mater. Sci.* **128**, 45 (2017).
- [80] S. Grimme, *J. Comput. Chem.* **27**, 1787 (2006).
- [81] A. Ambrosetti and P. L. Silvestrelli, *Phys. Rev. B* **85**, 073101 (2012).
- [82] P. L. Silvestrelli, *J. Chem. Phys.* **139**, 054106 (2013).

Effect of Noninteracting Intercalants on Layer Exfoliation in Transition-Metal Dichalcogenides

Jamil Missaoui^{✉,*}, Antonio Cammarata^{✉,†}, Florian Belviso[✉], and Tomas Polcar[✉]

Department of Control Engineering, Faculty of Electrical Engineering, Czech Technical University in Prague, Technická 2, 16627 Prague 6, Czech Republic

 (Received 12 November 2020; revised 21 May 2021; accepted 21 May 2021; published 16 June 2021)

The control of friction at the atomic scale is fundamental to optimize the exfoliation of layered materials. To this aim, we report a density-functional investigation of how intercalated molecules affect the nanoscale friction of van der Waals transition-metal dichalcogenides. We find that the molecule does not interact with the electronic density of the layers directly; nonetheless it determines the features of the valence band of the system. In particular, the valence-band width appears to be a promising parameter to correlate the electronic properties with the nanofrictional response; it then constitutes a guide for the automatic search of intercalation molecules suitable for layer exfoliation. The present outcomes also constitute a theoretical tool for future investigations of the effect that intercalated species have on the nanoscale friction in layered materials.

DOI: [10.1103/PhysRevApplied.15.064041](https://doi.org/10.1103/PhysRevApplied.15.064041)

I. INTRODUCTION

The discovery of graphene [1] opened up a new area of research into low-dimensional materials. Since then, many inorganic graphene analogs, such as boron nitride, borocarbonitrides, metal oxides, metal-organic frameworks, and transition-metal dichalcogenides (TMDs) [2,3] have attracted great attention because of their wide applicability in photovoltaic devices, lithium-ion batteries, hydrogen-evolution catalysis, transistors, photodetectors, DNA detection, memory devices, and tribological applications [4–7]. Among the compounds mentioned, we focus here on TMDs, lamellar structures held together by weak van der Waals forces.

Like graphene and other van der Waals solids, bulk TMDs can be exfoliated into single-layer or few-layer structures by physical or chemical routes, such as the adhesive tape technique [8], solvent-assisted exfoliation [9], and chemical exfoliation via ion intercalation [10–12]. Exfoliation of these materials into monolayer or few-layer thin films leads to additional exciting properties due to confinement effects, which are not seen in the bulk counterparts [13–18]. In this respect, great expectations are placed on finite two-dimensional systems, where transition-metal dichalcogenides play a fundamental role—the flexible chemistry and stoichiometry easily open several routes to engineer heterostructures with diverse functionalities at the nanoscale.

The fundamental starting point to build two-dimensional TMD-based systems is to obtain monolayer or few-layer TMD films. The crucial aspect involved in harnessing layer exfoliation is understanding the interlayer environment. In bulk TMD structures, the weak van der Waals forces allow relative sliding of adjacent layers and ease layer separation under external stimulations. Individual layers of TMDs can be isolated from the bulk parent via mechanical cleavage [19–21], liquid exfoliation [22,23], or ion intercalation [11,24–26]. Mechanical cleavage produces single-crystal flakes of high purity and cleanliness that are suitable for characterization and fabrication of individual devices. However, this method is not scalable yet, and does not allow systematic control of flake thickness and size [27]. A focused laser spot has been used to reduce MoS₂ bulk to monolayers by thermal ablation, but the requirement for laser scanning makes it challenging for scale-up [28]. On the other hand, liquid-phase exfoliation of TMDs is very promising. Sonication-assisted exfoliation in solvents [22,23,29,30] results in the production of single-layer and multilayer nanosheets that are then stabilized by interactions with the solvent and surfactant. This method has the advantage of being simple despite it producing high-quality small exfoliated nanosheets, but one of the main drawbacks is that very little is known about the stabilization mechanism [31]. Finally, ion intercalation has been regarded as an efficient way to reduce several layered compounds into thin sheets [32,33]; however, this method is time-consuming, is extremely sensitive to environmental conditions, and can result in structural deformations [34], besides the complication represented by ion removal and the subsequent reaggregation of layers

*missajam@fel.cvut.cz

†cammaant@fel.cvut.cz

[35]. The most-promising method would then seem to be the intercalation of inert species rather than ionic species to prevent unwanted interactions.

Computational investigations of exfoliation of layered materials have focused mainly on interlayer adhesion energies also in the presence of exfoliation-assisting molecules [36–40], and very few of them have dealt with TMD compounds [41]. Adhesion is the main force resisting the layer peeling, and is then one of the main structural responses to be harnessed to facilitate the exfoliation process. However, adhesion is inevitably accompanied by the resistance that adjacent atomic layers develop to prevent the relative parallel shift, this occurring because the exfoliation is initiated and done by mechanical stress at a tangent to the layer surface [42–45]: layer sliding and layer separation are the two main phenomena that must be controlled to obtain a facile exfoliation of the lamellar structure. Nanotribological properties of TMD layers therefore play a fundamental role in the exfoliation process.

Following the perspective outlined above, in the present work we focus on how inert molecules change the tribological properties of TMD layers when intercalated in the interlayer gap. The presence of the molecule induces an increase of the interlayer spacing and weakens the van der Waals interaction and hence the forces binding the layers together and preventing the layer sliding [44]; as a consequence, the layer gliding is favored, and the energy required to separate the layers is reduced. It has been shown [46] that intercalated water molecules in MoS₂ considerably hinder the sliding motion of the layer. Moreover, an enhancement of friction by water intercalation between graphene and mica by a factor of approximately 3 relative to dry mica was found [47]; this has been supported by density-functional-theory calculations that revealed that the water broadens the spectral range of graphene vibrations, leading to new excitation channels and increasing the overlap with the atomic vibrations of the mica substrate. We earlier observed that specific phonon modes play a fundamental role in energy transfer under tribological conditions in TMD-based materials [48]. In the present work, by means of quantum-mechanical simulations, we show that the nanotribological properties correlate with the modifications induced in the valence band of the pristine material. Although the molecule does not interact with the atoms of the TMD layer, we find that the electronic states of the molecule modify the relative M/X composition of the occupied states up to the Fermi level [49] together with the width of the valence band; the latter appears to be the quantity to control to tune the frictional response at the nanoscale in the presence of inert intercalated moieties. Finally, we discuss how the present outcomes could constitute a starting point to develop experimental guidelines for the selection of inert species to assist the exfoliation of layered materials, thus boosting the development of nanoengineered devices with wide applicability.

II. METHODS

A. Computational details

Pristine TMDs are layered structures, with the formula unit MX_2 , where M is a transition metal and X is a chalcogen atom; $M-X$ bonds are arranged in a trigonal prismatic configuration forming layers characterized by strong covalent character, which provides in-plane stability of the periodic structure; the layers are held together by weak out-of-plane van der Waals interactions, allowing easy relative sliding parallel to the layer planes. We select the hexagonal $P6_3/mmc$ $2H$ polymorphs [5] with M being Mo or W and X being S, Se, or Te as reference structures [50–55]. We also consider the presence of one CO₂ molecule or one N₂ molecule in the interlayer gap of a $2 \times 2 \times 1$ supercell of the pristine geometry. In this way, we build the model geometries for our simulations, which we name $Z-MX$, where M and X specify the kind of cation and anion forming the MX_2 layers, respectively, while Z (N₂ or CO₂) specifies the intercalated molecular species; $Z = 0$ indicates that no molecule is present in the unit cell and the structure is the pristine one (Fig. 1).

Our calculations are based on density-functional theory with projector-augmented-wave formalism for the specification of the atom pseudopotentials as implemented in the ABINIT package [56–59]. After preliminary benchmarks [60], we choose the Perdew-Burke-Ernzerhof energy functional [61] for the exchange-correlation potential and the DFT-D3(BJ) van der Waals correction [62] for the representation of the long-range interlayer interactions. We select a cutoff energy for the plane-wave basis set of 700 eV and sample the Brillouin zone by using a $7 \times 7 \times 5$ Monkhorst-Pack division [63]. The solution of the self-consistent-field equations is considered converged within an energy tolerance of 10^{-10} eV, while the atomic positions

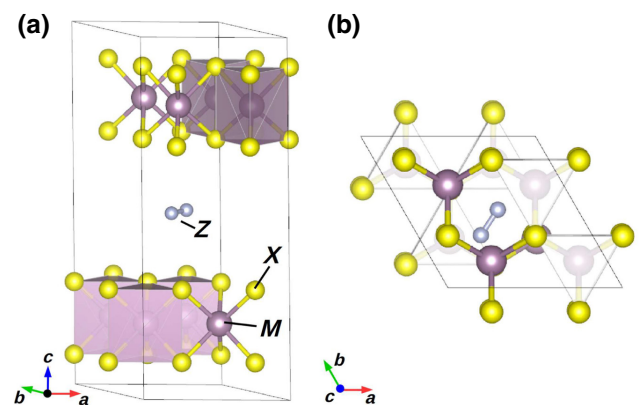


FIG. 1. Schematic of a $Z-MX$ model geometry; here, $Z = N_2$ as an example. Each M cation coordinates six X anions via covalent bonds, forming MX_2 layers; the Z molecule sits in the interlayer gap and modulates the van der Waals forces binding the layers together. (a) Lateral view; (b) view along the c axis.

and lattice parameters are fully relaxed with a tolerance of 5×10^{-6} eV/Å. We perform several geometric optimizations that differ in the starting position and orientation of the molecule. Despite the differences among the starting geometries, the corresponding final optimized configurations are identical within a tolerance of 10^{-4} Å; we then consider the ground-state geometries obtained to be well defined and we consider these in the present calculations. The stable geometries containing the intercalant molecule are reported in Supplemental Material [64].

We use PHONOPY [65] to diagonalize the dynamical matrix of the stable structures built with the finite-displacement method [66,67], whereas the force constants are evaluated on $2 \times 2 \times 2$ and $1 \times 1 \times 2$ supercells of the pristine and molecule-containing systems, respectively.

B. Sliding and breathing modes

The exfoliation process occurs because of the combined action of external forces acting along the shear and vertical directions with respect to the layer plane [42–45]; such forces are capable of overcoming the internal forces that bind the layers together. This can be visualized in the following way. If an external macroscopic force acts on the system with a non-null component at a tangent to the material surface, the atomic layers slide on shearing. As a response, internal forces opposing the shift develop, and the relative motion is realized as long as the external tangent force is active and larger than the internal forces. The internal forces manifest themselves as friction and are the result of several factors, such as asperities, dislocations, layer truncations, and defects; if such irregularities are not present, friction still occurs and is due to only the interatomic forces arising from the electronic density and the atomic geometry. In this latter case, we refer to it as “intrinsic friction” since it is an intrinsic characteristic of the system [60,68,69], and it is the subject of the present study.

Relative atomic motions are usually described by a set of Cartesian vectors, the components of which represent the atomic displacements. An equivalent description is obtained by using suitable linear combinations of phonon eigendisplacements, which are a complete geometric basis set and therefore provide complete information on the atomic configuration [70–72]. The phonon eigenvectors representing relative layer displacements parallel to the layer planes are named “sliding modes” [73,74]: they appear with the largest coefficients in the linear combination and keep active the layer sliding as long as their population is above a certain threshold [48,75]. The sliding modes may be visualized as restoring forces that return the layers to their equilibrium position; in the harmonic approximation, they are proportional to the square of the mode frequency. As a consequence, a low frequency associated with the sliding modes corresponds to a low

restoring frictional force and hence to low intrinsic friction and facile sliding.

In addition to parallel sliding, other kinds of displacements are significant during the exfoliation process. The lateral displacement of the layers generates an excessive overlap of the atomic electronic densities in the interlayer gap; as a consequence, a repulsive force arises due to Coulombic interaction and the Pauli exclusion principle. As the effect of the external force is to drag the layers along directions parallel to the MX_2 planes, such repulsive force results into an increased separation of the layers; if this movement were not allowed, then the repulsive force would push the layers laterally back, thus increasing the sliding energy barrier. This means that if the forces tying the layers together are weak, then it is easier to separate them, and the sliding is promoted. These forces arise mainly from the van der Waals interactions and manifest themselves as the *breathing* phonon modes; they may be regarded as the harmonic representation of adhesion forces. Analogously to the sliding modes, a low breathing frequency then corresponds to an easy variation of the interlayer distance and hence to low adhesion and facilitated sliding.

Both sliding and breathing modes are then active whenever two subsequent layers are laterally displaced to be separated; if the separation occurs because of only vertical forces, then solely the breathing modes are active and hinder the exfoliation. The control of both sliding and breathing frequencies is then desirable to optimize the exfoliation process. To this aim, we focus on the frequencies of both the sliding modes and the breathing modes. To reduce the number of parameters and facilitate the analysis, we consider the mean sliding frequency ω_{sl} , which reads

$$\omega_{sl} = \frac{1}{N} \sum_j^N \omega_j, \quad (1)$$

where ω_j is the frequency of the j th sliding mode and N is the total number of sliding modes considered; the mean breathing frequency ω_{br} is defined in an analogous way. In practice, the distinction between breathing modes and sliding modes is done by considering reference vectors parallel and perpendicular to the layer surface. The modes with large scalar projections along the parallel or perpendicular reference vectors are labeled as sliding modes and breathing modes, respectively. This characterization criterion has already been used for the mode decomposition of sliding trajectories [75].

III. RESULTS AND DISCUSSION

We begin our analysis by considering the features of the unit cell. As soon as a molecule is inserted into the interlayer region, the symmetries of the pristine structure are

reduced to those of the $P1$ crystallographic space group. For fixed M and X atomic species, lattice parameters a and b are not affected by the kind of molecule, while the main variation is observed for the c crystallographic axis, which accounts for the volume increase (Fig. 2); no significant difference is found instead for the cases with the two different molecules. In general, the presence of a molecule induces a lowering of ω_{sl} and ω_{br} with respect to the pristine case ($Z = 0$), irrespective of the chemical composition of the layers; this is expected, because the presence of the molecule increases the separation between the layers and screens the interaction between them, making the sliding (friction) and breathing (adhesion) restoring forces weaker. However, although the steric hindrance of the CO_2 molecule is larger than that of N_2 molecule, the effect on the mean sliding and breathing frequencies is a peculiarity of the system (Fig. 3): while the mean sliding frequency decreases in the sequence $0 > \text{N}_2 > \text{CO}_2$, the mean breathing frequency increases in the $Z\text{-MoS}$, $Z\text{-MoSe}$, and $Z\text{-WTe}$ systems when Z changes from N_2 to CO_2 . A comparison between Figs. 2 and 3 shows that

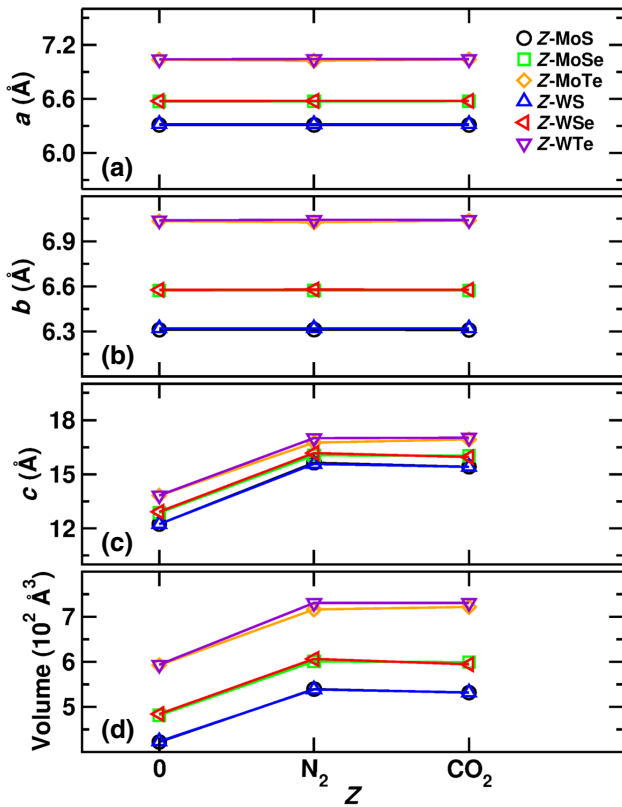


FIG. 2. (a)–(c) Length of the lattice vectors and (d) volume of the unit cell of the systems considered for different molecular moieties in the interlayer gap. The legend is common to all plots. For a fixed Z , the values relative to systems with the same X anion are very close and the corresponding data points almost overlap in all the plots.

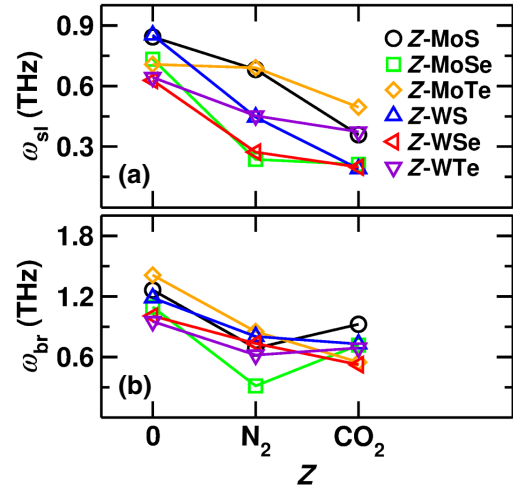


FIG. 3. Average frequency of (a) sliding modes and (b) breathing modes for the molecular moieties considered. The legend is common to both plots.

there is no direct relation between the cell volume and the frequency shift; ω_{sl} and ω_{br} increase or decrease with the volume according to the specific chemical composition (Fig. 4). The frequency shift is not then a mere result of the change in the geometry of the system but arises from the subtle interplay between the electronic features and the dynamic features. The phonon frequencies are obtained from the diagonalization of the dynamical matrix, which, in turn, is the normalized Fourier transform of the interatomic force constants [70,71]; these depend on the atomic types forming the system and determining the electronic environment in which they are embedded. Any change induced in the electronic distribution of the pristine material is therefore reflected in a change of the

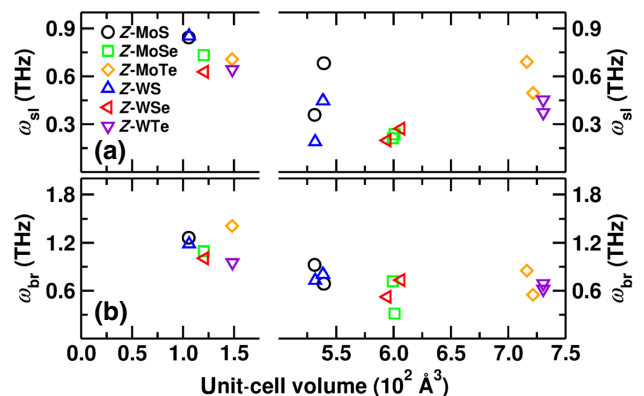


FIG. 4. Average frequency of (a) sliding modes and (b) breathing modes as a function of the unit-cell volume. Volumes in the left part of the plots correspond to the 0-MX systems. The legend is common to both plots.

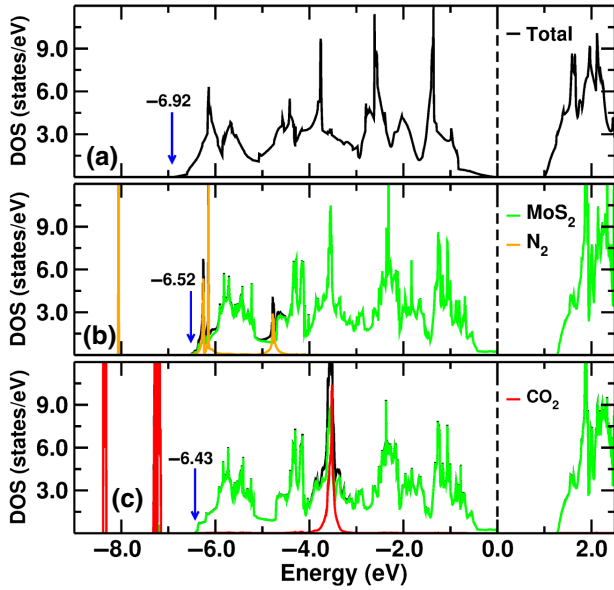


FIG. 5. Density of states of the (a) 0-MoS, (b) N_2 -MoS, and (c) CO_2 -MoS systems. The DOS are normalized by a factor chosen to optimize the visualization. In each plot, the Fermi level is set to 0 eV and is marked by a vertical dashed line, while the blue arrow indicates the position of the bottom of the valence band, with the corresponding value reported immediately above. The legends are common to the different plots as appropriate.

atomic interactions and the corresponding phonon frequencies. For this reason, we continue our analysis by focusing on the electronic density of states (DOS).

A typical profile of Z - MX electronic DOS is reported in Fig. 5, where we show the case of the Z -MoS systems.

The valence band of the pristine material covers the energy range from -6.92 to 0 eV [Fig. 5(a)]; once a molecule is inserted into the interlayer gap, the width of the valence band is narrowed by an amount that depends on the kind of molecule [Figs. 5(b) and 5(c)]. The atom-projected DOS reveals that the molecule contributes with its own states to the valence band; however, no hybridization occurs between the atomlike wave functions centered at the molecule and those centered at each surrounding X anion. This behavior is expected because N_2 and CO_2 are inert gases and any non-null wave-function overlap would indicate an interaction between the molecule and the layers. This is apparent from the analysis of the partial electronic density generated by our considering the energy bands relative to the range that includes the Z states in the valence band (Fig. 6): the partial electronic distribution is localized on the molecule and around the cation within the layer, while no density shared between the layers and the molecule is found. The effect of the orbitals of the molecule is then to change the width of the valence band by contributing to the wave function of the whole system without interacting with the orbitals of MX_2 layer, but yet determining the relative position of the latter within the valence band. By comparing Figs. 2 and 7(a), we see that the valence-band width does not correlate with the length of the lattice vectors nor with the system volume; interestingly, the width decreases in the sequence $0 > \text{N}_2 > \text{CO}_2$ irrespective of the chemical composition of the layers. Such behavior is similar to that found for the sliding and breathing frequencies (Fig. 3); ω_{sl} and ω_{br} seem to correlate with the width of the valence band [Figs. 7(b) and 7(c)]. In general, we observe that an increase of the valence-band width favors higher sliding and breathing frequencies; this

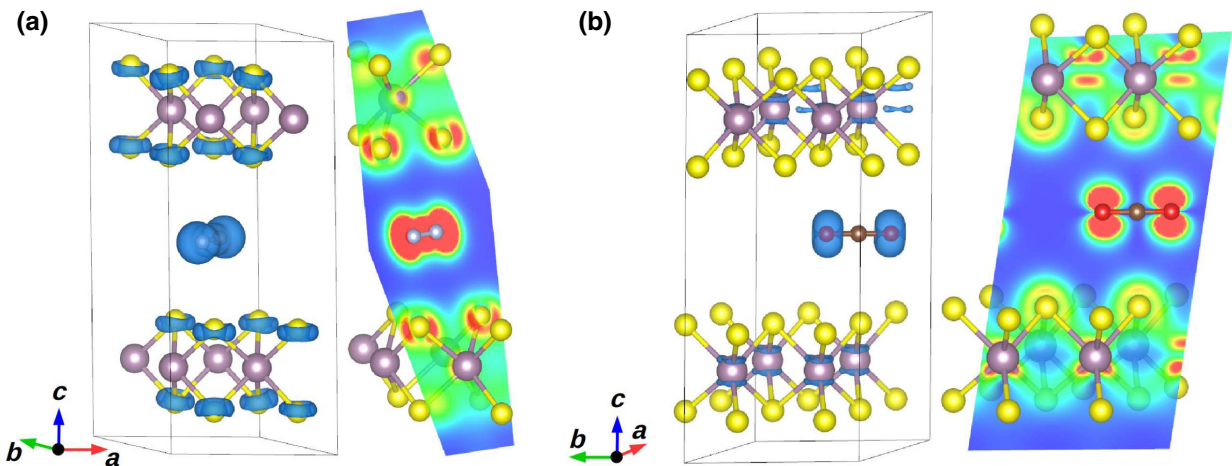


FIG. 6. Isosurface (blue) and plane projection of the partial charge density in (a) N_2 -MoS and (b) CO_2 -MoS obtained by our selecting the electronic bands in the range $[-6.5, -6.0] \cup [-5.0, -4.5]$ and $[-4.0, -3.2]$ eV, respectively, each including the corresponding Z states (see Fig. 5). No significant charge is found in the region between the molecule and the sulfur atoms, this showing that no hybridization occurs between the S-centered and molecule-centered atomic orbitals. The red-green-blue color gradient indicates decreasing charge density.

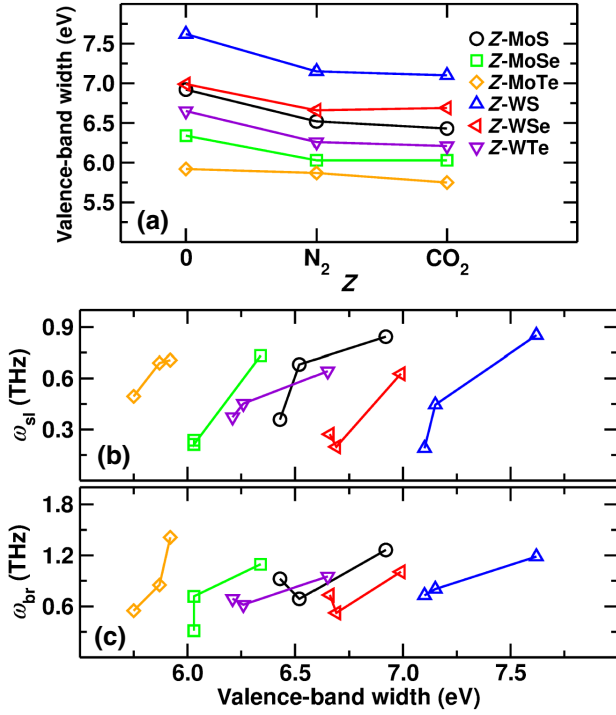


FIG. 7. (a) Width of the valence band as a function of the intercalated moiety. Average frequency of (b) sliding modes and (c) breathing modes as a function of the width of the valence band. The legend is common to all plots.

suggests that it is beneficial to narrow the valence band to reduce the lateral friction and the layer adhesion and hence to promote the layer exfoliation. In passing, we note that the variation range of the valence-band width depends on the specific atomic type forming the layers; for practical applications, it can be pre-evaluated in high-throughput calculations before the experimental validation of the selected exfoliation-assisting species. As shown above, although the orbitals of molecule are involved in the formation of the valence band, they do not interact with the atomlike orbitals pertaining to the M and X ions; however, the modification of the width of the valence band affects the relative position of the M and X orbitals. This has the effect of modulating the overlap of the M and X atom-projected wave functions generating the interatomic charge density and hence of determining the covalent character of the M — X bond. To quantify this effect, we calculate the covalency $C_{M,X}$ of the M — X bonds in terms of the M and X atomic contributions to the DOS in the valence band. The mathematical formulation of $C_{M,X}$ can be found, for example, in Ref. [76]; the integrals appearing in the formulation are evaluated in the range $[-w, 0]$, where w is the width of the valence band reported in Fig. 7. No clear behavior is found for $C_{M,X}$ as a function of Z [Fig. 8(a)]. While, for instance, a change of the Z species induces a variation of the covalency in the

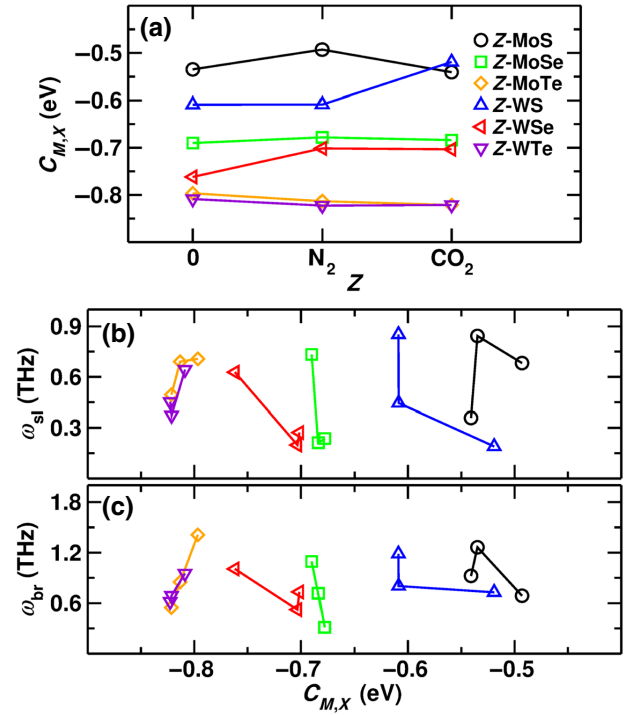


FIG. 8. (a) M — X bond covalency as a function of the molecular moiety. (b),(c) The average frequencies of the sliding modes and the breathing modes do not seem to correlate with the bond covalency as they increase or decrease with $C_{M,X}$ in a different way for different chemical compositions. The legend is common to all plots.

Z -WS and Z -WSe systems, no significant change occurs for the remaining systems. Correspondingly, no correlation is found between ω_{sl} or ω_{br} and $C_{M,X}$ [Figs. 8(b) and 8(c)], as the mean frequencies increase or decrease according to the atomic types forming the system. Incidentally, the ordering of the covalent character for $Z = 0$ is consistent with what we reported in Ref. [73], where different a van der Waals correction, energy cutoff and k -mesh sampling were used. To investigate the subtle variation in the electronic density induced by the Z species, we consider the orbital polarization [60,77,78] $\mathcal{P}_{a,b}$ defined as

$$\mathcal{P}_{j,k} = \frac{n_j - n_k}{n_j + n_k}, \quad (2)$$

where j and k are two sets of atomic orbitals, while n_j and n_k are their respective occupations. With this definition, $\mathcal{P}_{j,k}$ measures the excess of charge in the j orbital with respect to the k orbital. We choose atom-centered hydrogenlike orbitals to calculate the orbital polarizations \mathcal{P}_{p_x,p_y} , \mathcal{P}_{p_x,p_z} , and \mathcal{P}_{p_y,p_z} of the X atoms, and \mathcal{P}_{t_{2g},e_g} and $\mathcal{P}_{d_{x^2-y^2},d_{z^2}}$ of the M cations; in this way, we are able to partition the space according to the directional character of the orbital and to monitor possible preferential distributions of the

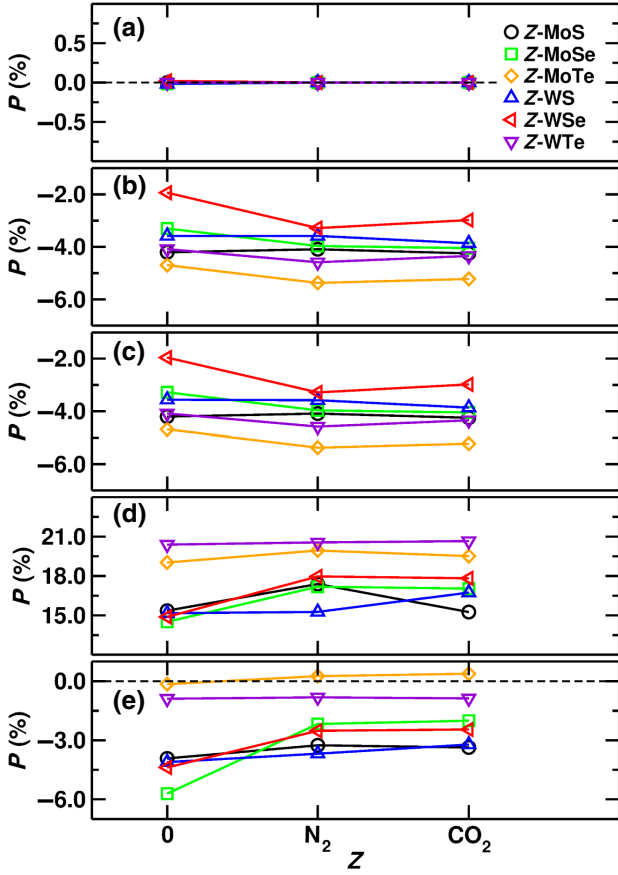


FIG. 9. Orbital polarization of the Z - MX systems versus the intercalated moiety: (a) X \mathcal{P}_{p_x,p_y} , (b) X \mathcal{P}_{p_x,p_z} , (c) X \mathcal{P}_{p_y,p_z} , (d) M \mathcal{P}_{t_{2g},e_g} , and (e) M $\mathcal{P}_{d_{x^2-y^2},d_{z^2}}$. Lines are a guide for the eye.

charge density for different M , X , and Z species. We first observe that, irrespective of the chemical composition, the p_x and p_y orbitals of the X anion are equally populated [Fig. 9(a)]; this is consistent with the fact that the kind of molecule does not affect lattice parameters a and b [Figs. 2(a) and 2(b)], while the equivalence between the a and b crystallographic axes is preserved within the MX_2 layers, such equivalence being present in the pristine system. The change in lattice parameter c with Z [Fig. 2(c)] is instead reflected in \mathcal{P}_{p_x,p_z} and \mathcal{P}_{p_y,p_z} [Figs. 9(b) and 9(c)]: while negative values indicate an excess of electrons at the X site along an axis orthogonal to the layer planes, the presence of a molecule induces, in general, a further accumulation along the same direction. The in-layer local equivalence between the a and b crystallographic axes is reflected in the fact that, for each Z - MX configuration, identical \mathcal{P}_{p_x,p_z} and \mathcal{P}_{p_y,p_z} values are realized. The positive values of \mathcal{P}_{t_{2g},e_g} indicate that an excess of electrons is found in the t_{2g} orbitals, thus favoring an in-plane distribution of the charge [Fig. 9(d)] irrespective of Z ; such a distribution is altered in a different way according to

the kind of molecule and by a different amount specific to the atomic types forming the layers. The largest variation is found for the Z - $MoSe$ and Z - WSe systems, in a way similar to that observed for $\mathcal{P}_{d_{x^2-y^2},d_{z^2}}$. The negative values of the latter point to a preferential distribution of the d_{z^2} orbital with respect to the $d_{x^2-y^2}$ orbital [Fig. 9(e)]; however, a comparison with \mathcal{P}_{t_{2g},e_g} excludes charge accumulation along an axis perpendicular to the layer planes. This analysis shows that there is no clear connection between the Z species and the charge arrangement within the layer; accordingly, no clear relation is found between the orbital polarizations and the sliding and breathing frequencies. This result is different from what we found in the pristine MX_2 systems under different stimuli, in which the orbital polarization plays instead a fundamental role in determining the nanoscale frictional behavior [60,69,79]. We conclude that the molecule suppresses the effect of the details of the electronic distribution inside the layer on the vibrational modes considered. In our analysis so far, we used the properties of the equilibrium geometry to estimate the response of the system during the layer sliding and separation (i.e., to predict the system behavior far from equilibrium). We now want to check the reliability of such a prediction. As a first step, for each of the systems considered, we create a *sliding path* along the M - X bond [Fig. 10(a)]. A sliding path is a sequence of configurations (atom positions and lattice parameters) that represent the relative parallel shift of two subsequent MX_2 layers. The initial guess of the paths is obtained by our considering linear combinations of eigenvectors corresponding to the sliding modes, according to the prescription of the *normal-modes transition approximation* [74]; in this way, we create a total of 11 configurations for each sliding path. We then perform a climbing-image nudged-elastic-band (CI NEB) [80,81] full relaxation (atom positions and lattice vectors) of the paths by means of the software program VASP [82,83]; the general parameters (e.g., mesh sampling, energy cutoff, and tolerances) are the same as those presented in Sec. II A. As a result of the climbing-image NEB calculations, we obtain the potential energy barrier ΔE_{bar} associated with the relative layer sliding. We can then define the average friction force f_{fr} as

$$f_{\text{fr}} = \frac{\Delta E_{\text{bar}}}{\Delta R_{\text{NEB}}}, \quad (3)$$

where ΔE_{bar} is the difference between the energy of the ground state and the maximum energy realized along the path, while

$$\Delta R_{\text{NEB}} = \sqrt{\sum_{i=1}^N |\mathbf{R}_{\text{bar}}^i - \mathbf{R}_0^i|}, \quad (4)$$

with $\mathbf{R}_{\text{bar}}^i$ being the position of the i th atom in the configuration realizing the energy maximum and \mathbf{R}_0^i being the

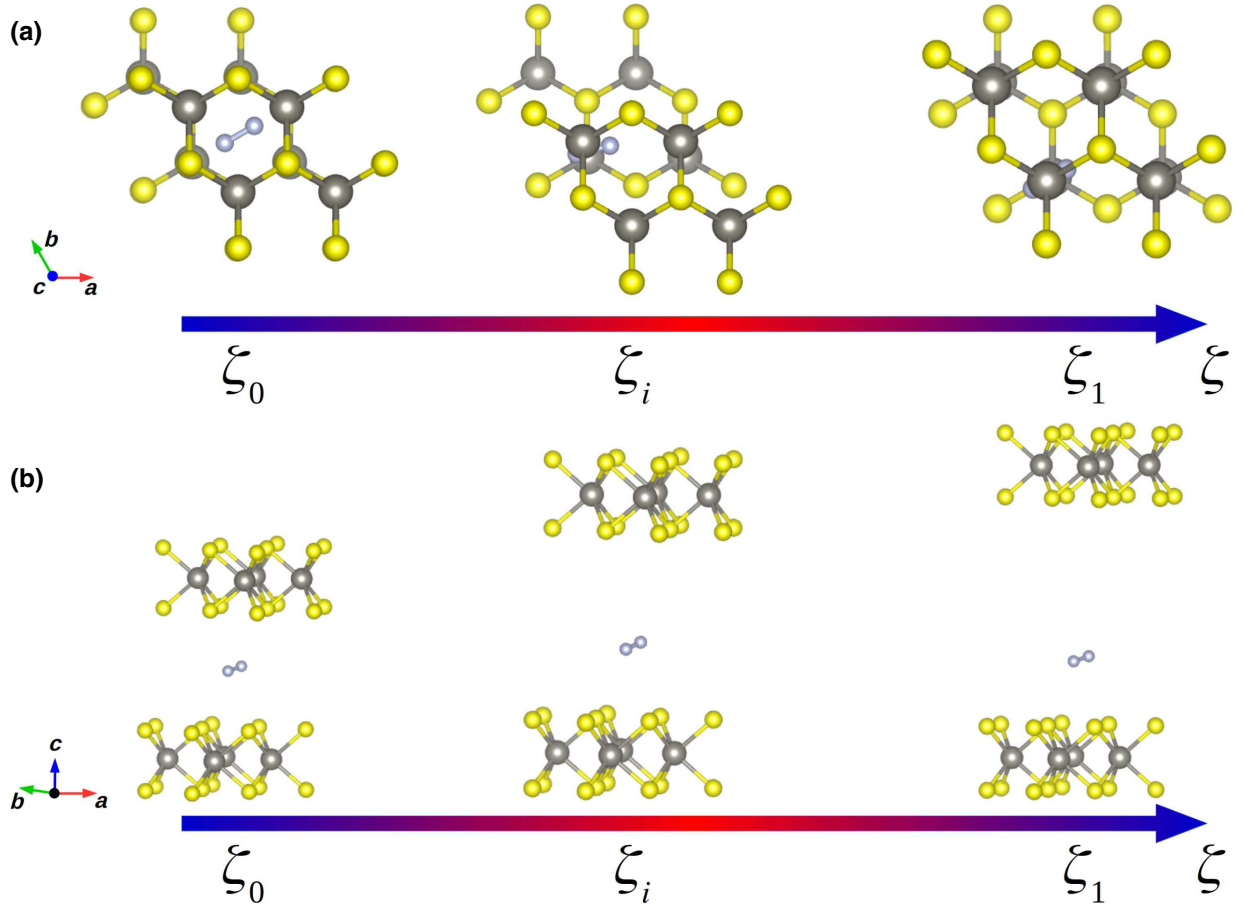


FIG. 10. Example of (a) sliding path and (b) layer separation. Along the configurational coordinate ζ , the initial state, an intermediate state, and the final state are indicated with ζ_0 , ζ_i , and ζ_1 , respectively.

position of the same atom in the equilibrium geometry. With this definition, ΔR_{NEB} is a measure of the displacement covered by the atoms during the sliding. As a second step, we estimate the adhesion force. Starting from the equilibrium geometry, we consider 11 geometric configurations in which the two layers are progressively shifted along the c -axis direction until the interlayer distance is approximately 15\AA [Fig. 10(b)]. For each configuration, we fix the lattice parameters and the positions of the M cations, and finally optimize the coordinates of the remaining atoms. By tracking the evolution of the system energy as a function of the interlayer distance, we observe an asymptotic behavior; this assures us that the last configuration corresponds to noninteracting (separated) layers. Analogously to the definition of the average friction force f_{fr} [Eq. (3)], we then define the average adhesion force f_{ad} as

$$f_{\text{ad}} = \frac{\Delta E_{\text{sep}}}{\Delta R_{\text{sep}}}, \quad (5)$$

where ΔE_{sep} is the difference between the energy of the ground state and the energy of last configuration, while ΔR_{sep} is the layer-layer distance. Similarly to what we observe for the sliding-mode and breathing-mode frequencies, the frictional and adhesion forces display large values in correspondence with large values of the band width (Fig. 11). Moreover, we notice that the adhesion forces are larger than the frictional forces, as the breathing frequencies are larger than the sliding frequencies; this supports the harmonic representation of the two forces discussed in Sec. II B. In the same section, we examined how both lateral friction and adhesion forces appear during the exfoliation process. This suggests we consider an average force $f_{\text{av}} = (f_{\text{fr}} + f_{\text{ad}})/2$ arising during the exfoliation; analogously, we consider the average frequency $\omega_{\text{av}} = (\omega_{\text{sl}} + \omega_{\text{br}})/2$. In general, we notice that both quantities increase with increasing valence-band width (Fig. 12). These results suggest that from the analysis of the equilibrium geometry (electronic structure, phonon spectrum) we may infer the response of the system far from equilibrium (layer sliding and separation); in this respect, the width of the valence

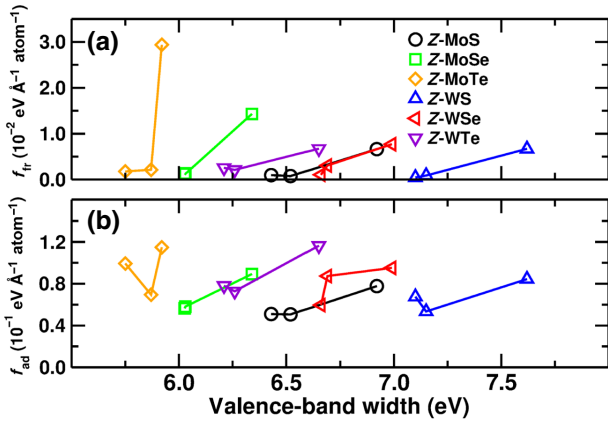


FIG. 11. (a) Lateral frictional force and (b) adhesion force as a function of the width of the valence band. The legend is common to both plots.

band seems to be a useful descriptor to parametrize the forces opposing the layer exfoliation in the presence of inert intercalated molecules.

To further confirm these findings, more inert species and geometries should be the subject of future studies in which the analysis method presented here is applied. Unfortunately, the presence of a molecule reduces the symmetries of the systems to only the translation (space group $P1$). This implies the need to evaluate the ground-state wave function by using a very dense Brillouin-zone sampling, and the calculation of the atomic forces on many distorted configurations, to obtain the phonon spectrum. Moreover, the identification of the stable geometry requires the optimization of several starting configurations differing in the initial molecule position, thus increasing further the computational needs to consider more kinds of intercalant species. For this reason, we limit our analysis to the study

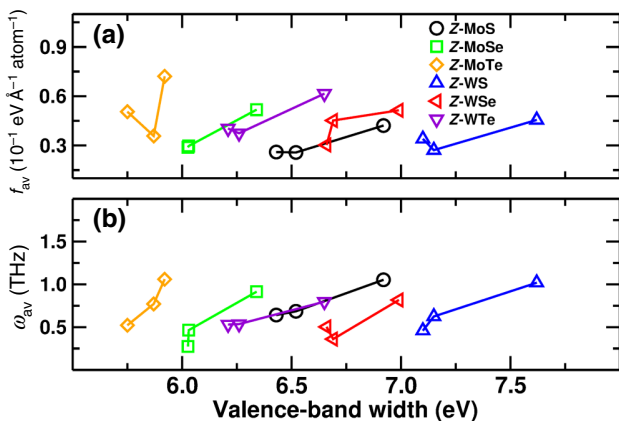


FIG. 12. (a) Average force and (b) average mode frequency as a function of the width of the valence band. Legend is common to all the subfigures.

cases presented. However, we believe that our results already point to an alternative route for how to investigate the relation between the electronic structure and the nanoscale mechanisms hindering the exfoliation. Finally, the width of the valence band seems to be a promising descriptor for automated engines aimed at screening databases in search of suitable exfoliation-assisting moieties, boosting the design of nanoengineered devices with targeted functionalities.

IV. CONCLUSIONS

We study how inert molecules modify the nanofrictional response when used as an intercalant for exfoliation in van der Waals transition-metal dichalcogenides. The exfoliation occurs if the applied external forces, aimed at separating the layers, are larger than the internal forces that return the atoms to their equilibrium positions; such internal forces manifest themselves as internal friction. If we are able to reduce the internal friction, we can facilitate the exfoliation process. We find that the inert intercalated molecule determines the width of the valence band although it does not interact with the atoms of the layers. The valence-band width seems to correlate with the vibrational properties related to the nanoscale friction: small widths correspond to small interlayer binding forces and hence to reduced friction and easy layer sliding and separation. A similar correlation is found with the friction and adhesion forces: the larger the valence-band width, the larger the forces. Since such forces arise during the exfoliation process, our results suggest that suitable values of the band width may ultimately assist the exfoliation. The analysis protocol presented can be used in systematic studies on the frictional response in the presence of inert intercalated species; this would help to define the potentiality and the limitations of the valence-band width as a friction descriptor. The present results also suggest suitable inert molecules to be used in combination with other methods directed at the fine control of the valence band, such as external electric fields [60].

ACKNOWLEDGMENTS

This work was done with the support of the Grant Agency of the Czech Technical University in Prague (Grant No. SGS19/175/OHK3/3T/13), the Czech Science Foundation (Project No. 17-24164Y), the project ‘‘Centre of Advanced Applied Sciences’’ (Grant No. CZ.02.1.01/0.0/0.0/16_019/0000778), and the project ‘‘SOLUTION,’’ which has received funding from the European Union’s Horizon 2020 research and innovation program under Grant Agreement No. 721642. This work was supported by the Ministry of Education, Youth and Sports of the Czech Republic through the e-INFRA CZ (ID:90140).

- [1] K. S. Novoselov, A. K. Geim, S. V. Morozov, D. Jiang, Y. Zhang, S. V. Dubonos, I. V. Grigorieva, and A. A. Firsov, Electric field effect in atomically thin carbon films, *Science* **306**, 666 (2004).
- [2] Dmitri Golberg, Yoshio Bando, Yang Huang, Takeshi Terao, Masanori Mitome, Chengchun Tang, and Chunyi Zhi, Boron nitride nanotubes and nanosheets, *ACS Nano* **4**, 2979 (2010).
- [3] C. N. R. Rao and Urmimala Maitra, Inorganic graphene analogs, *Ann. Rev. Mater. Res.* **45**, 29 (2015).
- [4] Hai Li, Jumiati Wu, Zongyou Yin, and Hua Zhang, Preparation and applications of mechanically exfoliated single-layer and multilayer MoS₂ and WSe₂ nanosheets, *Accounts Chem. Res.* **47**, 1067 (2014).
- [5] Manish Chhowalla, Hyeon Suk Shin, Goki Eda, Lain-Jong Li, Kian Ping Loh, and Hua Zhang, The chemistry of two-dimensional layered transition metal dichalcogenide nanosheets, *Nat. Chem.* **5**, 263 (2013).
- [6] A. K. Geim and I. V. Grigorieva, Van der waals heterostructures, *Nature* **499**, 419 (2013), *perspectives*.
- [7] Andrea Vanossi, Nicola Manini, Michael Urbakh, Stefano Zapperi, and Erio Tosatti, *Colloquium*: Modeling friction: From nanoscale to mesoscale, *Rev. Mod. Phys.* **85**, 529 (2013).
- [8] R. F. Frindt, Single crystals of MoS₂ several molecular layers thick, *J. Appl. Phys.* **37**, 1928 (1966).
- [9] Valeria Nicolosi, Manish Chhowalla, Mercouri G. Kanatzidis, Michael S. Strano, and Jonathan N. Coleman, Liquid exfoliation of layered materials, *Science* **340**, 1226419 (2013).
- [10] Per Joensen, R. F. Frindt, and S. Roy Morrison, Single-layer MoS₂, *Mater. Res. Bull.* **21**, 457 (1986).
- [11] Zhiyuan Zeng, Zongyou Yin, Xiao Huang, Hai Li, Qiyuan He, Gang Lu, Freddy Boey, and Hua Zhang, Single-layer semiconducting nanosheets: High-yield preparation and device fabrication, *Angew. Chem. Int. Edit.* **50**, 11093 (2011).
- [12] Zhiyuan Zeng, Ting Sun, Jixin Zhu, Xiao Huang, Zongyou Yin, Gang Lu, Zhanxi Fan, Qingyu Yan, Huey Hoon Hng, and Hua Zhang, An effective method for the fabrication of few-layer-thick inorganic nanosheets, *Angew. Chem. Int. Edit.* **51**, 9052 (2012).
- [13] Ting Cao, Gang Wang, Wenpeng Han, Huiqi Ye, Chuanrui Zhu, Junren Shi, Qian Niu, Pingheng Tan, Enge Wang, Baoli Liu, and Ji Feng, Valley-selective circular dichroism of monolayer molybdenum disulphide, *Nat. Commun.* **3**, 887 (2012).
- [14] Hualing Zeng, Junfeng Dai, Wang Yao, Di Xiao, and Xiaodong Cui, Valley polarization in MoS₂ monolayers by optical pumping, *Nat. Nano.* **7**, 490 (2012).
- [15] Kin Fai Mak, Keliang He, Jie Shan, and Tony F. Heinz, Control of valley polarization in monolayer MoS₂ by optical helicity, *Nat. Nano.* **7**, 494 (2012).
- [16] Kin Fai Mak, Changgu Lee, James Hone, Jie Shan, and Tony F. Heinz, Atomically Thin MoS₂: A new Direct-Gap Semiconductor, *Phys. Rev. Lett.* **105**, 136805 (2010).
- [17] Humberto R. Gutiérrez, Nestor Perea-López, Ana Laura Elías, Ayse Berkdemir, Bei Wang, Ruitao Lv, Florentino López-Urías, Vincent H. Crespi, Humberto Terrones, and Mauricio Terrones, Extraordinary room-temperature photoluminescence in triangular WS₂ monolayers, *Nano Lett.* **13**, 3447 (2013).
- [18] Xiaobo Yin, Ziliang Ye, Daniel A. Chenet, Yu Ye, Kevin O'Brien, James C. Hone, and Xiang Zhang, Edge nonlinear optics on a MoS₂ atomic monolayer, *Science* **344**, 488 (2014).
- [19] Andrea Splendiani, Liang Sun, Yuanbo Zhang, Tianshu Li, Jonghwan Kim, Chi-Yung Chim, Giulia Galli, and Feng Wang, Emerging photoluminescence in monolayer MoS₂, *Nano Lett.* **10**, 1271 (2010).
- [20] Simone Bertolazzi, Jacopo Brivio, and Andras Kis, Stretching and breaking of ultrathin MoS₂, *ACS Nano* **5**, 9703 (2011).
- [21] B. Radisavljevic, A. Radenovic, J. Brivio, V. Giacometti, and A. Kis, Single-layer MoS₂ transistors, *Nat. Nano.* **6**, 147 (2011).
- [22] Jonathan N. Coleman *et al.*, Two-dimensional nanosheets produced by liquid exfoliation of layered materials, *Science* **331**, 568 (2011).
- [23] Kai-Ge Zhou, Nan-Nan Mao, Hang-Xing Wang, Yong Peng, and Hao-Li Zhang, A mixed-solvent strategy for efficient exfoliation of inorganic graphene analogues, *Angew. Chem. Int. Edit.* **50**, 10839 (2011).
- [24] Minoru Osada and Takayoshi Sasaki, Exfoliated oxide nanosheets: New solution to nanoelectronics, *J. Mater. Chem.* **19**, 2503 (2009).
- [25] Martin B. Dines, Lithium intercalation via *n*-butyllithium of the layered transition metal dichalcogenides, *Mater. Res. Bull.* **10**, 287 (1975).
- [26] Goki Eda, Hisato Yamaguchi, Damien Voiry, Takeshi Fujita, Mingwei Chen, and Manish Chhowalla, Photoluminescence from chemically exfoliated MoS₂, *Nano Lett.* **11**, 5111 (2011).
- [27] Qing Hua Wang, Kourosh Kalantar-Zadeh, Andras Kis, Jonathan N. Coleman, and Michael S. Strano, Electronics and optoelectronics of two-dimensional transition metal dichalcogenides, *Nat. Nanotechnol.* **7**, 699 (2012).
- [28] A. Castellanos-Gomez, M. Barkelid, A. M. Goossens, V. E. Calado, H. S. J. van der Zant, and G. A. Steele, Laser-thinning of MoS₂: On demand generation of a single-layer semiconductor, *Nano Lett.* **12**, 3187 (2012).
- [29] Wei-Qiang Han, Lijun Wu, Yimei Zhu, Kenji Watanabe, and Takashi Taniguchi, Structure of chemically derived mono- and few-atomic-layer boron nitride sheets, *Appl. Phys. Lett.* **93**, 223103 (2008).
- [30] Yi Lin, Tiffany V. Williams, and John W. Connell, Soluble, exfoliated hexagonal boron nitride nanosheets, *J. Phys. Chem. Lett.* **1**, 277 (2010).
- [31] Graeme Cunningham, Mustafa Lotya, Clotilde S. Cucinotta, Stefano Sanvito, Shane D. Bergin, Robert Menzel, Milo S. P. Shaffer, and Jonathan N. Coleman, Solvent exfoliation of transition metal dichalcogenides: Dispersibility of exfoliated nanosheets varies only weakly between compounds, *ACS Nano* **6**, 3468 (2012).
- [32] Z. Ding, L. Viculis, J. Nakawatase, and R. B. Kaner, Intercalation and solution processing of bismuth telluride and bismuth selenide, *Adv. Mater.* **13**, 797 (2001).
- [33] H. S. S. Ramakrishna Matte, A. Gomathi, Arun K. Manna, Dattatray J. Late, Ranjan Datta, Swapan K. Pati, and C. N. R. Rao, MoS₂ and WS₂ analogues of graphene, *Angew. Chem. Int. Edit.* **49**, 4059 (2010).

- [34] S. Jiménez Sandoval, D. Yang, R. F. Frindt, and J. C. Irwin, Raman study and lattice dynamics of single molecular layers of MoS₂, *Phys. Rev. B* **44**, 3955 (1991).
- [35] Rabin Bissessur, Joy Heising, Wakgari Hirpo, and Mercuri Kanatzidis, Toward pillared layered metal sulfides. intercalation of the chalcogenide clusters Co₆Q₈(PR₃)₆ (q = s, se, and te and r = alkyl) into MoS₂, *Chem. Mater.* **8**, 318 (1996).
- [36] Gabin Yoon, Dong-Hwa Seo, Kyojin Ku, Jungmo Kim, Seokwoo Jeon, and Kisuk Kang, Factors affecting the exfoliation of graphite intercalation compounds for graphene synthesis, *Chem. Mater.* **27**, 2067 (2015).
- [37] Reza Rasuli and Azam Irajizad, Density functional theory prediction for oxidation and exfoliation of graphite to graphene, *Appl. Surf. Sci.* **256**, 7596 (2010).
- [38] Gregorio Garcia, Mert Atilhan, and Santiago Aparicio, In silico rational design of ionic liquids for the exfoliation and dispersion of boron nitride nanosheets, *Phys. Chem. Chem. Phys.* **18**, 1212 (2016).
- [39] Yoshiyuki Miyamoto, Hong Zhang, and David Tománek, Photoexfoliation of Graphene from Graphite: An *Ab Initio* Study, *Phys. Rev. Lett.* **104**, 208302 (2010).
- [40] Nina I. Kovtyukhova, Yuanxi Wang, Ayse Berkdemir, Rodolfo Cruz-Silva, Mauricio Terrones, Vincent H. Crespi, and Thomas E. Mallouk, Non-oxidative intercalation and exfoliation of graphite by brønsted acids, *Nat. Chem.* **6**, 957 (2014), article.
- [41] Guijian Guan, Shuangyuan Zhang, Shuhua Liu, Yongqing Cai, Michelle Low, Choon Peng Teng, In Yee Phang, Yuan Cheng, Koh Leng Duei, Bharathi Madurai Srinivasan, Yuangang Zheng, Yong-Wei Zhang, and Ming-Yong Han, Protein induces layer-by-layer exfoliation of transition metal dichalcogenides, *J. Am. Chem. Soc.* **137**, 6152 (2015).
- [42] Jack R. Brent, Nicky Savjani, and Paul O'Brien, Synthetic approaches to two-dimensional transition metal dichalcogenide nanosheets, *Prog. Mater. Sci.* **89**, 411 (2017).
- [43] Xianglu Yin, Yuewei Li, Wei Wu, Guangwen Chu, Yong Luo, and Hong Meng, Preparation of two-dimensional molybdenum disulfide nanosheets by high-gravity technology, *Ind. Eng. Chem. Res.* **56**, 4736 (2017).
- [44] Qingyong Zhang, Liang Mei, Xiehong Cao, Yuxin Tang, and Zhiyuan Zeng, Intercalation and exfoliation chemistries of transition metal dichalcogenides, *J. Mater. Chem. A* **8**, 15417 (2020).
- [45] Liangzhu Zhang, Cheng Chen, Jiadong Zhou, Guoliang Yang, Jiemin Wang, Dan Liu, Zhiqiang Chen, and Weiwei Lei, Solid phase exfoliation for producing dispersible transition metal dichalcogenides nanosheets, *Adv. Funct. Mater.* **30**, 2004139 (2020).
- [46] Giacomo Levita and Maria C. Righi, Effects of water intercalation and tribochemistry on MoS₂ lubricity: An ab initio molecular dynamics investigation (chemphyschem 11/2017), *ChemPhysChem* **18**, 1490 (2017).
- [47] Hyunsoo Lee, Jae-Hyeon Ko, Jin Sik Choi, Jin Heui Hwang, Yong-Hyun Kim, Miquel Salmeron, and Jeong Young Park, Enhancement of friction by water intercalated between graphene and mica, *J. Phys. Chem. Lett.* **8**, 3482 (2017).
- [48] Antonio Cammarata and Tomas Polcar, Control of energy dissipation in sliding low-dimensional materials, *Phys. Rev. B* **102**, 085409 (2020).
- [49] Qionghua Zhou, Qiang Li, Shijun Yuan, Qian Chen, and Jinlan Wang, Band-edge engineering via molecule intercalation: A new strategy to improve stability of few-layer black phosphorus, *Phys. Chem. Chem. Phys.* **19**, 29232 (2017).
- [50] B. Schönfeld, J. J. Huang, and S. C. Moss, Anisotropic mean-square displacements (msd) in single-crystals of 2H- and 3R-MoS₂, *Acta Crystallogr. B* **39**, 404 (1983).
- [51] V. L. Kalikhman, *Inorg. Mater.* **19**, 957 (1983).
- [52] L. H. Brixner, Preparation and properties of the single crystalline AB₂-type selenides and tellurides of niobium, tantalum, molybdenum and tungsten, *J. Inorg. Nucl. Chem.* **24**, 257 (1962).
- [53] W. J. Schutte, J. L. De Boer, and F. Jellinek, Crystal structures of tungsten disulfide and diselenide, *J. Solid State Chem.* **70**, 207 (1987).
- [54] V. L. Kalikhman, *Neorganicheskie Materialy* **19**, 1060 (1983).
- [55] A. A. Yanaki and V. A. Obolonchik, *Inorg. Mater.* **9**, 1855 (1973).
- [56] X. Gonze, G.-M. Rignanese, M. Verstraete, J.-M. Beuken, Y. Pouillon, R. Caracas, F. Jollet, M. Torrent, G. Zerah, M. Mikami, Ph. Ghosez, M. Veithen, J.-Y. Raty, V. Olevano, F. Bruneval, L. Reining, R. Godby, G. Onida, and D. R. Hamann, and D. C. Allan, A brief introduction to the ABINIT software package, *Zeitschrift für Kristallographie - Crystalline Materials* **220**, 558 (2005).
- [57] Marc Torrent, François Jollet, François Bottin, Gilles Zerah, and Xavier Gonze, Implementation of the projector augmented-wave method in the ABINIT code: Application to the study of iron under pressure, *Comput. Mater. Sci.* **42**, 337 (2008).
- [58] X. Gonze *et al.*, ABINIT: First-principles approach to material and nanosystem properties, *Comput. Phys. Commun.* **180**, 2582 (2009).
- [59] X. Gonze *et al.*, Recent developments in the ABINIT software package, *Comput. Phys. Commun.* **205**, 106 (2016).
- [60] Florian Belviso, Antonio Cammarata, Jamil Missaoui, and Tomas Polcar, Effect of electric fields in low-dimensional materials: Nanofrictional response as a case study, *Phys. Rev. B* **102**, 155433 (2020).
- [61] John P. Perdew, Kieron Burke, and Matthias Ernzerhof, Generalized Gradient Approximation Made Simple, *Phys. Rev. Lett.* **77**, 3865 (1996).
- [62] Axel D. Becke and Erin R. Johnson, A simple effective potential for exchange, *J. Chem. Phys.* **124**, 221101 (2006).
- [63] Hendrik J. Monkhorst and James D. Pack, Special points for brillouin-zone integrations, *Phys. Rev. B* **13**, 5188 (1976).
- [64] See Supplemental Material at <http://link.aps.org/supplemental/10.1103/PhysRevApplied.15.064041> for section "Geometry of the Z:MX₂ stable structures".
- [65] Atsushi Togo and Isao Tanaka, First principles phonon calculations in materials science, *Scr. Mater.* **108**, 1 (2015).
- [66] Laurent Chaput, Atsushi Togo, Isao Tanaka, and Gilles Hug, Phonon-phonon interactions in transition metals, *Phys. Rev. B* **84**, 094302 (2011).
- [67] K. Parlinski, Z. Q. Li, and Y. Kawazoe, First-Principles Determination of the Soft Mode in Cubic ZrO₂, *Phys. Rev. Lett.* **78**, 4063 (1997).
- [68] Antonio Cammarata and Tomas Polcar, Layering effects on low frequency modes in n-layered MX₂ transition

- metal dichalcogenides, *Phys. Chem. Chem. Phys.* **18**, 4807 (2016).
- [69] Antonio Cammarata and Tomas Polcar, Vibrational contributions to intrinsic friction in charged transition metal dichalcogenides, *Nanoscale* **9**, 11488 (2017).
- [70] D. M. Wallace, *Thermodynamics of Crystals* (John Wiley & Sons Inc, United States of America, 1972).
- [71] J. M. Ziman, *Electrons and Phonons: The Theory of Transport Phenomena in Solids* (Oxford University Press, London, 2001).
- [72] J. Safko, H. Goldstein and C. Poole, *Classical Mechanics* (Pearson Education, New York, 2002) 3rd ed. p. 238.
- [73] Antonio Cammarata and Tomáš Polcar, Tailoring nanoscale friction in MX_2 transition metal dichalcogenides, *Inorg. Chem.* **54**, 5739 (2015).
- [74] Antonio Cammarata and Tomas Polcar, Overcoming nanoscale friction barriers in transition metal dichalcogenides, *Phys. Rev. B* **96**, 085406 (2017).
- [75] Antonio Cammarata, Paolo Nicolini, Kosta Simonovic, Egor Ukraintsev, and Tomas Polcar, Atomic-scale design of friction and energy dissipation, *Phys. Rev. B* **99**, 094309 (2019).
- [76] Antonio Cammarata and James M. Rondinelli, Covalent dependence of octahedral rotations in orthorhombic perovskite oxides, *J. Chem. Phys.* **141**, 114704 (2014).
- [77] M. J. Han, C. A. Marianetti, and A. J. Millis, Chemical control of orbital polarization in artificially structured transition-metal oxides: La_2NiXO_6 ($X = \text{b, al, ga, in}$) from first principles, *Phys. Rev. B* **82**, 134408 (2010).
- [78] Antonio Cammarata and James M. Rondinelli, Octahedral engineering of orbital polarizations in charge transfer oxides, *Phys. Rev. B* **87**, 155135 (2013).
- [79] Antonio Cammarata and Tomas Polcar, Electro-vibrational coupling effects on "intrinsic friction" in transition metal dichalcogenides, *RSC Adv.* **5**, 106809 (2015).
- [80] Graeme Henkelman, Blas P. Uberuaga, and Hannes Jónsson, A climbing image nudged elastic band method for finding saddle points and minimum energy paths, *J. Chem. Phys.* **113**, 9901 (2000).
- [81] Graeme Henkelman and Hannes Jónsson, Improved tangent estimate in the nudged elastic band method for finding minimum energy paths and saddle points, *J. Chem. Phys.* **113**, 9978 (2000).
- [82] G. Kresse and J. Furthmüller, Efficiency of ab-initio total energy calculations for metals and semiconductors using a plane-wave basis set, *Comp. Mater. Sci.* **6**, 15 (1996).
- [83] G. Kresse and D. Joubert, From ultrasoft pseudopotentials to the projector augmented-wave method, *Phys. Rev. B* **59**, 1758 (1999).

Control of energy dissipation in sliding low-dimensional materialsAntonio Cammarata¹* and Tomas Polcar*Department of Control Engineering, Faculty of Electrical Engineering, Czech Technical University in Prague, Technicka 2, 16627 Prague 6, Czech Republic*

(Received 28 April 2020; revised 16 July 2020; accepted 27 July 2020; published 7 August 2020)

Frictional forces acting during the relative motion of nanosurfaces are the cause of energy loss and wear which limit an efficient assembly and yield of atomic-scale devices. In this research, we investigate the microscopic origin of the dissipative processes as a result of the frictional response, with the aim to control them in a subtle way. We recast the study of friction in terms of phonon modes of the system at the equilibrium, with no need to resort to dynamics simulations. As a case study, we here consider layer sliding in transition metal dichalcogenides thin films. We find that the population of specific atomic orbitals and the relative contribution of the atomic type to selected system vibrations are the crucial quantities which determine the frictional response in tribological conditions. A reduced amount of energy dissipation is found when the bond character is more ionic and the layer sliding is realized by a faster motion of the chalcogen atoms. The individuated relevant parameters governing the energy dissipation can be used as descriptors in high-throughput calculations or machine learning engines to screen databases of frictional materials. The presented framework is general and can be promptly extended to the design of tribological materials with targeted frictional response, irrespective of the chemistry and atomic topology.

DOI: [10.1103/PhysRevB.102.085409](https://doi.org/10.1103/PhysRevB.102.085409)**I. INTRODUCTION**

Manipulation and assembly of free-standing atomic layers into final devices, and their use in micro/nanoelectromechanical systems (MEMS/NEMS, e.g., sensors and actuators) require a deep knowledge and control of their frictional response and related energy dissipation characteristics [1]. Moving parts during device fabrication and operation are subject to nonconservative forces active during the relative motion of the involved surfaces; those forces limit the output efficiency by producing heat, fatigue and wear up until compromising the correct construction or functioning of the device. Indeed, the comprehension of mechanisms governing friction at the nanoscale is a forefront challenge to save energy and increase the lifetime and sustainability of miniaturized devices, in addition to improving their performance [2]. To this aim, in the present work we investigate the atomic detail of the dissipative processes generated by frictional forces occurring during relative motions of few atomic layers.

Several classical and quantum mechanical approaches have already been developed to study friction at the atomic scale, by considering both *ad hoc* defined interatomic force formulations and parameter-free *ab initio* descriptions [3–6]. The reliability of such approaches is a compromise between the accuracy of the system-dependent parametrizations and/or the width of the simulated time-window—this last being computationally expensive if *ab initio* methods are used [7–13]. We here follow a different approach, with the goal being to ob-

tain information on frictional and dissipative properties by the only knowledge of the static properties of the system, without the need to perform long and costly dynamic simulations; furthermore, we use a system-independent framework which is applicable to any kind of chemistry and atom topology. The approach that we adopt is based on the phonon modes calculated on the stable geometry; indeed, recent works have already drawn attention to the role of phonons in determining the frictional properties of tribological systems [14,15].

We already showed that any sequence of geometric configurations representing the layer sliding can be decomposed in terms of polarization vectors obtained by diagonalization of the dynamical matrix at any point of the reciprocal space [16,17]. This allowed us to recast the study of the frictional response in terms of *sliding* and *dissipative* phonon modes [18]. The sliding modes give rise to relative shifts of adjacent atomic layers. In terms of the classical picture, to each of these modes we can associate a harmonic restoring force $f \propto \omega^2$, where ω is the mode frequency; by lowering the mode frequency, it is then possible to lower the restoring force and hence facilitate the layer sliding. By going beyond the local harmonic description [18] we observed that the layer sliding occurs as long as the energy contained in the sliding modes (i.e., the phonon population) is above a certain threshold characteristic of the material. The *dissipative modes* instead are all those modes which subtract energy from the sliding modes by means of phonon recombination processes. Such processes correspond to energy dissipation since they degrade the ordered motion (sliding) into disordered vibrations (heat); in this way, we can define the *frictional forces* as those forces corresponding to phonon scattering events reducing the population of the sliding modes.

*cammaant@fel.cvut.cz

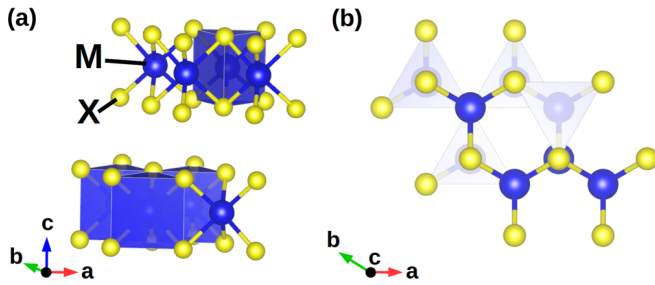


FIG. 1. (a),(b) Model structure of hexagonal $P6_3/mmc$ 2H polymorph of MX_2 TMD crystal. $M-X$ bonds form trigonal prisms arranged in parallel layers which can reciprocally slide thanks to weak van der Waals interactions.

In the present work, we discuss which are the relevant quantities that determine such energy dissipation, and how to act to deactivate specific dissipation channels. We also show that this can be achieved by using quantum mechanical static calculations on the fixed geometry of the stable system, thus saving computational time and investigation effort which would be required by standard dynamical approaches. As a case study, we consider layer sliding in transition metal dichalcogenides (TMDs) thin films, which are becoming ubiquitous in several technological applications spanning hydrogen evolution, energy storage, high-performance electronics, and photonic devices [19–21].

II. METHODS

A. Computational details

Transition metal dichalcogenides have general stoichiometry MX_2 , where M and X are a transition metal and a chalcogen atom, respectively. One M cation coordinates six chalcogen anions in a trigonal prismatic arrangement forming a periodic MX_2 layer with $M-X$ covalent bonds (Fig. 1). Adjacent layers are bound together by weak van der Waals forces which allow relative sliding under tribological conditions. We consider the 2H polymorph crystalline MX_2 compounds as reference structures [19], with $M = \text{Mo, W}$ and $X = \text{S, Se, Te}$, and hexagonal $P6_3/mmc$ symmetry (SG 194). The primitive unit cell of such geometry is formed by two adjacent layers arranged in such a way that a metal atom of one layer is aligned with two anions of the other one along the direction orthogonal to the layer planes (c -axis in our setting—see Fig. 1). Starting from the chosen reference geometries, we truncate the periodic image repetition along the c axis by setting the c lattice parameter at 65 Å, and consider only two, three, four, five, and six MX_2 subsequent layers. In this way, for each considered compound, we build five model systems that we name $MX-nL$, where M and X specify the kind of transition metal and chalcogen atom, respectively, while n corresponds to the number of MX_2 layers forming the unit cell; the corresponding space group is $P\bar{3}m1$ (#164) if n is odd and $P\bar{6}m2$ (#187) if n is even.

We perform density functional theory (DFT) calculations using the Perdew-Burke-Ernzerhof (PBE) energy functional [22] as implemented in VASP software [23,24]. We also take into account van der Waals interactions using the Grimme

correction [25], which correctly reproduces the structural features, as we reported in previous works and references therein [16,26,27]. The Brillouin zone is sampled with a minimum of a $7 \times 7 \times 1$ k -point mesh and plane wave cutoff of 500 eV. Full structural (atoms and lattice) relaxations are initiated from diffraction data [28–33] and the forces minimized to a 0.5 meV \AA^{-1} tolerance. We diagonalize the dynamical matrices of the stable systems with the aid of the PHONOPY software [34] and compute the first-order anharmonic phonon-phonon interaction strengths by means of the PHONO3PY software [35].

B. Theoretical background

In tribological conditions, the relative motion among subsequent MX_2 layers can be geometrically described in terms of eigendisplacements associated to the phonon modes of the stable geometry [16,17]. If we consider a system with N atoms, the degrees of freedom of the system is $3N$, with each atom being free to move along all the three spatial directions. At any \mathbf{q} vector of the Brillouin zone of the system, the diagonalization of the dynamical matrix yields $3N$ eigenvectors, each characterized by a polarization vector describing the atomic displacement pattern (i.e., the phonon mode pattern). The $3N$ eigenvectors are orthogonal and constitute a basis for the geometric description of the system; there is therefore a one-to-one correspondence between the degrees of freedom of a system and the eigendisplacements relative to any \mathbf{q} reciprocal vector [36], and any set of atomic displacements can then be represented as a linear combination of phonon modes. The projection of the geometric sequence representing the layer sliding onto the phonon eigenvectors allows to identify which phonons have the main role in the representation of the sliding motion: they are those with the largest coefficient in the linear combination, and we can name them as *sliding* modes. This phonon-based description of the layer sliding is not only a convenient geometric picture, but also provides fundamental information about the role of the phonons during the whole tribological process. This is apparent in the frequency analysis of dynamical trajectories [18]: sliding modes are active during the sliding motion while become silent once the sliding terminates. Layer sliding is active as long as the sliding modes own enough energy: scattering processes reduce the population of the sliding modes until the ordered motion (i.e., sliding) is completely downgraded to thermal vibration (i.e., heat) and the equilibrium is reached. The decomposition of sliding trajectories into phonon modes allows one to distinguish then between *sliding* and *dissipative* modes: the former are those who have an effective geometric contribution to the layer drift, while the latter reduce the population of the sliding ones via phonon-phonon recombination processes. In this description, the frictional forces are then all those forces which activate recombination processes that reduce the population of the sliding modes. In general, the main effect of friction during sliding is to increase the temperature of the system, while others like free charge production or structural deformations are minor ones; in our phonon-based description, we neglect such minor effects and frictional forces have the only consequence to convert work (ordered motion of the atoms represented by

the sliding) into thermal vibrations, hence heat which rises the temperature of the system.

It is worth noting that we do not need to make any assumption on the sliding direction since such information is automatically transferred into the eigenvector linear combination by the projection of the cartesian displacements onto the polarization vectors. Moreover, the roughness of interfaces and presence of defects can be straightforwardly included in the present approach without the need for specific working hypotheses, provided that such irregularities are represented by an appropriate choice of the atomic geometry and supercell size. However, our representation is valid if the set of phonon eigenvectors constitute a good description of the system in tribological conditions, that is, if the equilibrium atomic topology is not dramatically modified during the sliding events [18].

By indicating with $\lambda = (\mathbf{q}, j)$ a phonon mode with wave vector \mathbf{q} and band index j , the decrease of the population of the sliding mode λ occurs at a transition rate $\mathcal{P}_{\lambda, \lambda'}^{\lambda''}$ involving the λ' and λ'' dissipative modes, and is proportional to the square of the interaction strength $\Phi_{\lambda\lambda'\lambda''}$ [37]:

$$\mathcal{P}_{\lambda, \lambda'}^{\lambda''} \propto n n' (n'' + 1) |\Phi_{\lambda\lambda'\lambda''}|^2, \quad (1)$$

where n , n' and n'' are the phonon populations, while $\Phi_{\lambda\lambda'\lambda''}$ is a characteristic of the system. The phonon populations depend on the environment, e.g., the presence of thermal bath and irradiation or external intervention manifesting as external forces, load, and controlled sliding velocity. Such external parameters depend on the user, who can employ them to dynamically control the dissipation channels. We are here interested instead in modifying the intrinsic properties of the system to inhibit or mitigate specific dissipative processes, irrespective of the environment conditions. In fact, irrespective of the n , n' , and n'' populations, if $|\Phi_{\lambda\lambda'\lambda''}|^2$ is null, likewise the scattering probability in Eq. (1) is null and no dissipation will occur. A fine-tuning of the interaction strength tensor $\Phi_{\lambda\lambda'\lambda''}$ then allows to design tribological materials with controlled frictional response: as $|\Phi_{\lambda\lambda'\lambda''}|^2$ becomes lower, the $\lambda + \lambda' = \lambda''$ scattering becomes less probable and the lifetime of the sliding phonon λ increases. This implies that the magnitude of an external drift force needed to keep the sliding active is small when low values of $|\Phi_{\lambda\lambda'\lambda''}|^2$ are realized.

The interaction strength tensor $\Phi_{\lambda\lambda'\lambda''}$ is an intrinsic property of the material since it is determined by the atomic kinds and geometry forming the system which, in turn, determine the eigenvectors, eigenfrequencies, and interatomic force constants [36,37]:

$$\begin{aligned} \Phi_{\lambda\lambda'\lambda''} &= \sqrt{\frac{\hbar^3}{8N^3}} \frac{1}{\sqrt{\omega_\lambda \omega_{\lambda'} \omega_{\lambda''}}} \sum_{kk'k''} \frac{1}{\sqrt{m_k m_{k'} m_{k''}}} \\ &\times \sum_{\alpha\beta\gamma} e_\lambda^\alpha(\mathbf{r}_k) e_{\lambda'}^\beta(\mathbf{r}_{k'}) e_{\lambda''}^\gamma(\mathbf{r}_{k''}) \\ &\times \sum_{l'l''} e^{i\mathbf{q}\cdot\mathbf{r}_{kl}} e^{i\mathbf{q}'\cdot\mathbf{r}_{k'l'}} e^{i\mathbf{q}''\cdot\mathbf{r}_{k''l''}} \Phi_{\alpha\beta\gamma}(\mathbf{r}_{kl}, \mathbf{r}_{k'l'}, \mathbf{r}_{k''l''}), \end{aligned} \quad (2)$$

where \hbar is the reduced Planck's constant, N is the number of unit cells, ω_λ is the eigenfrequency of the mode λ , m_k is the mass of the k th atom, \mathbf{r}_{kl} ($\mathbf{r}_{k'l'}$, $\mathbf{r}_{k''l''}$) is the position of the k th

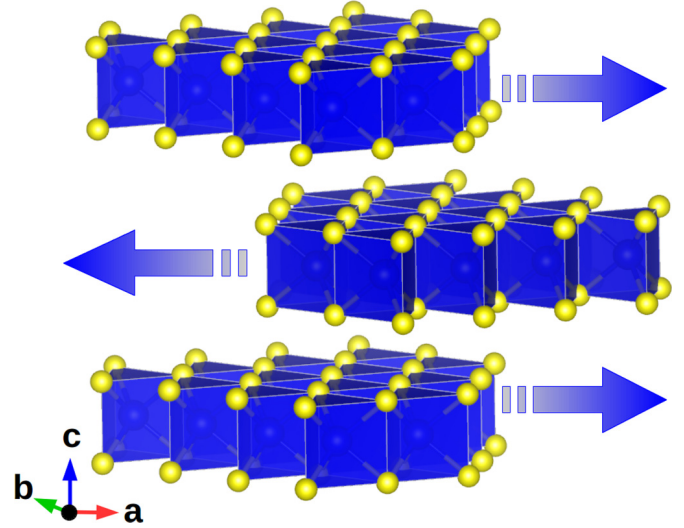


FIG. 2. Schematic example of one of the possible sliding modes in MX_3 - $3L$ systems: three adjacent MX_2 layers rigidly shifts along opposite directions according to the eigenvector $\mathbf{e}_{\Gamma,6}$.

(k' th, k'' th) atom in the l th (l' th, l'' th) cell replica, $e_\lambda^\alpha(\mathbf{r}_k)$ is the α th Cartesian component of the eigenvector associated to the mode λ and to the k th atom, and $\Phi_{\alpha\beta\gamma}$ is the third-rank Cartesian tensor of the cubic anharmonic force constants. We already observed [38] that it is possible to turn off or on any $\lambda + \lambda' = \lambda''$ scattering process by controlling the symmetries of the system; in fact, if Γ^{e_λ} , $\Gamma^{e_{\lambda'}}$, and $\Gamma^{e_{\lambda''}}$ are irreducible representations for which the eigenvectors \mathbf{e}_λ , $\mathbf{e}_{\lambda'}$, $\mathbf{e}_{\lambda''}$ are, respectively, a basis, then

$$\Phi_{\lambda\lambda'\lambda''} \neq 0 \Rightarrow \Gamma^{e_\lambda} \otimes \Gamma^{e_{\lambda'}} \otimes \Gamma^{e_{\lambda''}} \subseteq A, \quad (3)$$

which states that if the direct product among the irreducible representations contains the totally symmetric representation A , then the $\lambda + \lambda' = \lambda''$ scattering is allowed. Indeed, this result is general and applies to any multiphonon scattering at any order of anharmonicity. In what follows, we show that an other way to control the value of $\Phi_{\lambda\lambda'\lambda''}$ is to act on the subtle relation between the electronic density and the dynamic properties of the system.

In all the MX_n - nL systems, the sliding modes with main contribution to relative layer shift have wave vector $\mathbf{q} = (0, 0, 0) \equiv \Gamma$ and band indices which depend on n [38] (see Fig. 2 as an example; a schematic representation of the sliding modes at different n can be found in the Supporting Material of Ref. [38]). The number of sliding modes depends on the number of layers: the higher n , the higher the number of modes effectively contributing to the sliding, the higher the number of dissipative modes and corresponding dissipation channels. To track all the dissipative processes, we then consider the quantity $|\Phi|^2$, which we define as the sum of the squared modulus of all the $\Phi_{\lambda\lambda'\lambda''}$ elements involving both λ sliding and λ' , λ'' dissipative modes. By controlling $|\Phi|^2$, we can then control the energy dissipation in tribological conditions at the nanoscale. A quick inspection of Eq. (2) shows that $\Phi_{\lambda\lambda'\lambda''}$ can be decreased by simply choosing atoms with higher atomic masses m_k via isotope substitution: however, this would cause a decrease of the eigenfrequencies ω_λ , the

two quantities being related by a relation of the kind $\omega \propto 1/\sqrt{m}$. Instead, we will focus on the choice of the atomic type, which is the most adopted solution in practical applications.

The crucial quantity that determines $\Phi_{\lambda\lambda'\lambda''}$ is the third-order tensor of the anharmonic force constants defined as

$$\begin{aligned} \Phi_{\alpha\beta\gamma}(\mathbf{r}_{kl}, \mathbf{r}_{k'l'}, \mathbf{r}_{k''l''}) &= \frac{\partial^3 V}{\partial r_{kl} \partial r_{k'l'} \partial r_{k''l''}} \\ &= \frac{\partial^2}{\partial r_{k'l'} \partial r_{k''l''}} \left(\frac{\partial V}{\partial r_{kl}} \right), \end{aligned} \quad (4)$$

where V is the potential energy which is a function of the atomic positions. The term

$$\frac{\partial V}{\partial \mathbf{r}_{kl}} = -\mathbf{F}(\mathbf{r}_{kl}) \quad (5)$$

is obtained by calculating the forces $\mathbf{F}(\mathbf{r}_{kl})$, which depend on the kind of atoms and the topologic environment in which they are embedded. The accuracy with which such forces are calculated affects the estimation accuracy of the dissipative processes; *ab initio* descriptions of the interatomic forces should then be preferred whenever computationally affordable, especially if subtle electronic effects must be taken into account. This also shows that the atomic type, the geometry, and the consequent electronic distribution, determine concurrently the final $\Phi_{\lambda\lambda'\lambda''}$ values in a nontrivial way. Since it is not simple to map the behavior of $\Phi_{\lambda\lambda'\lambda''}$ against the atomic kind, we need to identify proper collective descriptors to guide us through the complex interplay between the electronic structure and the dynamic features of the system. To this aim, we will investigate what are the relations among phononic states, electronic density, and phonon-phonon interactions.

III. RESULTS AND DISCUSSION

We begin our analysis by noticing that, at fixed chemical composition, no significant variation of the a and b lattice parameters is observed with the number of layers. Irrespective of the kind of M and X ions, $|\Phi|^2$ monotonically increases with increasing n [Fig. 3(a)], in correspondence with the increase of the number of active dissipation channels. We then define $\bar{\omega}$ as the average frequency of the sliding modes, with the aim to capture how the eigenfrequencies determine the value of $|\Phi|^2$ at different number of layers. We observe that $\bar{\omega}$ is globally decreasing with n but the trend is not monotonic [Fig. 3(b)]; indeed, at a fixed number of layers, higher $|\Phi|^2$ is realized at higher frequencies [Figs. 3(c) and 3(d)], against the intuitive trend suggested by Eq. (2), where the eigenfrequencies appear at the denominator of the expression of $\Phi_{\lambda\lambda'\lambda''}$. Since by fixing n we are making a comparison at a fixed topology, the \mathbf{e}_λ vectors do not change significantly; the anharmonic force constants have then a key role in governing $\Phi_{\lambda\lambda'\lambda''}$ since, in this case, they depend only on the atomic kinds and how these determine the electronic density. To get more insight on how to control $|\Phi|^2$, we then need to analyze in detail the subtleties of the electronic distribution. To this aim, we analyze the covalency [39] $C_{M,X}$ of the $M-X$ bond, defined in terms of atomic contributions to the system wave function. The higher the $C_{M,X}$ value, the larger the covalent character of the $M-X$ bond; equivalently, the lower the $C_{M,X}$ value, the more ionic

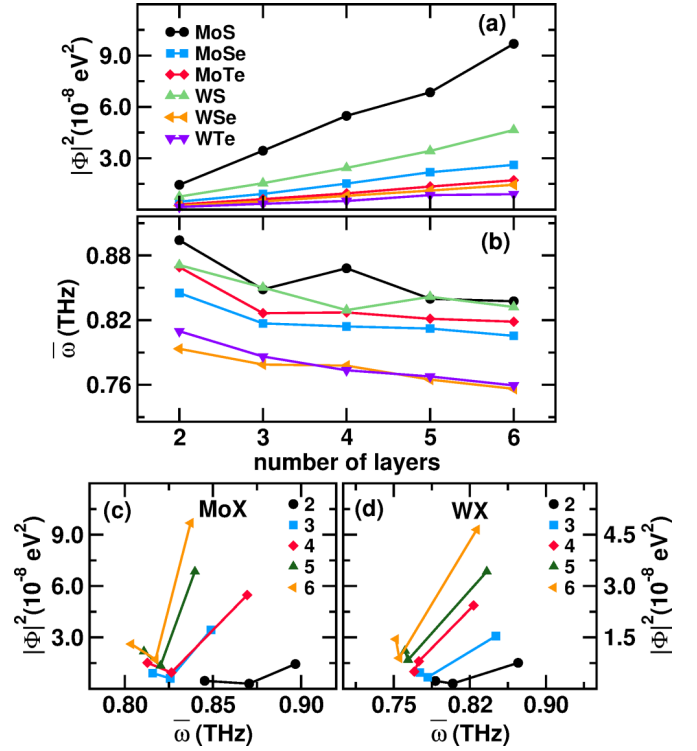


FIG. 3. (a) Sum of the square modulus of the interaction strengths involving both sliding and dissipative modes against the number of layers: the number of dissipation channels increases with n , producing an increase of the dissipated energy. (b) Average frequency of the sliding modes against the number of layers: at fixed composition the trend is not monotonic with n , showing the nontrivial relation between electronic and dynamic features of the systems; symbols are the same as in (a). (c),(d) $|\Phi|^2$ values of $\text{MoX-}n\text{L}$ and $\text{WX-}n\text{L}$ systems against eigenfrequency average comprising both sliding and dissipative modes: higher dissipation may be realized at higher frequencies due to the competition between ω_λ and $\Phi_{\alpha\beta\gamma}$ values; the value of n is indicated by the different symbols as shown in the legend. Lines are a guide for the eye.

the $M-X$ bond. We observe that the covalency can be considered constant with the number of layers [Fig. 4(a)]; the same result is obtained when we consider the difference among the atomic charges obtained either by integration of the atom-projected density of states or by performing a Bader analysis [40–43]. Irrespective of chemical composition and number of layers, we find that the more covalent the $M-X$ bond, the higher the $|\Phi|^2$ values hence the higher is the energy dissipation during layer sliding [Figs. 4(b) and 4(c)]. Concerning the dynamic aspect, at fixed n highest $M-X$ bond covalency realizes highest average frequencies $\bar{\omega}$ (Fig. 5); however, as we already observed, an increase of the $M-X$ bond covalency produces an increase of the dissipation [Figs. 3(b) and 3(c)], against the fact that the eigenfrequencies ω_λ appear at the denominator of the expression of $\Phi_{\lambda\lambda'\lambda''}$ [Eq. (2)]. This then confirms that the dominant contributions to the $\Phi_{\lambda\lambda'\lambda''}$ values are represented by the interatomic force constants. Analysis of the electron localization functions [44,45] does not show any strong evidence of charge redistribution along the $M-X$ bond at varying chemical composition [46]. This is the result of the subtle interplay between geometry, atomic kind, and

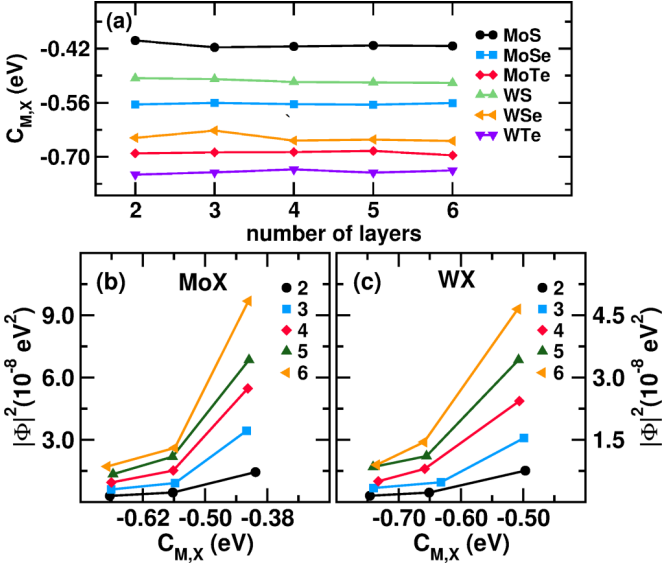


FIG. 4. (a) M - X bond covalency against the number of layers: at fixed composition, covalency does not change noticeably with varying n . (b),(c) $|\Phi|^2$ values of $\text{MoX-}n\text{L}$ and $\text{WX-}n\text{L}$ systems against the M - X bond covalency: irrespective of the chemical composition and the number of layers, more covalent bonds favor energy dissipation; the value of n is indicated by the different symbols as shown in the legend. Lines are a guide for the eye.

electronic distribution, which can be uncovered by a deeper investigation.

To this aim, we consider the orbital polarization [47–49] of the d and p orbital projections of the M and X ions, respectively [50].

Orbital polarization $\mathcal{P}_{l_1 m_{l_1}, l_2 m_{l_2}}$ of the $|l_1 m_{l_1}\rangle$ orbital relative to the $|l_2 m_{l_2}\rangle$ orbital is defined as

$$\mathcal{P}_{l_1 m_{l_1}, l_2 m_{l_2}} = \frac{n_{l_1 m_{l_1}} - n_{l_2 m_{l_2}}}{n_{l_1 m_{l_1}} + n_{l_2 m_{l_2}}}, \quad (6)$$

where $n_{l_1 m_{l_1}}$ and $n_{l_2 m_{l_2}}$ are the populations of $|l_1 m_{l_1}\rangle$ and $|l_2 m_{l_2}\rangle$, with orbital quantum number l_i and magnetic quantum number m_{l_i} , respectively. It measures the charge excess of the former orbital with respect to the latter: positive (negative) values indicate that $|l_1 m_{l_1}\rangle$ orbital is more (less) populated than $|l_2 m_{l_2}\rangle$ orbital. We observe that \mathcal{P}_{p_x, p_y} , \mathcal{P}_{p_x, p_z} and \mathcal{P}_{p_y, p_z}

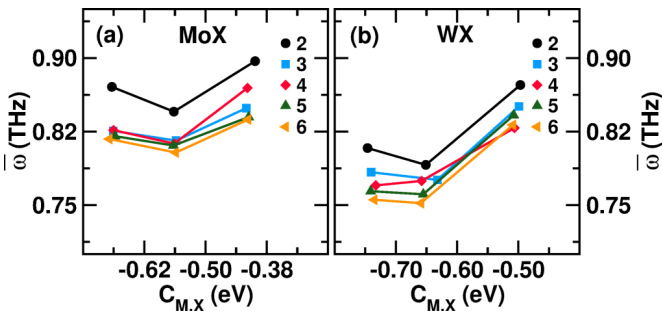


FIG. 5. Average frequency values of (a) $\text{MoX-}n\text{L}$ and (b) $\text{WX-}n\text{L}$ systems against the M - X bond covalency: higher frequencies are realized at increased values of the bond covalency. Lines are a guide for the eye.

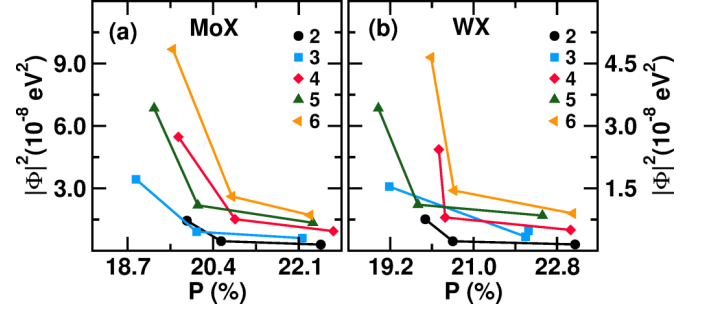


FIG. 6. $|\Phi|^2$ values of the (a) $\text{MoX-}n\text{L}$ and (b) $\text{WX-}n\text{L}$ systems as a function of the $\mathcal{P}_{t_{2g}, e_g}$ orbital polarization. An excess of population in the t_{2g} orbitals reduce energy dissipation during layer sliding. Lines are a guide for the eye.

is almost constant with the number of layers, while the greatest variation is observed for $\mathcal{P}_{t_{2g}, e_g}$ and $\mathcal{P}_{x^2-y^2, z^2}$. The symmetries of the system determine the relative occupation of the d orbitals: $\mathcal{P}_{t_{2g}, e_g}$ is higher (lower) for even (odd) number of layers; correspondingly, $\mathcal{P}_{x^2-y^2, z^2}$ has the opposite trend, while an exception is found for the WSe-3L system. A deeper analysis is needed to shed light on the origin of such behavior but for our purposes is not necessary and we will not investigate on it in this work. We already observed that the relative occupation of t_{2g} and e_g orbitals plays an important role in the determination of the sliding dynamics in TMDs [26,49]; indeed, we find that an excess of electrons in the t_{2g} orbitals, reduces the $|\Phi|^2$ values hence the energy dissipation during layer sliding (Fig. 6). The delicate balance among the orbital populations determine the value of the covalency. At a fixed number of layers, lowest covalency is realized

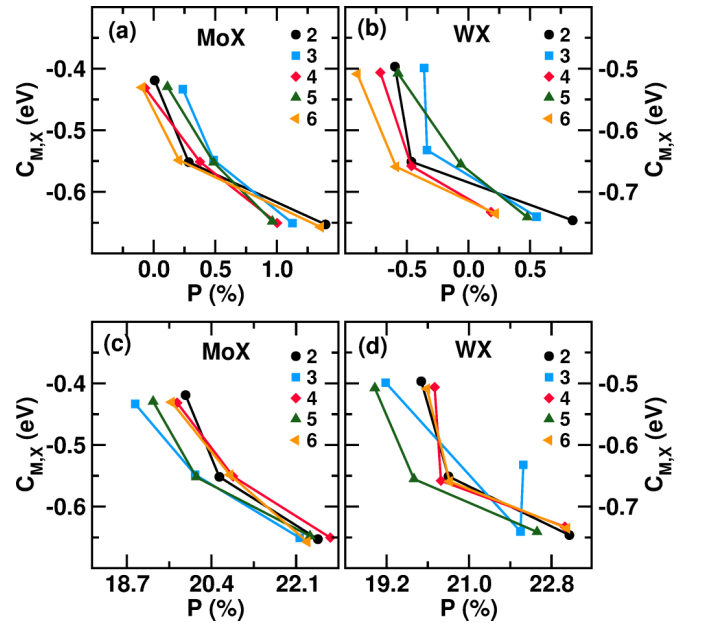


FIG. 7. Covalency of the MX bond against the orbital polarization of $\text{MoX-}n\text{L}$ and $\text{WX-}n\text{L}$ systems: (a),(b) X \mathcal{P}_{p_x, p_y} , (c),(d) M $\mathcal{P}_{t_{2g}, e_g}$. Lowest covalency values are in general realized when the population unbalance between the considered atomic orbitals is the largest. Lines are a guide for the eye.

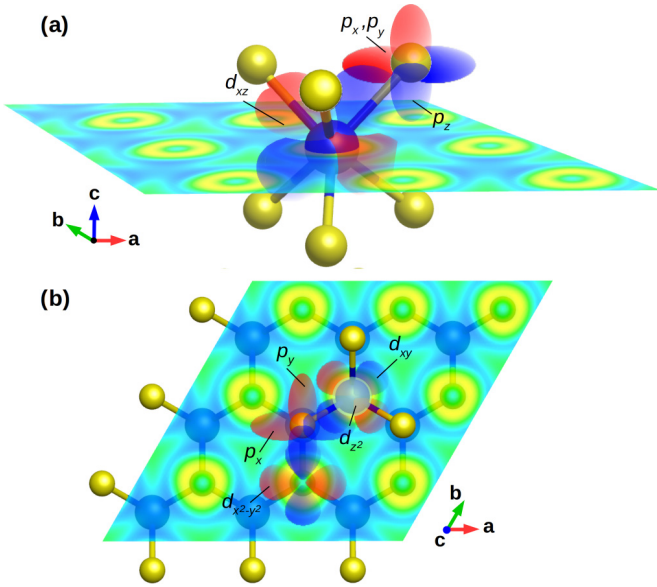


FIG. 8. Schematic of the electronic density projected on t_{2g} and p orbitals, depicted as red and blue lobes and centered on the M and X atoms, respectively; the plane containing the M cations is represented as a section of the electronic density, with RGB gradient showing density isovalues (red = highest, blue = lowest). The t_{2g} and p overlap is small, since the most of the t_{2g} orbitals extend into the region outside the $M-X$ bond axis; a charge shift towards the t_{2g} orbitals then makes the $M-X$ bond character more ionic. (a) Overlap among d_{xz} (and d_{yz} not shown for clarity), p_x and p_y is realized only by partial interpenetration of the orbital boundaries; (b) the same holds for the d_{xy} and p orbitals. The $d_{x^2-y^2}$ and p_y overlap is more effective and an increase of their population makes the bond character more covalent. The d_{z^2} orbital does not participate to the bond formation.

when the p_x orbital results to be slightly more populated with respect to the p_y orbital [Figs. 7(a) and 7(b)]; at the same time, low covalency values are in general realized when the population unbalance of the t_{2g} and e_g orbitals is the largest possible [Figs. 7(c) and 7(d)]. High values of \mathcal{P}_{p_x, p_y} and $\mathcal{P}_{t_{2g}, e_g}$ hence determine the formation of more ionic $M-X$ bonds (Fig. 8) which lower the energy dissipation during sliding, in agreement with what we observed above [Figs. 4(b), 4(c), and 6].

We now need a descriptor which is able to parametrize the atomic types and their contribution to the sliding dynamics of the system. To this aim, we will use the cophonycity metric [16] defined in terms of atom-projected phonon density of states. We evaluate the cophonycity $C_{ph}(M-X)$ of the $M-X$ pair in the frequency range $[0,1]$ THz, which corresponds to the eigenvectors with the highest contribution to the layer sliding. We observe that, irrespective of the chemical composition, cophonycity does not change significantly with the number of layers [Fig. 9(a)]. Positive $C_{ph}(M-X)$ values indicate that M and X ions contribute more to higher- and lower-frequency displacements, respectively; this means that M cations move faster than X anions when forming the global layer sliding motion, while the opposite holds for negative $C_{ph}(M-X)$ values. On the other hand, cophonycity close to zero corresponds to atomic displacements in which both M and X species move

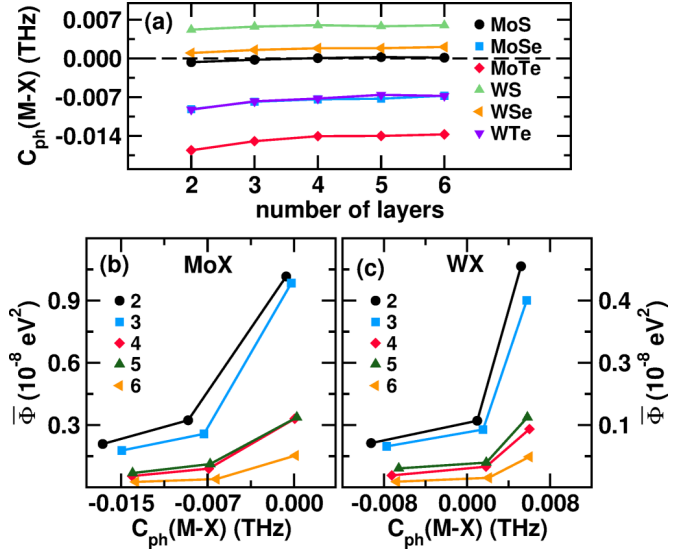


FIG. 9. (a) Cophonycity of the $M-X$ pair as a function of the number of layers; no significant variation is observed at fixed composition by varying n . (b, c) $|\Phi_{\lambda\lambda'\lambda''}|^2$ values of $\text{MoX-}n\text{L}$ and $\text{WX-}n\text{L}$ systems against the $M-X$ pair cophonycity; lowest cophonycity favors low-energy dissipation during layer sliding. Lines are a guide for the eye.

in average at the same speed. At a fixed number of layers, lowest cophonycity realises lowest $|\Phi|^2$ values at fixed cation type [Figs. 9(b) and 9(c)], suggesting that when anions displace faster than cations, the frictional force and the corresponding energy dissipation is lower. This dynamical effect is connected to the spatial extent and directionality of the electronic distribution. In fact, at fixed n , $C_{ph}(M-X)$ is monotonically increasing with $C_{M,X}$ [Figs. 10(a) and 10(b)]; at the same time, $C_{ph}(M-X)$ decreases with $\mathcal{P}_{t_{2g}, e_g}$ becoming negative, indicating that a charge transfer towards t_{2g} orbitals favors a faster motion of the X ions with respect to the M cations when forming the global sliding motion [Figs. 10(c) and 10(d)]. In other words, a higher t_{2g} population changes the character of the sliding motion from M -dominant to X -dominant contributions to the overall layer shift. In our previous works [16,27,49] we already used cophonycity to parametrize the atomic type and relate it to local harmonic forces which might contribute to the frictional response; here we can instead recognize that cophonycity can also be used to tune the anharmonic interactions which produce energy dissipation due to friction, hence going beyond the harmonic description.

Since covalency, cophonycity and orbital polarization descriptors appear to be tied together by simple monotonic relations, they can be easily fine-tuned to act as a knob to control $|\Phi|^2$, that is to control the energy dissipation due to the friction response during layer sliding. For example, we observed [16] that a specific $\text{Ti} \rightarrow \text{Mo}$ cation substitution in MoS_2 bulk induces local distortions in the ion environment which, in turn, determine a larger ionic bond character and a lower cophonycity. This coupled behavior resulted into a lowering of the sliding frequencies, and suggested that the individuated $\text{Ti} : \text{MoS}_2$ TMD phase should exhibit low friction when tangential external forces try to generate layer sliding. By following a similar approach, it is possible to

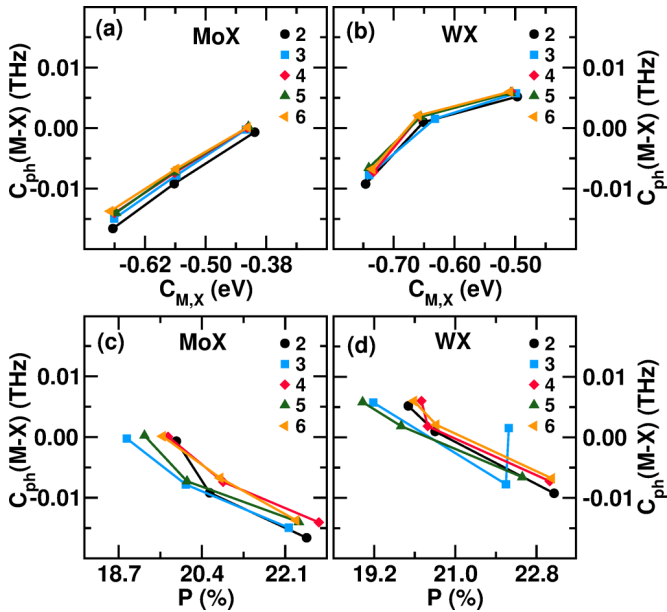


FIG. 10. (a),(b) Cophonicity of the $M-X$ pair of the $\text{MoX-}nL$ and $\text{WX-}nL$ systems as a function of the $M-X$ bond covalency: more covalent bond characters favor an increase of the $M-X$ cophonicity. (c),(d) Cophonicity of the $M-X$ pair as a function of the P_{t_{2g}, e_g} orbital polarization: an excess of electrons in the t_{2g} orbitals favor a decrease of the cophonicity values. Lines are a guide for the eye.

use the relation among covalency, cophonicity, and orbital polarization to select the proper atomic species to design new tribological materials with controlled energy dissipation. We finally notice that calculation of cophonicity, covalency, and orbital polarization is faster than the evaluation of the phonon-phonon strength of interaction $\Phi_{\lambda\lambda'\lambda''}$ since the latter requires the evaluation of atomic forces on hundreds of configurations each containing ~ 200 atoms. For this reason, the three descriptors can be used as a quick guide to select the proper atom to obtain low friction, or for fast high-throughput screening of potential low-dissipative layered materials.

IV. CONCLUSION

We showed how nonequilibrium dissipative processes arising in tribological conditions can be controlled by fine-tuning

the phonon-phonon interaction strengths, which are determined by the equilibrium configuration and atomic type of the system. In this way, it is possible to obtain information on the dynamic response without the need to run long and costly dynamic simulations. We applied our method to the study of layer sliding in transition metal dichalcogenides thin films. We recast the study of the frictional response in terms of sliding and dissipative phonons and observed that it is possible to tune the energy dissipation due to friction by fine tuning the sliding-dissipative phonon coupling. We found that an excess of charge in the t_{2g} orbitals of the M cation favors the formation of more ionic $M-X$ bonds and reduces the energy dissipation; dynamically, the cophonicity descriptor shows that the lowered dissipation is obtained thanks to a faster motion of the X atoms with respect to the M cations. Cophonicity, covalency, and P_{t_{2g}, e_g} orbital polarization are tied together by simple monotonic relations: the higher the t_{2g} orbital population, the more ionic the bond, the lower the cophonicity and the energy dissipation during sliding.

The combined use of electrostructural descriptors and phonon-based picture of the dissipative processes allows then to identify what are the relevant physical quantities to control the friction effect at the nanoscale. Such descriptors can also be used as parameters in high-throughput calculations or machine learning engines to screen large databases of compounds where anharmonic interactions are relevant. Finally, the presented approach is general and can be applied to the design of new tribological materials with targeted frictional response, irrespective of the chemistry and atomic topology.

ACKNOWLEDGMENTS

This work has been done with the support of the Czech Science Foundation (project No. 17-24164Y), and by the project ‘‘Novel nanostructures for engineering applications’’ No. CZ.02.1.01/0.0/0.0/16_026/0008396. This work was supported by The Ministry of Education, Youth and Sports from the Large Infrastructures for Research, Experimental Development and Innovations project ‘‘IT4Innovations National Supercomputing Center—LM2015070’’. The use of VESTA software [51,52] is also acknowledged.

- [1] E. Gnecco and E. Meyer, *Fundamentals of Friction and Wear on the Nanoscale*, 2nd ed., NanoScience and Technology (Springer International Publishing, Switzerland, 2015), p. 704.
- [2] A. Vakis, V. Yastrebov, J. Scheibert, L. Nicola, D. Dini, C. Minfray, A. Almqvist, M. Paggi, S. Lee, G. Limbert, J. Molinari, G. Ancaux, R. Aghababaei, S. E. Restrepo, A. Papangelo, A. Cammarata, P. Nicolini, C. Putignano, G. Carbone, S. Stupkiewicz, J. Lengiewicz, G. Costagliola, F. Bosia, R. Guarino, N. Pugno, M. Müser, and M. Ciavarella, *Tribol. Int.* **125**, 169 (2018).
- [3] A. Vanossi, N. Manini, M. Urbakh, S. Zapperi, and E. Tosatti, *Rev. Mod. Phys.* **85**, 529 (2013).
- [4] T. A. Sharp, L. Pastewka, and M. O. Robbins, *Phys. Rev. B* **93**, 121402(R) (2016).
- [5] D. Dietzel, J. Brndiar, I. Štich, and A. Schirmeisen, *ACS Nano* **11**, 7642 (2017).
- [6] A. Vanossi, D. Dietzel, A. Schirmeisen, E. Meyer, R. Pawlak, T. Glatzel, M. Kisiel, S. Kawai, and N. Manini, *Beilstein J. Nanotechnol.* **9**, 1995 (2018).
- [7] M. Igarashi, A. Natori, and J. Nakamura, *Phys. Rev. B* **78**, 165427 (2008).
- [8] W. K. Kim and M. L. Falk, *Phys. Rev. B* **80**, 235428 (2009).
- [9] P. Steiner, R. Roth, E. Gnecco, A. Baratoff, S. Maier, T. Glatzel, and E. Meyer, *Phys. Rev. B* **79**, 045414 (2009).

- [10] D. Perez, Y. Dong, A. Martini, and A. F. Voter, *Phys. Rev. B* **81**, 245415 (2010).
- [11] E. Cihan, S. Ipek, E. Durgun, and M. Z. Baykara, *Nat. Commun.* **7**, 12055 (2016).
- [12] M. Z. Baykara, M. R. Vazirisereshk, and A. Martini, *Appl. Phys. Rev.* **5**, 041102 (2018).
- [13] Z. Wei, Z. Duan, Y. Kan, Y. Zhang, and Y. Chen, *J. Appl. Phys.* **127**, 015105 (2020).
- [14] S. R. S. de Mello, M. E. H. M. da Costa, C. M. Menezes, C. D. Boeira, F. L. Freire, Jr., F. Alvarez, and C. A. Figueroa, *Sci. Rep.* **7**, 3242 (2017).
- [15] E. Panizon, G. E. Santoro, E. Tosatti, G. Riva, and N. Manini, *Phys. Rev. B* **97**, 104104 (2018).
- [16] A. Cammarata and T. Polcar, *Inorg. Chem.* **54**, 5739 (2015).
- [17] A. Cammarata and T. Polcar, *Phys. Rev. B* **96**, 085406 (2017).
- [18] A. Cammarata, P. Nicolini, K. Simonovic, E. Ukraintsev, and T. Polcar, *Phys. Rev. B* **99**, 094309 (2019).
- [19] M. Chhowalla, H. S. Shin, G. Eda, L.-J. Li, K. P. Loh, and H. Zhang, *Nat. Chem.* **5**, 263 (2013).
- [20] H. Tian, J. Tice, R. Fei, V. Tran, X. Yan, L. Yang, and H. Wang, *Nano Today* **11**, 763 (2016).
- [21] Y. Liu, N. O. Weiss, X. Duan, H.-C. Cheng, Y. Huang, and X. Duan, *Nat. Rev. Mater.* **1**, 16042 (2016).
- [22] J. P. Perdew, K. Burke, and M. Ernzerhof, *Phys. Rev. Lett.* **77**, 3865 (1996).
- [23] G. Kresse and J. Furthmüller, *Comp. Mater. Sci.* **6**, 15 (1996).
- [24] G. Kresse and D. Joubert, *Phys. Rev. B* **59**, 1758 (1999).
- [25] S. Grimme, *J. Comput. Chem.* **27**, 1787 (2006).
- [26] A. Cammarata and T. Polcar, *RSC Adv.* **5**, 106809 (2015).
- [27] A. Cammarata and T. Polcar, *Phys. Chem. Chem. Phys.* **18**, 4807 (2016).
- [28] B. Schönfeld, J. J. Huang, and S. C. Moss, *Acta Crystallogr. B* **39**, 404 (1983).
- [29] V. Kalikhman, *Inorg. Mater.* **19**, 957 (1983).
- [30] L. Brixner, *J. Inorg. Nucl. Chem.* **24**, 257 (1962).
- [31] W. Schutte, J. D. Boer, and F. Jelinek, *J. Solid State Chem.* **70**, 207 (1987).
- [32] V. L. Kalikhman, *Neorg. Mater.* **19**, 1060 (1983).
- [33] A. A. Yanaki and V. A. Obolonchik, *Inorg. Mater.* **9**, 1855 (1973).
- [34] A. Togo, F. Oba, and I. Tanaka, *Phys. Rev. B* **78**, 134106 (2008).
- [35] A. Togo, L. Chaput, and I. Tanaka, *Phys. Rev. B* **91**, 094306 (2015).
- [36] D. M. Wallace, *Thermodynamics of Crystals* (John Wiley & Sons., New York, 1972).
- [37] J. M. Ziman, *Electrons and Phonons: The Theory of Transport Phenomena in Solids* (Oxford University Press, New York, 2001).
- [38] A. Cammarata, *RSC Adv.* **9**, 37491 (2019).
- [39] A. Cammarata and J. M. Rondinelli, *J. Chem. Phys.* **141**, 114704 (2014).
- [40] W. Tang, E. Sanville, and G. Henkelman, *J. Phys.: Condens. Matter* **21**, 084204 (2009).
- [41] E. Sanville, S. D. Kenny, R. Smith, and G. Henkelman, *J. Comput. Chem.* **28**, 899 (2007).
- [42] G. Henkelman, A. Arnaldsson, and H. Jónsson, *Comput. Mater. Sci.* **36**, 354 (2006).
- [43] M. Yu and D. Trinkle, *J. Chem. Phys.* **134**, 064111 (2011).
- [44] A. D. Becke and K. E. Edgecombe, *J. Chem. Phys.* **92**, 5397 (1990).
- [45] A. Savin, O. Jepsen, J. Flad, O. K. Andersen, H. Preuss, and H. G. von Schnering, *Angew. Chem., Int. Ed. Engl.* **31**, 187 (1992).
- [46] See Supplemental Material at <http://link.aps.org/supplemental/10.1103/PhysRevB.102.085409> for more information on the section “Electron Localization Function Analysis”.
- [47] A. Cammarata and J. M. Rondinelli, *Phys. Rev. B* **87**, 155135 (2013).
- [48] M. J. Han, C. A. Marianetti, and A. J. Millis, *Phys. Rev. B* **82**, 134408 (2010).
- [49] A. Cammarata and T. Polcar, *Nanoscale* **9**, 11488 (2017).
- [50] See Supplemental Material at <http://link.aps.org/supplemental/10.1103/PhysRevB.102.085409> for more information on the section “Orbital Polarization Analysis”.
- [51] K. Momma and F. Izumi, *J. Appl. Cryst.* **41**, 653 (2008).
- [52] K. Momma and F. Izumi, *J. Appl. Crystallogr.* **44**, 1272 (2011).